THE NUMERICAL ANALYSIS OF TURBULENT FLOW

AROUND OFF-SHORE STRUCTURES

A thesis presented for the Degree of

Doctor of Philosophy

By

Ahmed Attia Ahmed MOUSTAFA

Division of Thermo-Fluid and Environmental Engineering

Department of Mechanical and Process Engineering

University of Strathclyde

Glasgow

January 1988

TO MY FAMILY

NAGWA, DINA AND KHALID

AND

MY PARENTS

ACKNOWLEDGMENTS

ABSTRACT

This study provides the physical, mathematical and numerical basis of analysis work performed for predicting the flow around three-dimensional bluff body configurations. The flow has been treated as steady, incompressible, turbulent. The predictions were made using a two-equation turbulence model, solving transport equations for turbulence kinetic energy K and the turbulence dissipation rate ξ, in addition to the partial differential equations for the conservation of mass and momentum.. The program used was the well tested computer code " PHOENICS-84 " based on work conducted by Prof. D.B. Spalding and Co-workers.

Several computations have been performed, for three models: a single cube, a pair of cubes with different spacing, and a rudimentary representation of an offshore oil platform stucture.

The prediction procedure was first tested for grid refinement and optimum solution domain size, until profiles at several locations for selected variables showed little change with further increase of domain size and grid points. The effect of different wind directions was investigated for the three models; in addition, different pitching conditions of the oncoming flow were also considered for the platform-model configurations.

Comparisons were made with wind tunnel test results on the same three models, and some discrepancies are noted,

particularly in regions of separated, recirculating flow. Also comparisons were made with certain empirical calculation procedures used for wind load estimation in maritime engineering. Overall wind loading is nevertheless reasonably well predicted.

Applications of the method in the area of wind loadings on a full scale offshore oil rig is discussed, and plans for refinement and extension of the present work are outlined. It is concluded that the present method can be used as a suitable starting point for generating a platform aerodynamics simulator. However, more work is required to this end, in order to represent adequately all aspects of platform-aerodynamics phenomena.

LIST OF CONTENTS

CHAPTER 1

INTRODUCTION

CHAPTER 2

SURVEY OF PREVIOUS WORK

CHAPTER 3

MATHEMATICAL ANALYSIS AND NUMERICAL TECHNIQUE

CHAPTER 4

PREDICTION OF 3-D TURBULENT FLOW OVER

RECTANGULAR BLUFF BODIES.

CHAPTER 5

PREDICTION OF 3-D TURBULENT FLOW OVER A

SIMPLE PLATFORM MODEL

CHAPTER   6

PREDICTION OF 3-D TURBULENT FLOW OVER A

FULL SCALE SEMI-SUBMERSIBLE.

CHAPTER   7

CONCLUSIONS AND RECOMMENDATIONS FOR FURTHER WORK..

LIST OF TABLES

LIST OF FIGURES

yaw angle.

NOMENCLATURE

Symbol	Meaning
a	express the influences of diffusion processes across cell boundaries (equation (3.26))
b	representation of the source term for all of the variables to be solved (equation (3.26))
C_c	side force coefficient
C_d	drag force coefficient
C_F	force coefficient
C_f	local skin-friction coefficient (Equ. 3.25)
C_ℓ	lift force coefficient
C_P	local pressure coefficient
C_x	axial body force coefficient
C_y	side body force coefficient
C_z	vertical body force coefficient
C_1, C_2 C_D, C_μ	turbulence constants (table 3.1)
E	roughness parameter (Equ. 3.22)
G	generation of turbulence kinetic energy (Equ3.18)
h	height of the cube model (chapter 4)
κ	kinetic energy of turbulence
k	Von Karman constant
L_d, L_u L_x, L_y	dimensions of solution domain (table 3.2)
ℓ	length scale of turbulence

ℓ_m	mixing length
ℓ_R	reattachment length
$\overset{\circ}{m}$	mass flow rate
n	normal to boundary
$\hat{P}$	instantaneous pressure
p	mean pressure
P	fluctuating pressure
P_∞	free stream static pressure
R_e	Reynolds number
R_ϕ	residual source (Equ. 3.28)
S_ϕ	source term (table 3.2)
T	time interval
t	time
U	mean velocity component in X-direction
$\hat{U}_i$	instantaneous velocity component
U'_i	mean velocity component
u	velocity fluctuation in X-direction
V	mean velocity component in Y-direction
v	velocity fluctuation in Y-direction
W	mean velocity component in Z-direction
w	velocity fluctuation in Z-direction
w^+	dimensionless near-wall velocity (Equ. 3.22)
X_j	cartesian coordinate
y	vertical cartesian coordinate
y_p	normal distance from the wall
y^+	normalised distance from the wall (Equ. 3.22)
$\propto$	wind yaw angle

θ	pitch angle
Γ_ϕ	exchange coefficient
ε	dissipation rate of kinetic energy
$\left.\begin{array}{l}\varepsilon_x \\ \varepsilon_y \\ \varepsilon_z\end{array}\right\}$	grid expansion ratios in X-, Y- and Z directions
μ	molecular viscosity
μ_{eff}	effective viscosity
ν	kinematic viscosity
ρ	fluid density
$\sigma_\kappa , \sigma_\varepsilon$	turbulence model constants (table 3.1)
τ_s	wall shear stress
ϕ	general dependent variable

1. INTRODUCTION

1.1 FLOW AROUND BLUFF BODIES.

In the past twenty years there have been some significant advances in our basic understanding of fluid flow around bluff bodies and in the application of this understanding to many practical problems of environmental and industrial fluid mechanics.

The bluff bodies studied in the atmosphere include hills, buildings, wind-energy devices, moving vehicles and aircraft, in the water environment, offshore structures and industrial problems, vortex flow, obstacles in pipes in nuclear reactors, baffles on the walls of mixing vessels, etc.

The advances in the basic understanding have come from

1) Laboratory studies of flow and diffusion around obstacles of simple shapes in uniform flow, shear flow, and laminar and turbulent boundary layers. These have been greatly helped by the use of new facilities for measuring these flows, new flow visualisation equipment (such as helium bubbles), new methods of measurement such as pulsed wire and laser Doppler anemometers (especially for high turbulence reversing flows) and fast response pressure measurements, and most importantly, new methods of analysis of data, both numerical and visual;

2) Field studies of air flow around large obstacles such as isolated buildings, hills and vehicles.

3) The growth in computer power has encouraged the development of sophisticated methods of computational analysis, to the extent that it is now possible to simulate complex three-dimensional turbulent flow problems to useful levels of accuracy. However, considerable caution must be exercised in the use of advanced numerical techniques and turbulence models, and skilled engineering judgement will continue to play a very important role in the interpretation of the results.

The aim of the present work is to provide the basis of a theoretical alternative to wind-tunnel testing of offshore structures to supplement the experimental testing, and to augment the usefulness of the wind tunnel. The benefits from an efficient and accurate " numerical wind tunnel" would be considerable in that it would allow the fast and economic prediction of such flow fields. Such predictions will lead to a better understanding of the factors influencing bluff body aerodynamics and can assist in improving the performance of existing designs, as well as influencing any consideration of new improved designs.

This thesis is concerned with steady, incompressible, turbulent flow over three-dimensional bluff bodies, as a step towards the application of the prediction procedure

to practical situations in engineering. The predictions were made using a two-equation turbulence model, solving transport equations for turbulence kinetic energy K and the turbulence dissipation rate ε, in addition to the mean velocity equations and an algebraic relation for an effective viscosity.

The program used was the version "PHOENICS-84" computer code developed by Prof.D.B.Spalding of Imperial college London, and co-workers, that has been successfully applied to a great variety of flow simulations, as testified by the papers contained in the proceedings of the first international PHOENICS Users conference (Sept. 1985) N.C. Markatos, D.C. Tatchell, M.Cross and N.Rhodes (1986).

1.2 CASES INVESTIGATED.

The aim of the present work is to assess the ability of the numerical method to model the aerodynamics of offshore-platforms. Four cases were investigated during the course of this work.

1) The first case was the 3-D turbulent flow over a cube, representing a typical deckhouse structure or element. The flow in this situation was examined with uniform velocity distribution in the incoming flow for the full range of wind yaw directions.

2) In the second case, the effects of shielding were examined for a full range of wind directions. For this case two identical cubes situated on the longitudinal axis with variable spacing were considered.

3) The third case was a simple four-legged platform model representing a rudimentry design of offshore platform. A number of the platform's features were changeable so that the sensitivity of the predicted wind loads to various platform parameters could be determined. As in cases (1) and (2), the effects of wind yaw angle were considered and additionally, the pitch angle of the incoming flow was varied.

4) The final case considered was a full scale "AKER H4.2" platform. This case was included to illustrate the use of PHOENICS in solving a more realistic problem.

4

However, the heavy demands on computational time made by this problem precluded the investigation of the effects of yaw and pitch angles.

Although the configurations examined are geometrically simple, the flow fields they provoke are comparatively complex and exhibit most, if not all, of the main features found in the practical situations.

Comparisons were made between predictions and experimental data for the first three cases, also comparisons were made with certain empirical calculation procedures used for wind load estimation in maritime engineering.

1.3. CONTENTS OF THE THESIS.

The thesis is divided into seven chapters of which three, chapters 4 to 6, contain the main contributions of the study. The background to the investigation is laid in chapter 2, which surveys relevant previous work. The literature was surveyed with two specific parts, in part one the experimental studies of 3-D bluff body flows were investigated to provide information for comparison with the present numerical results. The second part of the literature outlines previous efforts to predict laminar and turbulent flow over bluff bodies by approximate analytical or numerical methods.

Chapter 3, which provides the theoretical framework, begins by outlining the time averaged versions for the momentum conservation equations governing turbulent flow, and the associated boundary conditions. The chapter concludes with the presentation of the transport equations for kinetic energy and dissipation, whose solution, in conjunction with the momentum equations, enables the calculation of the turbulent Reynolds stresses.

Predictions for 3-D flows around single and double cubes situated on the longitudinal axis with variable spacing, representing a typical deckhouse structure are discussed in chapter 4. The predicted flow patterns are first displayed, then comparisons are made with the available data.

A parallel treatment to the above is adopted in chapter 5 for presenting the 3-D flow around a simple square four legged-platform as a rudimentary representation of a semisubmersible structure. In chapter 6, a full scale " AKER H-4.2 " platform is considered as an application of the prediction procedure to a practical problem.

Chapter 7 concludes the thesis with a summary of the achievements of the work and some suggestions for further work. Lists of references, together with the appendices and figures follow the final chapter.

2. SURVEY OF PREVIOUS WORK.

Since the present work had as its objective the prediction of steady-state turbulent flow over 3-D bluff bodies, the technical literature was surveyed with three specific purposes.

For the first purpose, the body of experimental information concerning the influence on bluff body flows of certain combinations of geometrical and hydrodynamic parameters was examined. This review defined the extent of present knowledge of these flows and thereby suggested the rule which flow predictions could usefully play in extending this knowledge.

The second purpose was to find pressure and force measurements of the flow around such bluff bodies which had been made in sufficient detail to provide test cases for evaluating prediction procedures.

The third purpose was to evaluate the successes and limitations of previous theoretical studies of flow around bluff bodies; these would serve as a standard against which to compare the theoretical advances used in the present work.

The review separately considers experimental and numerical investigations.

2.1 EXPERIMENTAL REVIEW.

For the present study, the principal value of the previous experimental studies of three-dimensional bluff body flows is in providing information for comparison with the numerical predictions. Experimental investigations of the flow over 3-D obstacles have been made for several geometries, and some of these studies are discussed in this section.

Chien el al.(1951) reported pressure distributions in a uniform upstream flow over a variety of bluff body shapes, including cubes and rectangular prisms, mounted normal or at 45° to the incident flow. The data of Baines (1963) included measurements of surface pressure coefficient on a cube in both uniform and boundary layer flow, and Leutheusser (1965) measured the pressure distribution on the faces of a cube at various degrees of boundary layer immersion.

The Engineering Sciences Data Unit, "ESDU" (1971) compiled results from several different sources to provide a comprehensive summary of pressure distributions over cubes, rectangular prisms, cylinders and other simple geometrical shapes for various angles of flow direction. Castro (1973) and Castro and Robins (1975) provided information on axial mean velocity and turbulence intensity as well as on surface pressure, for cubes in both uniform flow and a simulated atmospheric boundary

9

layer.

The behaviour of the flow between identical blocks placed side by side normal to a uniform flow was examined by Ishizaki and Sung (1971), for a variety of aspect ratios. The interaction has been noted to be particularly acute in the case of two rectangular obstacles of different heights where the tall obstacle lies downstream of the small one (Melbourne and Joubert, 1971; Wise, 1971). The nature of air flows over an offshore platform model was examined by M.E.Davies and P.G.O'.eill (1977) for a variety of deck layouts. B.L.Miller and M.E.Davies (1982) present measurements of the wind forces and moments on a model of a large steel jacket floating on auxiliary buoyancy tanks, measurements were made in uniform and (1/10)-th power law velocity profiles for wind directions from $0°$ to $345°$ in steps of $15°$.

The present work and that of P.Reeves and Z.Lattif was part of a major research project called PRESS, the name being an acronym for Performance Related Semi-submersible Stability undertaken at Strathcyde University. The project's general objective was to provide force measurement data for the evaluation of the stability of semi-submersible structures.

The data of P.Reeves and Z.Lattif (1987) included measurements of wind force and surface pressure distribution for single and double rectangular boxes for

10

the full range of wind dirction, also they provided
information on wind force for a simple four-legged
platform model with a variety of pitch and heel
conditions.

The increased detail data provided by P.Reeves and
Z.Lattif (1987) allowed a more extensive comparison with
the predicted results than was possible with other results
as well as the ESDU data. Thus, from the available
experimental studies, those by P.Reeves and Z.Lattif
(1987) and the ESDU were chosen for comparison with the
predicted results.

2.2 NUMERICAL REVIEW.

Although numerical methods have proven highly useful in many areas of fluid dynamics, the complexities assocated with air flow about bluff bodies have previously discouraged extensive numerical work in this area.

The common limitations of the numerical methods fall into three basic problem areas. First, there are problems associated with boundary conditions. The specification of numerical boundary conditions is a somewhat tricky, and sometimes subtle, exersise that requires considerable care and attention. For example, how to define arbitrarily shaped bodies, how to resolve boundary layers, how to calculate or define separation points, and how to prescribe inflow and outflow boundary conditions at the mesh perimeter. Second, the most important and most difficult problem associated with a numerical approximation is how to assess its accuracy. A related question is, what prescriptions can be used to determine a priori the numerical resolution necessary to achieve a desired level of accuracy; for example, what constitutes an adequate discretization of time and space, what is the importance of higher-order approximation schemes, would schemes based on finite element or Galerkin methods be superior to finite difference methods, and what are the limitations imposed on a solution by numerical stability requirements. Although no hard and fast rules can be established to give a satisfying answer to these questions

12

for all cases, there are some guidelines based on simple order-of-magnitude estimates.

Finally, there are miscellaneous problems, such as how to represent the effects of fluid turbulence, and how to optimize the solution algorithms to get the best results for a given expenditure of computer resources.

Nevertheless, it is the contention that the three-dimensional numerical simulation of air flow about bluff bodies is now feasible. Many examples have been calculated to demonstrate the capability of the numerical methods to model the aerodynamic phenomena affecting bluff bodies.

No attempt will be made to review all the advanced numerical schemes currently available. The rest of this chapter, demonstrates some of these examples.

The studies of Greenspan (1969) considered steady, incompressible, laminar flow over a thick rectangular obstacle mounted on one wall of a plane channel. Greenspan solved the equations of motion using the stream function and vorticity as dependent variables. He predicted the flow for several ratios of obstacle height to channel height and several Reynolds numbers, and he found that careful choice of finite difference grid distribution was necessary to secure convergence of the solutions. Friedman (1972) modified Greenspan's numerical scheme to extend the range of Reynolds numbers for which convergence could be obtained.

Vasilic-Melling.D (1977), considered the "SIMPLE" method, which is outlined in Patanker and Spalding (1972) and Caretto el al (1973), to simulate, steady, incompressible turbulent flow over a cube mounted on a flat plate of finite width. She concluded that the flow behaviour near the sharp edges of the obstacles was reasonably represented, however, the shear layer and recirculating flow which developed downstream were poorly predicted. The reason for that is thought to be connected with the mathematical turbulence model used in the modelling of the flow after separation at the front edges.

Many examples have been calculated by C.W.Hirt and J.D.Ramshaw,(1978), to demonstrate the capability of SOLA-3D (an acronym for SOLution Algorithm) technique, for predicting and interpreting air flows around different shapes of bluff bodies. In each case the calculations have been compared with wind tunnel data, their results show that many extensions and improvements are necessary before a code like SOLA-3D can be used for extensive practical applications.

The early version of "PHOENICS", was tested by N.G.Markatos (1983) to model the external aerodynamics of road vehicles. The results appeared physically realistic, but no claim was made concerning their quantitative accuracy. For architectural purposes, the control volume method has been applied by T.Hanson, D.M.Summers and C.B.Wilson (1986), to the problem of predicting the steady

14

state wind environment of a collection of buildings. Some

comparisons with wind tunnel measurements are presented,

and these indicated that the simulation can reproduce the

flow within the desired accuracy for architectural

interest.

3 MATHEMATICAL ANALYSIS AND NUMERICAL TECHNIQUE.

3.1 INTRODUCTION.

This chapter summarises the equations of motion, and a method for their solution, for 3-D turbulent flow of a uniform property fluid. The partial differential equations of continuity and conservation of momentum are given in time-dependent and time-averaged forms, and a general conservation equation for any property ϕ is formulated.

Finite-domain versions of the equations of continuity and ϕ-conservation are derived by integrating the partial differential equations over a micro control volume centred at a representative node of the finite domain grid. The method of solution of the finite domain equations is outlined, and a turbulence model, based on transport equations for the turbulence kinetic energy and the rate of dissipation, is discussed; the choice of this model for the prediction of bluff body flows is considered. Also, wall functions are presented which describe the low Reynolds number flow in the vicinity of solid boundaries of the solution domain.

3.2 DIFFERENTIAL EQUATIONS

3.2.1 Time-Dependent Continuity and Momentum Equations

For incompressible, constant property flow, in the absence of external body forces, the time-dependent forms of the mass and momentum conservation equations can be expressed in cartesian tensor notation (Hinze, 1959) as follows:

Mass conservation: Continuity equation

$$\frac{\partial \hat{U}_i}{\partial x_i} = 0 \qquad (3.1)$$

Momentum conservation (Navier Stokes equations):

$$\frac{\partial \hat{U}_i}{\partial t} + \hat{U}_j \frac{\partial \hat{U}_i}{\partial x_j} = -\frac{1}{\rho} \frac{\partial \hat{P}}{\partial x_i} + \nu \frac{\partial^2 \hat{U}_i}{\partial x_j \partial x_j} \qquad (3.2)$$

Where:

$\hat{U}_i$ are instantaneous velocity components,

x_i are Cartesian coordinates,

$\hat{P}$ is instantaneous pressure,

t is time,

ρ is fluid density   and

ν is kinematic viscosity.

Here the summation convention is adopted, i.e. terms containing repeated indices are summed over the three coordinate directions.

Equations (3.1) and (3.2) represent a closed set of equations which, with the provision of boundary conditions and a suitable finite-difference method of solution, are solvable for laminar flows. Although the same approach could in principle be used for turbulent flows, difficulties arise because important changes in the eddy structure occur over a spatial scale which is typically very small compared with the dimension of the flow domain of interest. Thus to resolve numerically the details of the flow would require a very large number of mesh points in the finite difference grid, far exceeding the capacity of contemporary computers. For practical purposes, however, every detail of the micro-scale turbulent motion need not be known; it is sufficient to solve equations for the time-averaged velocity and pressure fields, using a coarser grid and accounting for the effects of turbulence by the " modelling " approach already referred to.

3.2.2 Time-averaged continuity and momentum equations.

In a steady flow, the time-averaged (mean) values of velocity and pressure can be defined as:

$$
\left.
\begin{aligned}
U_i &= \frac{1}{T} \int_0^T \hat{U}_i \, dt \\[2em]
P &= \frac{1}{T} \int_0^T \hat{P} \, dt
\end{aligned}
\right\}
\qquad (3.3)
$$

Where:

T   is a time interval which is short compared with

the time scale of the main motion,

U_i are mean velocity components   and

P is mean pressure.

At any instant of time the instantaneous velocity and pressure can be expressed as the sum of their mean and fluctuating components:

$$\left. \begin{array}{l} \hat{U}_i = U_i + u_i \\ \\ \hat{P} = P + p \end{array} \right\} \qquad (3.4)$$

Where:

u_i are fluctuating velocity components,   and

p is fluctuating pressure.

Substituting (3.4) into (3.1) and (3.2), and integrating over time interval T, yields the following equations describing the mean motion of a steady flow of uniform density and viscosity.

Continuity equation:

$$\frac{\partial U_i}{\partial x_i} = 0 \qquad (3.5)$$

Momentum equation:

$$U_j \frac{\partial U_i}{\partial x_j} = - \frac{1}{\rho} \frac{\partial P}{\partial x_i} + \frac{\partial}{\partial x_j} \left(\nu \frac{\partial U_i}{\partial x_j} - \overline{u_i u_j} \right) \qquad (3.6)$$

The " Reynolds stress " term $(- \overline{u_i u_j})$ in equation

19

(3.6) is the time-averaged product of the velocity fluctuations u_i and u_j, it represents the transfer of momentum by the turbulent motion. The Reynolds stress term is a new unknown, for which additional equations must be found to enable the closure of the equation set. The full form of the turbulence models is given in the next section, but it is useful to introduce one aspect at this stage, namely the concept of a "turbulence viscosity μ_t"; this allows the equations to be recast into the form in which they will be solved. By analogy with the definition of molecular viscosity in a laminar flow, a turbulence viscosity, μ_t, may by defined such that

$$- \rho \, \overline{u_i u_j} = \mu_t \left(\frac{\partial U_i}{\partial x_j} + \frac{\partial U_j}{\partial x_i} \right)$$ (3.7)

where $i \neq j$

μ_t can be calculated in a number of ways (Launder and Spalding, 1972); one way is by evaluating from the kinetic energy of turbulence, K, and the dissipation rate of turbulence, $\mathcal{E}$, which were calculated from their own transport equations. The similarity in the forms of the laminar and turbulent stress relations allows an effective viscosity, μ_{eff}, to be defined as the sum of the molecular and turbulent viscosities, i.e.

$$\mu_{eff} = \mu + \mu_t .$$ (3.8)

Combining equations (3.5) to (3.8), the momentum

20

equations (3.6) can then be written in thier final forms as:

$$\frac{\partial \rho U_j U_i}{\partial x_j} = - \frac{\partial P}{\partial x_i} + \frac{\partial}{\partial x_j} \left[\mu_{eff} \left(\frac{\partial U_i}{\partial x_j} + \frac{\partial U_j}{\partial x_i} \right) \right] .$$

(3.9)

where the continuity equation has been used to express the left-hand side in conservation form; this facilitates derivation of the finite-difference equations.

3.3 TURBULENCE MODELS

3.3.1 Classification of Turbulence Models

The Reynolds stress term ($\overline{u_i u_j}$) equation (3.7), involves time averages of products of velocity fluctuations. They represent unknowns in the momentum conservation equation (3.6), and additional equations are, therefore, required to enable these Reynolds stresses to be calculated. The necessary algebraic or differential equations collectively constitute a " turbulence model ".

The criteria for the choice of a turbulence model include economy of computations, degree of universality and accuracy. A classification scheme for turbulence models and some examples of their applications are provided by **Markatos and Tatchell (1986).** Turbulence models can conveniently be classified according to the number of additional differential equations which they contain. Most zero- , one- and two-equation models represent the Reynolds shear stresses by way of a turbulence viscosity concept.

Typically, the turbulence viscosity is taken to be proportional to the product of a velocity scale and a length scale characteristic of the local turbulent flow. The zero-equation model employs the mixing length hypothesis (Prandtl, 1925) in which the length scale is specified by a " mixing length ℓ_m " and the velocity scale is of the form ($\ell_m \mid \partial w / \partial y \mid$); the velocity gradient

($\partial w / \partial y$) is calculated from local mean flow conditions. This model is applicable to simple two-dimensional boundary layer flow (Patanker and Spalding, 1970) where ℓ_m is easily prescribed empirically and the predominant mean velocity gradient does not change sign.

In one- and two-equation models, μ_t is related to the kinetic energy of turbulence, ($k = 0.5 \overline{u_i^2}$), and a length scale (ℓ) by the expression :

$$\mu_t = C_\mu \rho k^{1/2} \ell \qquad (3.10)$$

where C_μ is an empirical coefficient, about which more will be said later. C_μ is assigned a value of (0.5478) (Malin, M.R and Qin, H.Q (1985)) in accordance with experimental data.

The one-equation model solves differential transport equation for k but requires empirical specification of ℓ . Such a model was used with considerable success by Launder and Ying (1973) to predict the fully developed flow in a square duct, but this was one of the few situations where sufficient knowledge of the length scale distribution was available.

Two-equation models provide a more general approach by solving transport equations for both k and a quantity related to the length scale. In practice, it proves to be more satisfactory to solve for the turbulent dissipation, ε , rather than for the dissipation length

23

scale, ℓ . The two variables are related (Launder and Spalding, 1974) by the equation:

$$\epsilon = C_D \frac{k^{3/2}}{\ell}$$

(3.11)

where the constant C_D is assigned a value of (0.1643). By combining equations (3.10) and (3.11) the turbulent viscosity can be linked to k and ϵ thus:

$$\mu_t = C_\mu \, C_D \frac{k^2 \rho}{\epsilon}$$

(3.12)

Two equation models are the simplest available means of calculating turbulent stresses in recirculating or separated flow where the length scale distribution can not be prescribed algebraically. Such models have been applied to wall boundary layers (Ng, K.H, 1971; Jones and Launder, 1973), two-dimensional recirculating flow over a backward facing step (Matthews and Whitelaw, 1973), calculation of the air flow around moving van (Edwards J.P, 1985), etc .

For the study of three-dimensional turbulent flow over bluff bodies, a widely tested turbulence closure model is the two-equation " k-ϵ " turbulence model. This model requires the solution of two differential equations, for the two turbulence characteristics, the kinetic energy of the turbulence k, and its dissipation rate, ϵ .

3.3.2 Transport Equations for Turbulence Energy and Dissipation Rate

The exact transport equation for turbulence kinetic energy, first derived by Kolmogorov (1942), is obtained via the equation for the turbulent velocity fluctuations. The latter equation can be derived with the help of equation (3.4) by subtracting the time averaged momentum equation (3.6) from the time-dependent momentum equation (3.2). The result is :

$$U_j \frac{\partial u_i}{\partial x_j} = - u_j \frac{\partial U_i}{\partial x_j} - \frac{\partial}{\partial x_j} \left(u_i u_j - \overline{u_i u_j} \right) - \frac{1}{\rho} \frac{\partial p}{\partial x_i} + \nu \frac{\partial^2 u_i}{\partial x_j^2} \qquad (3.13)$$

where,

P represents the fluctuating pressure.

By multiplying the above equation by u_i , time averaging, and introducing the definition ($k = 1/2\, \overline{u_i^2}$), one can obtain the turbulence kinetic energy equation (Launder and Spalding, 1974):

$$U_j \frac{\partial k}{\partial x_j} = - \overline{u_i u_j} \frac{\partial U_i}{\partial x_j} - \frac{\partial}{\partial x_j} \left(\frac{\overline{u_j u_i^2}}{2} + \frac{\overline{u_j p}}{\rho} - \nu \frac{\partial k}{\partial x_j} \right) - \nu \overline{\left(\frac{\partial u_i}{\partial x_j}\right)^2} . \qquad (3.14)$$

introducing the "instantaneous kinetic energy $K' = 1/2\ u_i^2$ " leads to the alternative form :

$$U_j \frac{\partial k}{\partial x_j} = - \overline{u_i u_j} \frac{\partial U_i}{\partial x_j} - \frac{\partial}{\partial x_j} \left(\frac{\overline{u_j p}}{\rho} + \overline{u_j k'} - \nu \frac{\partial k}{\partial x_j} \right) - \varepsilon \qquad (3.15)$$

where;

25

$$\varepsilon = C_D \frac{k^{3/2}}{\ell} \tag{3.16}$$

Equation (3.15) expresses the fact that changes of kinetic energy of a small element of fluid occur (Launder and Spalding, 1972) as a result of an imbalance between generation of k by the interaction of Reynolds stresses with mean velocity gradients, diffusive transport by pressure fluctuations, velocity fluctuations and molecular diffusion, and destruction of k by viscous action. In high Reynolds number flows (i.e. flows for which the effect of molecular viscosity may be neglected), equation (3.15) can be modelled (Rodi, 1970) as:

$$\frac{\partial \rho U_j k}{\partial x_j} = \frac{\partial}{\partial x_j} \left(\frac{\mu_{eff}}{\sigma_k} \frac{\partial k}{\partial x_j} \right) + G - \rho \varepsilon \tag{3.17}$$

where;

G represents the term ($-\overline{u_i u_j} \frac{\partial U_i}{\partial x_j}$) of equation (3.15).

Within the context of a turbulent viscosity model, G can be expressed with the aid of equation (3.7) as:

$$G = \mu_{eff} \frac{\partial U_i}{\partial x_j} \left(\frac{\partial U_i}{\partial x_j} + \frac{\partial U_j}{\partial x_i} \right) \tag{3.18}$$

An exact equation for ε can be derived by a similar procedure to that used above (Harlow and Nakyama, 1968; Daly and Harlow, 1970). The resulting equation is long and

26

complicated, and will suffice here to state a modelled form (Launder and Spalding, 1974):

$$\frac{\partial \rho U_j \varepsilon}{\partial x_j} = \frac{\partial}{\partial x_j} \left(\frac{\mu_{eff}}{\sigma_\varepsilon} \frac{\partial \varepsilon}{\partial x_j} \right) + \frac{\varepsilon}{k} \left(C_1 G - C_2 \rho \varepsilon \right) \qquad , \qquad (3.19)$$

Details of the transport equations for k and ε are given by (C. Taylor and K.Morgan 1981). The values of the five empirical constants in the turbulence model appearing in equations ((3.10), (3.17) and (3.19)), have been evaluated based on extensive research and have been widely used for a variety of flow situations (Markatos 1978; Markatos and Moult, 1979; Markatos el al, 1982 and Markatos, 1983); these values employed by Markatos were, after discussion with staff at CHAM Ltd, adopted for the present study, and given in table (3.1) below

Table (3.1) :   Turbulence model constants

Constant	Value
C_D	0.1643
C_μ	0.5478
C_1	1.4400
C_2	1.9200
σ_k	1.0000
σ_ε	1.3140

3.4 THE GENERAL DIFFERENTIAL EQUATION FOR PROPERTY ϕ

In developing the finite difference versions of the partial differential conservation equation which govern turbulent flows, it will be convenient to deal with a single general equation for any dependent variable ϕ. The differential form of this equation is

$$\frac{\partial \rho U_j \phi}{\partial x_j} = \frac{\partial}{\partial x_j} (\Gamma_\phi \frac{\partial \phi}{\partial x_j}) + S_\phi \qquad (3.20)$$

in which the left hand side represents the transport of ϕ by convection. On the right hand side the diffusion of ϕ is taken as proportional to its spatial gradient; the proportionality factor, Γ_ϕ , is called the exchange coefficient. The " source term, S_ϕ ", contains quantities related to the generation or destruction of ϕ, as well as any other terms which are not accounted for in the convection and diffusion expressions. The similarity between equations(3.9), (3.17), (3.19) and (3.20) is evident, and so ϕ may represent any of the mean velocity components U_j , or any scalar property of the flow.

Equation (3.20) becomes in (x, y, z) cartesian coordinates for 3-D, steady, uniform-property flow;

$$\frac{\partial}{\partial x} (\rho U \phi) + \frac{\partial}{\partial y} (\rho V \phi) + \frac{\partial}{\partial z} (\rho W \phi) =$$

$$\frac{\partial}{\partial x} (\Gamma_\phi \frac{\partial \phi}{\partial x}) + \frac{\partial}{\partial y} (\Gamma_\phi \frac{\partial \phi}{\partial y}) + \frac{\partial}{\partial z} (\Gamma_\phi \frac{\partial \phi}{\partial z}) + S_\phi \qquad (3.21)$$

where;

28

U , V and W are the components of the mean velocity in the x-, y-, z-directions.

Table (3.2) below contains the definitions of Γ_ϕ and S_ϕ for all three momentum equations, the kinetic energy of turbulence and its dissipation rate.

.

29

Table 3.2 : Summary of the equations solved (Cartesian coordinate)

Equation	Quantity ϕ	Exchange coefficient, Γ_ϕ	Source term S_ϕ
Continuity	1	0.0	0.0
X-momentum	U	μ_{eff}	$\frac{\partial}{\partial x}(\mu_{eff}\frac{\partial U}{\partial x}) + \frac{\partial}{\partial y}(\mu_{eff}\frac{\partial V}{\partial x}) + \frac{\partial}{\partial z}(\mu_{eff}\frac{\partial W}{\partial x}) - \frac{\partial p}{\partial x}$
Y-momentum	V	μ_{eff}	$\frac{\partial}{\partial x}(\mu_{eff}\frac{\partial U}{\partial y}) + \frac{\partial}{\partial y}(\mu_{eff}\frac{\partial V}{\partial y}) + \frac{\partial}{\partial z}(\mu_{eff}\frac{\partial W}{\partial y}) - \frac{\partial p}{\partial y}$
Z-momentum	W	μ_{eff}	$\frac{\partial}{\partial x}(\mu_{eff}\frac{\partial U}{\partial z}) + \frac{\partial}{\partial y}(\mu_{eff}\frac{\partial V}{\partial z}) + \frac{\partial}{\partial z}(\mu_{eff}\frac{\partial W}{\partial z}) - \frac{\partial p}{\partial z}$
Turbulence energy	k	$\frac{\mu_{eff}}{\sigma_k}$	$G - \rho\varepsilon$
Dissipation rate	ε	$\frac{\mu_{eff}}{\sigma_\varepsilon}$	$\frac{\varepsilon}{k}(C_1 G - C_2\rho\varepsilon)$

3.5 BOUNDARY CONDITIONS

The differential equations of the form of (3.21) are solved within a prescribed solution domain. The boundaries of the solution domain may coincide with an upstream location at which a specified inflow occurs, solid walls, a plane of symmetry, a "free stream" as the location where the external stream is not influenced by the presence of the obstacle and a downstream location where out-flow takes place. Information must be provided about the values of the dependent variables or their normal gradients at all these locations. The practices employed in this study will now be outlined.

a) Inlet planes:

At an inflow plane, it is necessary to supply distributions of all variables, including U, V, W, κ and ε. Although pressure also appears as a dependent variable in the equations, there is no need to specify the upstream pressure boundary condition directly; instead,

mass and ϕ-fluxes coming into the cell, are specified.

b) Wall surfaces:

The application of boundary conditions at walls in turbulent flow requires a more elaborate treatment than at the inflow boundary. Thus, although the velocity components at the wall are set to zero, special formulae are necessary to calculate the resultant wall shear

stresses. These, together with the boundary conditions on the turbulence parameters k and ε, are deduced from " wall functions " derived from experimental data on near wall flow (see Launder and Spalding, (1974), Rodi, (1980)).

The wall function formulae used for the hydrodynamics can be summerised as follows:

$$w^+ = \frac{1}{\kappa} \ln (Ey^+) \qquad (3.22)$$

$$k = w_\tau^2 (C_\mu C_D)^{-1/2} \qquad (3.23)$$

$$\varepsilon = w_\tau^3/(\kappa y) \qquad (3.24)$$

where;

$w^+ = (W_{res} / W_\tau$) is a dimensionless near wall velocity,

W_{res} is the resultant velocity parallel to the wall,

$W_\tau = (\tau_s / \rho)^{1/2}$ is the resultant friction velocity,

τ_s is the resultant shear stress,

$y^+ = (W_\tau \, y_p/\nu)$ is a dimensionless wall distance,

y_p is the normal distance from the wall,

κ is the von Karman constant and

E

is a roughness parameter.

Thses conditions are applied to a point whose y^+ value is in the range ($30 < y^+ < 150$) (Malin, M.R and Qin, H.Q (1985). The constants K and E are given the values (0.41 and 8.60) respectively. The wall function (3.22) implies that the local skin friction coefficient, C_f is obtained from:

$$c_f = 2 \ / \ w^{+ \ 2} \qquad\qquad (3.25)$$

c) Symmetry plane :

The boundary conditions at a plane of symmetry can be stated comparatively simply as the normal velocity is zero, and the gradient of other quantites normal to the boundary is zero, i.e. ($\partial\phi/\partial n = 0$)

d) Free boundary :

The coditions at a free boundary are in principle known from the distributions of velocity, turbulence energy, etc, in the external stream. In practice, this information is not always available in complete detail and the extent of disturbances in the flow introduced by the obstacle is seldom known beforehand. Trial and error is therefore required to locate the computational free boundary sufficiently far from the obstacle that conditions imposed are without significant influence on the region of interest. The normal velocity is set equal to zero.

e) Outlet plane :

Provided that the downstream boundary is located where the velocity normal to the boundary is directed everywhere outwards, the boundary layer nature of the flow there ensures that downstream conditions have no influence on the upstream flow; hence, knowledge of these conditions is not required in the calculations. An exception to this rule is the normal velocity, which is needed in the absence of a specification for the streamwise pressure gradient. Fortunately a simple treatment of the following kind usually suffices : the outflow velocities are calculated by extrapolation from the adjacent upstream plane and then adjusted so as satisfy overall continuity.

3.6 NUMERICAL TECHNIQUE :

Computational fluid mechanics has been in progress for more than twenty years and it has some great successes to its credit. Complex three-dimensional flow phenomena, such as those which occur in combustion chambers, nuclear reactors and the prediction of turbulent flow over bluff bodies, are now being successfully simulated by computer; many features of turbulence are adequately represented by the so-called " turbulence model " equations.

Progress in the application of numerical models, in the refinement of the physical models, and in the refinement of the physical hypotheses which they embody, could be greatly accelerated if practitioners were enabled to employ a reliable and economical standard computer program, incorporating the well-established balance laws of fluid mechanics, heat and mass transfer, and structured so that particular material properties, geometries and boundary conditions could be easily incorporated. Such a program, if continuously and centrally maintained, could free the computer-modelling fraternity of chores of code development and maintenance; it would thus permit them to apply their innovative talents to the development and application of improved physical hypotheses.

The " PHOENICS " computer code is perhaps well enough established to require no detailed description here, it has been developed in order to meet this need. " It is gratifying to learn, from the contributions made at the

first international PHOENICS User's conferece (Sept.1985),

that many people are finding it useful. However, PHOENICS

is potentially more than that, it may become a new means

of promoting communication, understanding and

collaboration between scientists and engineers " (Prof.

D.B.Spalding) **Markatos (1986).**

Information on the structure, application and

limitations of the code is readily available (Spalding,

B.D and Rosten, H.I (1984); Malin, M.R (1983)), a brief

description of the " PHOENICS " code is given in the

following section.

3.7 THE PHOENICS FINITE-DOMAIN EQUATIONS. (FDE'S)

In order to derive the finite-volume analogue of the differential equations, a finite volume grid in cartesian coordinates is shown in figure (3.1). A typical node " $\underline{P}$ " and its neighbours, labelled $\underline{W}$, $\underline{E}$, $\underline{S}$, $\underline{N}$, $\underline{L}$ and $\underline{H}$ represent the locations at which all variables are calculated, except that the three velocity components U, V and W are calculated respectively at points $\underline{w}$, $\underline{e}$, $\underline{s}$, $\underline{n}$, $\underline{l}$ and $\underline{h}$ which lie mid-way between the grid nodes and are denoted by the arrows in figure (3.1). There are two advantages in so displacing the velocity locations. Firstly, they lie mid-way between the locations of the pressure which derive them; and secondly, the velocities are directly available for calculation of convective fluxes across the faces of the imaginary control volume surrounding the central node as indicated in the figure.

The finite-domain equations are derived by integrating the differential equation (3.21) over that control volume. The integrations involve interpolation assumptions concerning values of $\emptyset$ and values of $\emptyset$ gradients, prevailing at cell boundaries. The resulting equations normally connect each grid point $\emptyset$ with seven neighbour $\emptyset$'s, namely those at north, south, east, west, high, low and the previous time locations.

In algebraic form, the finite-domain equations (FDE'S) have the form:

$$a_p \phi_p = a_N \phi_N + a_S \phi_S + a_E \phi_E + a_W \phi_W + a_H \phi_H + a_L \phi_L + a_T \phi_T + b \qquad (3.26)$$

where;

a_p, a_N, ...etc, are positive coefficients, obeying:

$$a_p \geqslant a_N + a_S + a_E + a_W + a_H + a_L + a_T$$

The a's express the influences of (diffusion + convection) processes across cell boundaries.

b is a representation of all the source terms appropriate to the variable being solved. Subscripts have the meanings (see figure (3.1)).

P : Typical point (i.e. node) within cell;

N : North-neighbour node, in positive y-direction;

S : South-neighbour node, in negative y-direction;

E : East -neighbour node, in positive x-direction;

W : West-neighbour node, in negative x-direction;

H : High -neighbour node, in positive z-direction;

L : Low -neighbour node, in negative z-direction and

T : Grid node at earlier time.

3.8 SOLUTION PROCEDURE.

The set of FDE's (section 3.7) was solved by an iterative method, called SIMPLEST** , which is an improved version of the well known SIMPLE* algorithm outlined by Patankar and Spalding (1972) and Caretto el al. (1973).

The reason for using the SIMPLEST method was recognised independently by Patankar and Spalding as SIMPLE provides good velocity fields (satisfying continuity at least) but poor pressure fields. In SIMPLEST, therefore, with refernce to equation (3.26), a_N, a_S, a_E, a_W, a_H and a_L of the momentum equations contain only diffusion contributions; the convection terms are added in to source term b. The complete solution proceeds by the iterative repetition of the following steps:

1) First, since the pressure appearing in the momentum equations are not known beforehand, guessed values are first substituted into the momentum equations, which are then solved to yield a field of intermediate velocities. These velocities will not generally satisfy the continuity equation until the correct pressures are obtained.

2) The pressure correction is made such that the resulting velocity corrections will reduce the mass sources from the continuity equation to zero.

---

* The name is an acronym for "Semi-implicit method for pressure linked equations"
** SIMPLEST stands for SIMPLE-shortend.

3) The general discretization equation (3.26) is then solved successively for the remaining dependent variables, which in the present study are K and $\mathcal{E}$.

4) The resulting field of variables is now used as the starting point for the next iteration and this process is repeated until a converged solution is obtained.

3.9 NUMERICAL STABILITY, CONVERGENCE CRITERIA AND ACCURACY

3.9.1 Numerical Stability

Because of the non-linearities of the partial differential equations and the strong inter-linkages between them, numerical instability may develop leading to divergence of the solutions during the computations. These instabilities usually lead to imbalance in conservation of a property ϕ within each control volume and hence over the whole domain, and to oscillation of the calculated values of a variable over successive iterations.

Three important factors which may provoke instabilites include poor specification of initial fields, inappropriate choice of under-relaxation factors, and incomplete solution of the equations during iteration. Possible methods of avoiding these instabilities are outlined below.

Under-relaxation promotes stability by carrying forward from one iteration to the next a value, ϕ_{new}, which is a weighted mean of the value ϕ, calculated from equation (3.26), and the value ϕ_{old} from the previous iteration in the form :

$$\phi_{new} = \alpha_\phi \ \phi + (1-\alpha_\phi) \ \phi_{old} \qquad (3.27)$$

where, α_ϕ is the under-relaxation factor ($|\alpha_\phi| < 1$). The only available method for choosing the most satisfactory factors is that of trial and error, but it is a good

practice to limit the maximum value of x_ϕ for the momentum equation to 0.50. For the solution in velocity and turbulence parameters, a "false time step" is used to provide under-relaxations. The effect is to add mass flux to the denominator of each finite-volume equation, and that quantity times the in-memory value of the dependent variable to the numerator. The recommended values should be no larger than the length of a typical cell side divided by a typical velocity; it may be that the smallest cell side divided by the largest velocity should be employed. For the kinetic energy of turbulence, k and its dissipation factor ε , the recommended values are of the order somewhat smaller than (k/ε).

3.9.2 Convergence Criteria

The convergence of the iterative procedure is assessed by examination of the residual sources of the difference equations and the fractional changes in the ϕ's between iterations. The first criterion is based on the residual source of ϕ, R_ϕ which is defined from equation (3.26) as:

$$R_\phi \equiv a_P \phi_P - \sum_n a_n \phi_n - S_\phi \qquad (3.28)$$

and should, of course, be zero if the current solution satisfies equation (3.26). The physical meaning of R_ϕ depends on the equation to be solved. In the momentum

equation R_{ϕ} represents an imbalance in conservation of momentum, and for the continuity equation it represents an imbalance in mass conservation. The criterion applied is :

$$\Sigma |R_{\phi}| < \lambda_R \cdot (R_{\phi})_{ref}$$

(3.29)

where;

$(R_{\phi})_{ref}$ is some reference value

In the present study the reference value used was the incoming mass flow rate and (λ_R) was 10^{-5}

3.9.3 Accuracy of Solutions

There are four factors which may influence the accuracy of the solution. These are the degree to which the solution satisfies the differential equations, the degree to which it satisfies the FDE's, the location of and conditions imposed at the boundaries, and the adequacy of the turbulence model.

The first factor results from discretization errors, which are a consequence of representing the continuous distribution of ∅ in terms of values at the grid nodes, and interpolating between them. These errors can be reduced by reducing the spacing between nodes to an acceptable level, preferably by using a non-uniform grid, with nodes concentrated in regions of high gradients. Evidence of the existence or otherwise of discretization errors is obtainable from grid refinement tests, in which

43

the number of grid nodes are systematically increased until changes in the solution become smaller than an acceptable tolerance.

The extent to which the current solution satisfies the FED's can be assessed by ensuring that the residual sources for each variable have been reduced to an acceptable level. In the present work iterations were continued until the residual mass source was less than the limit specified by equation (3.29).

Errors caused by inappropriate location of the boundaries or specification of boundary conditions can be detected by adjusting the locations and conditions and determining the sensitivity of the solution to such changes.

3.9.4 Computer Requirements

The calculations were performed on VAX-E system. The following table summarizes the computing times for the simple case, of single cube with zero wind yaw-angle.

grid nodes (NX,NY,NZ)	No. of sweeps to convergence	Total CPU Sec.
16,21,31	80	1730
16,21,34	90	2166
16,21,38	110	2894
16,25,38	120	4031

4. PREDICTION OF 3-D TURBULENT FLOW OVER RECTANGULAR BLUFF BODIES.

4.1 INTRODUCTION.

This chapter is concerned with the prediction of turbulent flow over surface mounted cube bodies in order to estimate the wind loads on typical semi-submersible deck structures.

Two cases were considered. The first case considers the flow over a single cubical body on a horizontal plane in a free stream with uniform flow, whereas in the second case two cubes at various spacings were considered to examine the effect of one body shielding the downstream body.

The prediction procedure was first tested for grid refinement and optimum solution domain size. The influence of wind direction was considered for the full range of wind yaw angle for each case.

The flow fields predicted for each case were displayed by way of velocity vector plots and surface pressure contours.

Comparisons were made between predictions and other sources of numerical and experimental data. Also comparisons were made with certain empirical calculation procedures used for wind load estimation in maritime engineering.

4.2 PREDICTION OF 3-D TURBULENT FLOW OVER A SINGLE CUBE.

4.2.1 Geometry and Boundary Conditions.

The diagram shown in figure (4.1) defines the general situation for the three-dimensional flow over a cube fixed to a horizontal plane in a free stream. Where h, is the height of the cube, L_{ux} and L_{dx}, are the lengths of the solution domain upstream and downstream in the X-direction, the corresponding lengths in the Z-direction are, L_{ux} and L_{dx}. The height L_y, is the vertical length from the top face of the cube.

The wind yaw angle α, was defined as the angle between wind direction and body axis parallel to z-direction, when the incident wind was normal to the face of the cube i.e.($\alpha = 0^{\circ}$), the flow will be parallel to Z-direction and hence, $L_{ux} = L_{dx} = L_y$.

Since the model is symmetric about x and z axis, the wind yaw angle was varied from 0° to 45° in 15° increments. The free stream velocity was considered as a uniform flow with the value of (20 m/s) over the inlet boundary of the solution domain.

Predictions for this case were made by solving the governing partial differential equations using the solution procedure described in chapter 3. These solutions yielded the three-dimensional fields of the components of the mean velocity vector (transverse U, vertical V, and axial W), the pressure P, the turbulent kinetic energy K

46

and its dissipation rate ε.

The boundary conditions for U, V, W, K and ε imposed at the surfaces of the solution domain labelled (1 to 6) in figure (4.1), are summarized in table (4.1).

TABLE (4.1): BOUNDARY CONDITION

LABLE	YAW ANGLE α	BOUNDARY	VELOCITY COMPONENTS			MOM. FLUX $(Kg/m^2.s)$	K $(m/s)^2$	ε (m^2/s^3)
			U (m/s)	V (m/s)	W (m/s)			
1	$\alpha = 0.0^\circ$ $0^\circ < \alpha < 90^\circ$	INLET.	0.0 $Q.\sin\alpha$	0.0 0.0	Q $Q.\cos\alpha$	$\rho.Q$ $\rho.W$	$C.Q^2$	$K^{3/2}/\ell =$ $\ell = 0.55h$
2	$\alpha = 0.0^\circ$ $0^\circ < \alpha < 90^\circ$	OUTLET.	NOT NEEDED			0.0	NOT NEEDED	
3	$\alpha = 0.0^\circ$ $0^\circ < \alpha < 90^\circ$	OUTLET.	NOT NEEDED			0.0	NOT NEEDED	
4	$\alpha = 0.0^\circ$ $0^\circ < \alpha < 90^\circ$	FLOOR.	WALL Fun.	0.0	WALL Fun.	NOT NEEDED	WALL FUNCTION (see. sec. 3.4)	
5	$\alpha = 0.0^\circ$ $0^\circ < \alpha < 90^\circ$	OUTLET. INLET.	NOT NEEDED $Q.\sin\alpha$	 0.0	 $Q.\cos\alpha$	0.0 $\rho.U$	NOT NEEDED $C.Q^2$	NOT NEEDED $K^{3/2}/\ell; \ell = 0.55h$
6	$\alpha = 0.0^\circ$ $0^\circ < \alpha < 90^\circ$	OUTLET.	NOT NEEDED			0.0	NOT NEEDED	

C is a constant = 3.25 E-3

Q is the free stream velocity

4.2.2 Grid Dependence.

It is important to recognise that although economy requires that the number of grid nodes be minimised, the solution domain must be large enough so that the boundaries are located far enough away from the obstacle such that the flow conditions are known or where uncertainties about them are unimportant. Experience indicates that the nodes must be closely spaced near the obstacle where steep gradients of flow properties occur, but can be distributed more widely towards the boundaries.

Two series of tests were considered to select the optimum solution domain. The first set of tests was carried out to estimate the optimum domain size, whereas the second set examined the grid refinement.

a) Optimum Domain Size Tests.

The question of the optimum domain size was examined, by fixing the expansion ratios of the non-uniform grid distribution $\mathcal{E}_x$, $\mathcal{E}_y$, $\mathcal{E}_{ux}$ and $\mathcal{E}_{dx}$ in the X- , Y- , upstream Z- and downstream Z-directions respectively, these ratios are listed in table 4.2 . Obtaining solutions by increasing the solution domain dimensions until a stage is reached where the solution exhibits negligible change with further increase in the domain size. Four different domains were examined, with wind yaw angle ($\alpha = 0$), the geometrical characteristics for these domains are listed in table 4.2

Table 4.2 : Geometry of solution domains and grid

expansion ratios

Solution domain		(1)	(2)	(3)	(4)
Solution	L_x	3.5h	5h	8h	10h
domaine	L_y	3.5h	5h	8h	10h
dimensions	L_{uz}	3.5h	5h	8h	10h
	L_{dz}	10.5h	15h	8h	30h
Grid	ε_x	1.25	1.25	1.25	1.25
expansion	ε_y	1.25	1.25	1.25	1.25
ratios.	ε_{uz}	0.80	0.80	0.80	0.80
	ε_{dz}	1.50	1.50	1.50	1.50

the expansion factor, ε_{uz}, upstream of the cube is less than unity because the grid was contracting in the direction of increasing Z over this region of the solution domain.

Results shown in figures (4.2 to 4.7) indicate the effect of the domain size on the streamwise distributions of pressure coefficient C_p, the axial velocity component W and the kinetic energy of turbulence K.

Figures (4.2 and 4.3) illustrate the pressure coefficient profiles on a line through the centre of the cube parallel to Z-direction and on a line through the middle of the cube at (Y/h = 1.0333), parallel to Z-

direction respectively. The C_p profiles show some change at the upstream region just at the edges of the front face where separation takes place. However at the downstream region the C_p profiles show little difference; the values of which are as shown in table (4.3) below.

Table 4.3 : Solution domain size sensitivity of C_p

SOLUTION DOMAIN	C_p		
	Centre-Front	Edge-Top	Centre-Rear
(4)	1.0625	-1.3375	-0.285
(3)	1.0025	-1.2917	-0.342
(2)	0.9935	-1.2680	-0.338
(1)	0.9886	-1.2570	-0.339

Figures (4.4 to 4.7) illustrate the profiles of the axial velocity, W and the kinetic energy of turbulence, K in the same test sections . The axial velocity profiles show no change with various domain size. Nevertheless, there is some change in the value of the kinetic energy of turbulence, K at the front face of the cube between case 4 and the rest of the other cases.

Optimum domain size was also assessed from the values of reattachment length ℓ_R. Figure (4.8) shows the variation of ℓ_R with solution domain size, table (4.4)

gives the values of ℓ_R/h for each domain size.

Table 4.4 : Solution domain size sensitivity of ℓ_R/h

	Solution domain (1)	Solution domain (2)	Solution domain (3)	Solution domain (4)
ℓ_R/h	2.074	2.230	2.234	2.237

The values of ℓ_R show a strong change from domain 4 to the values of the other domains. The apparently strong change of ℓ_R arises from its sensitivity to details of the velocity distribution near the rear face of the cube and to the size of the downstream region of the solution domain.

The domain size tests discussed above showed that, domain 2 (5h upstream, 5h vertical and 15h downstream lengths) produce a stable solution. This solution remained unchanged with further increase in the domain size.

b) Grid Refinement Test.

The selection of the optimum finite-difference grid to predict turbulent flow is a complex task. The basic aim is to establish a grid with the smallest possible number of nodes for which the finite-volume solutions are essentially those of the original differential equations.

52

In order to decide when a grid-independent solution had been obtained, for the optimum domain size estimated in the previous section, a series of grid refinements were considered. Starting with small numbers of grid points in X- ,Y- and Z-directions and by increasing these grid points until profiles at several locations for selected variables showed little change with further increase of the grid points.

Results are shown for three grids whose distributions are summarized in table 4.5 below:

Table 4.5^a: Grid refinement

Case	Z-Direction		Y-Direction	X-Direction	
	upstream	downstream		L-side	R-side
24x16x24	8	8	8	8	8
28x18x28	10	10	10	10	10
32x20x32	12	12	12	12	12

The number of grid points employed at the cube itself for the three cases were (8x8x8). Figures (4.9 to 4.11) show examples of the effect of grid refinement on the distributions of the pressure coefficient C_p, the axial velocity W, and the kinetic energy of turbulence K along a line lying on the symmetry plane of the flow and passing through the cube centre. From these figures it appeared

that grid refinement produces no changes on the values of these variables at the upstream region. However at the downstream region, a small change in C_p profiles appear between case (24x16x24) and the other cases. The corresponding profiles along a line lying on the symmetry plane of the flow near the top surface of the cube, are shown in figures (4.12 to 4.14). These profiles give no significant difference in the values of the selected variables between the grid nodes (28x18x28) and (32x20x32).

The conclusion which can be drawn from the grid refinement test is that, the grid distribution with (28x18x28) grid points in X- ,Y- and Z-directions is suitable and sufficient to predict such flow. For each test it was necessary to obtain a fully converged solution (see section 3.8) in order to make a valid comparison for the results.

Grid dependence was also assessed from values of the reattachment length l_R. Four grids distribution were considered, these are tabulated in table (4.5-b) below:

Table (4.5-b). Grid dependence of l_R

Grid nodes	No.of nodes downstream	l_R/h
(16,21,31)	12	2.476
(16,21,34)	15	2.485
(16,21,38)	19	2.519
(16,25,38)	19	2.530

4.3 PREDICTED FLOW BEHAVIOUR.

4.3.1 General Features Of Flow

The main features of the predicted flow patterns are presented in this section in the form of projections of the velocity vectors on to various co-ordinate planes and surface pressure contours.

Before discussing the predictions, some comments will be made about the expected flow pattern, which should be reproduced by the predictions. The following description is based on the experimental observations (I.P.Castro and A.G.Robins 1975).

1) Flow Pattern Upstream of The Obstacle

The flow approaching the body is deflected by the build-up of the pressure as the fluid impinges on the front face, as in figure (4.15 (a, b)). The adverse pressure gradient ahead of the body acting on the slower moving fluid in the thin floor boundary layer, for the case of uniform upstream flow, provokes the formation of a reverse flow region along the base in front of the body.

Similar behaviour occurs in the boundary layer upstream flow case, but here the reverse flow region is larger because of the thicker boundary layer. Deceleration of the flow at the front face and its deflection around the sides and top of the obstacle cause a zone of high positive pressure particularly near the centre of the

see Fig.

55

front face where the flow approaches stagnation. The existence of a vertical gradient of free stream velocity in the boundary layer flow shifts the location of the maximum surface pressure nearer the top of the surface because of the higher dynamic pressure associated with the faster moving fluid near the top. When the free stream velocity is yawed relative to the body the location of the maximum surface pressure moves nearer to the edge of the surface, until the case with yaw angle equal to 45° the stagnation point should be near the centre of the leading edge for the uniform inlet flow case. On the other hand for the boundary layer flow the location of the stagnation point on the leading edge again is nearer to the top corner (fig 4.15b).

2) Flow Pattern at Sides and Top Faces of The Obstacle.

Separation of the flow occurs at the sharp leading edges of top and side faces and forms an eddy with a tranverse axis on the top surface and a " horseshoe vortex " along the side surfaces. The static pressure P just downstream of separation is approximately equal to that in the main flow immediately prior to separation; because the flow accelerates in passing all around the front face, P is less than P_{∞}, with the result that the pressure coefficient becomes negative in the separated flow . A small negative pressure gradient exists from front to back

56

on the top surface (figure 4.15-a) for the uniform upstream flow, while for the boundary layer case the figure shows a positive pressure gradient on this surface, with a relatively small value of C_{r} at the front leading edge.

The surface pressure coefficient distribution on the side face is similar to that on the top with a small negative pressure gradient in the Z-direction.

3) Flow Pattern Downstream of The Obstacle.

Behind the obstacle, the fluid forms a large recirculation zone with characteristics of low velocity and pressure similar to those already observed in the separated zones of top and sides. A small negative pressure gradient is observed in the uniform flow case from bottom to top on the rear surface; this induces a gentle flow towards the top of the obstacle as part of the pattern of recirculating flow. Immediately behind each vertical trailing edge a standing vortex has been observed (Castro I.P (1973)), while for the boundary layer case figure (4.15-a) shows reduced and more uniform suction on the rear face of the obstacle than observed in the uniform flow case.

The recirculation region at the rear of the obstacle is followed by a region in which two prominent contra-rotating streamwise vortices are formed as a consequence of an interaction between the horseshoe vortex and small

streamwise vortices generated by the body itself near the
rear corners of the top face. Figure (4.15-c) shows a
sketch of the flow pattern around a cube in the case of
zero yawing angle (Fackrell (1982)). More detailed
information regarding the above discussion are given in
(Castro, I.P and Hunt, J.C.R (1984)).

4.3.2 Surface Pressure Contours and Vector Velocity Fields.

In this section the flow fields predicted will be
displayed by surface pressure contours and velocity vector
plots for two cases, where the wind yaw angle was zero and
45°. Comparisons were made between the predicted surface
pressure contours and those published by the Engineering
Science Data Unit " ESDU 1972 ".

a) Surface pressure contours.

Figures (4.16 to 4.22) show predicted surface
pressures plotted as contours of constant pressure
coefficient, C_p, on the cube surfaces and the
corresponding contours from " ESDU "; for the two
considered cases. Starting with the first case, where yaw
angle α is zero. Figure (4.16) shows the distribution of
the pressure coefficient on the front face of the cube,
the maximum value of C_p is near to the centre of the face,
where the flow impinges almost normally to the front face.

Near the edges, a sharp drop exists in, C_p values due to the flow deflection around the sides and over the top leading edge of the cube.

The predicted contours over the front face show a great similarity with that from " ESDU " data, however the prediction gives more details near the edges.

Figures (4.17 and 4.18) show the surface pressure contours on the side and top faces of the cube respectively. The high negative values of the pressure coefficient appear at the leading edges of these faces as the result of the accelerated flow passing over these edges. The predicted C_p values are too high over this region of the top and side faces compared with the values from " ESDU " data. At the downstream edges the predictions produce lower values of C_p than the corresponding values observed from "ESDU" .

The surface pressure coefficient contours on the rear face of the cube are shown in figure (4.19), for both prediction and experimental data from " ESDU ". The predicted distribution of C_p over the rear face is slightly lower than that from ESDU data. The reason for the lower suction is thought to be connected with the mathematical turbulence model used in the modelling of the flow after separation at the front edges.

Both predictions and experimental contours for the second case, where the wind yawing angle, α =45°, are illustrated in figures (4.20 to 4.22). Over the upstream

faces, figure (4.20) shows a great similarity between prediction and " ESDU " contours, the maximum value of C_p is located near the centre of the front leading edge of the cube as the result of the diagonal flow.

Typical pressure coefficient contours on the top face of the cube for the same case are given in figure (4.21), prediction and experiment agree that separation takes place from the top leading edges, however, prediction appears to under-predict the size of the separation at that region as suggested by the lower negative C_p values.

The downstream faces are in fully separated flow, a small negative pressure gradient exists from the leading edge to the trailing edge as shown in figure (4.22). But the pressure recovery as suggested by prediction appears to be high at the top corner of the vertical leading edge of this face. However the average pressure coefficient values acting on these faces are in fairly good agreement.

b) Vector velocity plots.

The details of the velocity field as produced by predictions will be presented in the form of projections of the velocity vectors in three views for the two considered cases. Some vectors were too small to be shown clearly on the velocity scale so that only the flow fields around the cube were plotted . For simplicity the velocity vectors in each view of the flow field will be discussed separately.

1) Side elevations of the flow field (Y - Z planes)

The predicted flow pattern in the plane of symmetry figure (4.23-a) shows a strong upwards deflection immediately upstream of the cube. The deflection is reduced at the plane through the side of the cube figure (4.23-b) where the flow can deviate horizontally around the cube as well as vertically. A very small downward flow is predicted near the front base of the cube, showing the existence of a thin upstream boundary layer. The separation bubble over the front leading edge of the roof is indicated by the zone of small negative velocity vectors. The velocities in the region just above this zone are positive with a slight upwards inclination. The downstream region is clearly indicated by a large recirculation zone with the characteristics of low velocity. The pattern immediately adjacent to the side of the cube figure (4.23-b) indicates a recirculation zone near to the top edge, marked B, which was fed by fluid from the large downstream separation zone.

2) Top views of the flow field (Z - X planes)

Figure (4.24) show the vector velocity pattern at different heights of the flow field. At a plane near to the floor (y/h=0.1), the strongest sideways deflection of the oncoming flow takes place as well as the lateral separation bubble on the side faces of the cube. This behaviour is predicted to occur with minor variation up to

the top of the cube. Over the top surface ($y/h=1.005$),
two rotating eddies can be seen as the result of the
separated flow at the leading edge of the top face. The
recirculation zone downstream is indicated by the region
of negative velocity vectors decreasing gradually up to
the top.

3) End elevation of the flow field (X- Y planes)

Projections of the total velocity vectors on to
various cross stream planes are shown in figure (4.25).
At a plane immediately adjacent to the front face of the
cube figure (4.25-a), an outward lateral deflection is
prominant near the floor and an upward component of
velocity is greatest near the symmetry plane. The minimum
velocity vector indicated that the stagnation point is
located near to the centre of the front face. Figure
(4.25-b), gives the velocity vector in a plane immediately
adjacent to the rear of the cube where the axial velocity
components are nearly equal to zero. The downstream
recirculation zone has an upward component on the rear
face, while near the top corners there is a small
recirculation zone as a consequence of a lateral pressure
gradient, causing fluid to move inward in opposition to
the predominant outward and upward flow.

The corresponding flow patterns with wind yaw angle
($\alpha = 45°$) are given in figures (4.26 to 4.28). Figure
(4.26-a) shows the projections of the vector velocity

field on the upstream face, the figure shows that the upward deflection of the oncoming flow takes place at the front leading edge of this face as well as the top edge. Whereas at the lower part of that face most of the flow runs horizontally. On the downstream face figure(4.26-b), the recirculating flow indicated by reverse velocity vectors is most prominent over this face. The upward deflection along the leading edge indicates the flow separation along this edge, while the downward deflection over the top edge of this face causes the flow to reattach.

Figures (4.27 and 4.28) show the variation of the flow pattern at different heights of the cube. The flow pattern close to the floor figure (4.27-b) shows a large recirculation zone provided by two vortices, marked (I) and (II), the recirculation zone size decreasing gradually up to the top of the cube. The symmetry of the flow pattern is illustrated in this plane view.

Near to the top surface, figure (4.28-a), the flow pattern shows the deflection of the velocity vectors at the top leading edges . While the recirculation zone at the top plane is indicated by small velocity vectors. At a plane slightly above the top, figure (4.28-b) shows the existence of the symmetrical diagonal flow pattern.

4.4 WIND LOADING ON A SINGLE RECTANGULAR BLUFF BODY MOUNTED ON A HORIZONTAL PLANE.

In order to estimate the accuracy of the codes of practice used for calculating wind loads on semi-submersible deck structures , the prediction of turbulent flow over a simplified rectangular model representing, say, a typical deckhouse structure or element was considered,to evaluate the pressure values acting over the surface of the model. These predicted pressure values were used to calculate the body forces coefficients.

The overall wind load on the model could then be determined by resolving these forces into the windward direction to produce a drag force and vertically to produce a lift force.

For the analysis of the results two distinct axis systems were used, one related to the wind (wind axis system) giving the drag force coefficient C_d, the side force coefficient C_C and the lift force coefficient C_ℓ. While the other one related to the model (body axis system) giving the axial body force coefficient C_X, the side body force coefficient C_y and the vertical body force coefficient C_z.

Figure (4.29) illustrates the relationship between the two systems. As a guide to the similarity between prediction and experimental results, some of the results obtained were presented in terms of pressure coefficient distribution diagrams with the relevent body and wind axis

64

force coefficients also given.

4.4.1 Surface Pressure Coefficients.

The results given in this section are the average pressure coefficients on a complete face of the cube. For convenience in reference to a particular face, the faces of the cube have been lettered as in figure (4-29) and the appropriate letter is added as a suffix to C_p in referring to the pressure coefficient on a particular face.

Figure (4-30) shows the variation of the average pressure coefficients for the isolated cube with wind yawing angle x, based on PHOENICS results and experimental (REEVES and LATTIF (1987)) results. The figure shows a good agreement is observed for the upstream faces; however over the downstream faces, the pressure recovery suggested by PHOENICS appears to be underpredicted, the reason for that is probably due to the mathematical turbulence model used in the numerical calculations.

4.4.2 Distribution Of Local Pressure Coefficient On The Cube Faces.

Figures (4.31 to 4.34) show the local pressure coefficient distributions over the cube faces at (0° & 45°) wind yawing angles for the computational and experimental results respectively. For zero wind yaw angle, a great similarity is observed on the front face between PHOENICS and experimental distributions.

Over the top and sides faces, the predicted C_r values appear too high over the leading edges of these faces compared with the measured values from experiment, while over the trailing edges of these faces the predicted distribution is under-estimated compared with the experimental one. Over the rear face again the predicted distribution gives lower values. In the second case i.e. wind yaw angle ($\alpha = 45^\circ$), it can be seen that the general form of the distributions compare well over the upstream faces, while over the downstream and top faces, the prediction shows a lower suction distribution .

4.4.3 Force coefficients

Comparisons of the body axis force coefficients obtained from the predicted results were made with those published by the Engineering Science Data Unit " ESDU 1972 ", the experimental results, (REEVS and LATTIF (1987) and those calculated using empirical formulas provided by the classification societies codes (American Bureau of shipping (ABS), 1980 and Det norske Veritas (DnV), 1981 & 1985). A brief description of the empirical wind load calculations specified by the classification society codes (ABS and DnV) are given in appendix [A].

Discussion of the graphical results are presented in this section.

Figure (4.35) compares the body axis force coefficients based on PHENICS results, experimental

66

results and data obtained from " ESDU ". The predicted results show a good correlation between the experimental results and " ESDU " data, except the slight diviations at (75° and 15°) wind yawing angle for C_x and C_y respectively, which are due to changes in flow separation and reattachment on the model side.

Figure (4-36) illustrates the profiles of the wind axis force coefficients C_d and C_C over the full range of the wind yaw angles for predictions, experimental and " ESDU " data. The drag force coefficient C_d profiles compare well in the region (30° to 60°) wind yaw angles, although the predicted values indicate under-predictions at (0° and 90°) yaw angles as the result of the low suction pressure predicted over the downstream faces in these conditions. However the experimental values at (15° and 75°) yaw angles show slight deviations as expected from C_x and C_y results. The cross-stream force coefficient C_C indicates the difference between predictions and experiment more clearly at (15° and 75°) yaw angles.

Figure (4.37) illustrates the comparison of predicted values of C_d and C_C with those based on the classification society codes (DnV). The DnV estimation are based on a SINE/COSINE variation with wind yaw angle , γ . Two sets of estimation were considered , the first one based on DnV(1981), and the second for DnV(1985). There is good agreement between PHOENICS and the DnV (1981)

results, however the estimated coefficients based on DnV (1985) give higher values.

Figure (4-38) gives the wind force coefficients C_d and C_c based on DnV and ABS codes with the corresponding values produced by PHOENICS results. The ABS code allow only for the calculation of the drag force in the wind direction. The ABS code gives values which closely follow the predicted trend; however the DnV (1985) gives a higher value of C_d over the full range of yaw angle.

The cross-stream force coefficient C_c as estimated from DnV is equal to zero at any value of wind yaw angle due to the estimation based on SINE/COSINE variation for C_x and C_y.

4.5 PREDICTION OF 3-D TURBULENT FLOW OVER TWO RECTANGULAR BOXES.

4.5.1 Interference From Neighbouring Obstacles.

The flow pattern around an obstacle located close to other obstacles, which interact with the fluid stream, depends on geometrical parameters such as the distance between the obstacles, their relative heights, their shapes, and the angles of incidence and inclination of the flow.

The interaction has been noted to be particularly acute in the case of two rectangular obstacles of different heights where the tall obstacle lies downstream of the small one (Melbourne and Joubert, 1971; Wise, 1971). Leutheusser (1971) measured surface pressure on a group of prismatic obstacles having different aspect ratios, but all oriented at the same angle of incidence to the free stream flow. By comparing these pressures with those obtained on the same models standing in isolation, he found a reduction of C_p on the front face of a sheltered model, but the negative pressures on the sides, top and rear surfaces were increased in magnitude by as much as a factor of two. The overall surface loading was thus more severe for a " Sheltered " model than for an isolated one.

The behaviour of the flow between identical blocks placed side by side normal to a uniform air stream was

examined by (Ishizaki and Sung (1971)), for a variety of aspect ratios, the velocity reached a maximum value between 1.2 and 1.4 times that in the undisturbed flow, when the separation of the blocks was roughly equal to their streamwise dimension.

Because of the wide variety of situations which may exist, it is difficult to generalise about the effects of interference. Extensive systematic experimental tests, such as those of Bailey and Vincent (1943), are thus required to establish trends in the flow behaviour. For simplicity, the case of two identical cubes situated on the longitudinal axis with variable spacings for the full range of wind directions was considered to examine the effect of shielding on the downwind cube.

4.5.2 Geometry and Boundary Conditions.

The geometrical characteristics of the solution domain for two rectangular boxes situated on the longitudinal axis with variable spacings are illustrated in figure (4.39); where d, is defined as the geometric distance of the intervening space. The external domain characteristics are similar to those defined in section (4.2.1). Two spacing conditions were considered with the full range of wind directions to examine the shielding effect on the downwind box.

The geometrical characteristics of the computed domain are listed in table (4.6), while the boundary conditions for U,V,W,K and $\mathcal{E}$ imposed at the surfaces of the solution domain are similar to those in table (4.1) section 4.2.

Table 4.6 : Geometry of solution domains

	Yaw Angle $\alpha = 0^{\circ}$	Yaw Angle $\alpha > 0^{\circ}$
L_{U_x}	5h	5h
L_{d_x}	5h	15h
L_y	5h	5h
L_{U_x}	5h	5h
L_{d_x}	15h	15h
d	h & 2h	h & 2h

* h is the length of the cube sides.

4.5.3 Grid Distribution .

The " model " in this case was taken to be the two cubes plus the intervening cavity. Prediction of the flow pattern within this region is obviously of major importance. So, the grid distribution in the following regions, i.e. upstream, downstream and vertical outside the " model " was considered as a result of the grid refinement tests for the case of single rectangular box (section 4.2.1). However, for the model region, the criterion for the choice of the grid distribution was to place the grid nodes close enough to the model surfaces where steep gradients of the flow properties occur.

Four grid distributions were tested for the case where the distance between the cubes was, $d = h$, (i.e. a cubical cavity was formed), and zero yaw angle, the grid distributions for these cases are summerized in table (4.8) below.

Table 4.7 Grid distributions for two cubes model:

Grid nodes	(26,16,42)	(28,18,44)	(32,22,48)	(34,24,50)
X direction				
Up-stream	10	10	10	10
Downstream	10	10	10	10
Y direction	10	10	10	10
Zdirection				
Up-stream	10	10	10	10
Downstream	10	10	10	10
Cavity region				
X-	6	8	12	14
Y-	6	8	12	14
Z-	6	8	12	14

* An 8 grid point distribution in z-direction was retained for each cube

In order to decide when a grid independent solution has been obtained, profiles at several locations for selected variables were required to show little change with further refinement. To avoid overlapping of points which either coincide or are very close to each other, three cases only were plotted for comparison. Two test sections were considered . The first test section is the symmetry plane of the flow at different location,

z/h=0.0333 (immediately adjacent to the rear face of the upwind cube), z/h=0.50 (at the middle of the cavity) and z/h =0.967 (immediately adjacent to the front face of the downwind cube) . While the second test section is a plane immediately adjacent to the side face of the cavity at the same locations (z/h).

Grid sensitivity of the pressure coefficient C_p profiles, the axial velocity W profiles and the kinetic energy of turbulence K profiles at the consideréd test sections are discussed in the following paragraphs.

1) Grid Sensitivity Of C_p.

Figures (4.40) gives the pressure coefficient profiles on the plane of symmetery (x/h=0.50) at different locations (z/d). From these profiles it appeared that, there was no change in C_p values between the grid nodes (12,12,12) and (14,14,14) for the cavity region in X- ,Y- and Z-directions respectively.

A small positive value of C_p appears near the top of the cube (y/h=1.0) at the plane adjacent to the front face of the rear cube, this is possibly due to the reattachement flow at the top edge of that region .

At the second test section, near the side face of the model (x/h=0.967), figure (4.41) illustrates the C_p profiles at the same location (z/d). The figure gives slight differences between grid nodes (12,12,2) and (14,14,14) at (z/d=0.0333), just behind the upwind cube,

the reason for that is probably due to the outward flow at
that location. While at the rest of the test locations the
profiles indicate good agreement between the two grid
node distributions in the cavity region.

2) Grid Sensitivity of The Axial Velocity : W

Figures (4.42 and 4.43) illustrate the profiles of
the axial velocity, W in the same test sections they show
similarity of the axial velocity values for the cases with
(12x12x12) and (14x14x14) grid nodes in the cavity region
for both test sections.

A high velocity region appears near y/h = 1.0 due to
flow separation along the top leading edge of the front
face of the downwind cube. Also the reverse flow (
negative values of W) in the lower part of the cavity
region and the positve values of W in the upper part as a
result of the clockwise vortex motion at the cavity region
are in fairly good agreement.

3) Grid Sensitivity of The Turbulence kinetic Energy K.

A final check on grid refinement test was considered
for the kinetic energy of turbulence K. Figures (4.44 and
4.45) give the profiles of K at the considerd test
sections indicate similarity between the (12x12x12) and
(14x14x14) grid points in the cavity region.

The grid dependence tests discussed above showed that
a grid of (12x12x12) nodes in the lateral, vertical and

75

axial directions respectively was a reasonable compromise for the cavity region, which improved gradually with further refinement of the grid, and the rapidly increasing computing time and storage requirements.

A second series of predictions, with the distance between the cubes was, d= 2h, used a similar grid distributions (12x12x12) grid nodes in the cavity region, with suitably enlarged cell dimensions at the centre of the cavity.

4.6 PREDICTED FLOW BEHAVIOUR.

The main features of the predicted flow pattern for the case of two rectangular boxes at various spacings are presented in this section in the form of projections of the velocity vectors and pressure contours. Nevertheless the situation with the bluff body model is more complex and it is convenient to describe the various views of the flow field separately. There are strong interactions between each view which belie the simplicity of these descriptions.

Two cases were considered where yawing angle = 0° and 45°, each with cavity space equal h and 2h. Comparisons were made between surface pressure distribution produced by prediction and that from experiment (Reeves and Lattif (1987)) in the next section.

4.6.1 Vector Velocity Field.

The velocity vectors as produced by predictions for the considered cases were presented in the region around the model . For simplicity the velocity vectors in each view of the flow field will be discussed separately for 0° and 45° wind yaw angle conditions.

A) Vectors Plots for 0° Yaw Angle.

1) Side Elevations of The Flow Field (Y - Z planes).

The predicted flow pattern in the plane of symmetry (x/h =0.50) for the considered cases are shown in figure (4.46) indicate the expected behaviour of the flow field. In the upstream region, the predictions show the downward flow occurs in the region (y/h < 0.5), forming the reverse flow region along the front base of the upwind cube, while near the midheight of the cube the velocity vector indicates the stagnation point.

The upward flow takes place in the region (y/h > 0.50). The deflection at the top leading edge of the front face, where the separation of the flow forms an eddy bubble on the roof of the upwind cube. For the cavity region, the majority of the flow rides over the top of the cavity (sometimes called skimming flow), causing the trapped flow between the obstacles to rotate slowly . When the spacing is large (d=3h) (T.V.Lawson. 1980) the wind comes down to the ground level between the obstacles. So the upwind obstacle creates enhancement of wind speed in the area in front of the downwind one in which the wind is travelling against the mean stream. For the intervening spacing (1<d/h<3) an oscillatory flow pattern occurs.

Figure (4.46) gives an important difference between the vector velocity field in the cavity region at the symmetry plane for both (d=h and d=2h).

The upward deflection of the flow in the second case indicates more negative pressure on the leading edge of the top face of the downwind cube than in the first case. Also more positive pressure values are produced over the upper part of the front face of the upwind cube in the second case than in the first one. This will be discussed in the form of pressure coefficient contours in the next section.

The downstream region confirms the existence of the recirculation zone, with a reattachment length ℓ_R. This length was shorter in the first case than in the second one. This feature shows more flow disturbance by the downwind cube in the second case than in the first case.

The corresponding vectors plots at a plane through the side face of the model (x/h=1.0) are illustrated in figure (4.47). The figure shows the upward and downward deflections of the velocity vectors were reduced, as the flow can deviate horizontally around the obstacle as well as vertically. Reverse flow occurs at the lower part of the side face of the upwind cube for both cases (d=h and d=2h), forming a recirculating zone on that face which is fed by fluid from the cavity region. On the roof of the model, no reverse flow was predicted, where the vectors run almost parallel to the top face in both cases. Near the downstream edge of the top surface, the predicted flow deflects downwards and separates as it leaves the roof and a recirculation zone is formed. On the lower part of the

side face for the downwind cube a recirculation zone
occured as part of the large vortex zone in the cavity
region.

2) End Elevations of The Flow Field (X-Y) Planes.

Figure (4-48) shows the most interesting features
of the flow field in the transverse plane immediately
adjacent to the front face of the downwind cube at
(z/d=0.975) for the two considered cases. The downward
flow which is provided by a clockwise vortex in the
cavity region is the mean flow at that plane . While the
outward lateral deflection is prominant near the floor as
well as at the side edges, indécating that the flow moves
faster in the second case than in the first one.

A further difference between the two cases occurs
near the top edge of the front face, where some upward
flow occured in the second case indicating the existence
of reattachment flow near the top leading edge of the
front face of the downwind cube for cavity space (d=h).

3) Top View of The Flow Field (X-Z) Planes.

Top views of the flow field at different heights were
plotted in figures (4-49 to 4-51) for the two considered
cases. Figure (4-49) shows the vector velocity field near
the floor, the strongest sideways deflection of the
oncoming flow occured on the front face of the upwind
cube.

The lateral separation bubble on the side faces of the upwind cube was pronouced in the lowest plane and became smaller toward the top of the cube. In the cavity region the main flow was the reverse flow, which was provided by a clockwise vortex in the cavity. On the side faces of the downstream cube, separation takes place, while the width of the separation bubble on these faces is less than those for the upwind cube. In the downstream region of this plane, the recirculating flow was characterized by two vortices I and II just behind the obstacle.

Near the midheight of the model (y/h=0.5). Figure (4.50) gives a minor variation of the sideways deflection of the oncoming flow, and on the size of the separation bubble on the side faces of the upwind cube, while the flow on the corresponding faces of the downwind cube moves parallel to the main stream flow. In the cavity region, the vectors indicate no axial components.

At the top surface, Figure (4.51) gives a recirculation zone on the roof of the upwind cube as a result of the flow separation at the front leading edge of the top surface. In the cavity region the flow was travelling in the direction of the main stream as well as at the top of the downstream cube.

B) Vector Plots for 45° Yaw Angle.

In order to discuss the diagonal flow pattern by

means of the velocity vectors as predicted for the two considered cases, the flow field at different heights are plotted in figures (4.52 to 4.55).

The flow pattern close to the floor shows a large recirculation zone provided by two vortices, marked I and II behind the downstream faces of the cubes for both cases. The recirculation zone decreases gradually up to the top of the cube. A general similarity of the flow behaviour for both cases was observed.

4.6.2 Surface Pressure Contours.

The predicted surface pressure/plotted as contours of constant pressure coefficient, C_p, on the downwind cube surfaces, for the two considered cases (d=h and d=2h), in order to show the shielding effect. For simplicity the pressure contours will be discussed separately for 0° and 45° wind yawing angle conditions.

a) Surface Pressure Contours for 0° Yaw Angle.

Typical surface pressure coefficient contours on the cube surfaces for the two considered cases are illustrated in figures (4.56 and 4.57).

Figure (4.56-a) gives the contours over the front face of the cube. For the first case (d=h) a small positive pressure gradient is observed near the top edge of the surface, while for the second case (d=2h) a positive pressure coefficient value on this surface occure

as a result of reattachment flow, which supported the earlier observation from the vector pattern figure (4.48).

The pressure coefficient contours over the top surfaces are given in figure (4.56-b), *The* show a small negative pressure gradient from front to back on that surface. The upward velocity vectors at the top leading edge of the front face for the second case (figure (4.48)) lead to a relatively higher negative, C_p, at the leading edge of the top face than in the first case.

On the side face, a low pressure region occurs just after the leading edge of the front face, as a result of flow separation. Figure (4.57-a) gives a small positive pressure gradient on the side face of the cube for both cases. Figure (4.57-b) gives the C_p contours on the rear face of the cube, *showing* a small negative pressure gradient . . .

. from bottom to top for the both cases. This induces a gentle flow upwards to the top of the cube as part of the recirculating pattern. A great similarity exists between the two cases although there is a more uniform suction distribution for the second case.

b) Surface Pressure Contours for 45° Yaw Angle.

The surface pressure contours on the upwind faces are illustrated in figures (4.58 to 4.60). The figures indicate good agreement between C_p, contours on the unshielded face in the first and second cases. The maximum C_p values appear near the leading edge of the upwind

faces, indicating that the stagnation point is located near the centre of the leading edge as a result of the diagonal flow. A negative pressure gradient is observed from the leading edge to the trailing edge of the unshielded face for both cases. On the other hand, the C_p contours on the shielded faces give an interesting difference. The suction region on that face for the first case occupies about half of the area of that face, while for the second case, it appears near the rear edge. The reason for this was probably due to the momentum through the cavity region in the first case being less than the corresponding momentum through the same region in the second case.

Over the downwind faces of the cube, fully separated flow was predicted. Figure (4.59) shows the C_p contours on these faces for the two cases, a small negative pressure gradient exists on these faces for both cases, the average pressure coefficients on these faces for the two cases were quite similar.

Typical pressure coefficient contours on the top faces are given in figure (4.60). The figure shows that separated flow occurs on the leading edges of the top surfaces for both case.

4.7 WIND LOADING ON A SHIELDED CUBE MOUNTED ON A HORIZONTAL PLANE.

In order to estimate the overall wind loading on a shielded cube mounted on a horizontal plane, the predicted surface pressure coefficients C_p, acting over the cube faces, were used to estimate the overall wind loading using the same analysis described in section (4.3).

As a guide to the similarity between prediction and experimental results, three sets of comparisons were presented. The first set of comparisons are given in terms of average pressure coefficient on the cube faces for the full range of wind yaw angle, the second set present the pressure coefficient distribution diagrams over the cube faces with the relevent body and wind axis forces coefficients, and the third set of comparisons give the overall force coefficients over the cube for the full range of wind yaw angle.

4.7.1 Surface Pressure Coefficients.

Figures (4.61 and 4.62) show the profiles of the average pressure coefficients over the shielded cube faces, for the full range of wind yaw angle, based on predictions and experimental results. Over the top surface of the cube (face-a) the prediction profile gives relatively high values of C_p for the cavity space (d=h), however for the cavity space (d=2h) a fairly good agreement between PHOENICS and experimental results is

85

observed. Although over (face-b) the under prediction for the recirculating flow appears more clearly at moderate yaw angle ($0°<$ $x < 15°$), with further increase in wind yaw angle, the front face (b) of the shielded cube is in attached flow, and predictions give an accurate distribution of C_p. While on (face-c) the average pressure coefficient values compare well except at small values of wind yaw angle. Over the downstream faces (face-d and face-e), the profiles indicate good agreement except when the face was completely shielded.

4.7.2 Distribution of The Local Pressure Coefficient Over The Shielded Cube Faces.

Figures (4.63 to 4.70) give the local pressure coefficient distributions over the shielded cube faces for cavity spacing (d=h and d=2h).

Two sets of results are given where wind yaw angle equal to zero and 45° for PHOENICS and experimental distributions respectively. For zero yaw angle, where the rear cube is completely immersed in the turbulent wake of the front one, the distribution of C_p, on the front face of the cube indicates the extent of under-prediction of the recirculating flow by PHOENICS. Although the shape of the distribution is fairly well simulated with the experimental shape. Increasing the cavity space, d, shows little difference between PHOENICS and experimental

results.

At 45° wind yaw angle, the front face of the
shielded cube is in attached flow, and prediction gives an
accurate distribution of C_p, on the upstream faces,
PHOENICS results follow the experimental results in shape,
but with small differences in magnitude.

4.7.3 Force Coefficients.

Figure (4.71) shows both prediction and experimental
profiles of the body axis force coefficients with wind
yawing angle for the two considered cases.

At moderate yaw angle ($0° < \alpha < 30°$), the axial
body force coefficient C_x profiles produced by PHOENICS
show under-estimated values, while over the range ($45° < \alpha < 90°$) wind yaw angle, the predicted results appear to
be over-estimated. On the other hand the profiles of the
side body force coefficient C_y indicate remarkably close
agreement over the full range of wind yaw angle.

The corresponding wind axis force profiles are given
in figure (4.72), it can be seen that the drag coefficient
profiles compare well over the full range of wind yaw
angle except for the small values of yaw angle ($0° < \alpha < 15°$). For the cross-stream force coefficient C_c, the
predicted results indicate lower values when compared with
the experimental results for the region ($60° < \alpha < 90°$)
wind yaw angle.

4.7.4 Shielding Effect on The Force Coefficients.

The effect of shielding on the force coefficients acting on the cube can be summarised as follows.

Figure (4.73) shows the force coefficients variation with wind yaw angle for the shielded and unshielded cube. The general trend for the variation for the shielded model force coefficients with wind yaw angle is that the values approach those obtained for the isolated model with increasing yaw angle and increasing cavity space d.

At zero yaw angles i.e. the cube totally shielded, the axial body force coefficient C_x, is much reduced when compared with the isolated case, as well as the drag coefficient C_d. The shielding effects on the side body force coefficient, C_y, are much less pronounced with the main differences between the isolated and shielded models occurring between zero and 30° wind yaw angles. While for the cross-stream force coefficient, C_c, the differences between the isolated and shielded results appear over the full range of yaw angles.

5.PREDICTION OF 3-D TURBULENT FLOW OVER A SIMPLE PLATFORM MODEL.

5.1 INTRODUCTION.

From an aerodynamic viewpoint an offshore platform is essentially a large bluff body supported on legs above the sea surface. The wind causes an airflow over and around the platform which is unsteady in both direction and strength. This flow in addition to exerting forces on the platform may influence the safety, efficiency or reliability of certain operations.

The detailed pattern of air flows over offshore platforms is a complex matter, being dependent on the precise configuration of the installation, the state of the sea and the general atmospheric environment.

Offshore platforms usually comprise an assembly of rectangular blocks, lattice structures and, in relation to their overall size, small protuberances. The main flow features are generated by the overall bulk of the platform, while the effects of small protuberances and, to some extent, lattice or porous structures can initially be assumed small in general, but can, of course, have pronounced local effects. With experience a reasonable picture of the overall flow pattern can be built up from the characteristics of flow over rectangular blocks.

The primary objective of this chapter is to determine the sensitivity of wind loading to various platform

parameters. A simple four-legged model representing a rudimentary structure of an offshore platform was considered as a base line case (figure 5.1). A number of the platform's features were considered so that the sensitivity of the predicted wind load to various platform parameters could be determined. The parameters which were examined are the freeboard ratio, deck layout, helideck siting and lattice structures such as derricks and cranes.

The influence of wind direction was considered for a full range of wind yaw angle and additionally, the pitch angle of the incoming flow was varied.

Comparisons of the wind force coefficients obtained from the predicted results were made with those based on the empirical calculation provided by the classification societies codes (ABS and DnV) and experimental results (Reeves and Lattif (1987)).

5.2 CLEAR DECK AND THE INFLUENCE OF WIND LOADS AT EVEN KEEL.

The square plain platform model, figure (5.1) was considered, to illustrate the ability of PHOENICS to deal with wind forces on a platform structure. For ease of computation at this stage, it was decided to adopt a cartesian coordinate system and predict for legs of square section. The obvious discrepancies which this produces may be removed later, at some cost in grid complexity and computing time. Their effect is not as great as it might appear, however, as for a typical semi-submersible the contribution to overall wind loading from the legs is quite small (especially when wind shear profile of the incoming flow is included).

In any case, the gross effects can be closely simulated by suitable choice of leg size. It is only in localised areas such as leg-deck interaction that the use of the wrong cross-sectional shape may cause serious discrepancies, and the effect of these on overall loading is unlikely to be significant.

The rectilinear grid adopted is shown in figure (5.2), while table (5.1) summarizes the geometrical characteristics for the solution domain and grid distributions.

Figure (5.3) illustrates the profiles of the wind drag force coefficient, C_d, over the full range of the wind yaw angles for predictions, experimental

91

measurements, and those based on the classification society codes (DnV and ABS). The PHOENICS prediction uses square section legs, while the experimental model had circular section legs; it is clear that the predicted drag coefficient is higher than the measurements except when the shielding effect of the legs were important at zero and 90° wind yaw angles.

When the platform has a corner into the wind (i.e the flow is oblique i.e $x = 45°$) there are marked differences between the predicted and measured values of the drag coefficient. This is due to the two trailing vortices which emanate from the upstream corners of the leading edges of the legs. However, the trend of the drag coefficient as predicted by PHOENICS follows the empirical estimation, while the magnitude was lower over the full range of wind yaw angle. This is due to the fact that interference effects between the platform legs (shielding effect) are neglected in the empirical calculations for this situation.

Table (5.1):Geometry of solution domain and grid

distribution for even keel model

Direction	"Solution domain" Length in m	Grid nodes
X	5.0	40
Y	2.0	40
Z	5.0	20

5.3 INCLINED PLATFORM AND INFLUENCE OF WIND LOADS.

5.3.1 Treatment of Boundary Condition for Inclined Platform model.

Throughout this section and the remainder of this chapter a pitch term will be used to describe the rotation of the platform about a horizontal axis through the origin, which is parallel to the side of the deck. The centre of the origin and rotation was chosen to be at water level because in practice its position is unknown and will vary. It is, therefore, convenient to use a constant position and the position chosen is consistent with common practice. Figure (5.4) clarifies the terminology used to describe the inclination of the platform.

The inclination of the platform can be achieved by producing a sloping surface for the bottom of the solution domain equal to the pitching angle in question, and simultaneously inclining the inlet flow by the same angle.

The sloping bottom of the solution domain can be formed in three ways. Firstly, by using the body fitted coordinate method, the surface friction and boundary layer effects can be well represented as well as the geometry of the model. The heavy demands on computational time and storage capacity made by this method precluded the investigation of the pitching platform by this method.

Secondly, a finite stepped grid can be used for the bottom surface of the solution domain. The validity of the turbulent wall functions applied near the surfaces of the stepped bottom cells is open to question, due to the sharp corners of the stepped cells.

Thirdly, by intoducing a special treatment using the concept of partial porosity to produce the sloping bottom, the effect of the sharp corners of the stepped cells can be suppressed. To represent the wall functions for the sloping surface in this case, it is necessary to locate the near-wall grid nodes very close to the sloping wall. However, modification of the dimensionless near wall velocity calculation (sec 3.5 equation 3.22), to represent the situation of the sloping bottom is not difficult to achieve using a special subroutine which is called by the PHOENICS package at pre-set points of the solution cycle.

Since, small angles of inclination were used, it was considered a reasonable approximation to simulate the wall friction on the sloping surface of the solution domain using a wall function on the horizontal sides of the cells only. This avoided the need for special programming.

5.3.2 Inclined Platform Calculations.

In order to examine the effect of pitch angle on the wind load over the offshore platform, the simple four-legged model (figure 5.1) was considered with a freeboard ratio of 0.60 and pitch angles of zero, 10° and 20° for zero incidence of oncoming flow. Note that, for 10° and 20° pitch angles, two conditions were considered for each case, firstly when the platform leading edge is tilted up into the wind, and secondly, when tilted down into the wind. Since the flow is symmetric about the centre plane of the model, the solution domain in X-Y plane represents only one-half of the flow field . Table (5.2) summarizes the grid nodes adopted for each case.

Figure (5.5), shows the effect of pitch angle on the drag and lift force coefficients for the predicted results compared with experimental results (Reeves and Lattif 1987) and the estimated values based on empirical formula provided by (DnV 1985). One may deduce that the drag force coefficient is greatest when the leading edge of the platform was tilted up into the wind, this is due to the wind impinging on the underside of the deck which created a contraction between the platform deck and the sea surface. At the same time, the exposed area of the leading legs to the wind flow were increasing as the pitching condition takes place, so, the drag force will be increased. On the other hand, when the platform was angled

down, the air was directed up over the platform and, because there is no restriction to the flow over the top surface of the platform deck, this presents less of an obstruction to the wind and consequently results in lower drag coefficient, as well as the reduction of the leg area exposed to the wind in this case. Thus the drag coefficient curve was asymmetric about the even keel position.

Both numerical and experimental results agree with these features, while the empirical code results gives a symmetric profile of C_d, with high values. The figure shows that a good agreement is observed between the experimental and numerical results.

The lift coefficient curve figure (5.5), shows that the numerical results closely followed both the experimental and empirical trends.

Table (5.2): Grid distributions for pitching model.

Pitch angle	Grid nodes		
	X-direction	Y-direction	Z-direction
10°	40	28	20
20	40	32	20

5.4 THE SENSITIVITY OF WIND LOADS TO THE PLATFORM PARAMETERS.

5.4.1 Effect of Freeboard.

Only the simplistic model form was tested for freeboard ratio values of 0.60, 0.40 and 0.20. Figure (5.6) shows the effect of freeboard on drag and lift coefficients at even keel over the full range of wind yaw angle. The effect of freeboard on the drag coefficient is apparently linear with increase in the freeboard ratio, these changes are due to the diminishing amount of the leg presented to the wind. The peak of this effect is at 45° wind yaw angle when the frontal area presented to the wind is at its greatest. As the clearance between the deck underside and the floor is reduced the separation of the flow underneath the deck is restricted, increasing the leading edge suction. A slight increase in the lift coefficient was produced with decreased freeboard values. As expected the square model at even keel produces a symmetrical drag and lift profiles with wind yawing angle. Figure (5.7) compares the drag coefficient as produced from the predicted pressure and those based on the empirical calculation. It is evident from the figure, that as the freeboard ratio is reduced from 0.60 to 0.20, the discrepancies between the three curves become smaller. Obviously, this result is due to the reduced significance of the shielded area at low freeboard ratio.

Figure (5.8) shows how the wind force coefficients vary with freeboard ratio at zero, 10° and 20° pitch angles. The effect of inclination on the vertical force is not a simple vectoring of the drag foce, and the force does not vary symmetrically between positive and negative pitch angles, however, the same linearity between the wind force and freeboard ratio for pitching condtion was observed.

5.4.2 Effect of Deck Layout.

Four different deck configurations were considered to examine the influence of deck layout on the wind loads and flow characteristics over the platform structure for both pitching and yawing conditions. These cases represent general plant and storage on deck. To recap, the four deck types were:

1) Clear deck : Clear flat square deck, has a length to thickness ratio (l/t =19.0).

2) Deck2 : clear solid square deck, with length to thickness ratio (l/t =7.0).

3) Deck3 : Flat square deck, with a solid strip along the leading edge.

4) Deck4 : Flat square deck, with two solid strips of different heights fixed on the upstream and downstream edges of the main deck respectively.

The principal dimensions for these configurations, and the grid distributions for each case are summarized in table (5.3) below.

Table (5.3): Principal dimensions and grid distribution

for platform models.

DECK TYPE		grid distributions		
		YAW	PITCH (10°, 20°)	
		(Nx, Ny, Nz)	(Nx, Ny, Nz)	(Nx, Ny, Nz)
CLEAR DECK.	0.048 m 0.048 m 0.025 m	40, 20, 40	40, 28, 20	40, 32, 20
DECK-2	0.07 m	40, 23, 40	40, 31, 20	40, 35, 20
DECK-3	0.08 m	40, 25, 40	40, 33, 20	40, 37, 20
DECK-4	0.08 0.12 m 0.16 m 0.044 m	40, 30, 40	40, 38, 20	40, 42, 20

Figure (5.9), shows the variation of the drag
coefficient with wind direction at even keel, based on
both numerical and empirical results. Marked reductions
between PHOENICS values of C_d and the estimated values
from the empirical codes occured whenever two legs are
aligned in the wind direction; this is due to the fact
that mutual interaction and shielding effects for the legs
are not (ABS)(or in limited form (DnV)) taken into
account. As the presented area to the wind increased a
fairly good agreement between the prediction and empirical
results is observed.

The position of an obstruction on the deck has a
significant effect on the drag coefficient values. One may
expect that the wind force on an obstruction positioned
near the downstream edge of the deck, will be affected by
the boundary layer presence on the platform deck. This
effect is clearly shown on the predicted profile of C_d for
"deck3" at zero and 180° wind yaw angles. However the
empirical calculation is not affected by the position of
the obstruction on the main deck, as it produced symmetric
profiles of C_d with wind yawing angle.

In describing the effect of deck layout on the wind
loads as the platform inclined, the predicted wind force
for the considered cases was displayed in terms of both
body and wind axis coefficients.

Figure (5.10), illustrates the effect of the

102

length/thickness ratio (l/t) of the deck on the wind loads
for different pitching conditions. When the platform is
made up of such a block of low (l/t), a three-dimensional
effect will be produced with a significant wake of
turbulent flow behind the deck resulting in a higher drag
coefficient. Also, for low (l/t), one would expect that
separated flow is likely to cover the whole of the
platform deck, with a reduction in the lift force as shown
in the figure.

The influence of placing an additional block
structure to the clear deck on the wind force is very
dependent on the scale of the object. If the object is
sufficiently large a deep separated zone develops at the
rear; furthermore, a significant separated zone may form on
the object itself. The wake of such a structure would be
highly disturbed, with downdraughts. One may anticipate
intensive interaction of the flow between two blocks as an
intensified wind flow or alternatively large trapped
vortices may form in the gap between the blocks. Figures
(5.11 and 5.12) show the profiles of both body and wind
axis force cofficients with pitch angles for (deck3) and
(deck4) compared with the clear deck profiles. It is clear
from these variations that the major influence on the
overall wind force arises from the gross bulk and
dimensions of the solid obstruction.

5.4.3 Effect of a Helideck Siting.

In considering the siting of a helideck on an offshore platform, the designer is clearly restricted by numerous other important considerations mostly non-aerodynamic in nature. Nevertheless, the landing area should be located so that a clear approach and take-off is available, preferably into the prevailing winds, and is least affected by structure induced turbulence or by high temperatures.

A rectangular helideck was added to the clear deck platform model in order to examine the effect of the helideck siting on the overall wind loads. Two cases were considered for the helideck positioned on the longitudinal axis of the platform. The first location of the helideck was at the upstream leading edge of the main deck, while the second location was at the downstream edge. The geometrical characteristics of the model and the grid distributions are given in table (5.4).

Figures (5.13 and 5.14) show the effect of a cantilevered helideck on the wind force coefficients in comparison to the clear deck for both yawing and pitching conditions. When the helideck was positioned upstream it produced a positive increment in lift force for both positive and negative pitch. The reverse was true for the case when the helideck was at the downstream position with a decrement in lift force for all pitch angles, while the

drag coefficient was increased mainly due to the helideck

base.

Table (5.4): Geometrical characteristics and grid distributions

for platform model with a helideck

	Grid distribution		
	YAW	PITCH (10°,20°)	
	(Nx,Ny,H₀)	(Nx,Ny,H₀)	(Nx,Ny,H₀)
Up-stream Helideck 0.25 m 0.005 m 0.08 m	45,28,40	45,36,20	45,40,20
Dwonstream Helideck 0.25 m 0.08 m 0.005 m	45,28,40	45,36,20	45,40,20

5.4.4 Effect of Lattice Structures.

A) The Nature of Air Flows Around Lattice Structures.

The effect that a non-solid object, (e.g. flare or derrick), has on the wind flow pattern depends on the solidity ratio, (shadow area of truss/ area enclosed by truss boundaries). When this ratio is small, most of the wind passes through, but as it is increased, more and more is deflected resulting in a two fold effect. The resistance of the members and the acceleration of the jets through the open spaces both increase causing resistance.

" All such obstacles of lattice steelwork necessarily have a drag force due to the wind and hence a wake of retarded and disturbed fluid. Although this wake is spread over a dimension related to the overall dimensions of the object, it is primarily composed of small scale elements emanating from the lattice members. Also, because of the multi-directional arrangements of these members and the fact that they are of relatively short span, it is expected that the wake would not produce large scale coherent motions and on the whole a flow of random small scale turbulent motions would result" (J.WILSON 1983). Experimental studies carried out at the National Maritime Institute (Davies, M.E and Cole, R June 1976) would appear to verify this, indicating that when a semi-submersible possesses a lattice tower the overall wind pattern was little changed except for some additional turbulence in

the wake of the tower. It would therefore seem that these structures do not significantly affect the overall wind flow pattern around an offshore structure. However, one should not forget that often they are constructed on a solid base which could localy disturb the flow significantly.

B) Treatment of Boundary Condition for Lattice Structure.

It is impossible to model individual structural members of truss-work (e.g Derrick or Cranes), because to do so will require an excessive number of computational cells. However, it is possible to set up a porous obstruction which models many of the important features of the flow around such structure, with a much more economical use of grid points. By using the concept of partial porosity to represent the solidity ratio of the lattice structure in question. However the flow through these porous cells is physically unrealistic, because no losses are associated with the flow acceleration and subsequent deccleration. Thus by introuducing a force coefficient source term, via a sutable algorithm included in the coding sequence for the whole region of such a structure as a function of its solidity ratio, one can represent the losses through the lattice members.

These resistance source terms need empirical data to identify a reasonable formula for such losses. As a first

approximation the resistance of the members of the lattice structures can be simulated by introducing the concept of wall friction on the sides of the cells within the lattice structure region.

To confirm this and to help in assessing the accuracy of the numerical solution, a case was considered for a plain platform with a derrick structure at the centre of the deck for even keel condition with zero incidence of the oncoming flow. The numbers of grid-nodes used in the X-, Y-, and Z-directions were (23, 30, 50), the grid distributions were highly non-uniform, in each coordinate direction, so as to give a good resolution of the solution in the areas of interest. Figure (5.15) shows the grid distribution around the platform model in both (z-y) and (x-y) planes.

Comparisons were made between prediction and empirical estimation of drag force for the derrick structure. The classification society codes, considered 30% of the overall areas of each the windward and leeward sides as an effective area of the truss-work structures. This is higher than the actual solidity which is used in such structures, and consequently results in higher drag force.

Table (5.5) illustrates the drag force for the derrick based on both numerical and empirical results.

Table (5.5) Drag force on the derrick model

Method	Drag force (N)
PHOENICS	0.1087
ABS	0.1625
DnV	0.2120

5.5 WIND EFFICIENCY OF THE PLATFORM STRUCTURE.

The wind loading on a platform is predominantly controlled by the main deck, columns, derrick, helideck and topside modules. Of these factors the most important are the topside modules and the main deck.

The total wind loading on a platform is dependent as seen from the previous sections, not only on the geometric configuration of the platform, but also on the wind direction and the pitching angle of the structure. However, this section will summarise the steps that can be taken to improve the wind flow pattern, thereby reducing the overall wind force.

1) Lower length/thickness ratio for the main deck; this reduces the wind projected area and decreases the size of the vortex bubbles generated on the sides and back of the platform deck.

2) Length to breadth ratios for any isolated structure closer to unity; this reduces the variations in wind loading produced by changes in wind direction.

3) Large isolated features should be avoided; if sufficiently large, they can produce deep swirling vortices both behind and in front of themselves.

4) Large modules should be placed near to the centre of the platform; this is beneficial in a number of ways.

Firstly the effect of the module on the vessel stability since it has a minimum effect on any tendency for the vessel to heel and pitch, and secondly the area subjected to the turbulent separated flow of the modules has an effect to reduce the overall wind force on these faces.

5) When large modules are separated through necessity it is not advisable to place the structures close to one another. Blocks that are too close together produce strong interference effects with the wind in certain directions. Increased separation will reduce the interaction between the side edge wakes of the two blocks.

6) Introduction of curves. The curving of sharp edges and the introduction of shapes that "smooth out" highly curved edges. This means of reducing the drag coefficient is likely to prove useful for both the platform deck and individual modules.

7) Avoid excessive cantilevering of the helideck; this is beneficial to the vessel stability.

6 PREDICTION OF 3-D TURBULENT FLOW OVER A FULL SCALE SEMI-SUBMERSIBLE .

6.1.INTRODUCTION

The main objective of the present work is to assess the ability of numerical methods to model the aerodynamics of offshore platforms. To conclude the work for this thesis, the prediction of wind flow over an actual operating semi-submersible platform was considered.

A full scale "AKER H4.2" series semi-submersible platform was used to illustrate the use of PHOENICS in solving a more realistic problem. However, the heavy demands on computational time made by this problem precluded the investigation of the effects of yaw and pitch angles. Only the even keel condition with zero incidence of oncoming flow was considered. Comparisons were made between predicted wind force and certain empirical calculation procedures used for wind load estimation in maritime engineering.

The flow fields predicted were displayed by way of velocity vector plots. The predictions have proved their ability to represent, at least qualitatively, the flow behaviour over the platform structure.

6.2 PLATFORM GEOMETRY AND BOUNDARY CONDITIONS.

The rig tested was an "AKER H4.2" semi-submersible platform. A limited number of drawings were available and from these a schematic representation is shown in figure (6.1) and a photograph of the completed rig is presented in figure (6.2).

The principal dimensions of the platform are shown below:

Length overall	115.0 m
Breadth overall	73.2 m
Length upper hull	87.5 m
Breadth upper hull	67.0 m
Column diameter	9.6 m
Draft operating	23.5 m
Derrick height	42.0 m
Displacement	41400 tones

The solution domain in X-Y plane represents only one-half of the flow field since the flow is symmetric about the centre plane of the rig for the considered case. By using a variable mesh, it is possible to keep reasonably good mesh resolution around the body while having the boundaries of the mesh far enough away from the body, such that the flow conditions are known or where uncertainties about them are unimportant.

The numbers of grid-nodes used in the lateral,

vertical and axial directions were 25x35x60 respectively. The geometrical characteristics of the solution domain and the grid distributions are listed in table (6.1) below.

Table 6.1   Geometry of the solution domain and grid

distributions

DIRECTION		CHARACTER	DISTRIBUTION
Solution domain	Z-	Length = 500 m.	100 (Upstream) 100.5 (Rig region) 299.5 (Downstream)
	Y-	Height = 150 m.	62 (Rig region) 88 (Up over the rig)
	X-	Half width =133.3 m.	33.3 (Rig region) 100 (From the rig side)
Grid nodes	Z-	60 grid nodes	8 (Upstream) 42 (Rig region)
	Y-	35 grid nodes	27 (Rig region)
	X-	25 grid nodes	17 (Rig region)

Figure (6.3) illustrates the grid construction in the region around the rig in both side and end elevation views. A uniform distribution of the axial velocity at the inlet surface of the solution domain was specified with a value of (20 m/sec), while the turbulence kinetic energy k and its dissipation rate ε are considered as was explained in section 4.2.1 (table 4.1). At the plane of symmetry the normal velocity and normal gradients of other quantities were set to zero.

115

6.3 CHARACTER OF THE PREDICTED FLOW PATTERN.

The detailed pattern of air flow over offshore platforms is a complex matter, being dependent on the precise configuration of the installation, the state of the sea and the general atmospheric environment.

When wind flows over such a structure it suffers a violent distortion of flow pattern and the regular wind velocity profile is significantly distorted. The air is forced around the platform and the high shear stresses at the windward edge induce a thick layer of turbulence which envelopes the platform and trails out leewards. Some idea of the basic flow patterns have been constructed from knowledge of the flow over single, double blocks and a simple model (chapter 4 and 5). Unfortunately there are strong interactions between the flow over individual items for some configurations.

The flow over such items of the structure in isolation depends upon their relative dimensions, length/breadth (aspect ratio), length/depth, the velocity profile and turbulence structure of the oncoming wind and the scale of the flow as characterised by the Reynolds number. Strong interactions can exist between the flows due to these items when they are closely grouped. A common example is the shielding of downstream bodies within the wakes of those upstream. This may be described as the general pattern of wind flow over the offshore platform

structure.

The main features of the predicted flow patterns are presented in the form of projections of the velocity vectors on to various coordinate planes. Figure (6.4) shows the velocity vectors for the region over the upper deck of the rig in side elevation of the Y-Z plane immediately adjacent to the symmetry plane. The figure shows the most interesting features of the flow field. Upstream of the rig the flow is diverted upwards over and sideways around the deck; high upwash velocities occur near the separation edge. Above the deck the flow is accelerated, but reduces rapidly through the separated shear layer and , near the deckhousing, may reverse. The trapped flow takes place as the result of the interference from neighbouring obstacles. Downstream there is a strong downwash which is highly recirculating.

Figure (6.5) shows the vector velocity pattern at different heights of the flow field. The figure indicates that the strongest sideways deflection of the oncoming flow takes place at the front leading edge as well as the lateral separation on the side faces of the deck layout, whereas at the rear faces the recirculation zone is indicated by small velocity vectors.

Figure (6.6) gives the top view of the flow field passing through the mid height of the rig columns, where

the shielding effect becomes more pronounced.

6.4 WIND FORCE ON THE FULL SCALE "AKER H4.2"

Traditionally, the calculations of the wind loads on a semi-submersible platform has been performed using empirical formulae provided by the classification Societies. Typically, a dimensionless coefficient for drag is introduced for an individual item (such as columns, deckbeams, deckhouses, derrick etc.) depending upon its geometry. The drag force due to wind on such item is calculated by multiplying this coefficient with the dynamic pressure and the projected area to the wind direction. The sum of all forces from different components provides the total wind drag force on a semi-submersible.

The calculation of the wind forces on any offshore platform is at best, far from an exact science, due to the complexity of design configurations and the strong interactions between the flow over individual items. These interactions are difficult to quantify and are the main reason that wind tunnel tests are often the only reliable method for estimating wind forces and moments.

It is widely accepted that the accuracy of the empirical calculation procedures is uncertain, and it should also be recognised that these procedures are seldom sufficiently explicit to prevent different individual interpretations leading to appreciable differences in

118

design loading estimates. It is a general consensus that the empirical formulae give , higher values than actual wind forces. Boonstra and Leynse (1982) state that empirically calculated wind forces are (30%-40%) higher than the forces obtained from the wind tunnel tests.

Although basically similar, the ABS and DnV rules have distinctive differences; appendix [A] summarize their approaches to these calculations.

In order to accomplish the objectives of the present study, the predicted pressure on each item of the tested semi-submersible "AKER H4.2" was used to estimate the wind drag force. Table (6.2) presents the comparison between the predicted wind force and those estimated by the classification Societies rules for the structural components labelled in figure (6.1). The remainder of this chapter discusses the differences between the predicted and empirical results for each item.

Table 6.2 Drage force in KN

Item	Empirical Codes			PHOENICS
	ABS	DnV (1981)	DnV (1985)	
L_1	30.514	38.900	44.900	37.826
L_2	30.514	15.970	18.400	9.735
L_3	30.514	5.390	6.070	5.128
L_4	30.514	2.210	2.500	10.095
PT	57.000	59.600	68.240	64.134
A	34.770	34.660	42.150	28.510
B	22.000	26.000	27.080	18.400
C	5.134	5.600	6.120	3.100
D	18.340	22.060	24.840	20.926
E	3.420	3.630	4.090	2.850
F	0.978	1.030	1.500	1.020
G	2.050	2.500	3.390	1.780
H	1.528	0.798	0.930	0.435
Derrick	1.320	1.700	1.920	0.700
Crane	1.470	2.010	2.310	0.620
Total	270.066	222.058	254.440	205.259

a) Wind Loads on The Rig Columns.

The predicted wind force on the upstream column (L_1) was in a good agreement with the average value from the empirical codes. For the shielded columns, the very crucial limitation of the ABS rule is the neglect of the shielding effect in the calculations. In contrast, shielding allowances by the DnV rules are permitted where the separation between members is less than seven times the diameter of the upwind member.

For the shielding columns, the predicted results show under-estimation for the second column, while the third column compared well. For the rear column the empirical codes suggested a very low wind force, while the predicted results by PHOENICS indicate that the wind force on this column is higher than that on the intermediate columns. This is believed to be due to the suction force provided by the large recirculation zone downstream of the final column.

b) Wind Load on The Main Deck and Deck-housing.

For the general case of a deck structure with platform at even keel, the position of the structure on the deck has no effect on the calculation of wind forces by the empirical codes. However, the results from PHOENICS indicate that variation of wind forces with position does exist; in particular the drag force on a body positioned away from the platform leading edge is generally lower

than if it is positioned near. This is believed to be due to the presence of an increasingly large boundary layer on the platform deck. For the main deck, PT, the predicted wind force compared well with the code results. The effect of the position of the deck-housing from the leading edge occurred on the items D, E, and F, as a relatively small reduction in the wind force. However the combined effect of the position and boundary layer appear on the result of the items B, C, and G, especially for items C and G which are thought to be completely immersed in the boundary layer as result of its small aspect ratio. The effects of position, shielding, boundary layer and interactions between deck layout are clearly demonstrated in the predicted results for items A and H.

c) Wind Loads on Lattice Towers (Derrick and Crane)

The empirical code allows a designer to estimate the effective area of the truss-work (cranes and derrick) structures by taking 30% of the overall areas of each of the windward and leeward sides together. This is higher than the actual solidity which is used in such structures.

The conclusion which can be drawn from the preceding comparison is that the numerically predicted wind force falls between the ABS and DnV calculations for the majority of the rig compounents.

Although the grids used in these calculations were not fine enough to draw any firm conclusions about the potential accuracy of numerical methods for this problem, it is clear that even with limited computational resources, worthwhile estimates of wind loading are possible. Further grid refinement would place great demands on computer time and storage capacity.

7. CONCLUSIONS AND RECOMMENDATIONS FOR FURTHER WORK.

The present investigation aimed to validate a prediction procedure for calculating the properties of turbulent flows with recirculation in three-dimensional configurations, as a step towards the application of the same prediction procedure to practical situations in engineering. The benefits from efficient and accurate numerical techniques is to provide the basis of a theoretical alternative to wind-tunnel testing.

The governing partial differential equations for the conservation of mass, momentum, kinetic energy of turbulence and energy dissipation rate are solved by a well-tested finite-volume, fully implicit, iterative solution method. The solution of the equations yields the three-dimensional fields of velocity and pressure, and auxiliary parameters of interest, such as pressure-, drag- and lift-coefficients. The method is also adaptable to the incorporation of different inlet and boundary conditions and to changes in geometry without fundamental changes to the solution procedure.

The reported results and computer requirements demonstrate that it is now feasible to perform three-dimensional, turbulent flow around bluff-bodies. It was found, by comparison with experimental results of surface pressure distributions, that the region up-stream of the obstacle was very closely predicted. This showed that the

prediction procedure is able to describe a region of flow with strong pressure gradients and severe flow deflection, provided a suitably fine grid and solution domain size were used. Although the existence of reverse flow on the top and side surfaces of the obstacles was predicted, the strength of this flow was underestimated, leading to poor prediction of the surface pressures on these faces and the back face of the obstacles. It would appear that the main source of difficulty is the inability to predict accurately the formation of the shear layers originating from the sharp edges of the obstacles. The likely causes of the discrepancies between the predictions and the measurements are the turbulence model, and the wall functions used over the surfaces of the structure from which the shear layers develop.

Other quantitative deficiencies were, found in the predicted results, particularly in the regions of recirculating flow, lattice structures and inclined surfaces. Recommendations in this respect are made in the following notes:

1) Use of an alternative turbulence models which allow for non-isotropic effects to the shear stress near the wall .

2) Use of the " Body fitted coordinate " for better

representation of the surface geometry of :

    a) inclined surfaces

    b) curved structures (e.g. rig support column).

3) Improved modeling of lattice structures using semi-empirical loss coefficients to predict pressure drop through the lattice-work.

4) Increased computer power will allow the use of a finer mesh, hence better resolution of regions with strong velocity gradients and more precise definition of complicated structures will be possible.

REFERENCES

ABS, American Bureau of Shipping,New York (1980)
"Rules for Building and Classing Mobile Offshore Drilling
Units".

Bailey, A. and Vincent, B. (1943)
"Wind pressures on buildings including effects of
adjacent buildings", J. Inst. Civil. Engrs., 20,243.

Baines, W.D (1963)
"Effect of velocity distribution on wind loads and flow
patterns on buildings". Proc. of conf. on wind effects on
Buildings and structures, Teddington, England,197.

Boonstra, H. and Leynse, C. (1982)
"Wind tunnel tests on a model of a semisubmersible
platform and comparison of the results with full scale
data"., 14th. Offshore Technology Conference, Houston
paper OTC-4245.

Caretto, L.S, Gosman, A.D, Patanker, S.V and Spalding,
D.B. (1973)
"Two calculation procedures for steady three-dimensional
flows with recirculation", Proc. of Third Int. Conference
on Numerical Methods in Fluid Mechanics II 60, Springer-
verlag, Heidelberg.

Castro, I.P. (1973)
"An experimental investigation of the flow around a
surface mounted cube in a uniform free stream". C.E.G.B.
report R/M/N687.

Castro, I.P. and Robins, A.G. (1975)
"The effect of a thick incident boundary layer on the
flow around a small surface mounted cube". C.E.G.B report
R/M/N795.

Chien, N., Feng, Y., Wang, H.J. and Siao, T.T (1951)
"Wind-tunnel studies of pressure distribution on
elementary building forms". Iowa Institute of Hydraulic
Research, State University of Iowa, Iowa city.

Connell, S.D. (1983)
"Numerical solution of the equations of viscous flow"
Ph.D thesis University of Nottingham, England

Connell, S.D. and Stow, P. (1986)
" A discussion and comparison of numerical techniques
used to solve the Navier Stokes and Euler equations" Int.

J. for numerical methodes in fluids, vol 6. 155-163.

Daly, B.J. and Harlow, F.H. (1970)
"Transport equations of turbulence" Phys, Fluids,13,2634.

Davies, M.E. and Cole, R. (1976)
" Nature of air flow over offshore platforms", National
Maritime Institute, R-14,OT-R-7726

DnV, Det norske Veritas, Norway, (1981,1985)
"Rules for the construction and classification of mobile
offshore units.

Edwards, J.P. (1985)
" PHOENICS-84 input examples " CHAM report UK/TR/101/3

ESDU, Engineering Science Data Unit (1971)
"Data sheet 71016: Fluid forces and moments on
rectangular blocks".

Fackrell, J.E (1982)
"Flow behaviour near isolated buildings ", C.E.G.B report
No TPRD/M/1254/N28.

Freathy, P.E. (1985)
"Wind loads on floating offshore structures", M.Sc,
Thesis, University of Western Ontario

Friedman, M. (1972)
"Laminar flow in a channel with a step." J. Eng. Math.,
6,285.

Greenspan, D. (1969)
"Numerical studies of steady, viscous, incompressible
flow in a channel with a step", J. Eng. Math., 3.21.

Hanson, D.M. And Wilson C.B. (1986)
"A three dimensonal simulation of wind flow around
buildings", Int. J. for Numerical Methodsa in Fluids
vol. 6, 113-127.

Harlow, F. H. and Nakayama, P. (1968)
"Transport of turbulence energy decay rat", LOs Alamos
Science Lab., Univ. of California, report LA-3854.

Hinze, J.o (1959)
TURBULENCE, McGraw-Hill, New York

Hirt, C. W. and Ramshaw, J.D. (1978).
"Prospects for numerical simulation of Bluff Body
Aerodynamics", in Aerodynamic Drag Mechanisms, Sovran,
G., Moral,T., and Mason,W., Editors, Plenum Press, N.Y.

Ishizaki, H. and Simg, I.W. (1971).

"Influence of adjacent buildings to wind", Proc. of third Int. Conf. on wind effects on buildings and structures, Tokyo, Japan, 145.

Jones, W.P. and Launder, B.E. (1973).
"Prediction of low Reynolds number phenomena with a two-equation model of turbulence". Int. J. Heat Mass Transfer 16,1119.

Kolmogorov, A. N. (1942).
"Equations of turbulent motions of an incompressible turbulent fluid.", Izv. Akad. Nauk SSSR ser. Phys. VI,56.

Lattif, Z. (1987)
Ph.D THESIS University of Strathcylde, Glasgow (in preparation)

Launder, B.E. and Spalding, D.B. (1972)
" Mathematical Models of Turbulence ", academic press, London.

Launder, B.E. and Spalding, D.B. (1974)
" The numerical computation of turbulent flow ", Computer Methods in Appl. Mech.. and Eng. vol3, pp. 269-289.

Launder, B.E. and Ying, W.M. (1973)
" Prediction of flow and heat transfer in duct of square cross-section. Heat and Fluid flow, 3.115

Leuthusser, H.J. (1965)
" Pressure distribution on a cube at various degrees of boundary layer immersion ", Univesity of Toronto, Mech. Eng. report, TP6502.

Leutheusser, H.J. (1971)
" Static wind loading of grouped buildings ", Proc. of Third Int. Conf. on wind effects on buildings and structures, TOKYO, JAPAN, 211

Liakopoulos, A. (1985)
" Computation of high speed turbulent boundary layer flows using the K-ε turbulence model ". Int. J. for numerical methods in fluids vol5, 81-97.

Malin, M.R and Qin, H.Q. (1985-a)
" PHOENICS-84 turbulence model validation- free flows " CHAM Technical Report

Malin, M.R and Qin, H.Q. (1985-b)
" PHOENICS-84 turbulence model validation- External flow" CHAM Technical Report

Markatos, N.G. (1983)
" The theoretical prediction of external aerodynamics of

road Vehicles" , Int. J. of Vehicle design series, SP3, Impact of aerodynamics on vehicle design, pp 387-400.

Matthews, L. and Whitelaw, J.H. (1973)
" Plane-jet flow over a backward facing step ". Heat and fluid flow, 3, 133.

Melbourne, W.H. (1971)
" Comparison of pressure measurements made on a large isolated building in full and model scale ", Proc. of Third Int. Conf. on wind effects on buildings and structures, TOKYO, JAPAN, paper No. 118.

Miller, B.L. and Davies, M.E. 91982)
" Wind loading on offshore structures: a summary of wind tunnel studies ". National Maritime Institute, Feltham, NMI/R136 OT-R-8225.

Moustafa, A.A.A, Grant, A.D and Reeves, P. (1987)
" Prediction of wind loading on structures ". Numerical methods in laminar and turbulent flow. Proc. of the Fifth Int. Conf. held in MONTREAL, August 1987.

Ng, K.H. (1971)
" Predictions of turbulent boundary layer developments using a two-equation model of turbulence ", Imperial College, London, Mech. Eng. Dept. report HT75/71/2,

Patankar, S.V. and Spalding, D.B. (1970)
" Heat and mass transfer in boundary layer", Intertext books, London, second edition.

Patankar, S.V. and Spalding, D.B. (1972)
" A calculation procedure for heat, mass and momentum transfer in three-dimensional parabolic flows ". Int. J. Heat Mass Transfer 15,1787.

Prandtl, L. (1925)
" Bericht Uber unter suchungen zur ausgebildeten Turbulenz, ZAMMS,136 "

Reeves, P. (1987)
Ph.D Thesis University of Strathclyde, Glasgow (in preparation)

Rodi, W. (1980)
"Turbulence models and thier applications in hydraulics" Book publication, Delft.

Rodi, W. (1970)
" Basic equations for turbulent flow in cartesian and cylindrical coordinates", Imperial College, Mech. Eng. Dept. report BL/TN/A/36.

Spalding, D.B (1982)
" Turbulence models: Lecture course ". CFDU Report
CFD/82/4. Imperial College. Univ. of London.

Spalding, D.B. and Rosten, H.I. (1984)
" PHOENICS-84 Reference Handbook ". CHAM Report
UK/TR/100.

Vasilic-Melling, D. (1977)
" Three-dimensional turbulent flow past rectangular bulff
bodies ". Ph.D. Thesis, Imperial College. Univ. of
London.

Wilson, J. (1983)
" The creation of wind efficient Topside profiles " Msc.
Thesis, Univ. of Strathclyde, Glasgow.

Wise, A.F.E. (1971)
" Effects due to groups of buildings ", Phil. Trans. Roy.
Soc. A269, 469.

APPENDIX A : EMPIRICAL CALCULATION OF WIND LOADS

The calculation of wind loading in any offshore structure is far from exact due to the complexity of design configurations and is complicated further by the selection of appropriate drag and lift coefficients.

A number of different techniques are employed in design practice to deal with wind loading with varying degrees of success and application suitability. The two calculation methods in general use today are those supplied by the American Bureau of Shipping (ABS 1981) and Det norske Veritas (DnV 1981, 1985). The 1985 version of DnV code has come to our attention with regard to lift force estimation.

At present the above water forces are determined by breaking down the semi-submersible's above water structure into discrete elements of defined shape such as rectangular, cylindrical, spherical or lattice.

The following discussion provides a brief description of the empirical wind load calculation methods specified by the classification societies codes (ABS & DnV).

A.1 American Bureau of Shipping (ABS).

In the calculation of wind pressure, the following equation is to be used

$$P = 0.06230 \ (V_Y)^2 \ C_h \ C_s \qquad kg/m^2$$

$$P = 0.00338 \ (V_Y)^2 \ C_h \ C_c \qquad lb/ft^2$$

where;

P = pressure in (kg/m^2 or lb/ft^2)

V_Y = wind velocity (m/s or Kn)

C_h = height coefficient, which tabulated as a function of the vertical distance between the design water surface and the centre of the area considered (table A.1)

C_s = shape coefficient as a function of the shape of the component (table A.2)

The wind force is to be calculated in accordance with the following equation for each vertical area and the resultant force and vertical point of application is to be determined.

$$F = P.A$$

where;

F = force in (kg or lb)

P = pressure in (kg/m^2 or lb/ft^2)

A = projected area in (m^2 or ft^2) of all exposed

surfaces in either the upright or heeled condtion.

In calculating the wind forces, the following procedures are recommended:

1) In the case of units with columns, the projected areas of all columns are to be included; i.e. no shielding allowance is to be taken.

2) Areas exposed due to heel, such as underdecks etc., are to be included using the appropriate shape coefficients.

3) The block projected area of a clustering of deck houses may be used in lieu of calculating each individual area. The shape coefficient may be assumed to be 1.1.

4) Isolated houses, structural shapes, cranes, etc., are to be calculated individually using the appropriate shape coefficient (table A.1).

5) Open truss work commonly used for derrick towers, booms and certain types of masts may be approximated by taking (30%) of the projected block areas of both the front and back sides; i.e. 60% of the projected block area of one side for double sided truss work. The shape coefficient is to be taken in accordance with (table A.1).

Table (A.1): Values of C_h

height				C_h
meters		feet		
over - not exceeding		over - not exceeding		
0.0	15.30	0.0	50	1.00
15.30	30.50	50	100	1.10
30.50	46.00	100	150	1.20
46.00	61.00	150	200	1.30
61.00	76.00	200	250	1.37
76.00	91.50	250	300	1.43
91.50	106.5	300	350	1.48
106.5	122.0	350	400	1.52
122.0	137.0	400	450	1.56
137.0	152.5	450	500	1.60
152.5	167.5	500	550	1.63
167.5	183.0	550	600	1.67
183.0	198.0	600	650	1.70
198.0	213.5	650	700	1.72
213.5	228.5	700	750	1.75
228.5	244.0	750	800	1.77
244.0	256.0	800	850	1.79
256.0		850		1.80

Table (A.2): Values of C_s

Shape	C_s
Cylindrical shapes (all sizes)	0.500
Hull (surface type)	1.000
Deck houses	1.000
Isolated structural shapes (cranes, angles, channels, beams, etc.)	1.500
Under deck areas (smooth surfaces)	1.000
Under deck areas (exposed beams and girders)	1.300
Rig derrick (each face)	1.250

135

A.2 Det norske Veritas (DnV 1981 & 1985)

1) Dnv (1981)

The wind force normal to flat surfaces or normal to the axis of members not having flat surfaces, is to be calculated by the formula:

$$F_w = C \left(V_Y^2 / 16 \right) \sin \alpha \cdot A$$

where;

F_w = wind force in Kp, including the effect of suction on the leeward side.

C = Shape coefficient

V_Y = wind speed in m/s at height Y

α = angle between wind direction and the surface (or axis) of the member

A = projected area of the member in square metres taken as normal projection on a plane normal to the direction of the considered force.

The following procedures are recommended in calculating the wind forces

1) The shape coefficient C considers two dimensional flow over long individual members and allows for suction on the leeward side. When short individual members (three-dimensional flow) are used the following correction is to be applied:

$$C = C_\infty \left(0.50 + 0.1(1/d) \right)$$

where;

136

l = length of member

d = the cross-sectional dimension normal to the direction of the considered force.

C_∞ gives three alternatives for "long (slender) individual members "

a) flat bars, rolled sections, plate, box girders and other sharp-edged sections

$$(C_\infty = 2.0)$$

b) Rectangular sections with cross-sectional dimension in the wind direction more than two times that normal to the wind direction :

$$(C_\infty = 1.50)$$

c) smooth cylindrical members:

$d < 0.30$ m. , $C_\infty = 1.20$

$d \geqslant 0.30$ m. , $C_\infty = 0.70$

2) An allowance for shielding is made if two members are located behind each other in the wind direction. The shielding effect may be taken into account if the distance L centre to centre, is less than seven times the width (diameter) of the windward member. This may be done by considering a reduced exposed area of the leeward member according to the formula:

137

$$(A_2)_{\text{exposed}} = u \; A_2$$

as:

$$u = 1 - (d_1/d_2)(1 - (L/7d)) \quad \text{for} \; d_1 < d_2$$

$$u = L/7d_1 \qquad\qquad\qquad \text{for} \; d_1 \geqslant d_2$$

$$u = 1 \qquad\qquad\qquad\quad \text{for} \; L \geqslant 7d_1$$

where;

Suffixes 1 and 2 refer to the windward and leeward member respectively.

Note: If more than two members are located in line with the wind direction, the above formulae are applicable, taking suffix 2 to refer to the considered member, and suffix 1 to refer to that of the windward members leading to the smallest u.

3) For trusses or similar girders, if 0.2> solidity ratio $\rangle$ 0.8, the drag coefficient may be multiplied by 0.80. If the ratio is less than 0.2 no correction is made and if the ratio ^{is} above 0.80 the enclosed area is treated as solid.

2) DnV (1985):

The basic equation for the estimation of the aerodynamic forces (Lift and Drag) on a general element provided by DnV (1985) is:

$$P_d = 0.50 \; C_s \; V^2 \; bl \; \cos\beta \qquad \text{KN}$$

where;

P_{cd} = the steady flow force component acting in the plane of the cross-section of a slender member

ρ = air density

C_s = shape coefficient

V = flow velocity in flow direction

b = cross-sectional dimension perpendicular to the force component

l = length of member

β = angle between flow direction and the cross-sectional plane of the member

For the DnV (1985) code it is usual to calculate aerodynamic forces referenced to the body's own coordinate system. For the general slender rectangular element, two forces are considered. that parallel to the longest side of the cross-section, P_{cd1}, and that perpendicular to it , P_{cd2}.

To calculate P_{cd1} and P_{cd2} separate values of C_s and b will be required. For members with a length/cross-sectional dimension ratio, l/b > 5 C_{s1} for the perpendicular force will be given by

$$C_{s1} = 2\ K_r\ \text{sine}\ \alpha$$

where;

K_r is a factor which takes into account the effects of corner rounding (equal to 1.0 for sharp edges)

α is the angle between the longest side of the

cross-section and the flow component in the cross-sectional plane

C_{sz} for the force parallel to the longest side of the cross-section is given by :

$$C_{sz} = (\ 1 + (b_2/b_1)\ )\ K_r\ \cos \alpha \qquad (\text{ for } b_2 < b_1 < 2b_2\ )$$

$$C_{sz} = 1.50\ K_r\ \cos \alpha \qquad (\text{ for } b_1 \geqslant 2b_2\ )$$

The DnV (1985) does suggest correction factors to deal with 3-D flow over a member with an l/b ratio less than 5 provided by the formula:

$$f = 1 - c (\ 1 - (l/5b)\ )$$

where;

c = 0.1 for smooth circular cylinders

= 0.2 for other cross-sections

l = length of member

b = characteristic cross-sectional dimension i.e. b_1

or b_2 depending on force being calculated

The use of this reduction formula allows for the forces on deck mounted structures to be estimated by taking the cross-sectional reference area to be parallel to the deck plane.
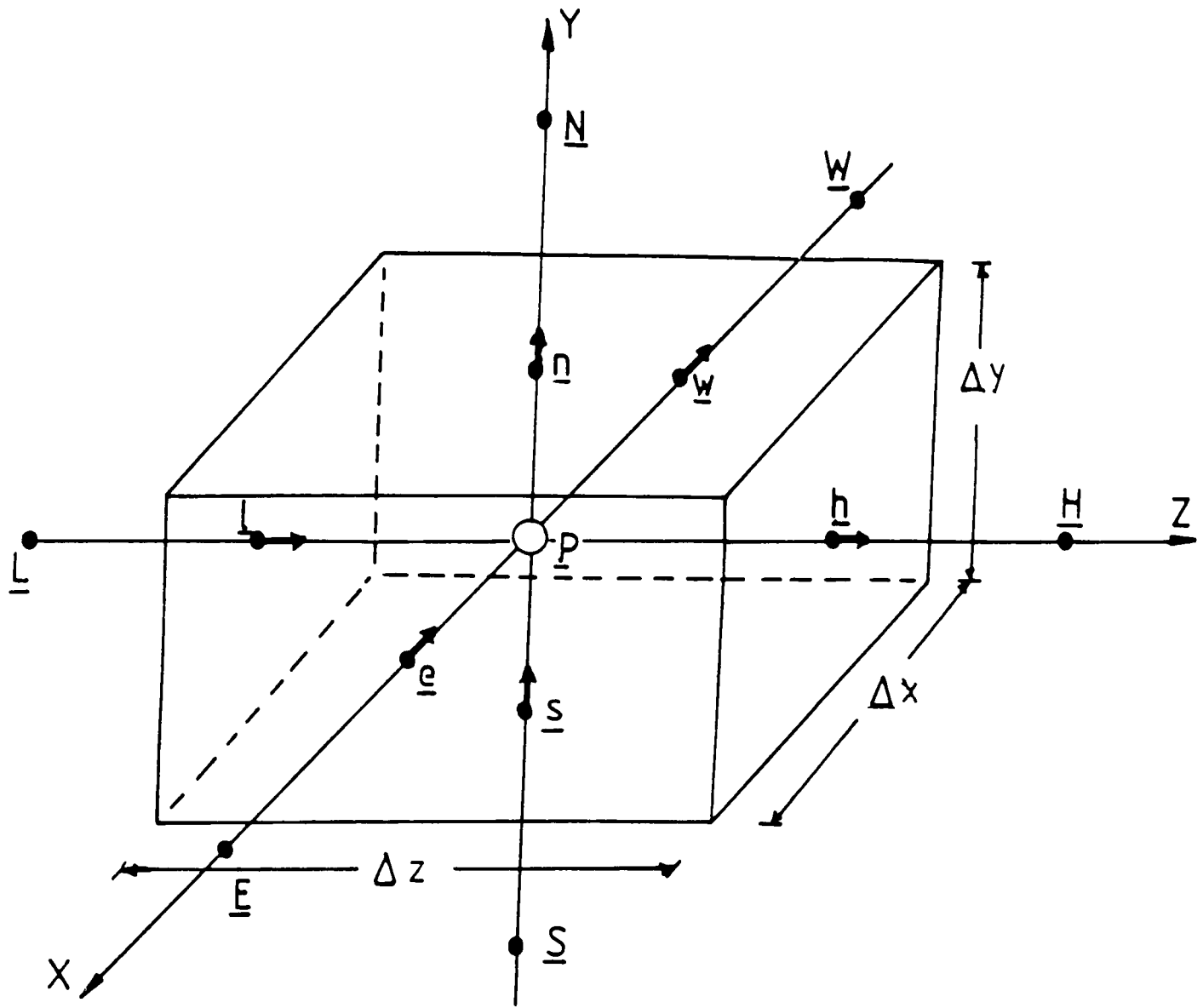
Figure (3.1): 3-D Control Volume Grid.
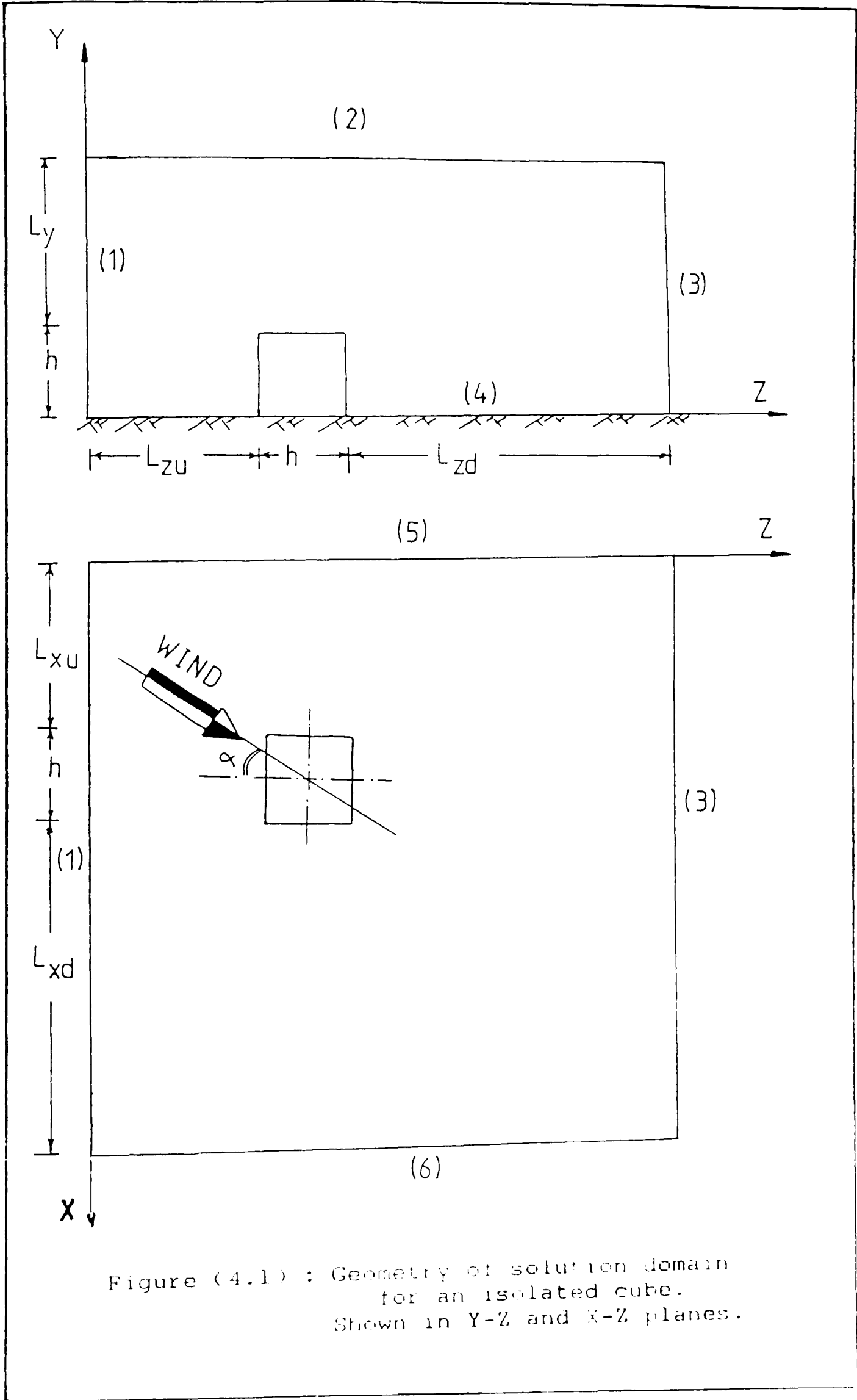
Figure (4.1) : Geometry of solution domain
for an isolated cube.
Shown in Y-Z and X-Z planes.
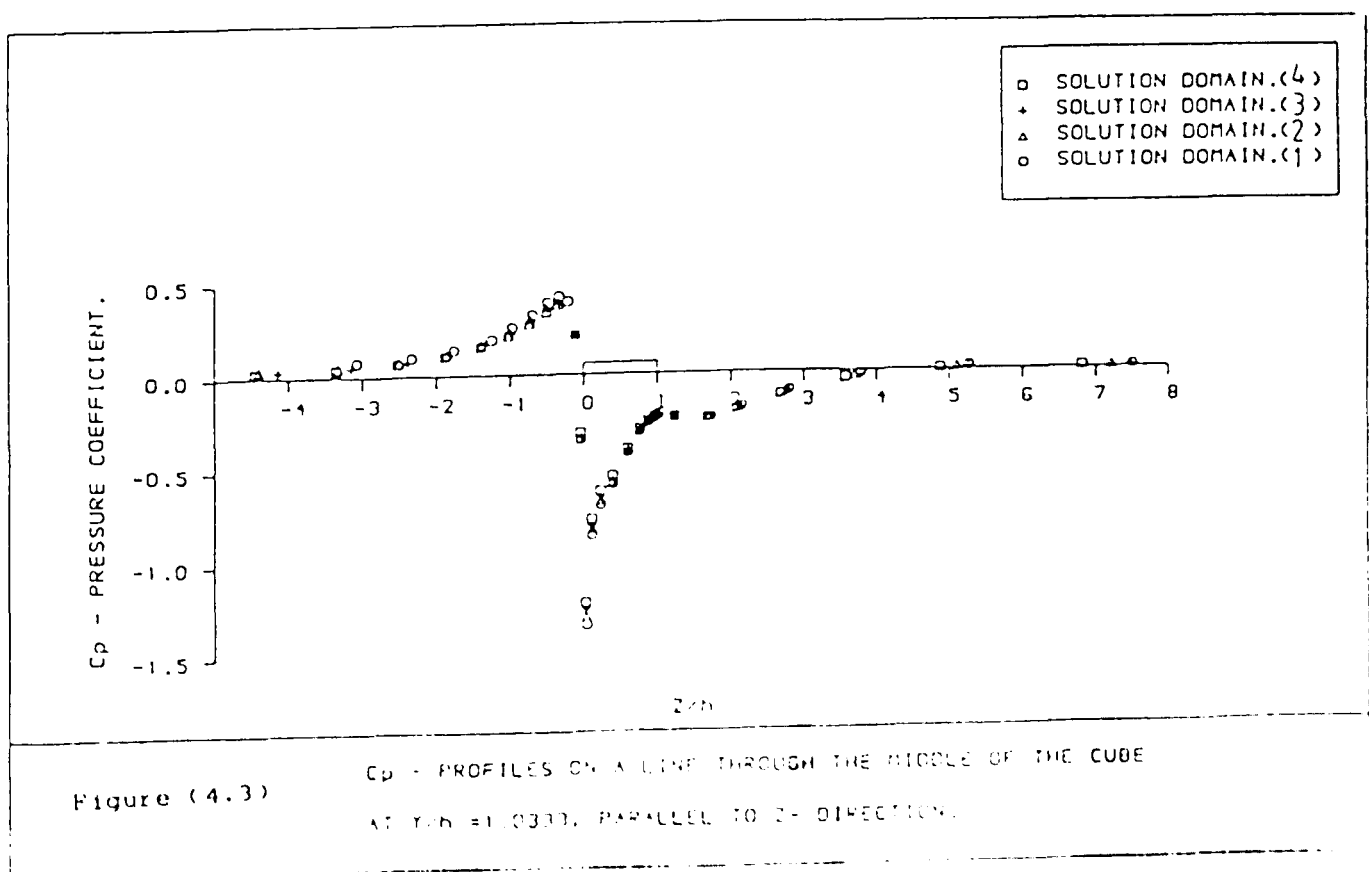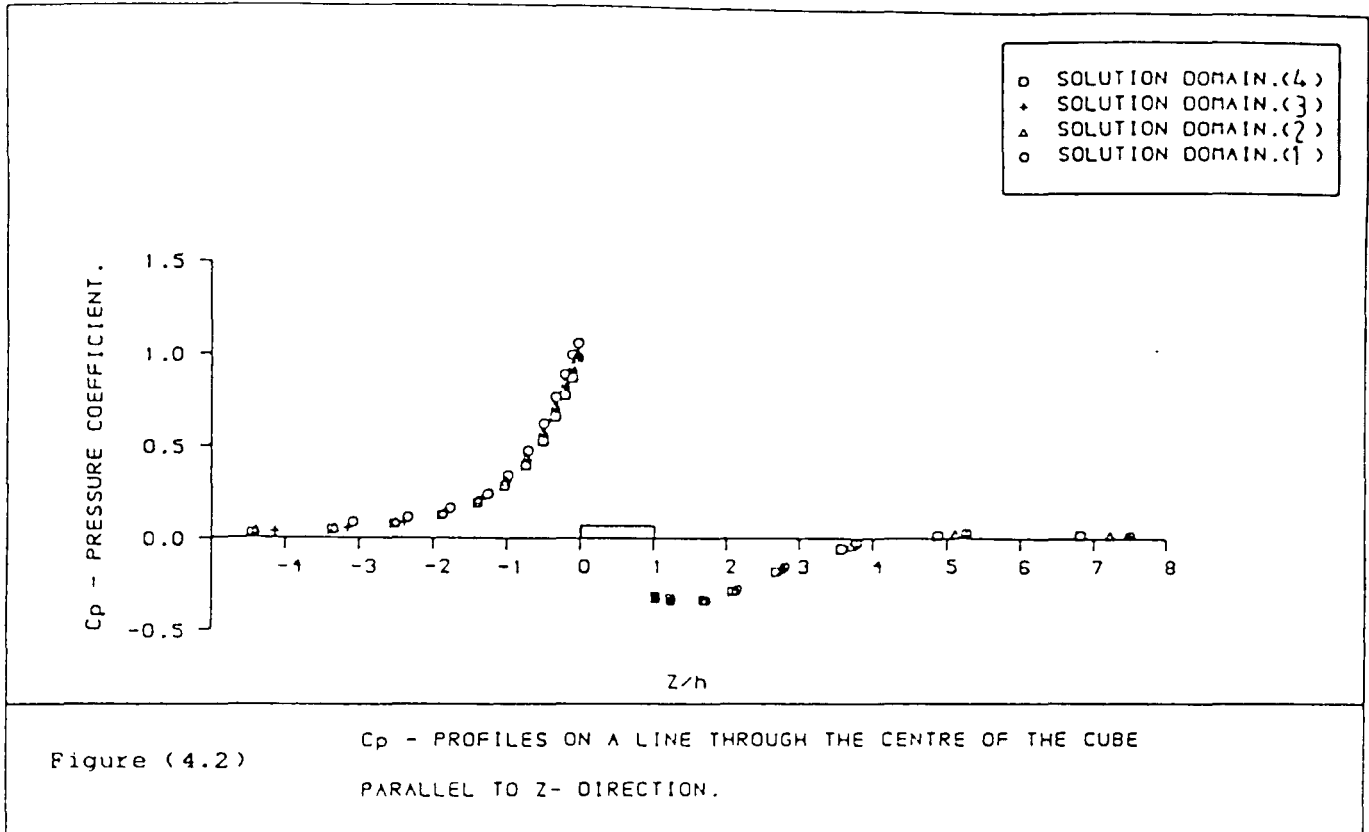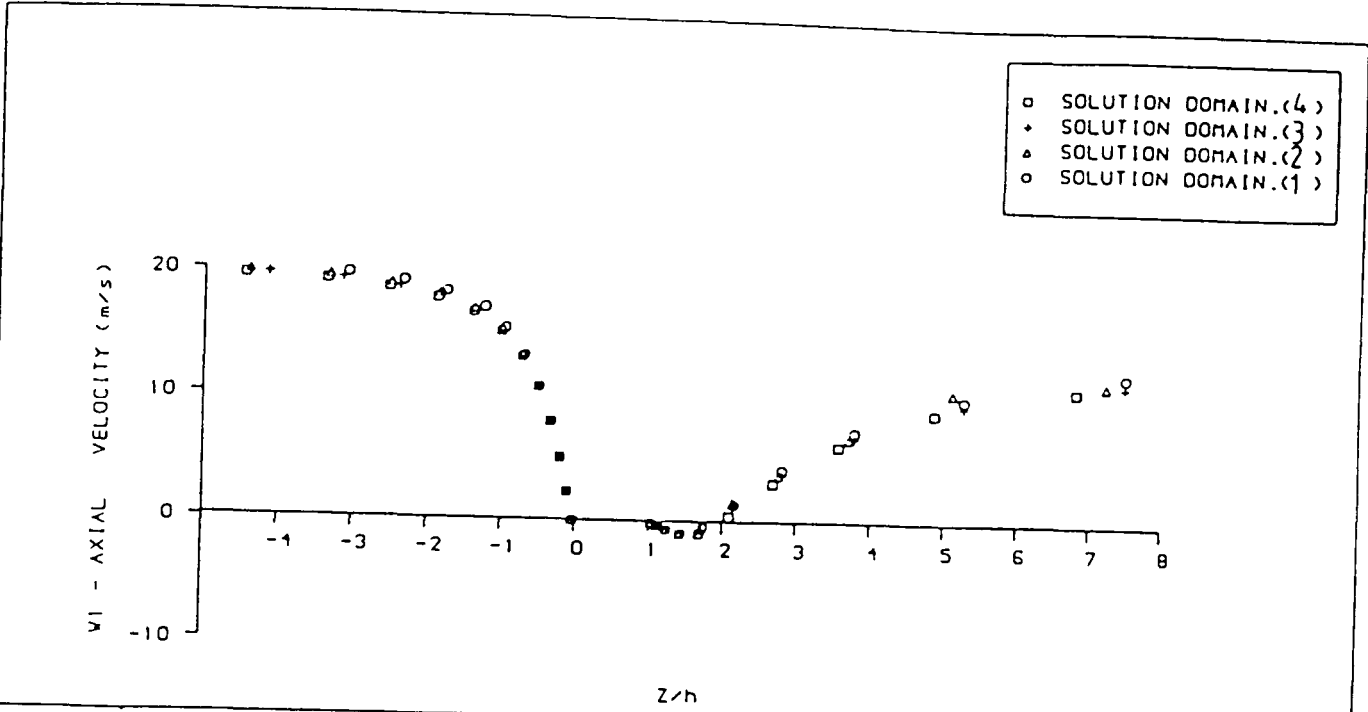
Figure (4.2)　　　　Cp - PROFILES ON A LINE THROUGH THE CENTRE OF THE CUBE
PARALLEL TO Z- DIRECTION.

Figure (4.3)　　　　Cp - PROFILES ON A LINE THROUGH THE MIDDLE OF THE CUBE
AT Y/h =1.0333, PARALLEL TO Z- DIRECTION.

FIG(4 .4) WI - AXIAL VELOCITY PROFILES ON A LINE THROUGH THE CENTRE OF THE CUBE PARALLEL TO Z - DIRECTION.

Figure (4.5) WI - AXIAL VELOCITY PROFILES ON A LINE THROUGH THE MIDDLE OF THE CUBE AT Y/h =1.0333, PARALLEL TO Z- DIRECTION.

Figure (4.6)   K - PROFILES ON A LINE THROUGH THE CENTRE OF THE CUBE
PARALLEL TO Z - DIRECTION.

Figure (4.7)   K - PROFILES ON A LINE THROUGH THE MIDDLE OF THE CUBE
AT Y/h =1.0333, PARALLEL TO Z- DIRECTION.

145

a) $l_r = 2.07\,h$
    $0.3586\,L_d$

b) $l_r = 2.23\,h$
    $0.242\,L_d$

c) $l_r = 2.234\,h$
    $0.157\,L_d$

d) $l_r = 2.237\,h$
    $0.114\,L_d$
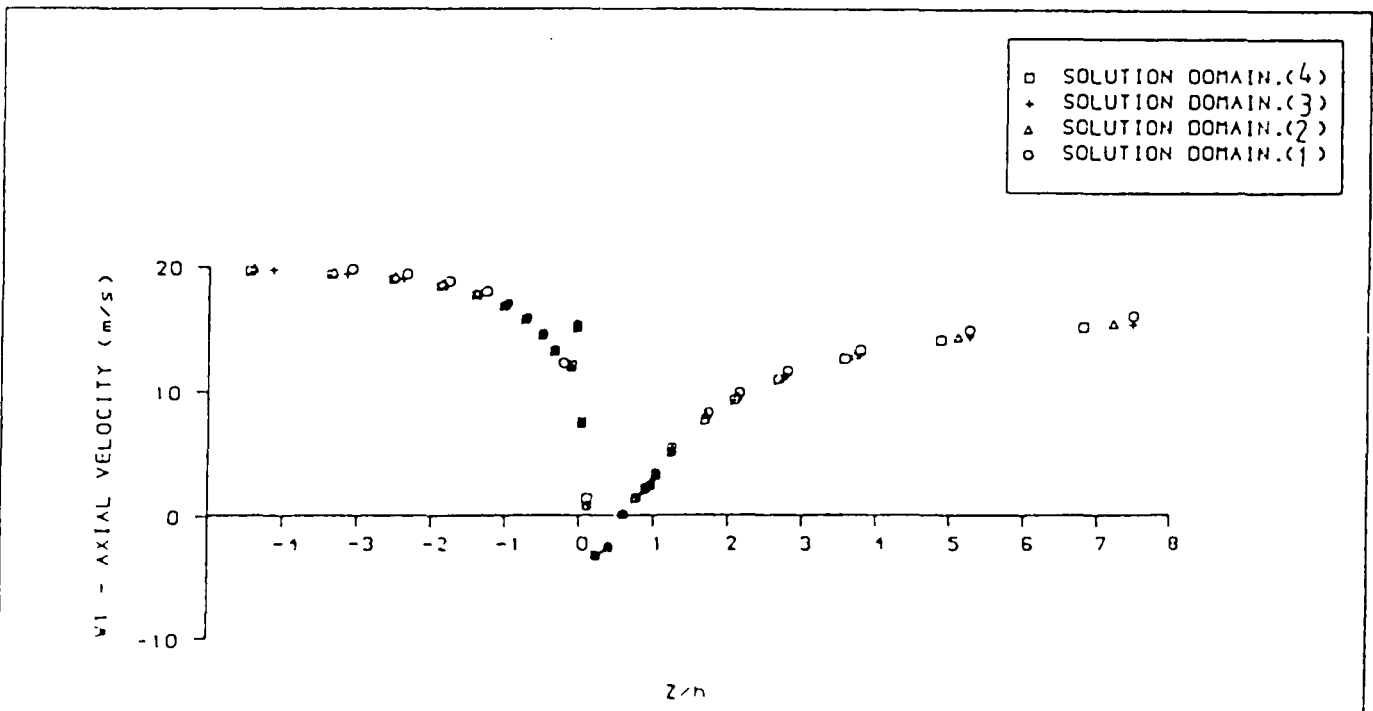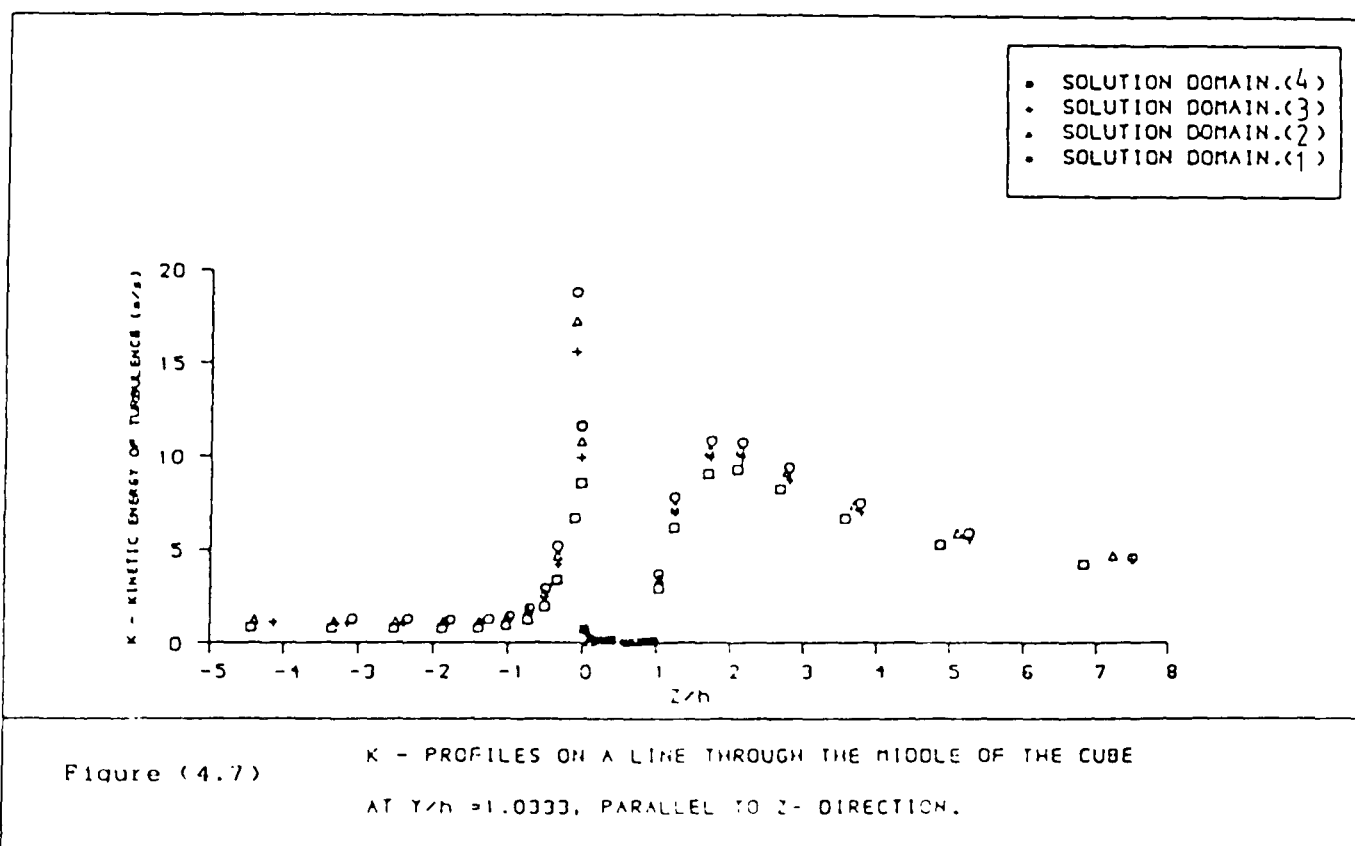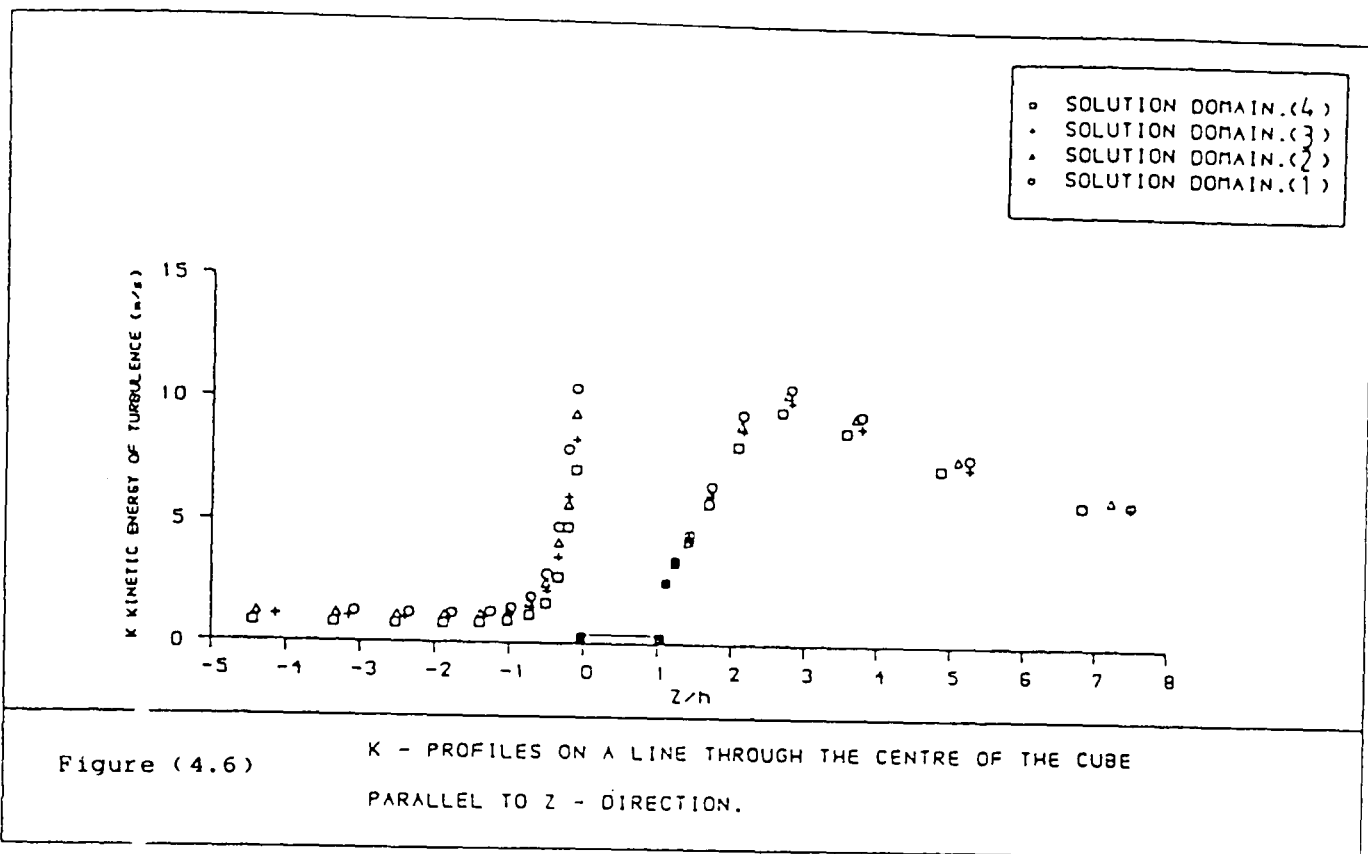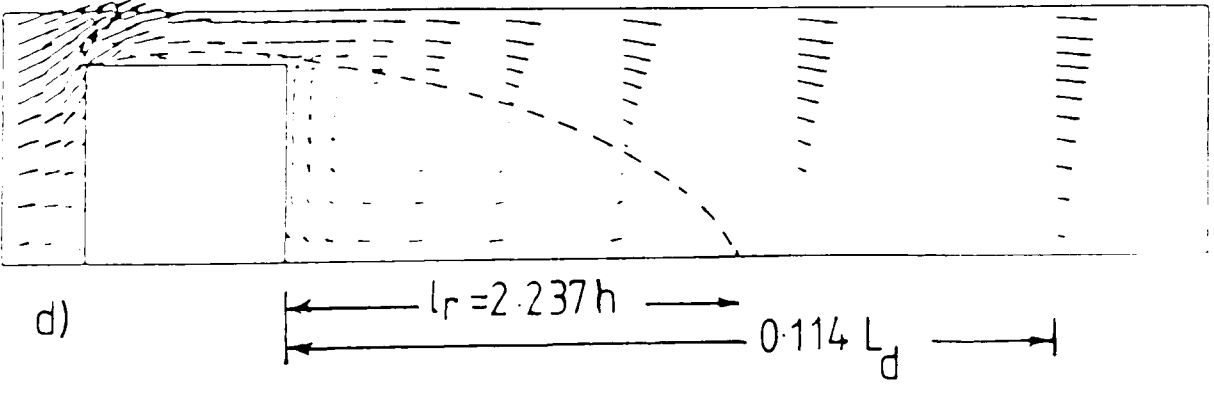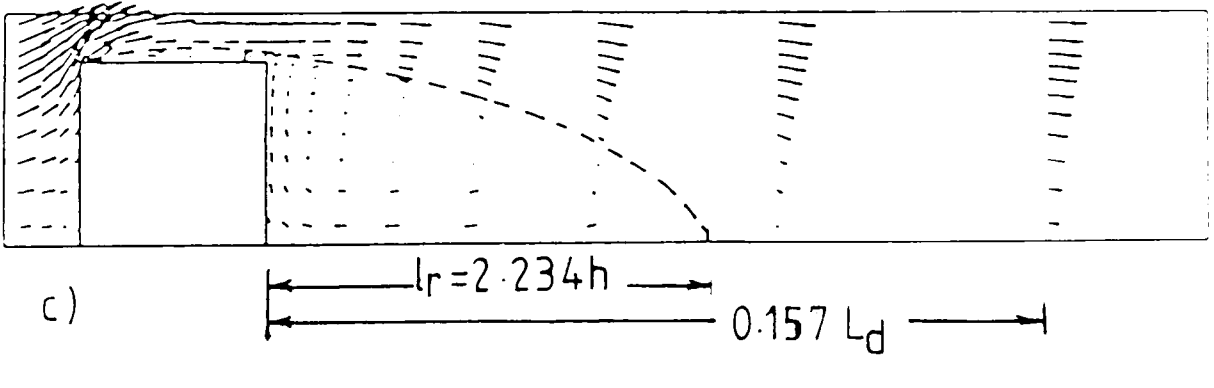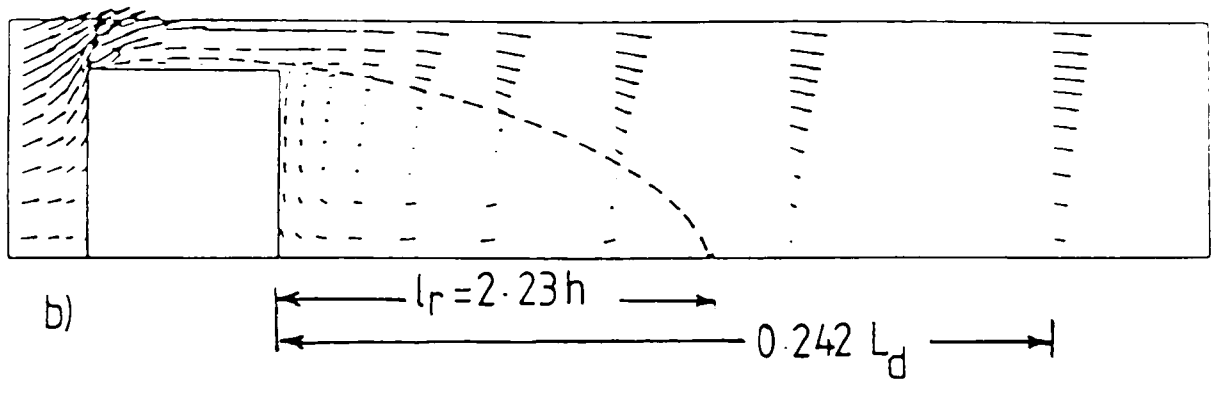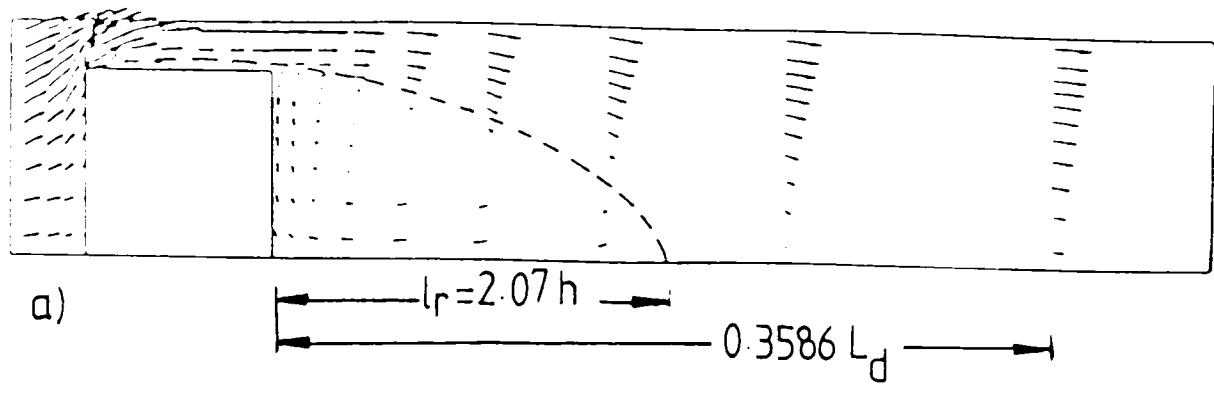
Figure (4.9)   SENSITIVITY OF ATTACHMENT LENGTH
               FOR DOMAIN SIZE

146
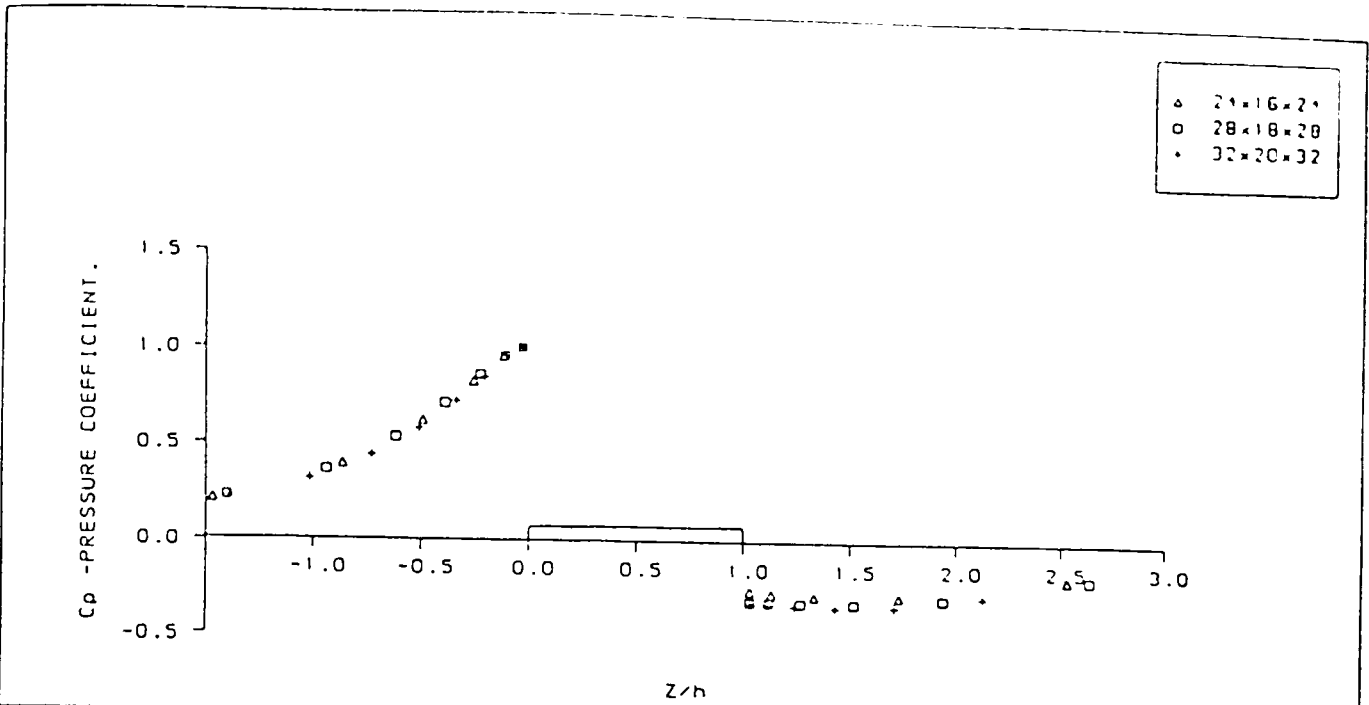
Figure (4.9) GRID DEPENDENCE:Cp -PROFILES ON A LINE THROUGH THE CENTRE OF THE CUBE
PARALLEL TO Z - DIRECTION. .
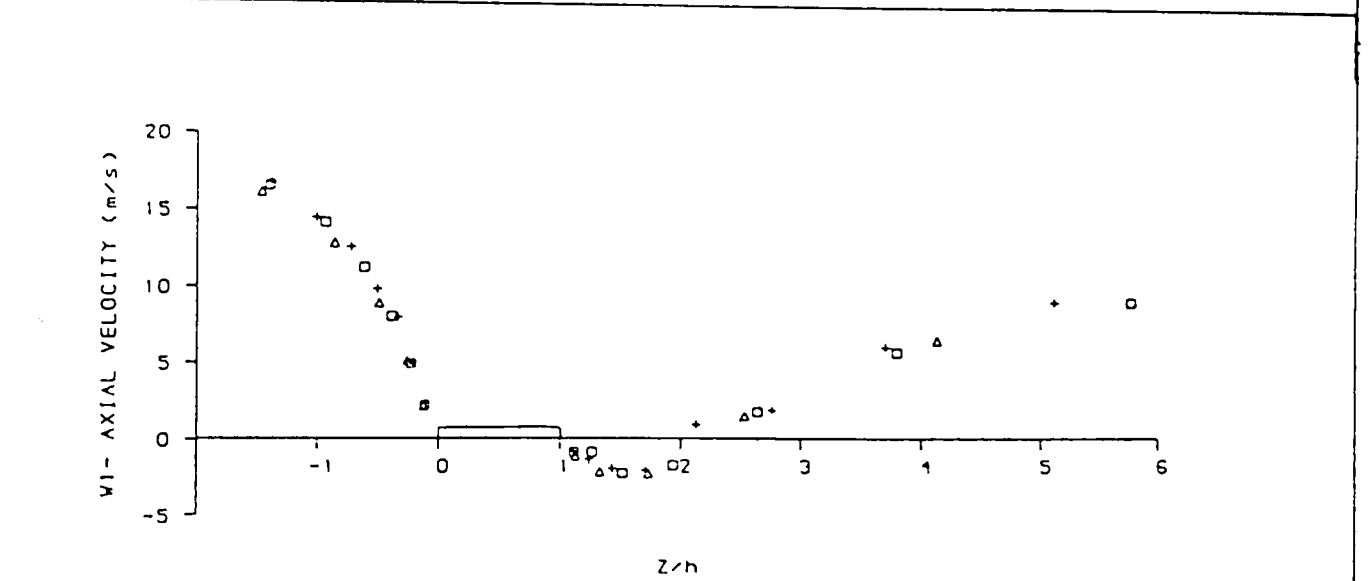
Figure (4.10) GRID DEPENDENCE:WI- PROFILES ON A LINE THROUGH THE CENTER OF THE CUBE
PARALLEL TO Z - DIRECTION.
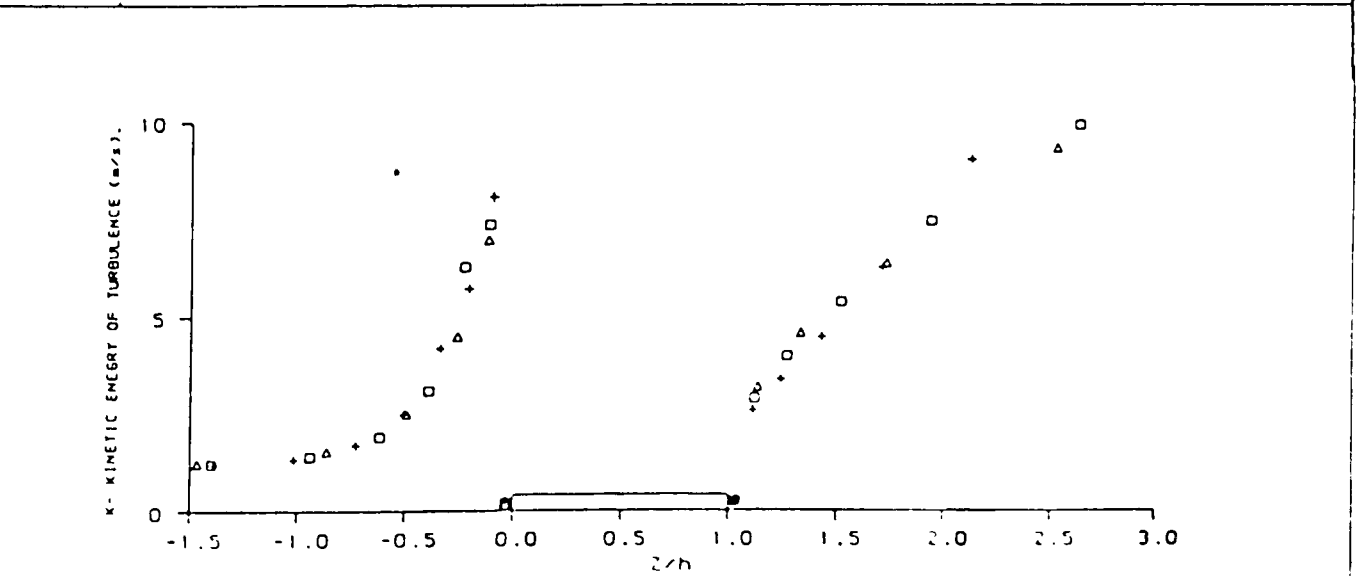
Figure (4.11) GRID DEPENDENCE:K- PROFILES ON A LINE THROUGH THE CENTRE OF THE CUBE
PARALLEL TO Z- DIRECTION.
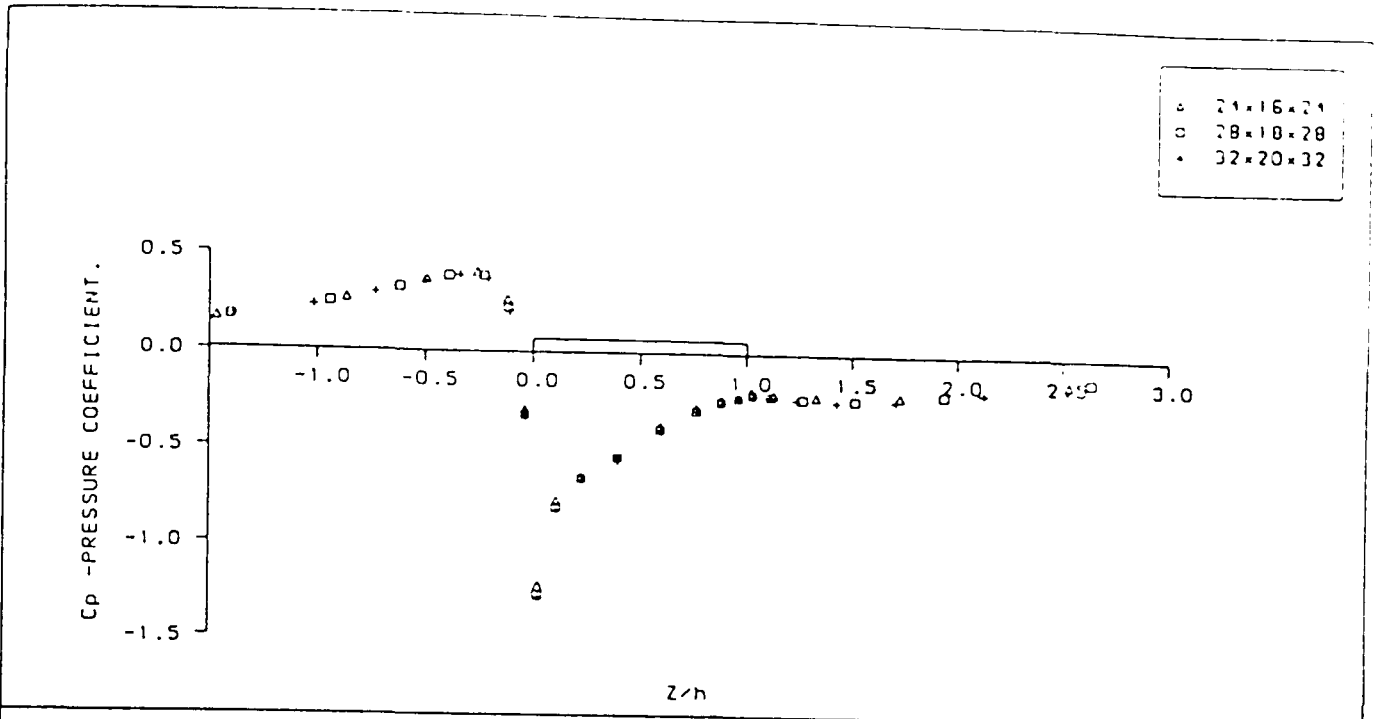
Figure (4.12)   GRID DEPENDENCE:Cp- PROFILES ON A LINE THROUGH THE MIDDLE OF THE CUBE
                 AT Y/h=1.03333,PARALLEL TO Z- DIRECTION.
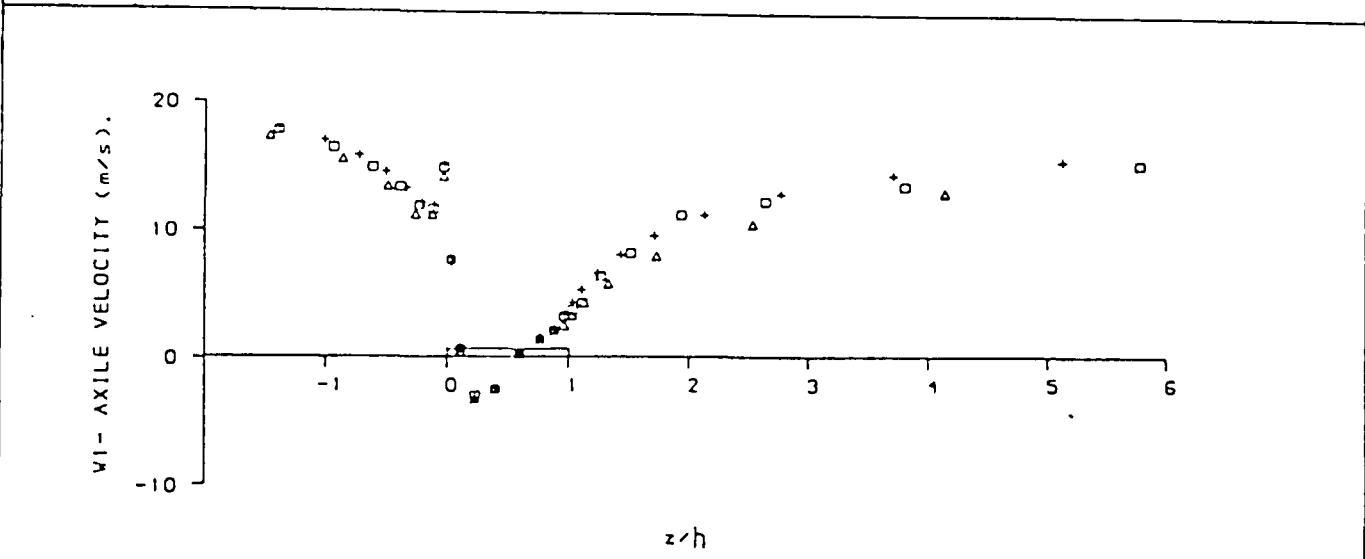
Figure (4.13)   GRID DEPENDENCE:W1- PROFILES ON A LINE THROUGH THE MIDDLE OF THE CUBE
                 AT Y/h=1.0333,PARALLEL TO Z -DIRECTION.
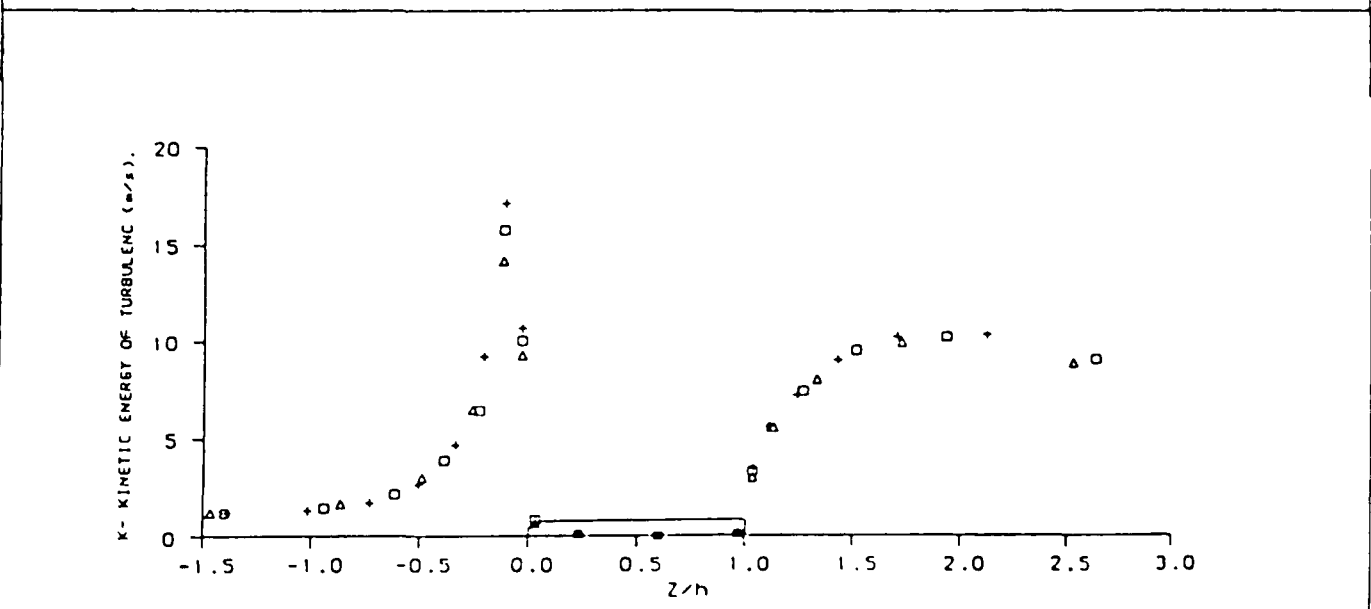
Figure (4.14)   GRID DEPENDENCE:K- PROFILES ON A LINE THROUGH THE MIDDLE OF THE CUBE
                 AT Y/h=1.0333,PARALLEL TO Z- DIRECTION.

148

$\alpha = 0°$

Rear

-0.4
-0.5
-0.55
-0.6
$\sim$ -0.1

-0.1
-0.2
-0.4
-0.6
-0.8
-0.91

-0.65
-0.64
-0.68
-0.66
-0.62
-0.60

0.4   0.8   0.4
0.85
0.8   0.9
0.8
0.99
0.8   0.98
-0.95

Front

Boundary layer
upstream flow

Uniform upstream
flow

Figure (4.15-a)

PRESSURE CONTOURS ON CUBE NORMAL TO
THE INCIDENT FLOW (CASTRO and ROBINS, 1975)
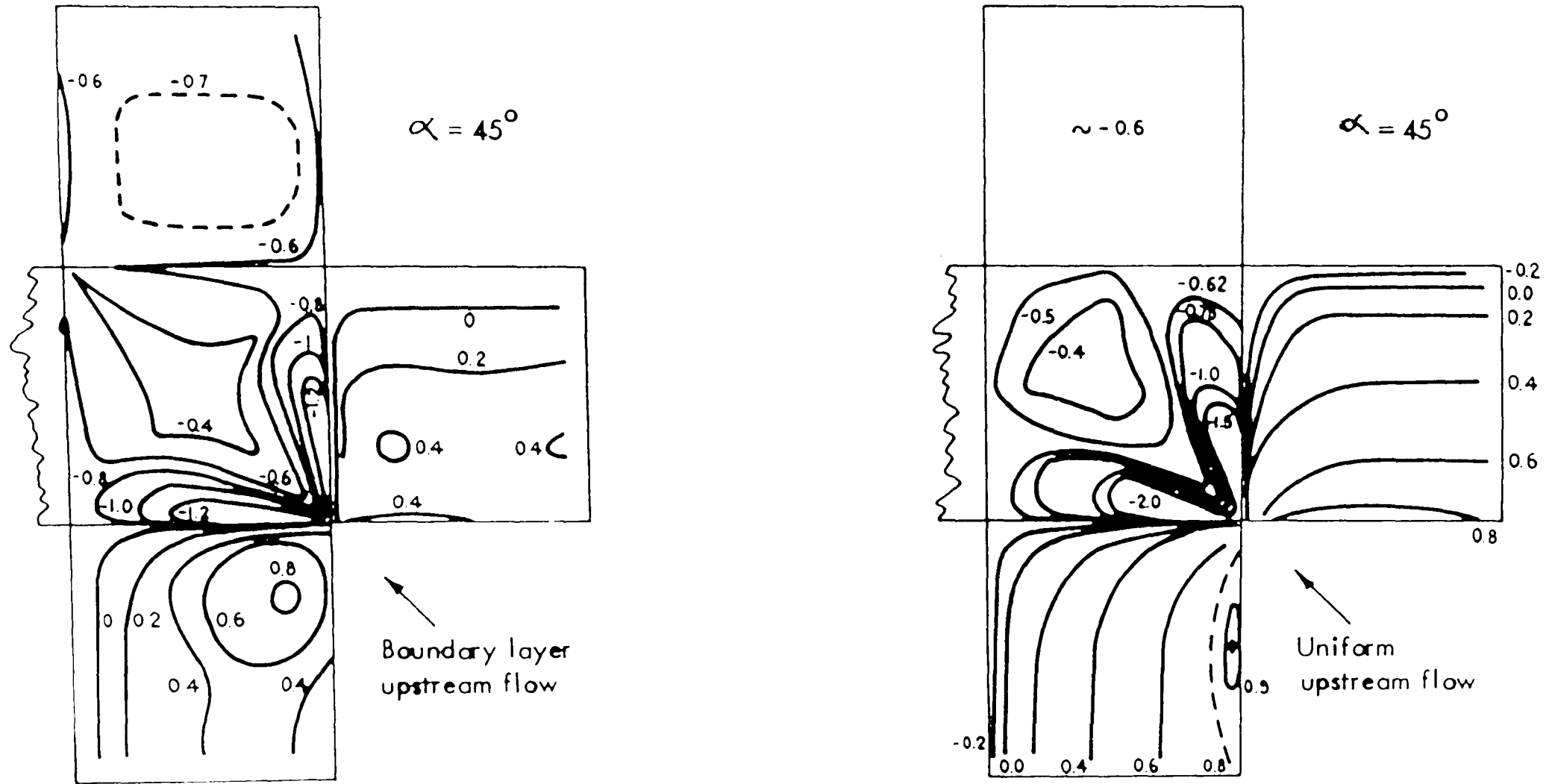
Figure (4.15-b): PRESSURE CONTOURS ON CUBE AT 45 INCIDENT FLOW
(CASTRO and ROBINS, 1975)

150

I) Sketch of flow pattern
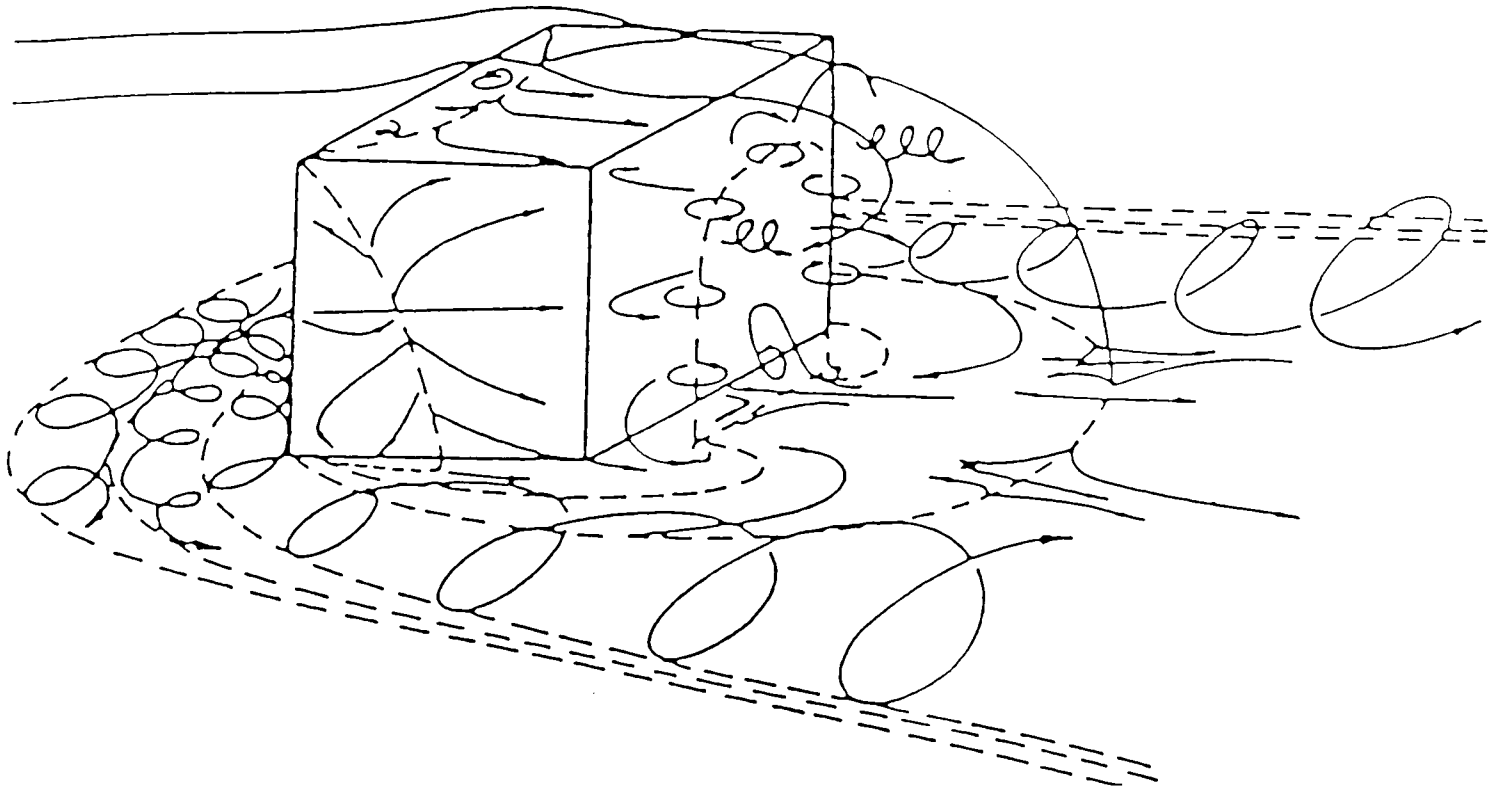
II) Flow on centreline

Streamline

Reattaching
roof flow

Recirculating
near wake region

Primary
horseshoe vortex

h

L_r
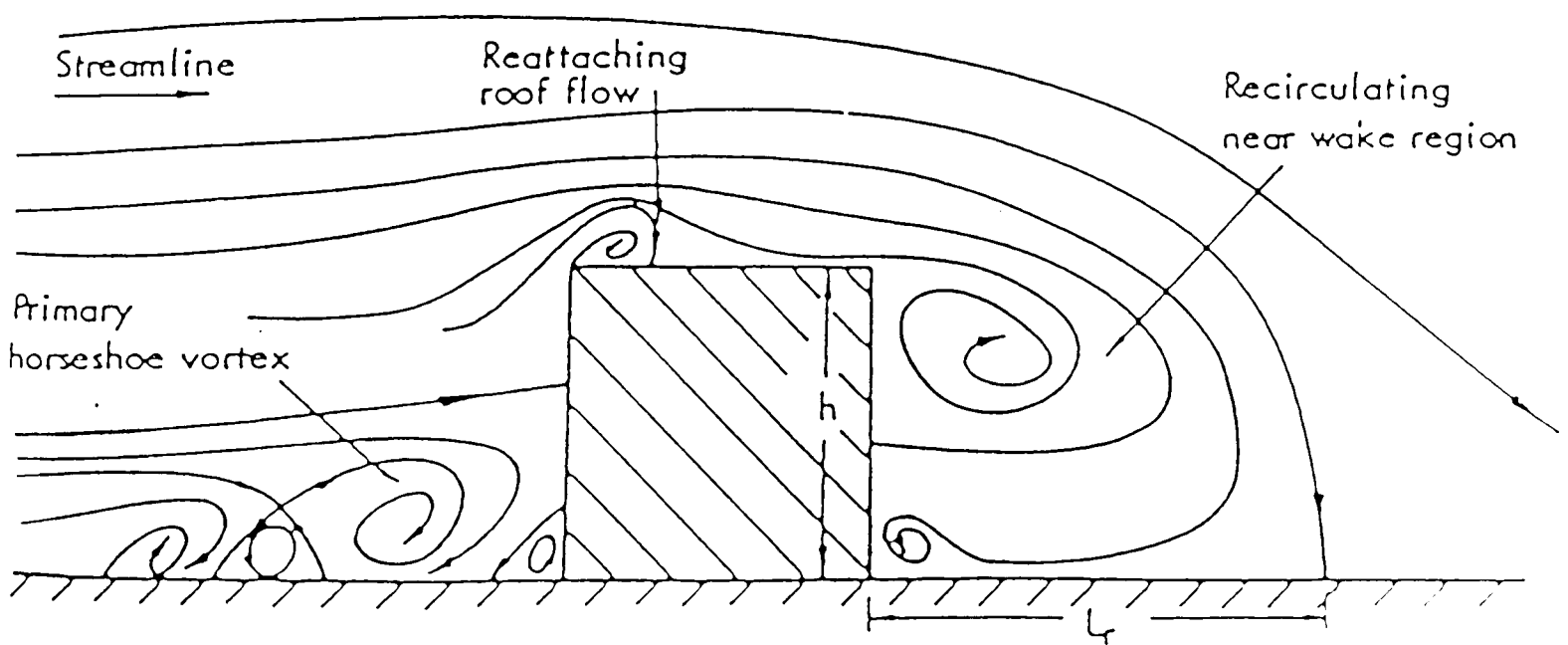
Figure (4.15-c) :Sketch of flow pattern around an isolated cube

(FACKRELL, 1982)

151
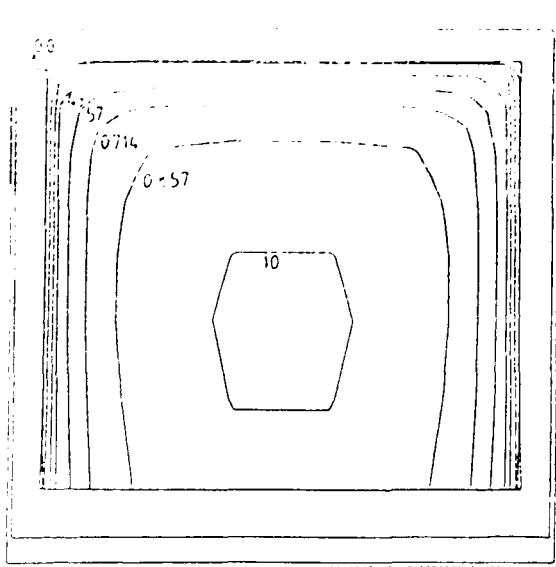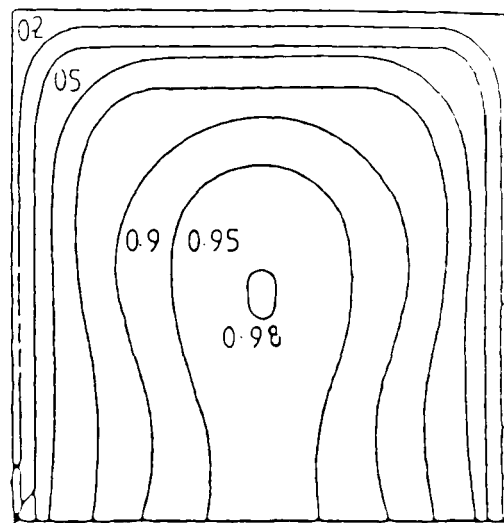
"PHOENICS"   "ESDU"

Figure (4.16): Comparison, surface pressure contours
                on the front face of an isolated cube
                (α = 0°)
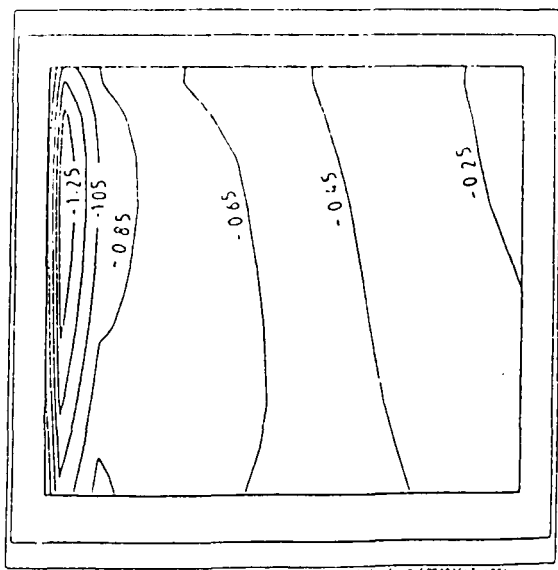
"PHOENICS"   "ESDU"

Figure (4.17): Comparison, surface pressure contours
                on the side face of an isolated cube
                (α = 0°)
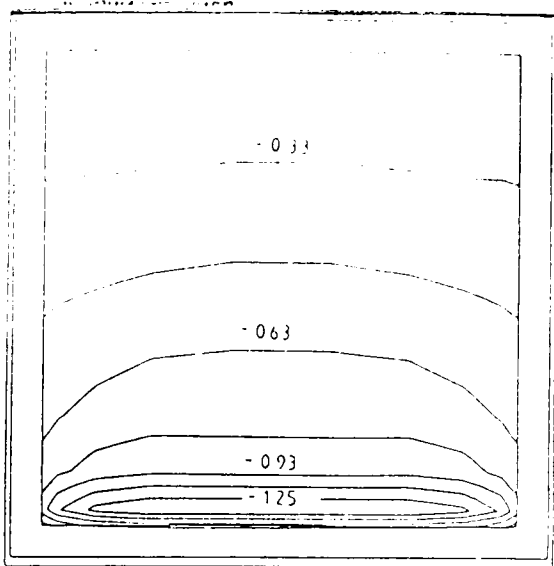
"PHOENICS"   "ESDU"

Fugure (4.18): Comparison, surface pressure contours
              on the top face of an isolated cube

              (∝ = 0°)
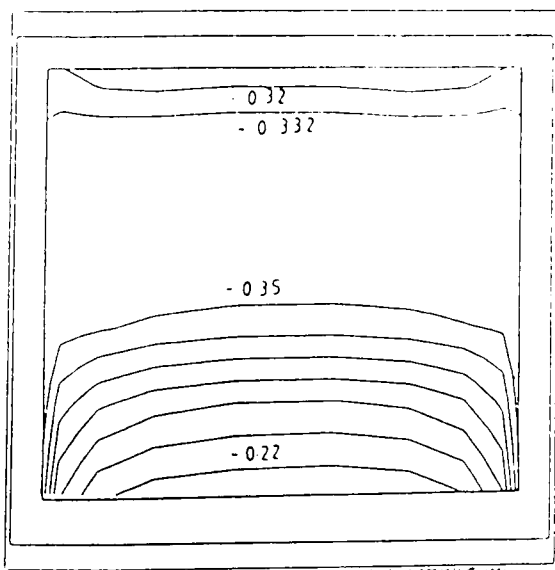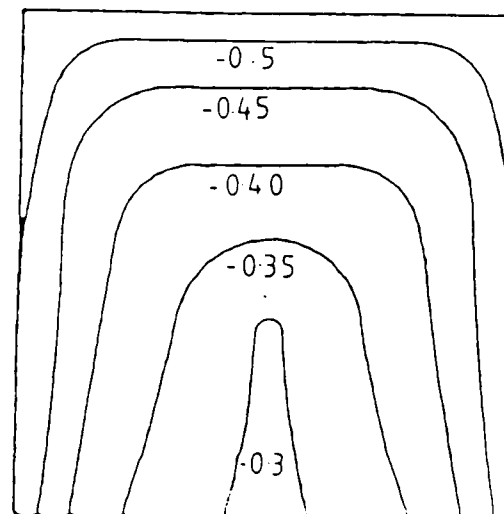
"PHOENICS"   "ESDU"

Figure (4.19): Comparison, surface pressure contours
              on the rear face of an isolated cube

              (∝ = 0°)

153
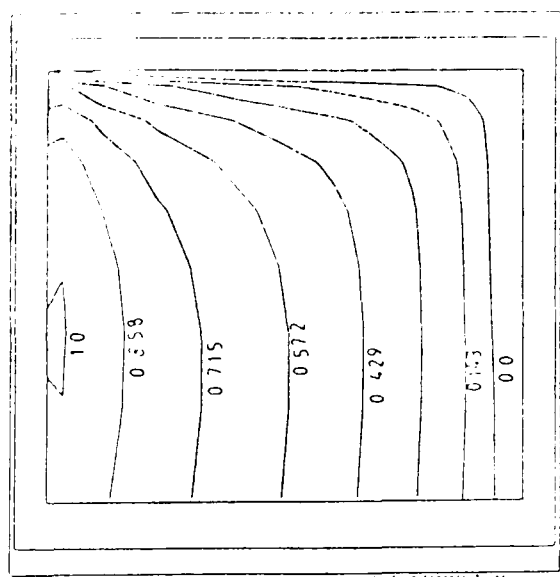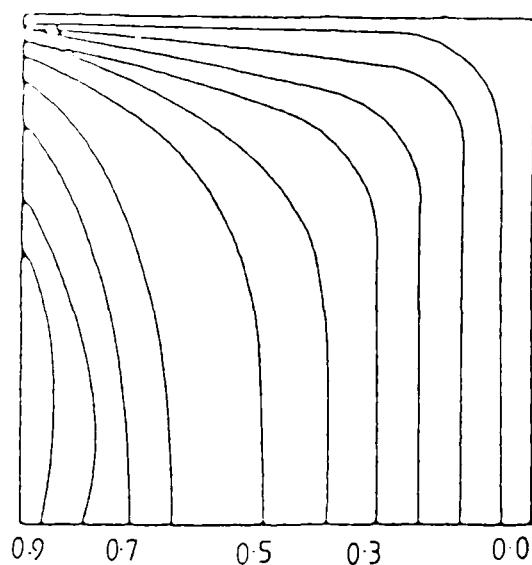
"PHOENICS"

"ESDU"

Figure (4.20): Comparison, surface pressure contours on the upstream face of an isolated cube

(α = 45°)

"PHOENICS"

"ESDU"

Figure (4.21): Comparison, surface pressure contours on the top face of an isolated cub (α = 45°)
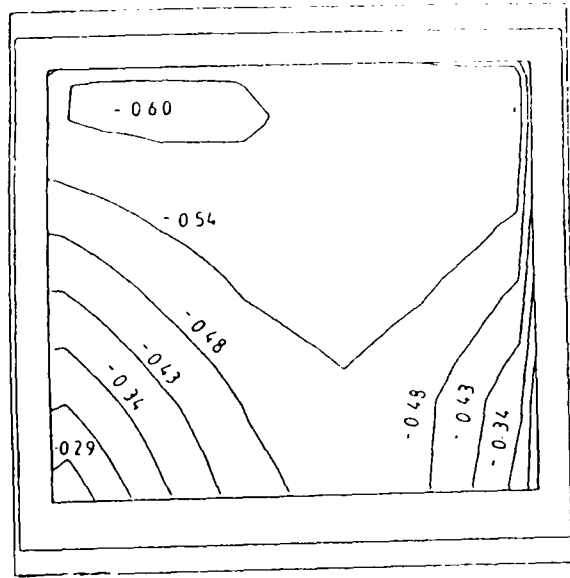
"PHOENICS"
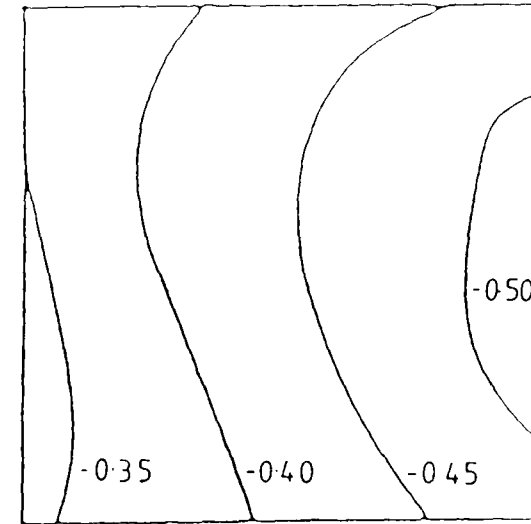
"ESDU"

Figure (4.22): Comparison, surface pressure contours on the downstream face of an isolated cube ($\alpha = 45°$)
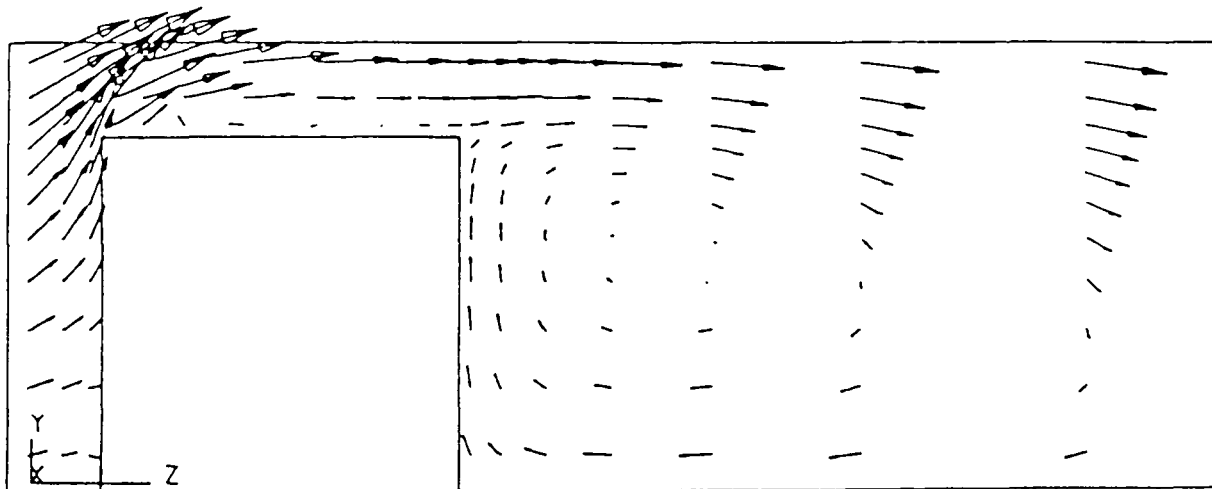
a) Symmetry plane.
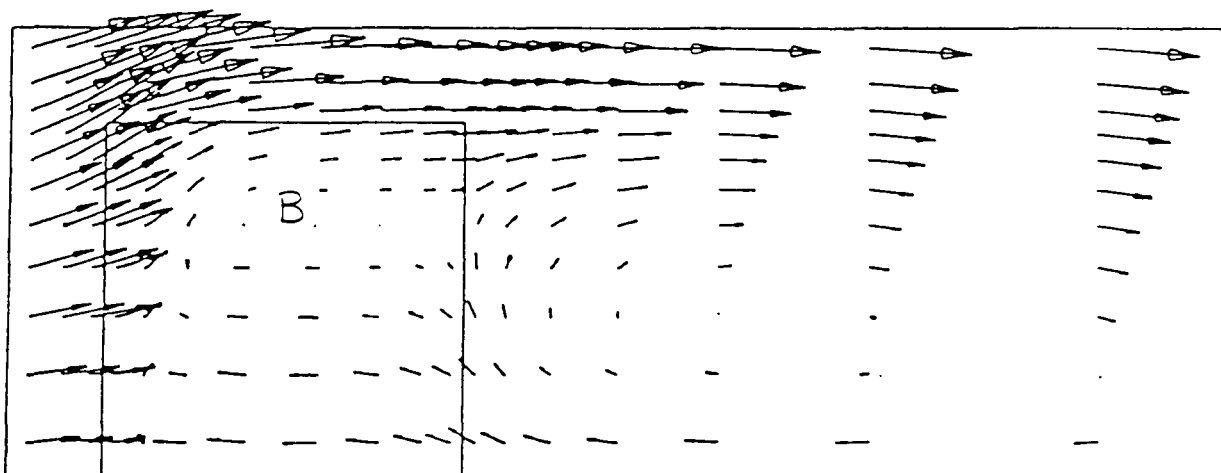
b) Adjacent to side face.

Figure (4.23): Side Elevation of flow field over
                an isolated cube (α = 0°)
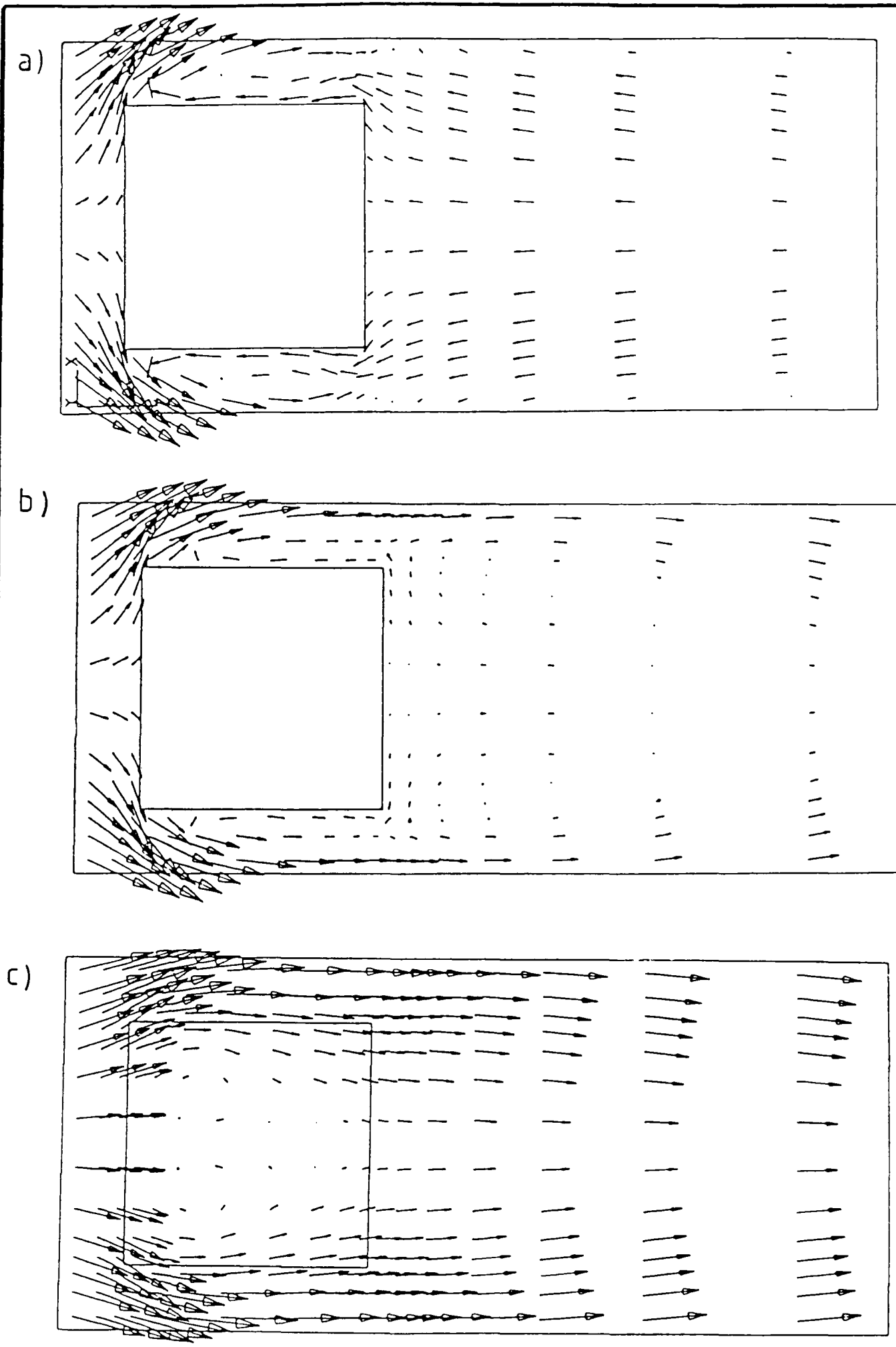
Figure (4.24):   Top view of flow field over
                  an   isolated cube (α = 0°)

a) y/h = 0.1   b) y/h = 0.5   c) y/h = 1.005
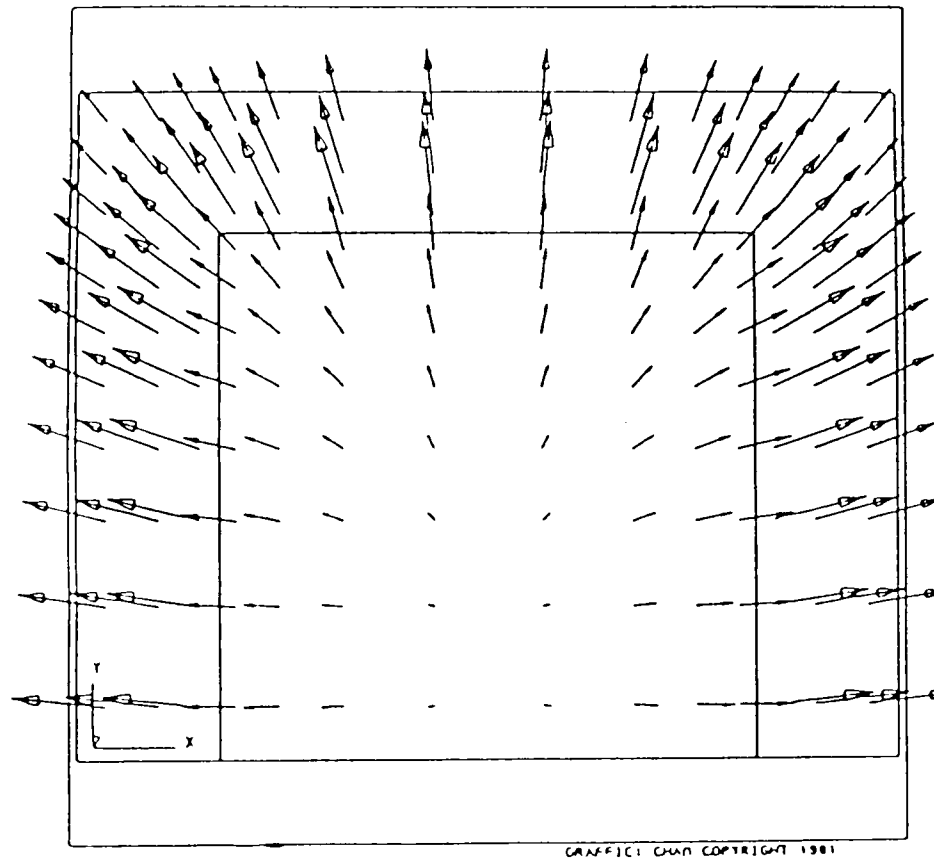
a) Adjacent to front face
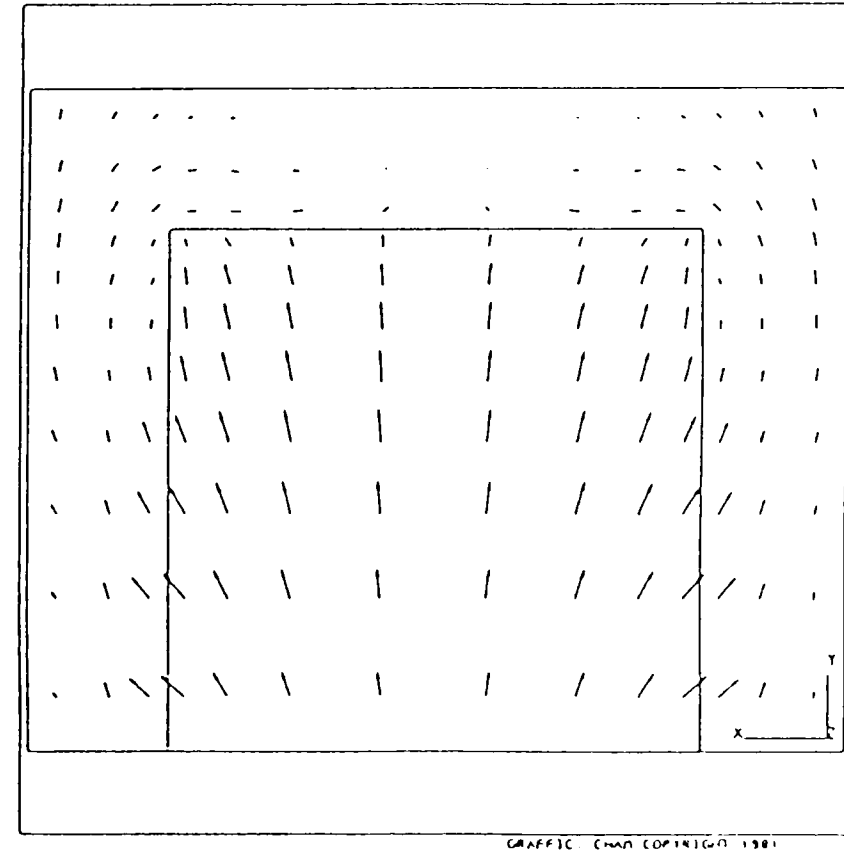
b) adjacent to rear face

Figure (4.25): End Elevation of flow field over
an isolated cube ($\alpha = 0°$)
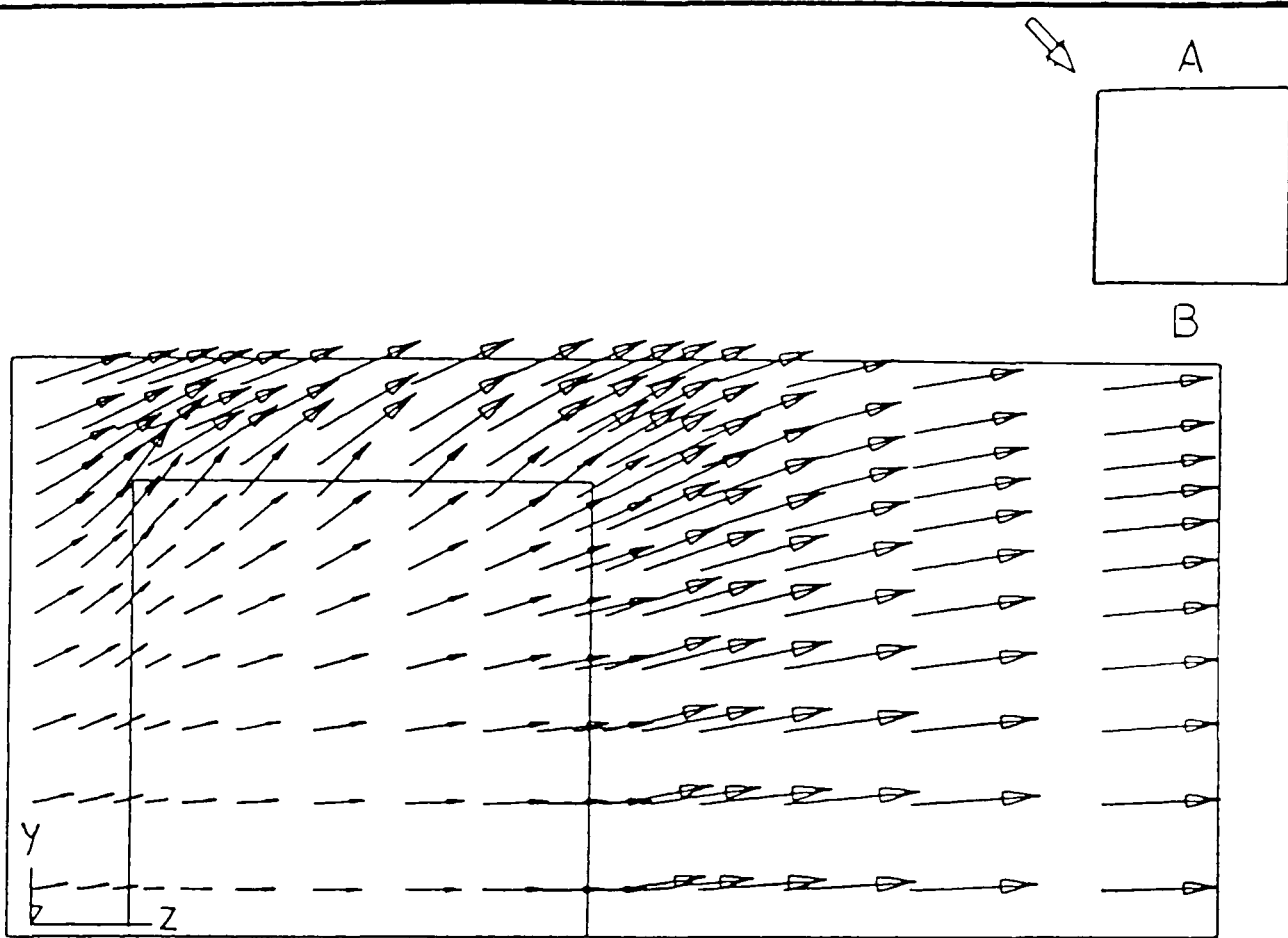
a)Upstream face "A"
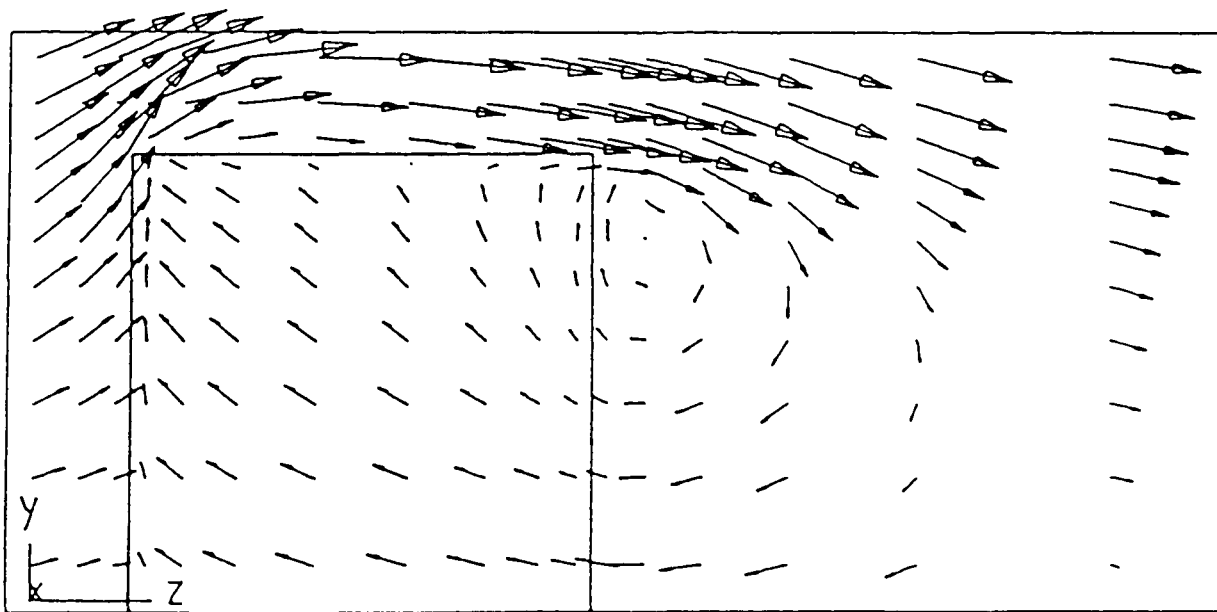
b)Downstream face "B"

Figure (4.26): Side Elevation of flow field over
an isolated cube (α = 45°)
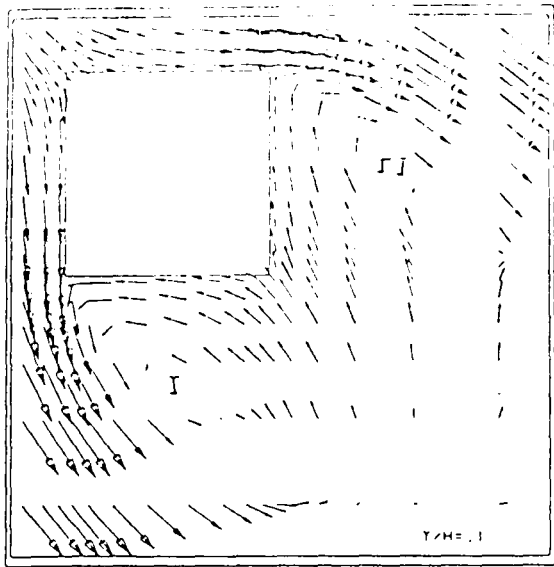
a） y/h =0.05
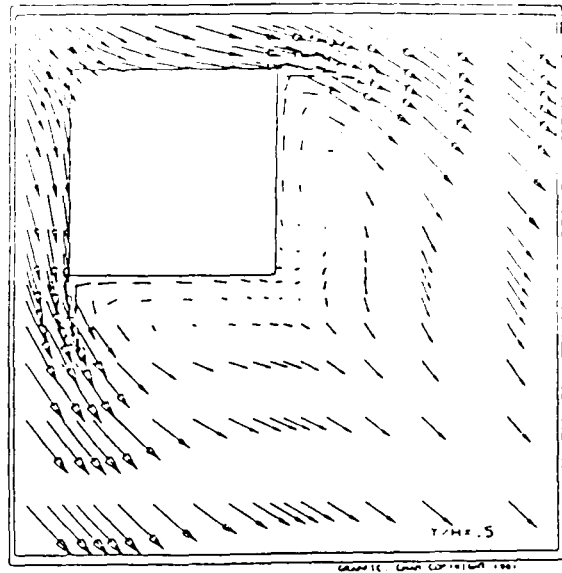
b） y/h = 0.50

Figure （4.27）: Top view of flow field over
an isolated cube （∝ = 45° ）
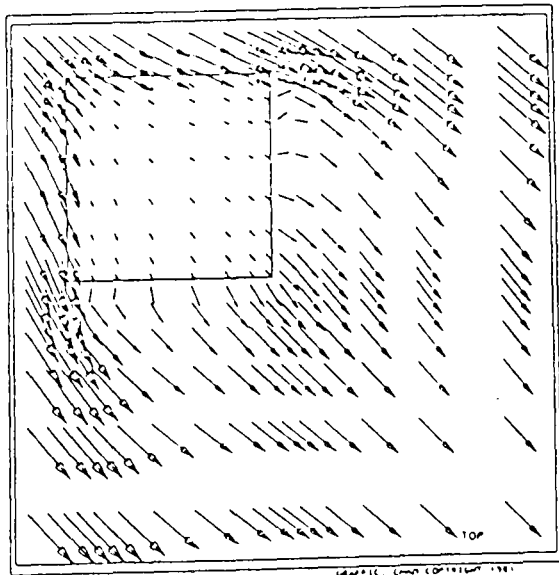
a） y/h = 1.005
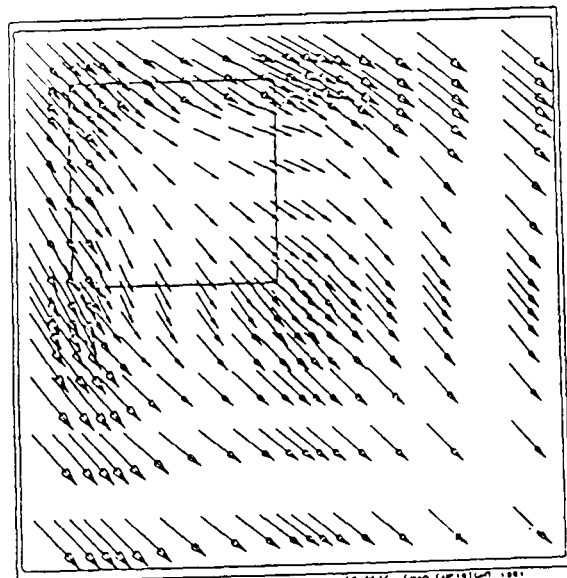
b） y/h =1.10

Figure （4.28）: Top view of flow field over
an isolated cube （ ∝ = 45° ）

160
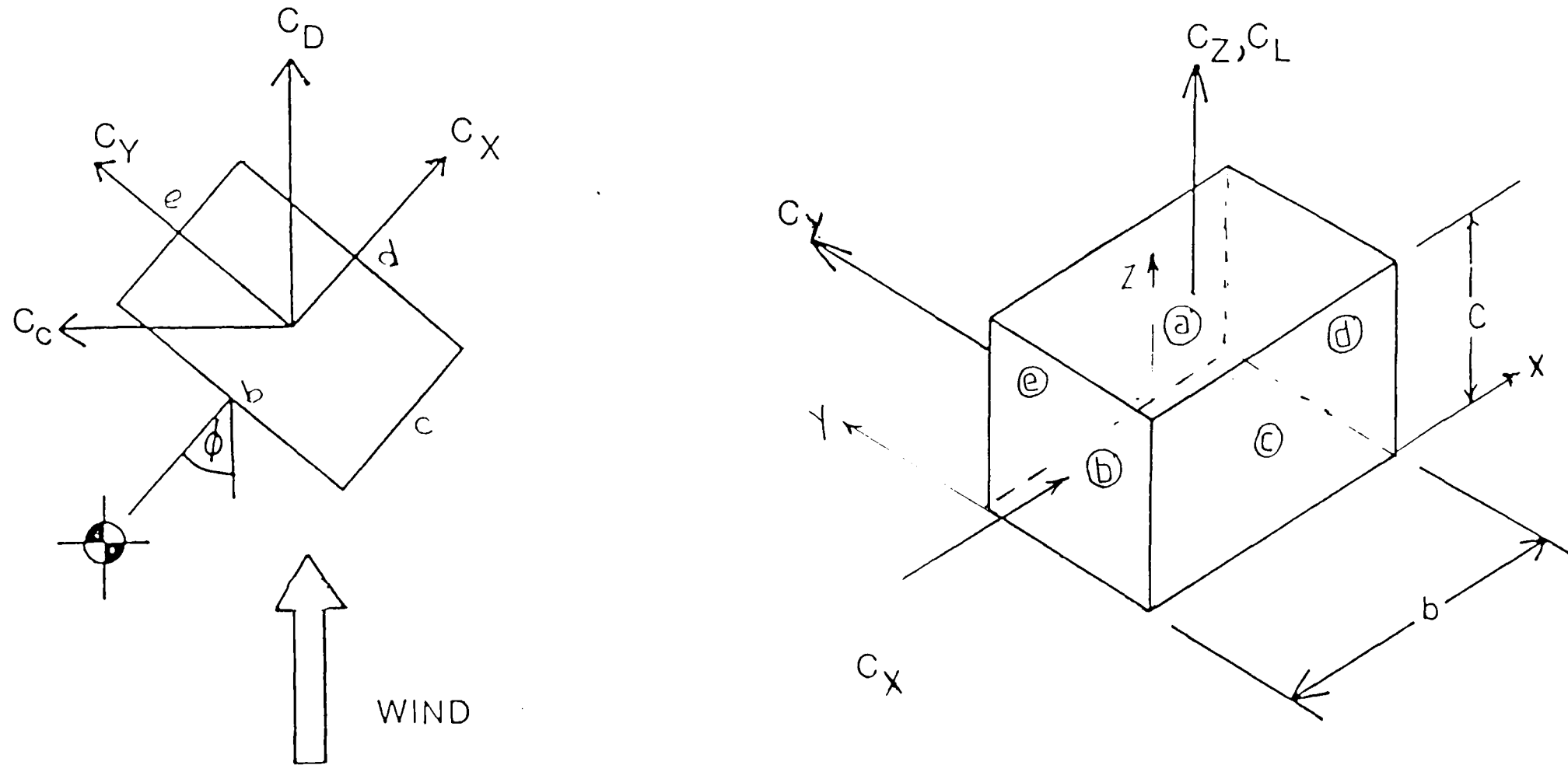
Figure (4.29): AXIS SYSTEMS AND MODEL DIMENSIONING NOMENCLATURE.

Phoenics
Exp

(Face -a)

Wind Yaw Angle,α,(Degrees)

(Face -b)

Wind Yaw Angle,α,(Degrees)

(Face -c)

Wind Yaw Angle,α,(Degrees)

(Face -d)

Wind Yaw Angle,α,(Degrees)

(Face -e)

Wind Yaw Angle,α,(Degrees)
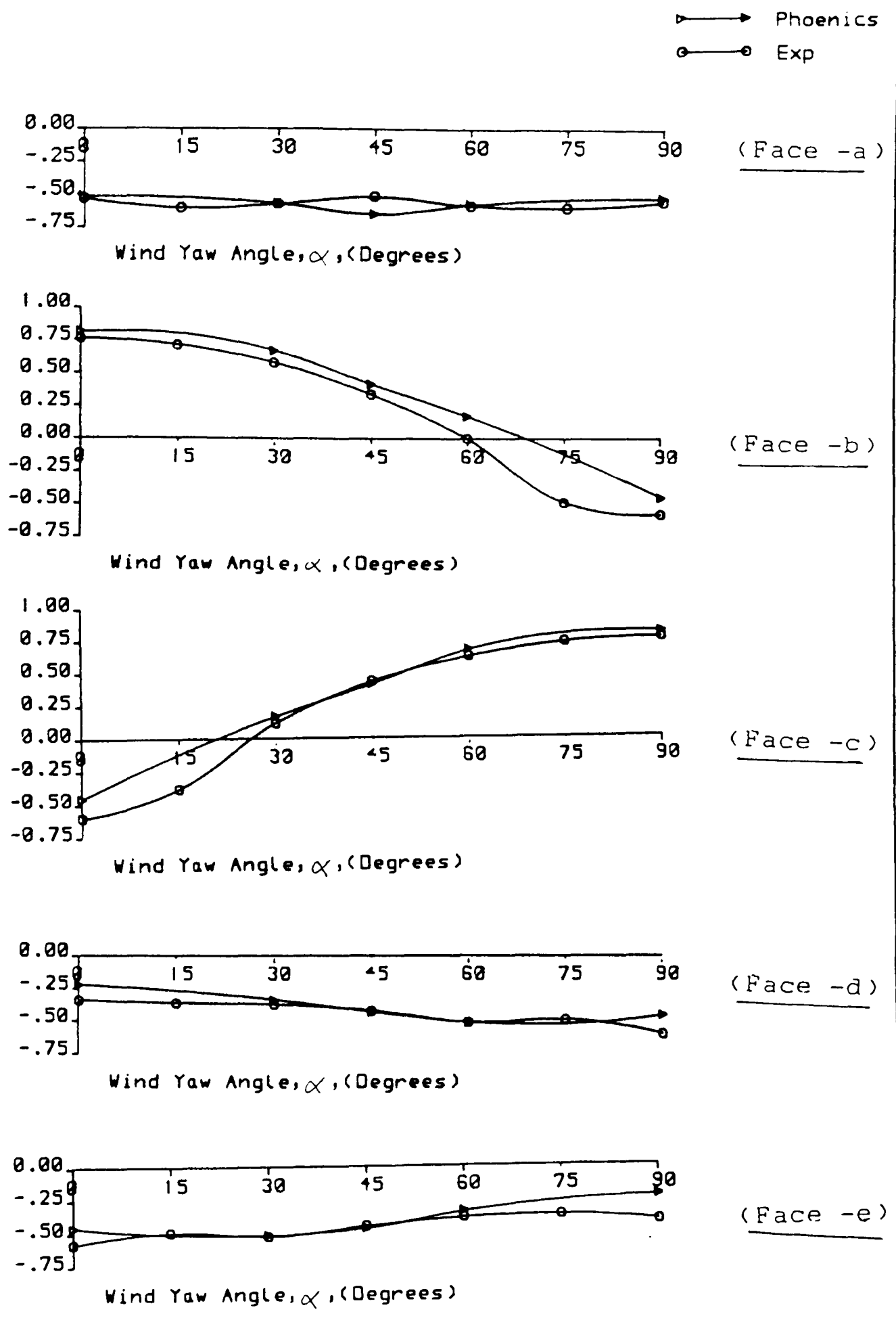
Figure(4.30):

Variation of the average pressure coefficient
on a complete face of an isolated cube with
wind yaw angle

162

Figure (4.31)   ISOMETRIC VIEW OF PREDICTED PRESSURE COEFFICIENT DISTRIBUTION OVER UNSHIELDED RECTANGULAR BOX.

(Based on PHOENICS   prediction of Cp)

Re =   .206E 6
α =   0 degrees

Cp

Top Surface

Rear Surface

Left Side

Right Side

Front Surface

FORCE COEFFICIENTS
Body Axis System
Cx = 1.044
Cy = 0.001
Cz = 0.519
Wind Axis System
Cd = 1.044
Cr = 0.001
Cl = 0.519
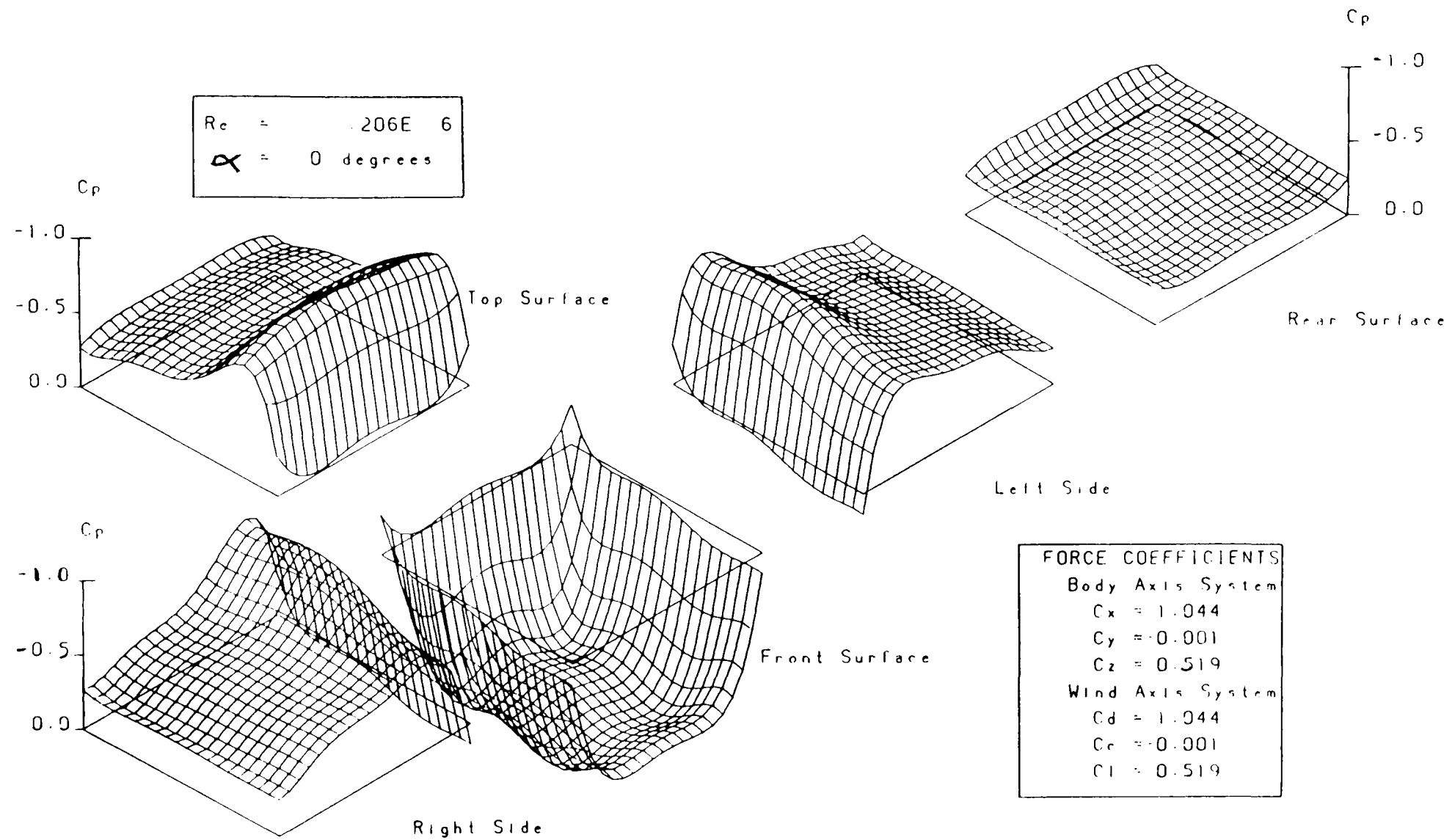
Figure (4.32)   ISOMETRIC VIEW OF PREDICTED PRESSURE COEFFICIENT DISTRIBUTION OVER UNSHIELDED RECTANGULAR BOX.

(Based on Wind Tunnel measurements of Cp)

Re = .202E 6
α = 0 degrees

Cp
-1.0
-0.5
0.0

Top Surface

Cp
-1.0
-0.5
0.0

Left Side

Cp
-1.0
-0.5
0.0

Rear Surface

Front Surface

Cp
-1.0
-0.5
0.0

Right Side
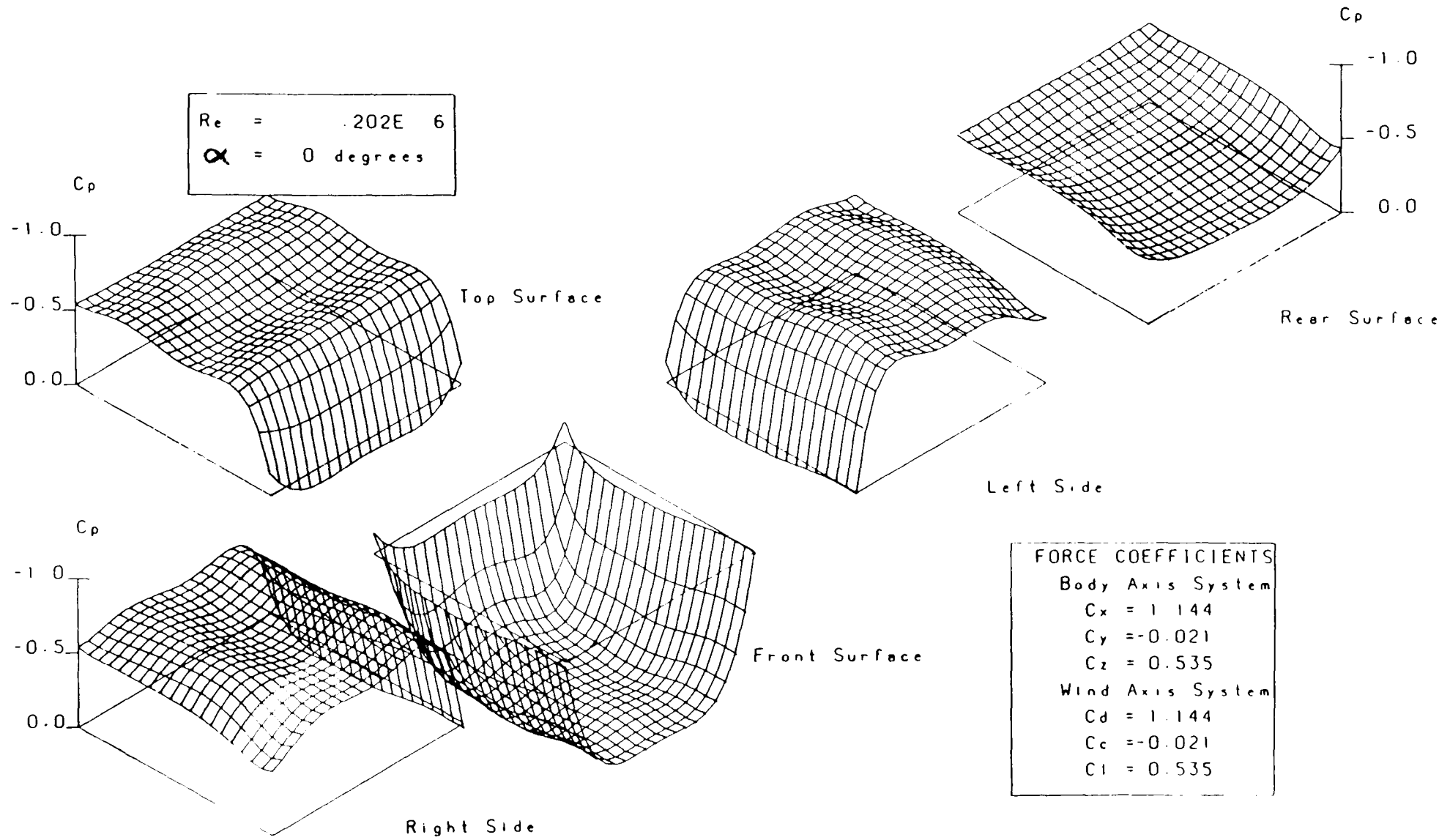
FORCE COEFFICIENTS
Body Axis System
Cx = 1.144
Cy = -0.021
Cz = 0.535
Wind Axis System
Cd = 1.144
Cc = -0.021
Cl = 0.535

164

Figure (4.33) ISOMETRIC VIEW OF PREDICTED PRESSURE COEFFICIENT DISTRIBUTION OVER UNSHIELDED RECTANGULAR BOX.

(Based on PHOENICS prediction of Cp)

Re = .206E 6
α = 45 degrees

Top Surface

Rear Surface

Left Side

Right Side

Front Surface

FORCE COEFFICIENTS
Body Axis System
C_x = 0.897
C_y = 0.868
C_z = 0.651
Wind Axis System
C_d = 1.247
C_c = 0.020
C_l = 0.651
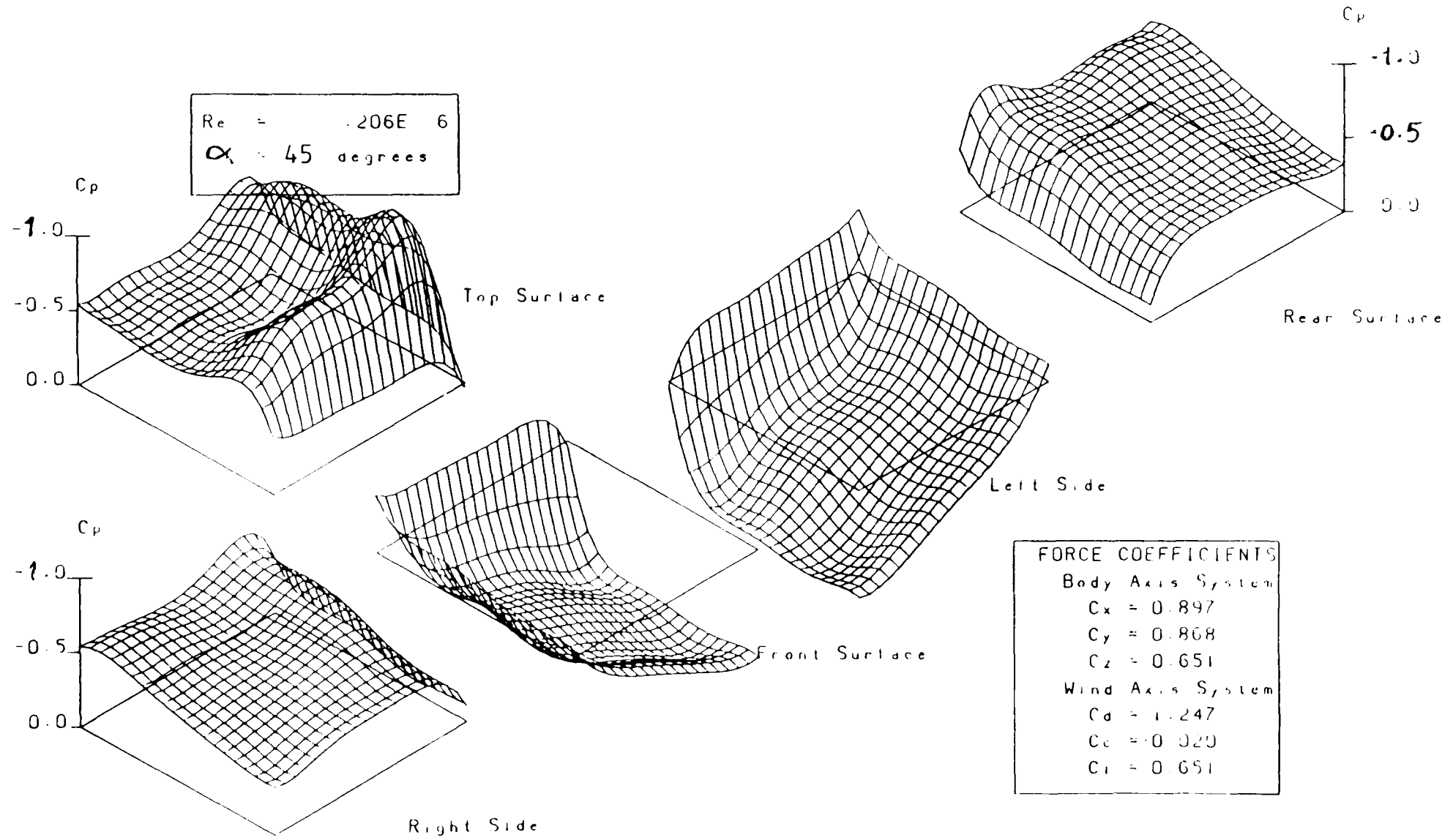
Figure (4.34) ISOMETRIC VIEW OF PREDICTED PRESSURE COEFFICIENT DISTRIBUTION OVER UNSHIELDED RECTANGULAR BOX.

(Based on Wind Tunnel measurements of Cp)

R_e = .200E 6

α = 45 degrees

Top Surface

Rear Surface

Left Side

Front Surface

Right Side

FORCE COEFFICIENTS
Body Axis System
C_x = 0.758
C_y = 0.875
C_z = 0.512
Wind Axis System
C_d = 1.154
C_c = 0.083
C_l = 0.512

VARIATION OF THE FORCE COEFFICIENT WITH WIND YAW ANGLE
FOR AN ISOLATED CUBE

Phoenics
Exp
ESDU

167
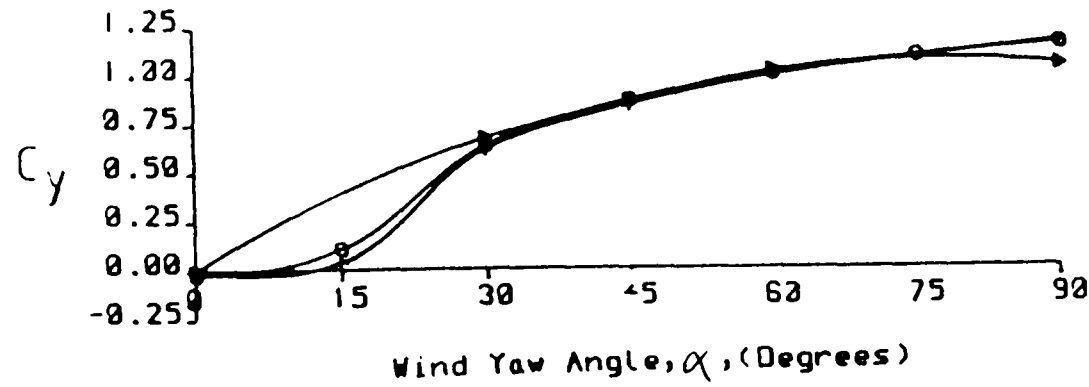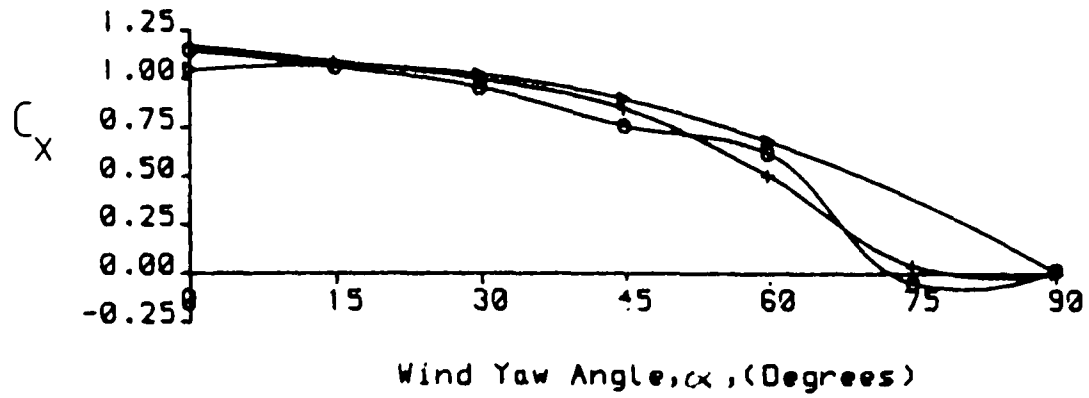
Figure (4.35):
Body axis force coefficients
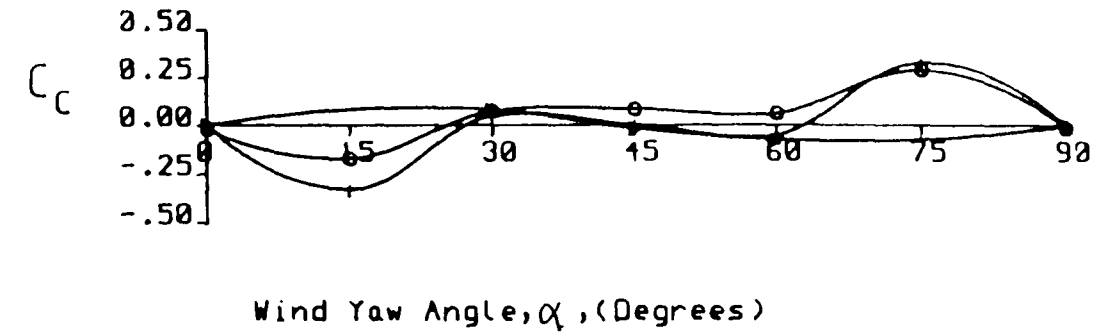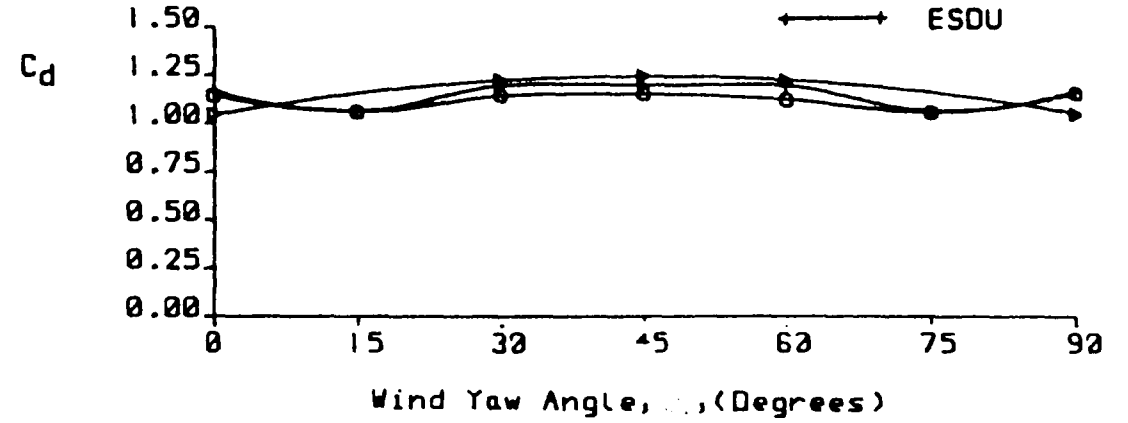
Figure (4.36):
Wind axis force coefficients

VARIATION OF THE FORCE COEFFICIENT WITH WIND YAW ANGLE
FOR AN ISOLATED CUBE
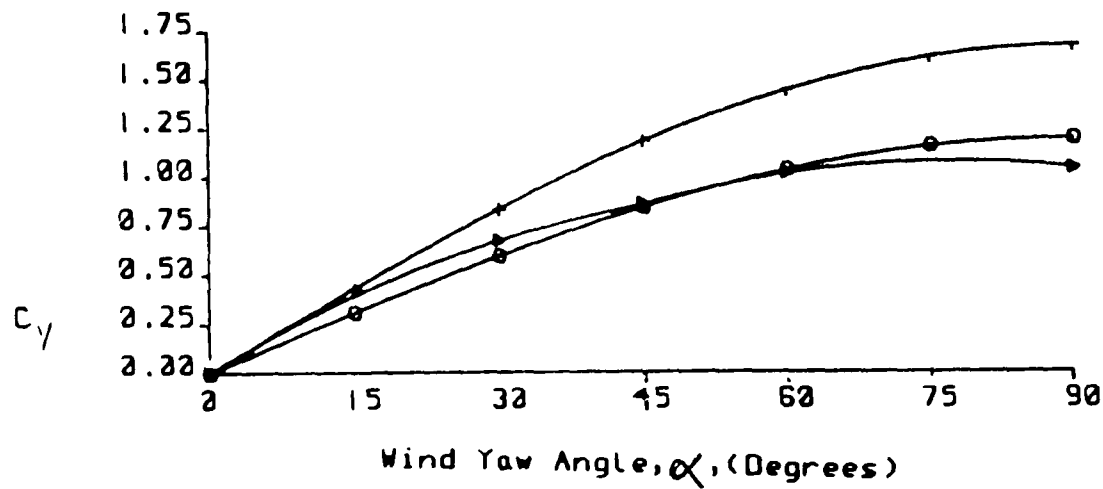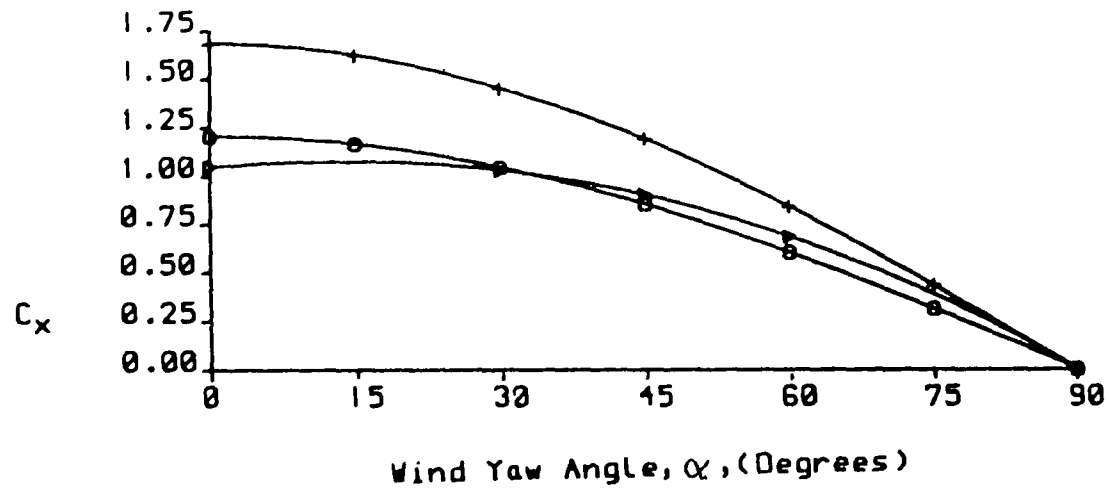
Figure (4.37):
Body axis force coefficients
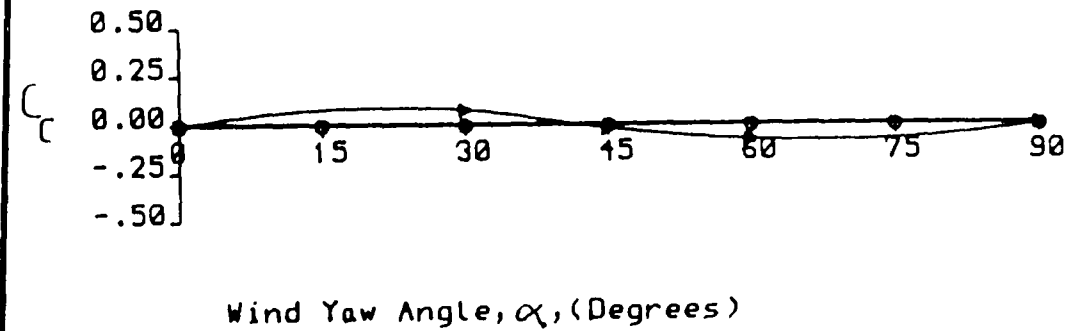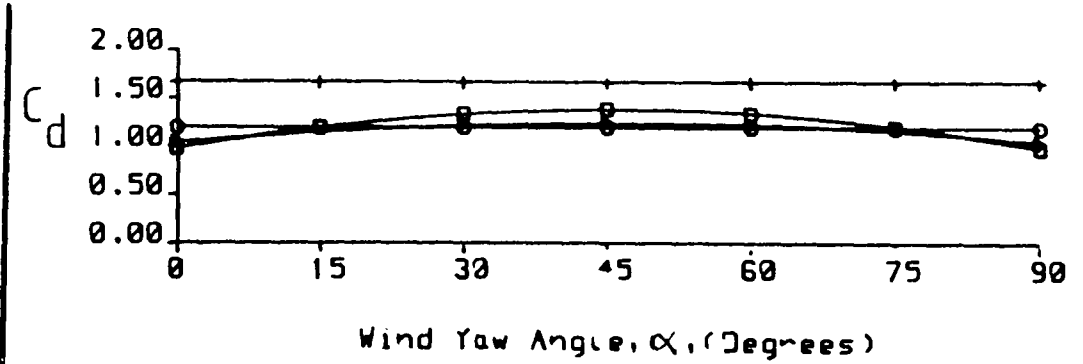
Figure (4.38):
Wind axis force coefficients

188
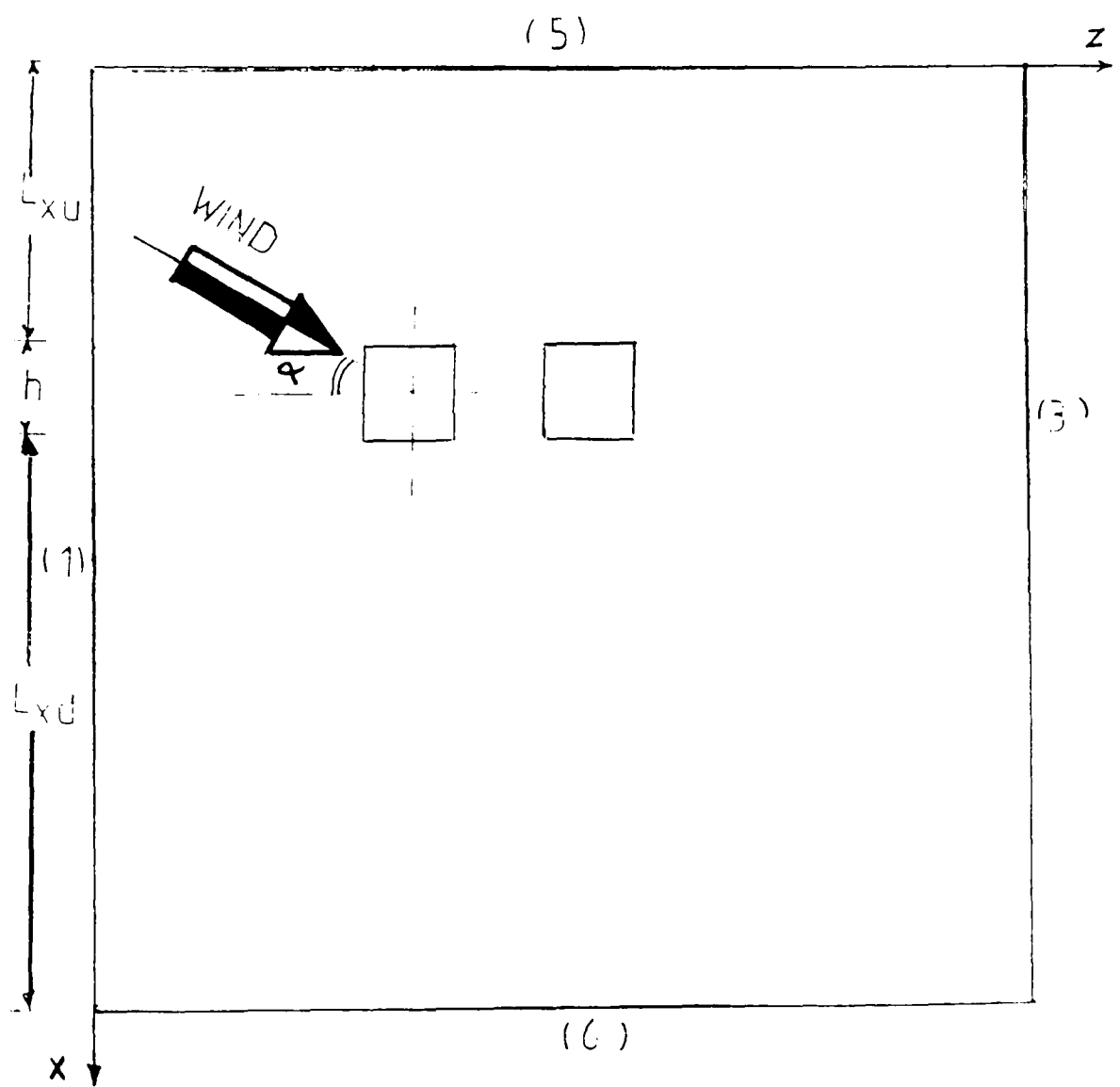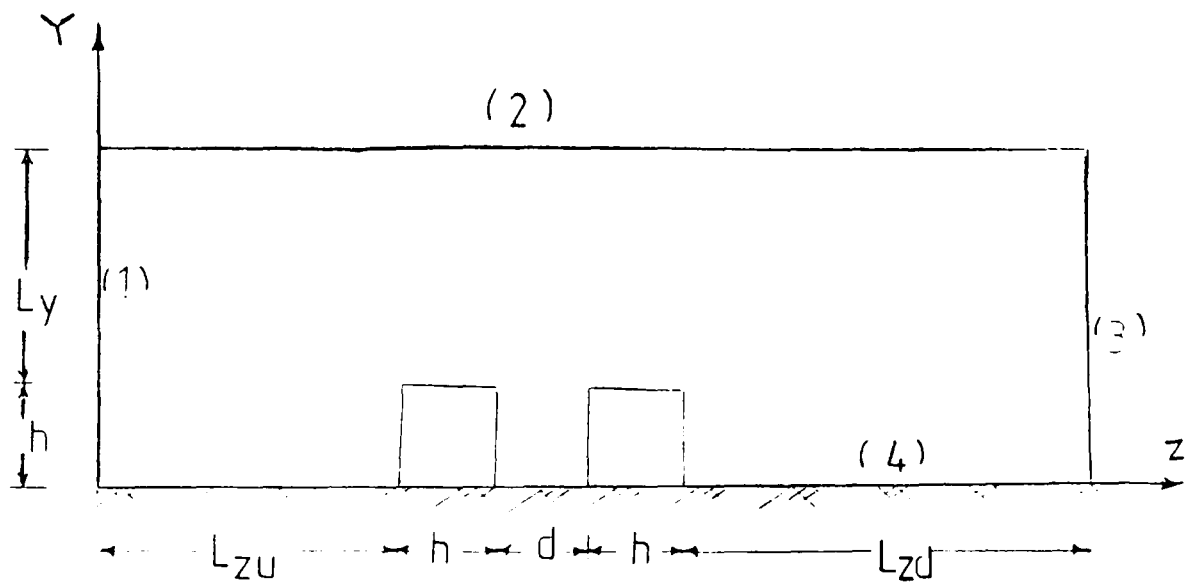
Figure (4.39): Geometry of solution domain for double cube. shown in Y-Z and X-Z planes.
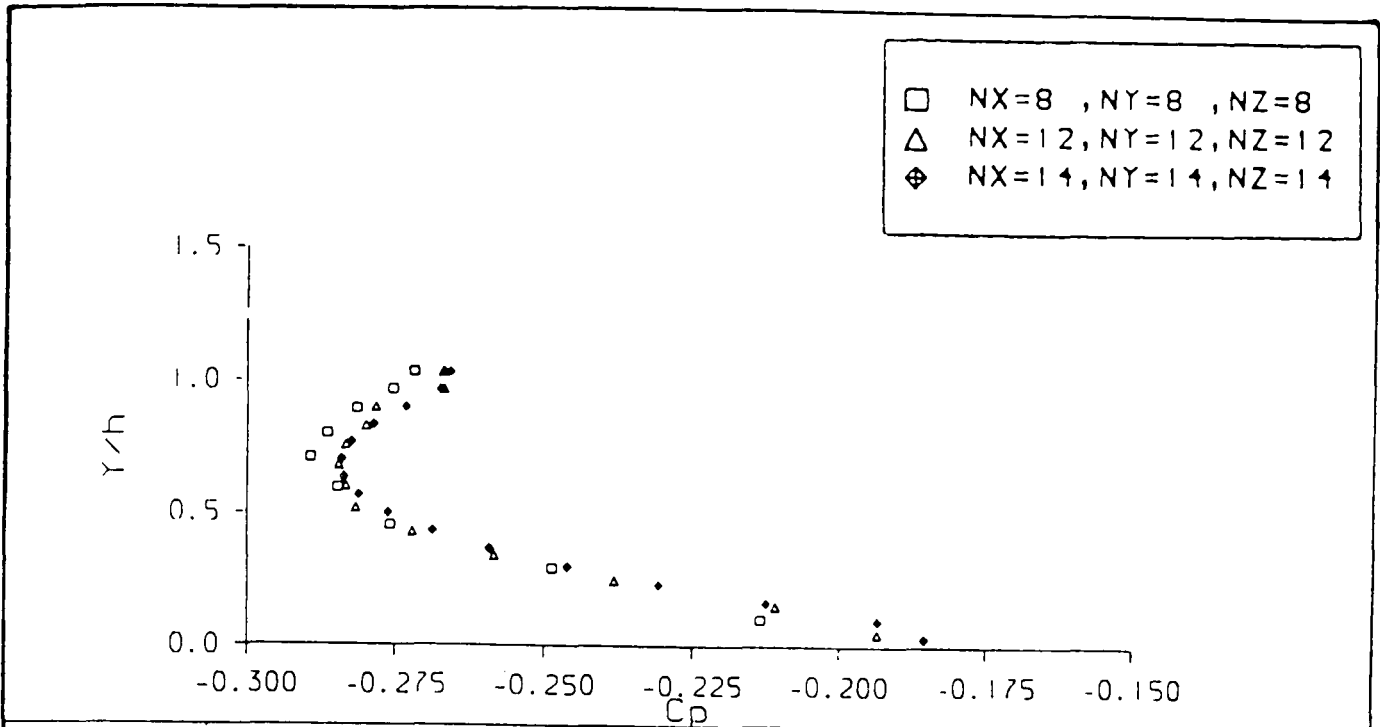
Figure (4.40-a)   Cp :PROFILES AT (X/h =0.50 & Z/d =0.0333)
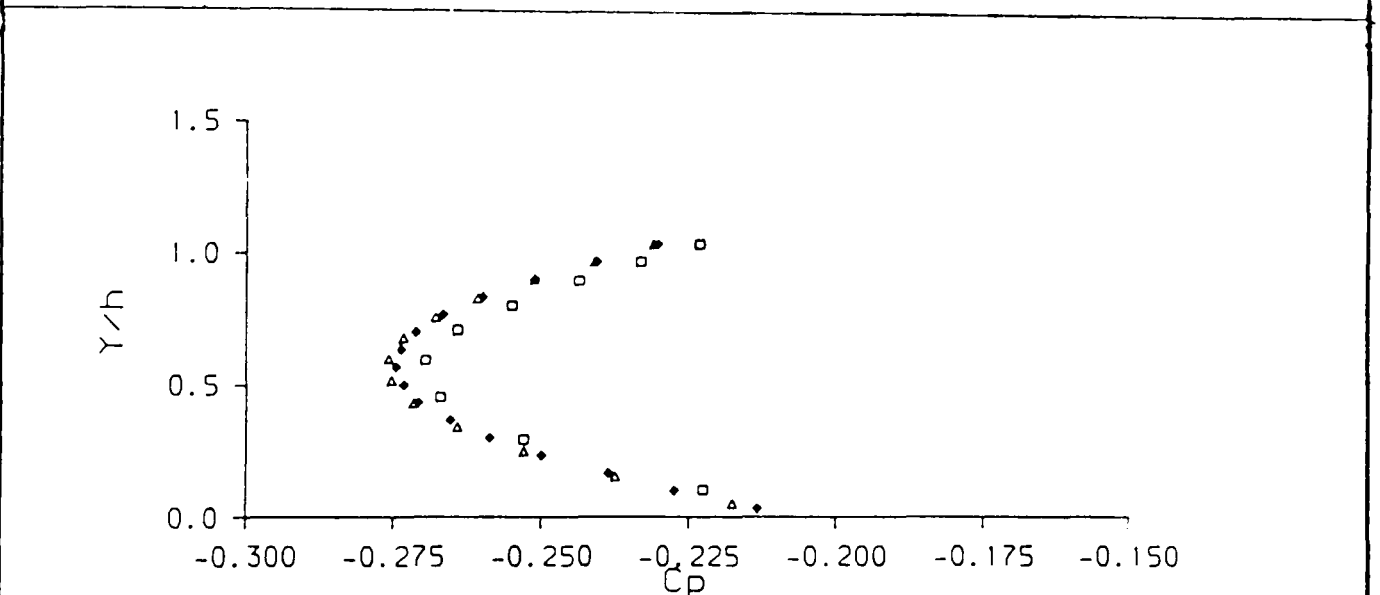
Figure (4.40-b)   Cp : PRPFILES AT (X/h =0.50 & Z/d =0.50)
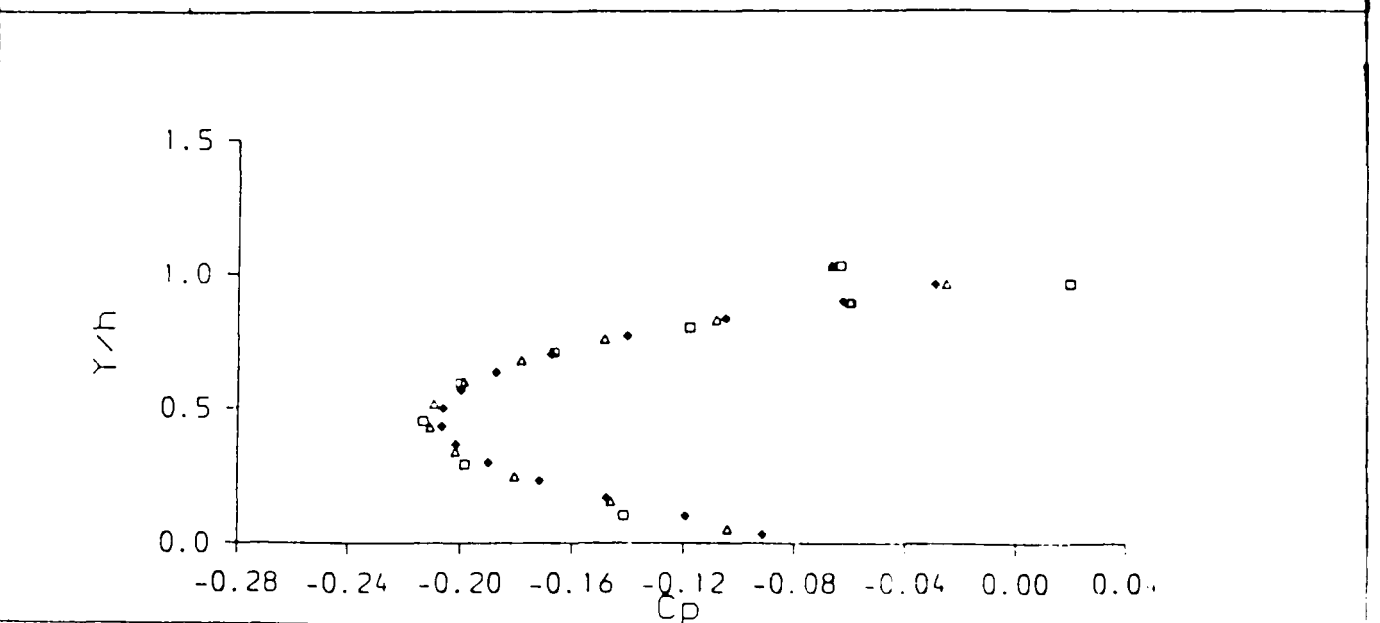
figure (4.40-c)   Cp :PROFILES AT (X/h =0.50 & Z/d =0.367).
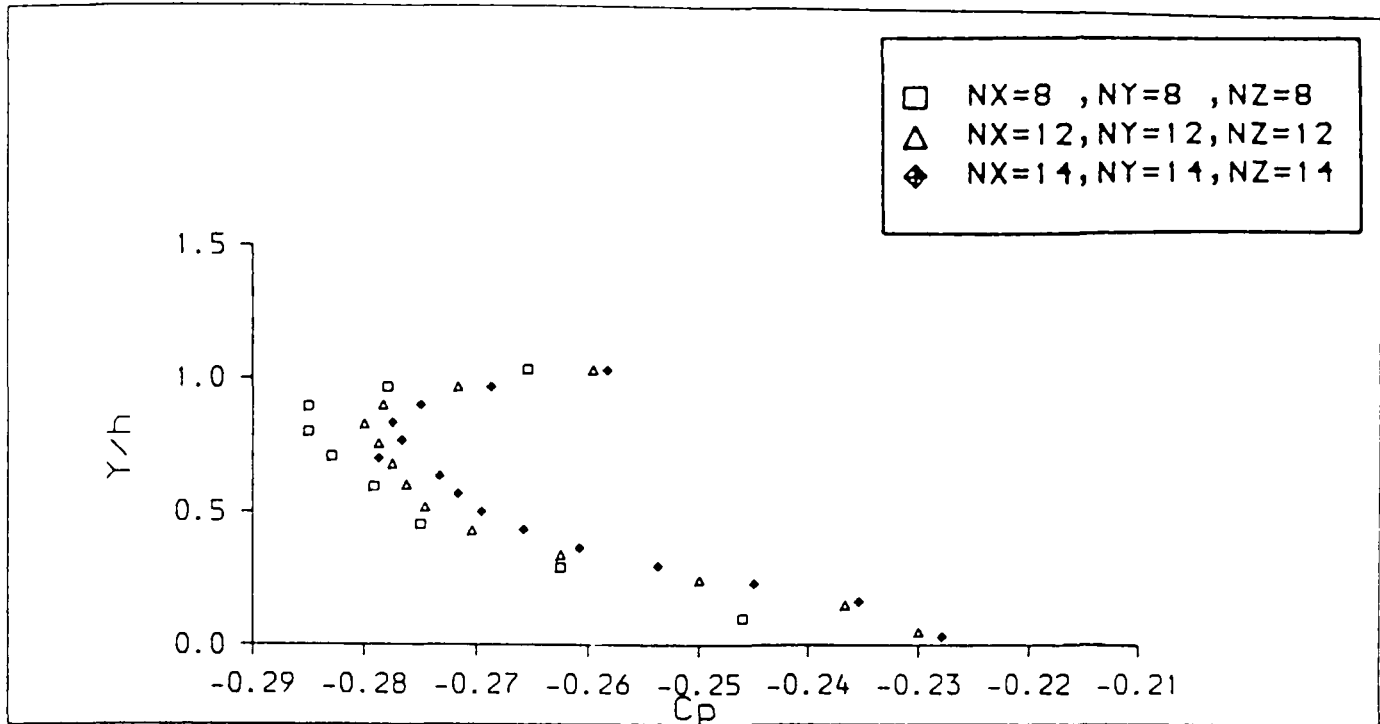
Figure (4.41-a) Cp :PROFILES AT (X/h =0.967 & Z/d =0.0333)
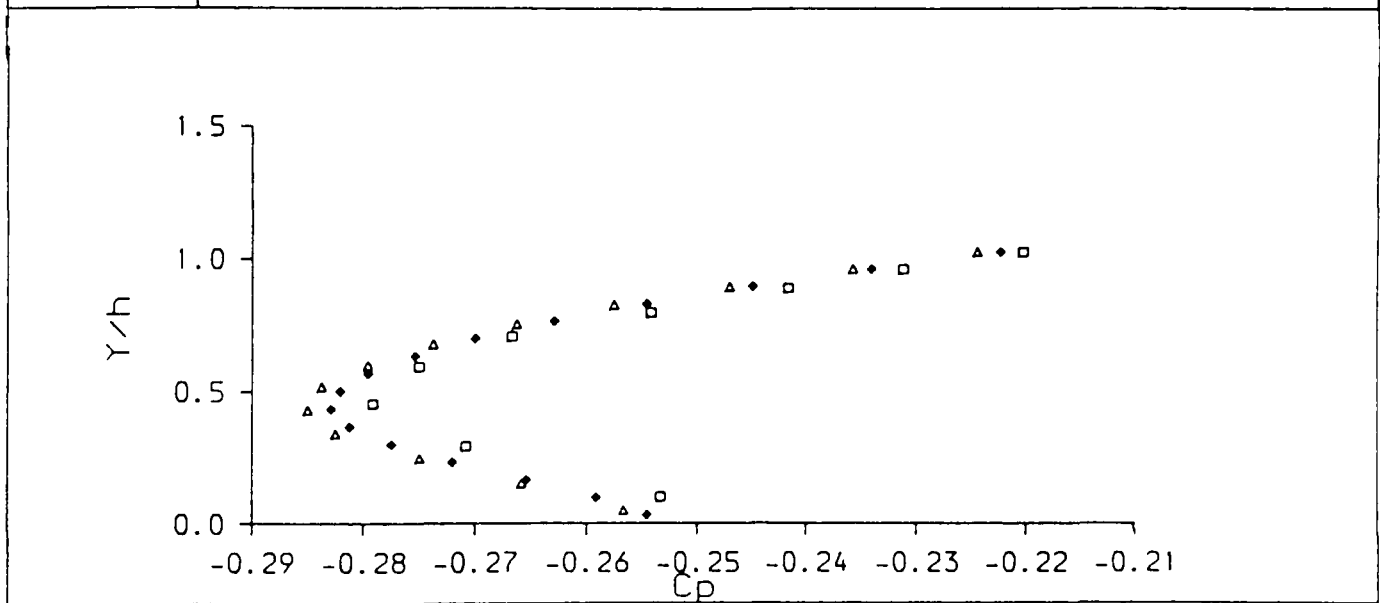
Figure (4.41-b) Cp :PROFILES AT (X/h =0.967 & Z/d =0.50)
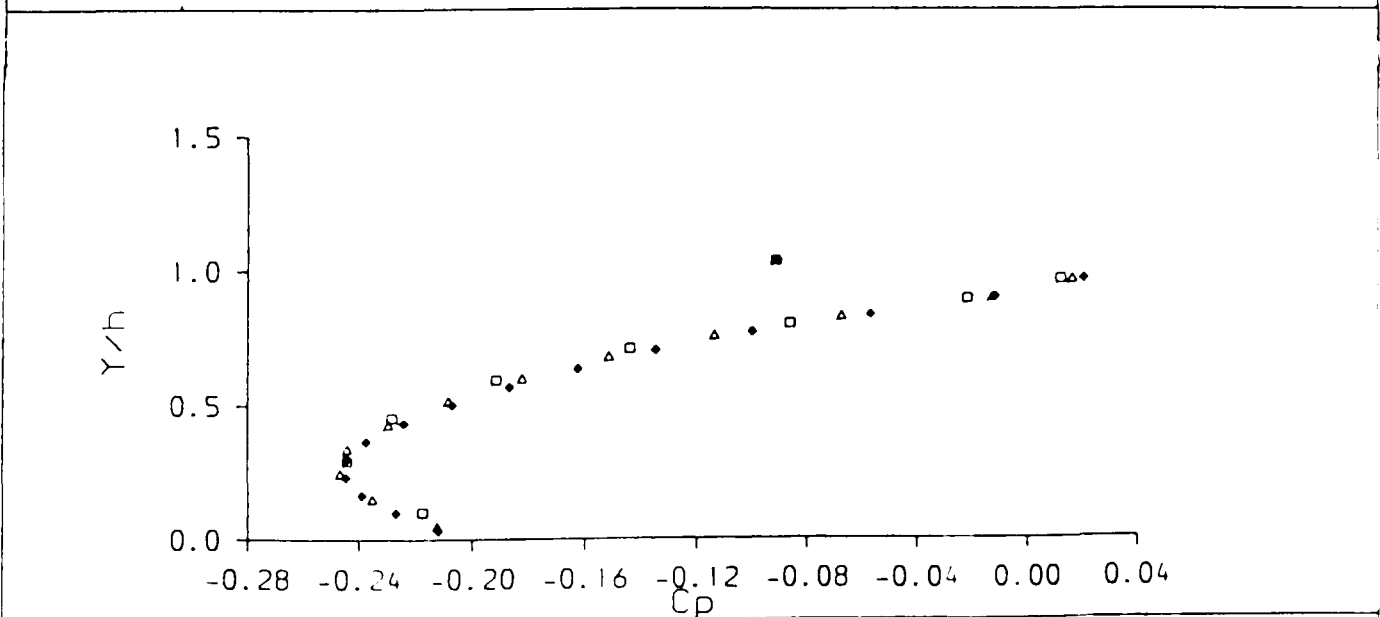
Figure (4.41-c) Cp :PROFILES AT (X/h =0.967 & Z/d =0.967)
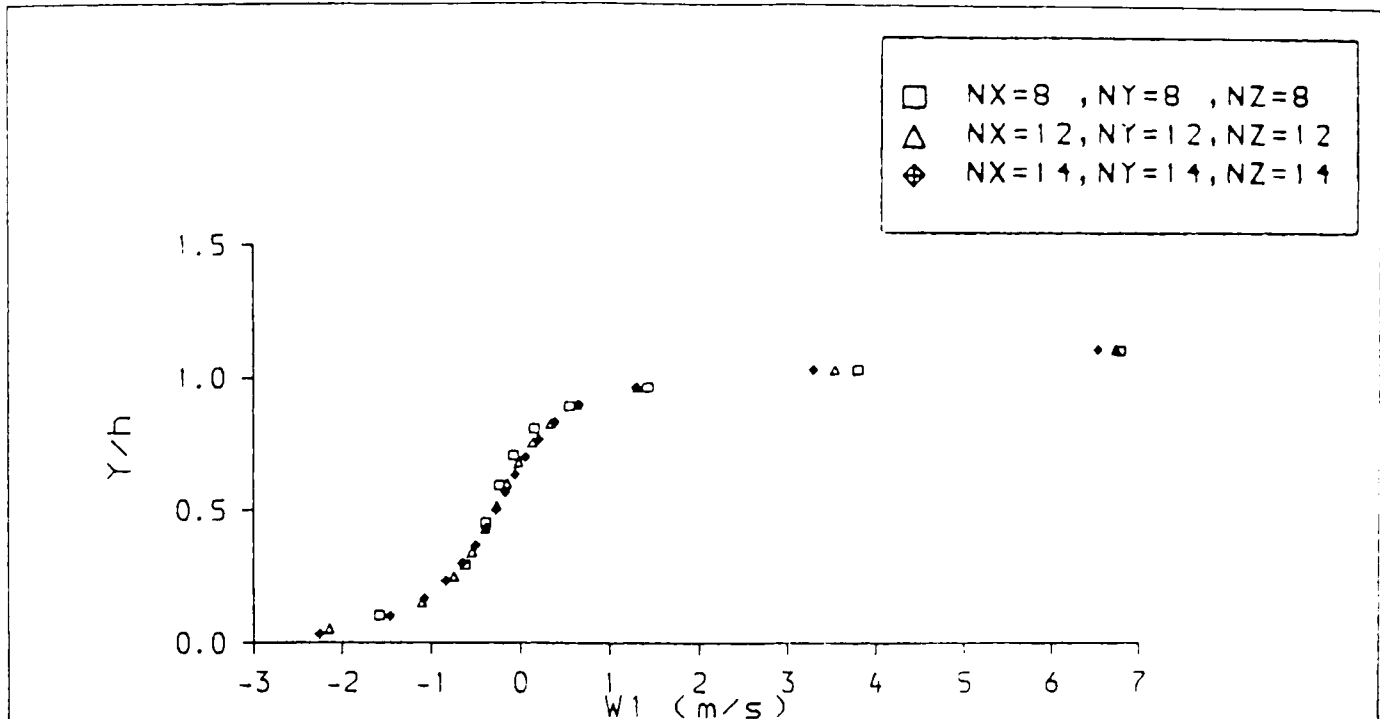
Figure (4.42-a)

W1 : AXIAL VELOCITY PROFILES AT (X/h =0.5 & Z/d =0.0333)
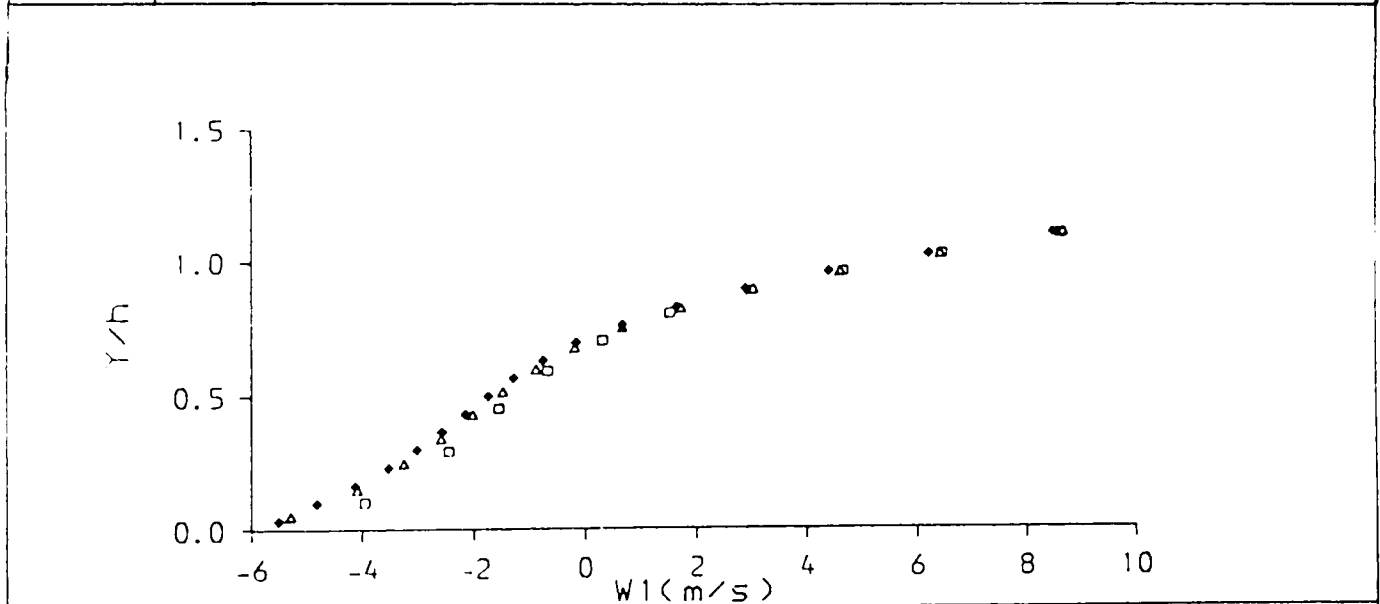
Figure (4.42-b)

W1 :AXIAL VELOCITY PROFILES AT (X/h =0.50 & Z/d =0.50)
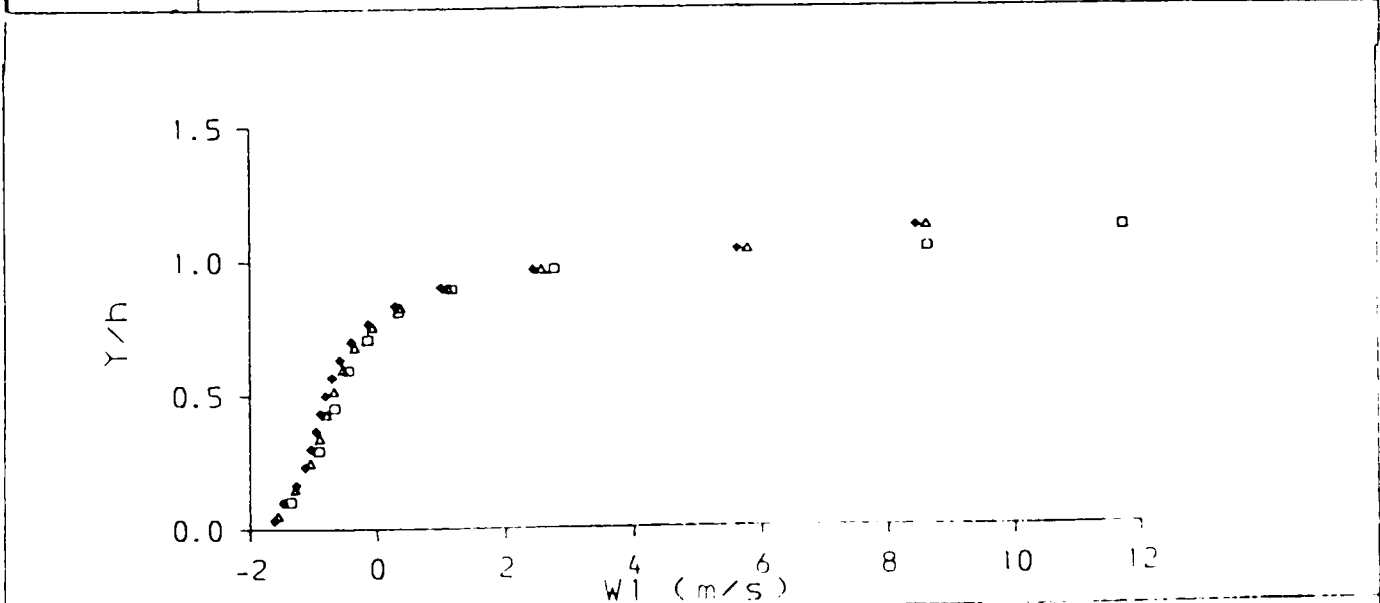
Figure (4.42-c)

W1 :AXIAL VELOCITY PROFILES AT (X/h =0.50 & Z/d =0.925)

172
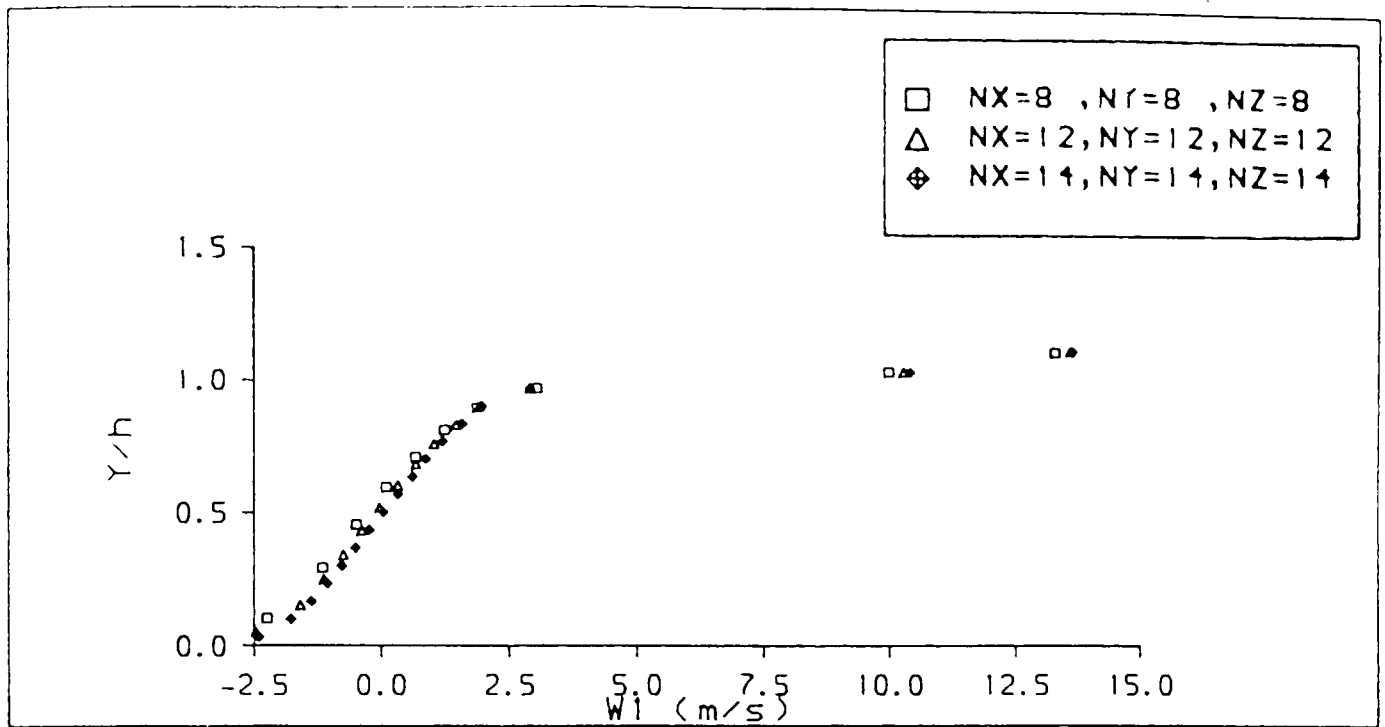
Figure (4.43-a)

W1 :AXIAL VELOCITY PROFILES AT (X/h =0.95 & Z/h =0.0333)
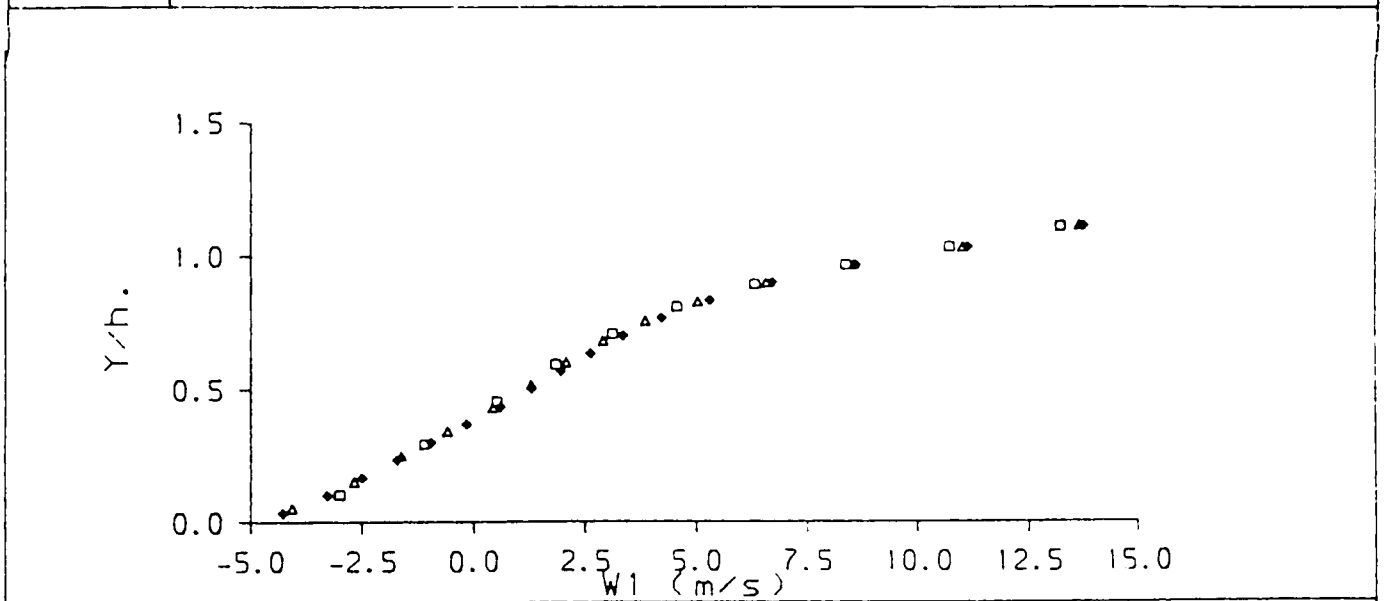
Figure (4.43-b)

W1 : AXIAL VELOCITY PROFILES AT (X/h =0.95 & Z/d=0.50)
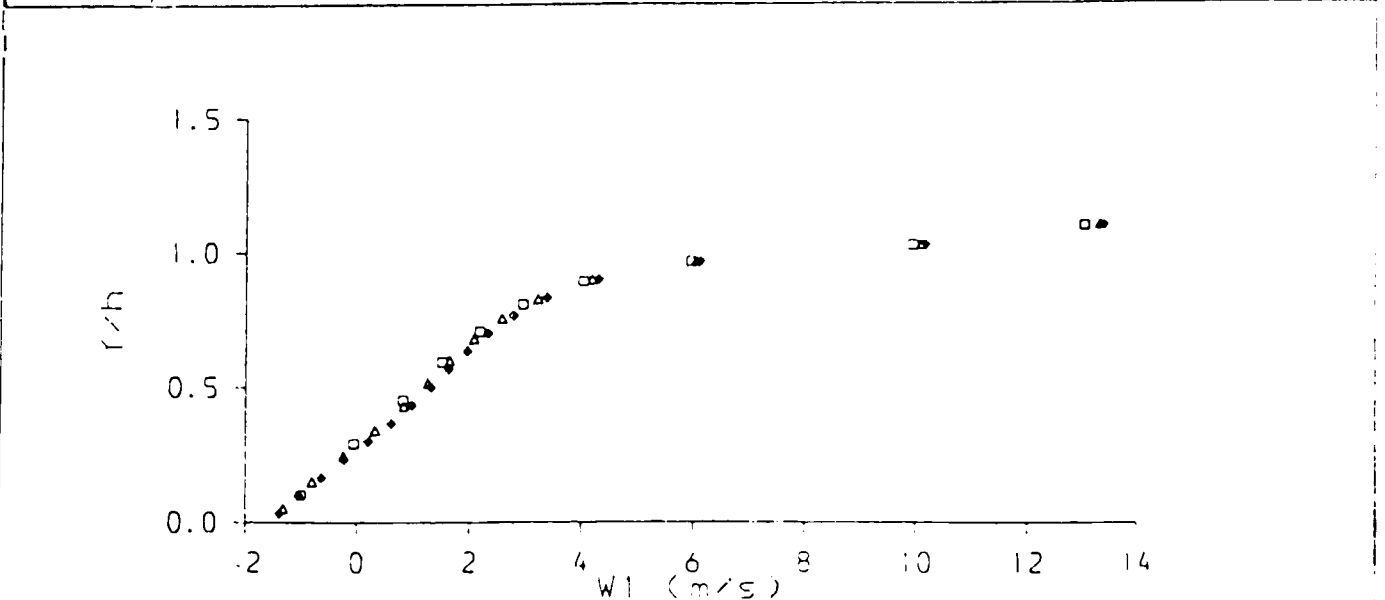
Figure (4.43-c)

W1 :AXIAL VELOCITY PROFILES AT (X/h =0.95 & Z/d = 0.925)

173
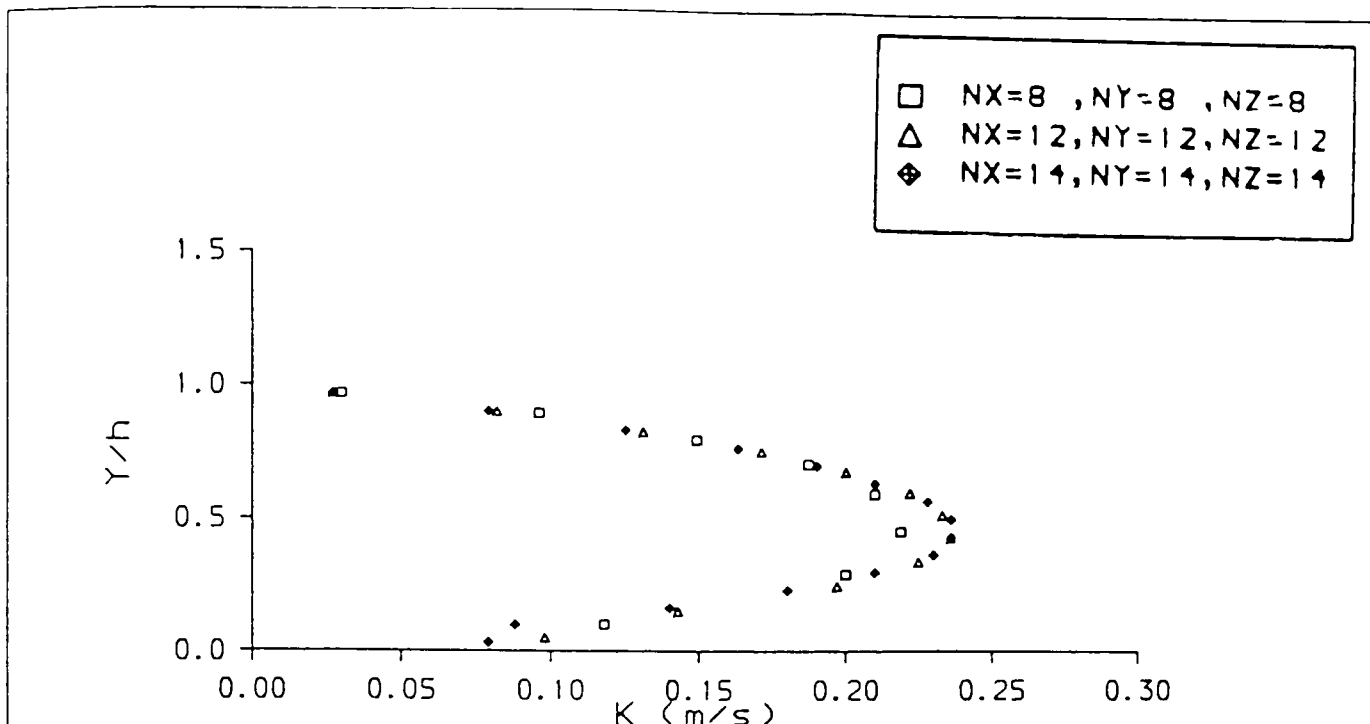
Figure (4.44-a)   K :PROFILES AT (X/h =0.50 & Z/d =0.0333)
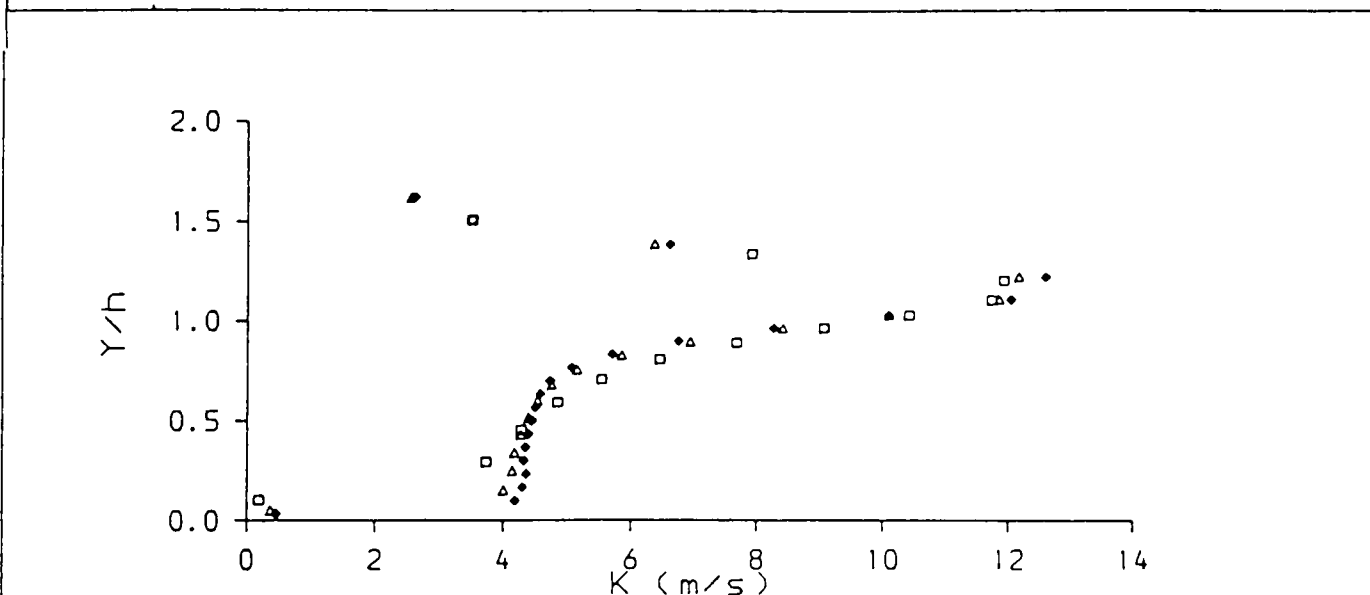
Figure (4.44-b)   K : PROFILES AT (X/h =0.50 & Z/d =0.50)
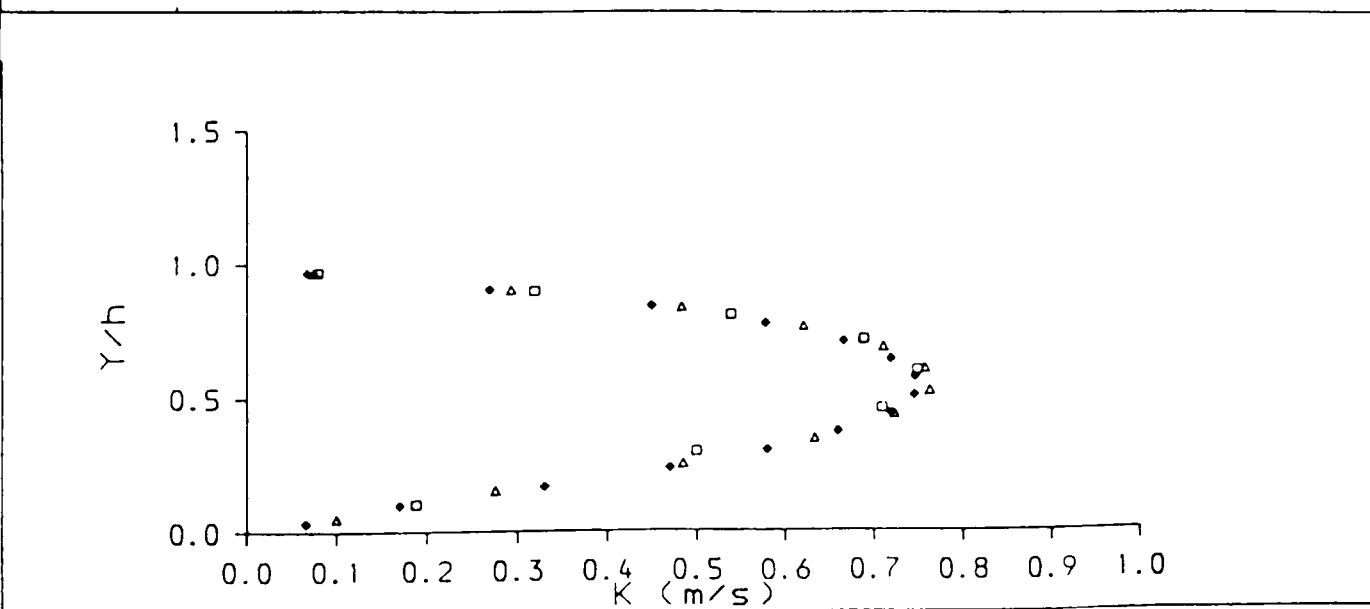
Figure (4.44-c)   K :PROFILES AT (X/h =0.50 & Z/d =0.967)
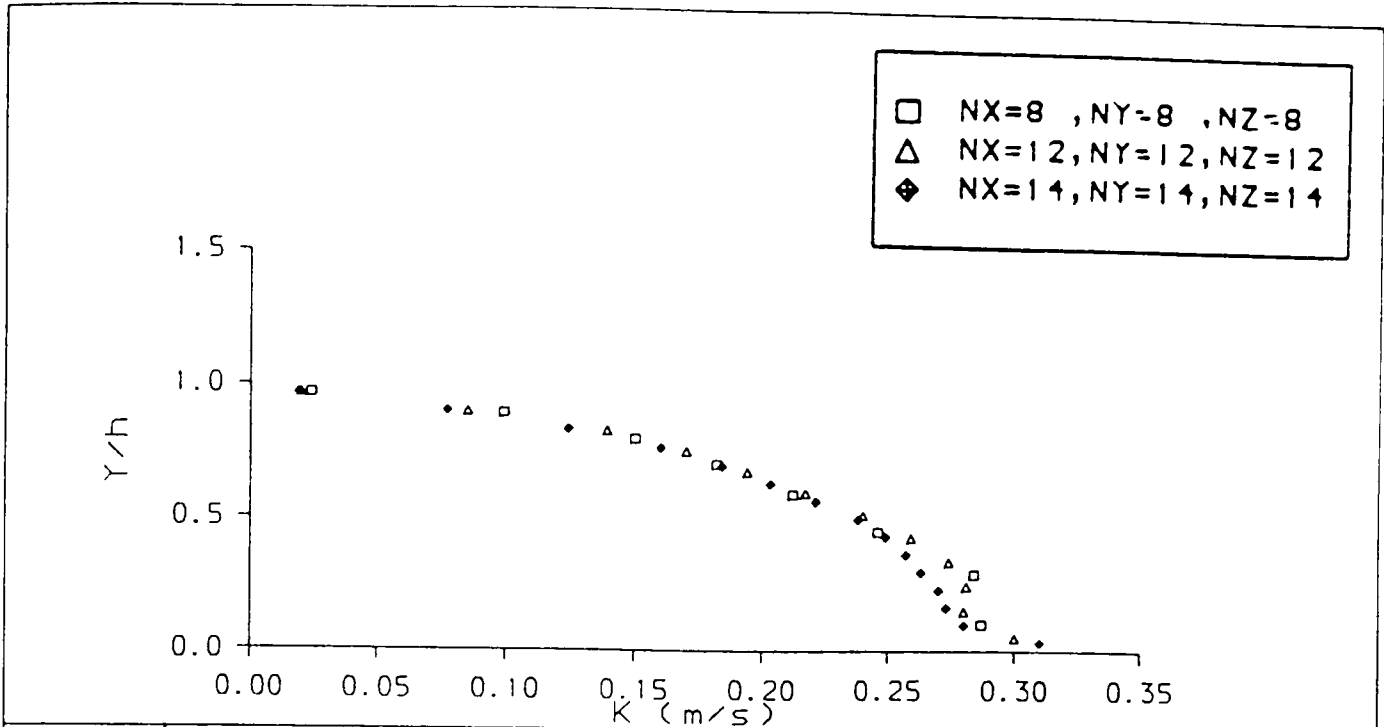
Figure (4.45-a)   K :PROFILES AT (X/h =0.967 & Z/d =0.0333)
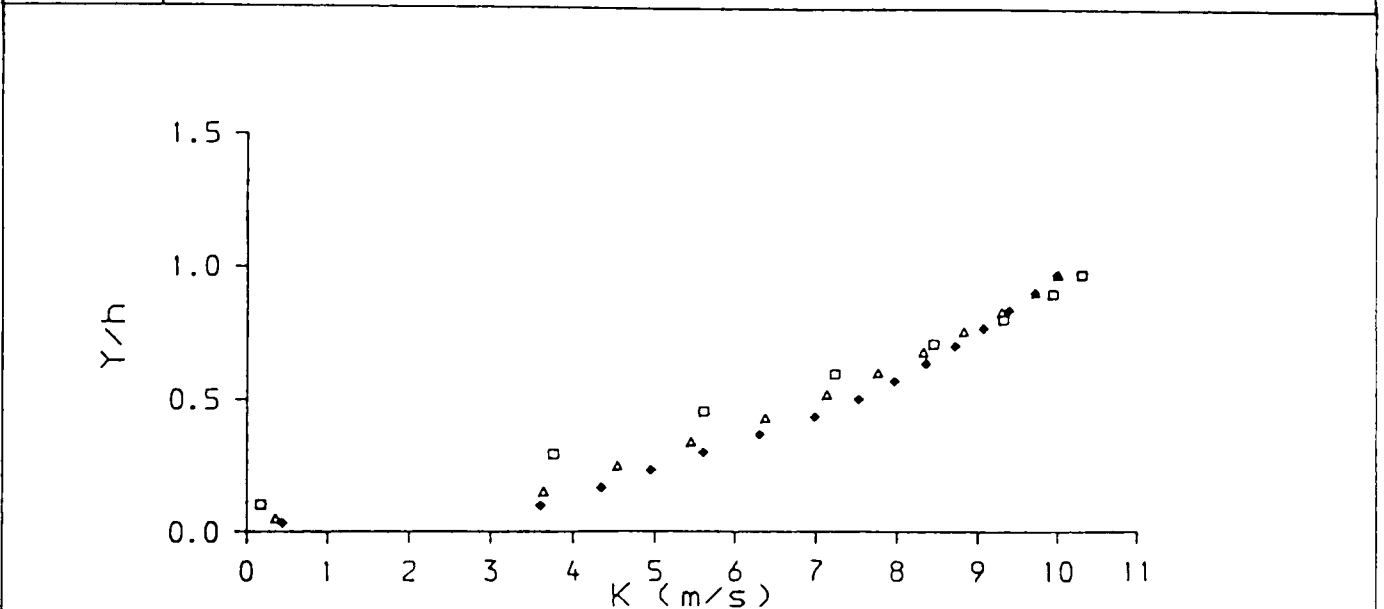
Figure (4.45-b)   K :PROFILES AT (X/h =0.967 & Z/d =0.50)
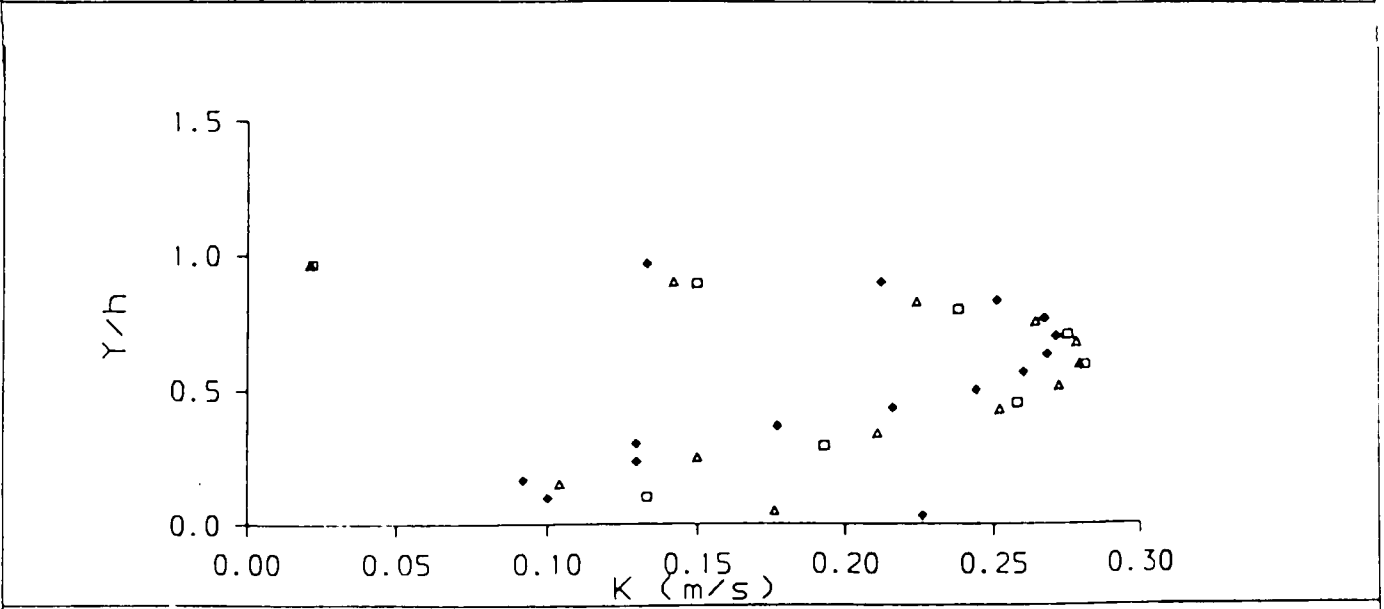
Figure (4.45-c)   K : PROFILES AT (X/h =0.967 & Z/d =0.967)

a) d = h

$\ell_r = 2.05 h$

b) d = 2h

$\ell_r = 2.15 h$
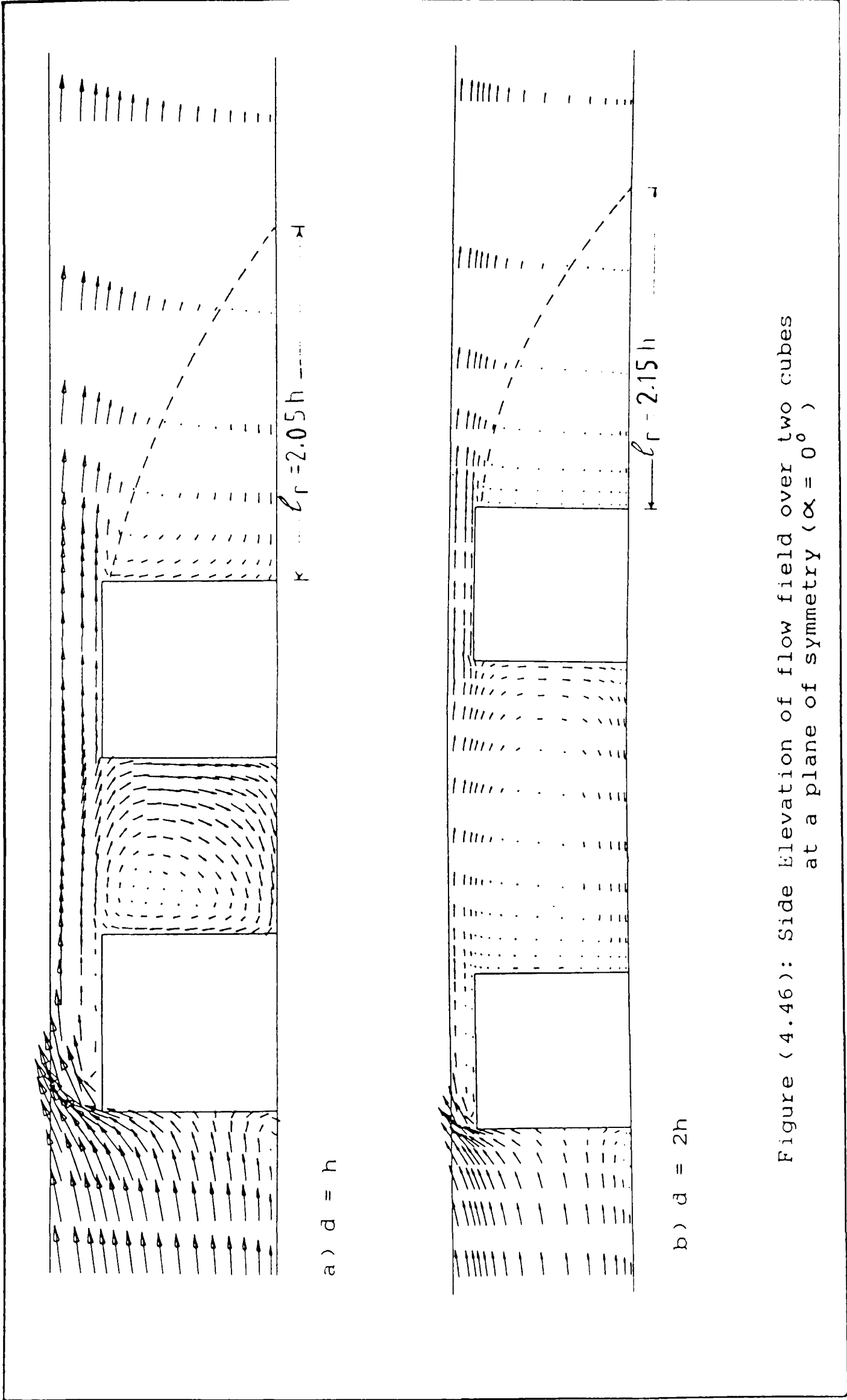
Figure (4.46): Side Elevation of flow field over two cubes
at a plane of symmetry ($\alpha = 0^\circ$)

176
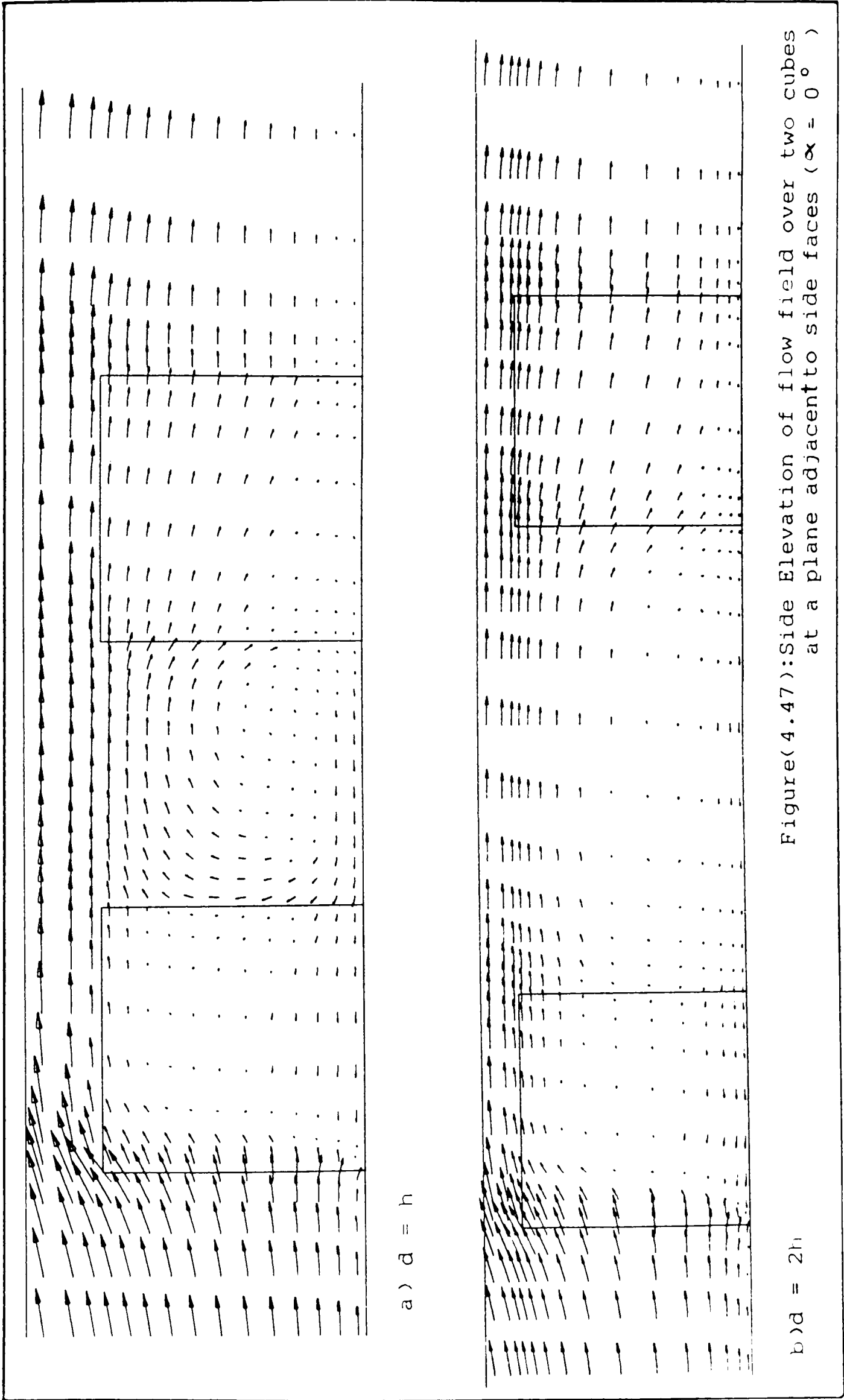
Figure(4.47):Side Elevation of flow field over two cubes at a plane adjacent to side faces ($\alpha = 0°$)

a) d = h
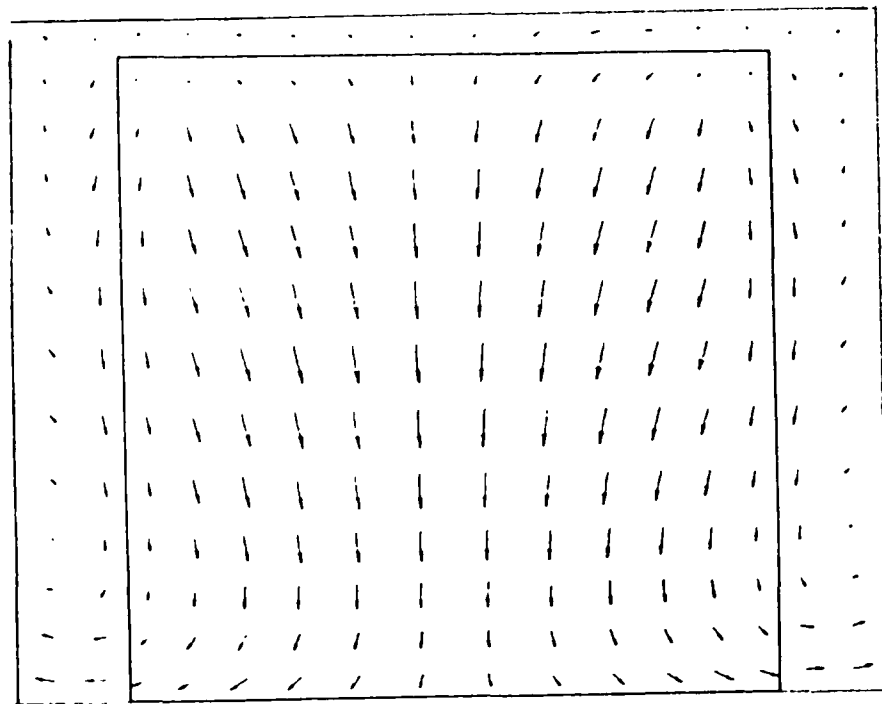
b)d = 2h

a) d = h
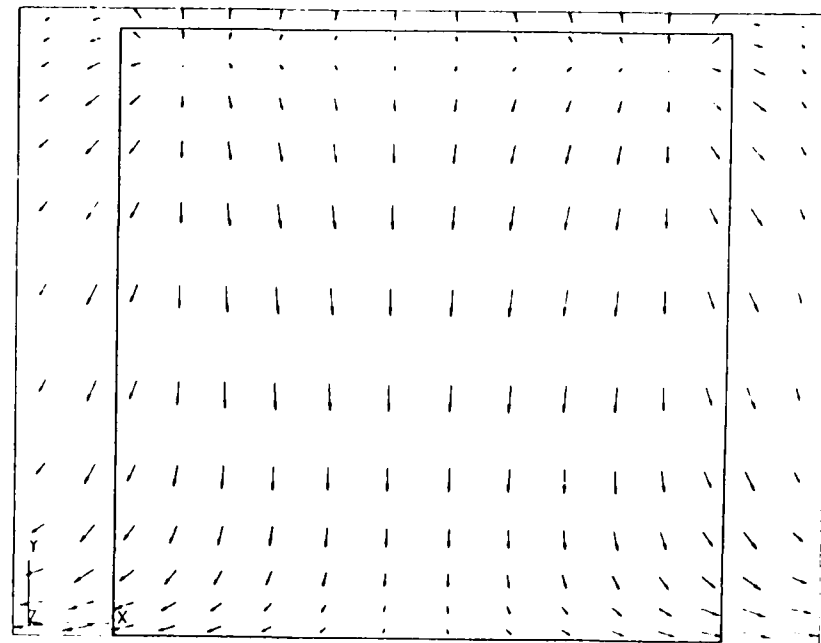
b)d = 2h

Figure(4.48):   End Elevation of flow field over the front
face of the downstream cube (∝ = 0°)
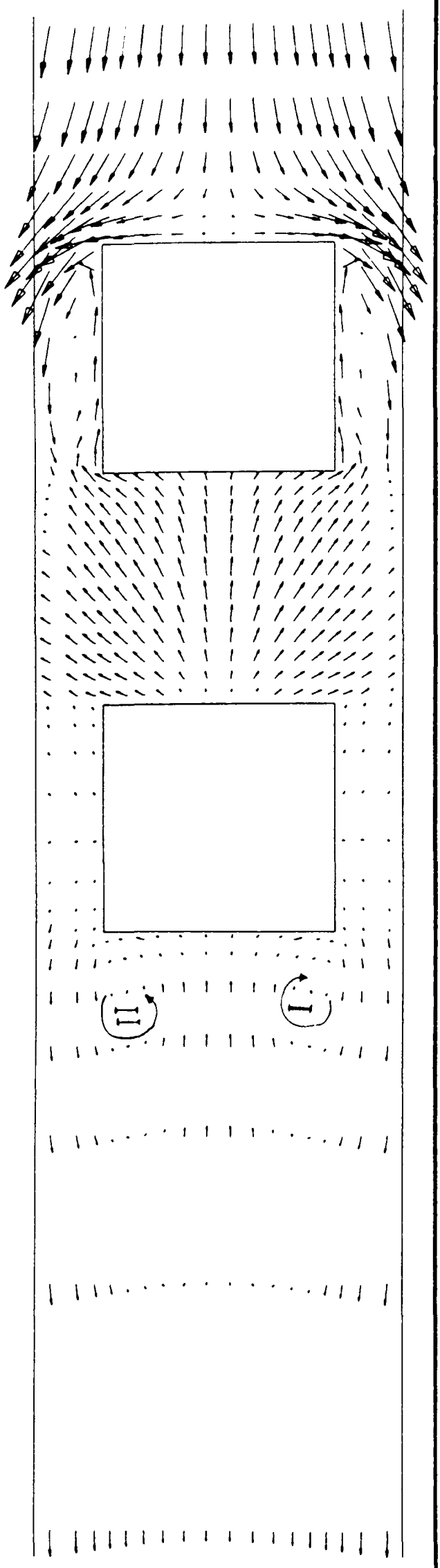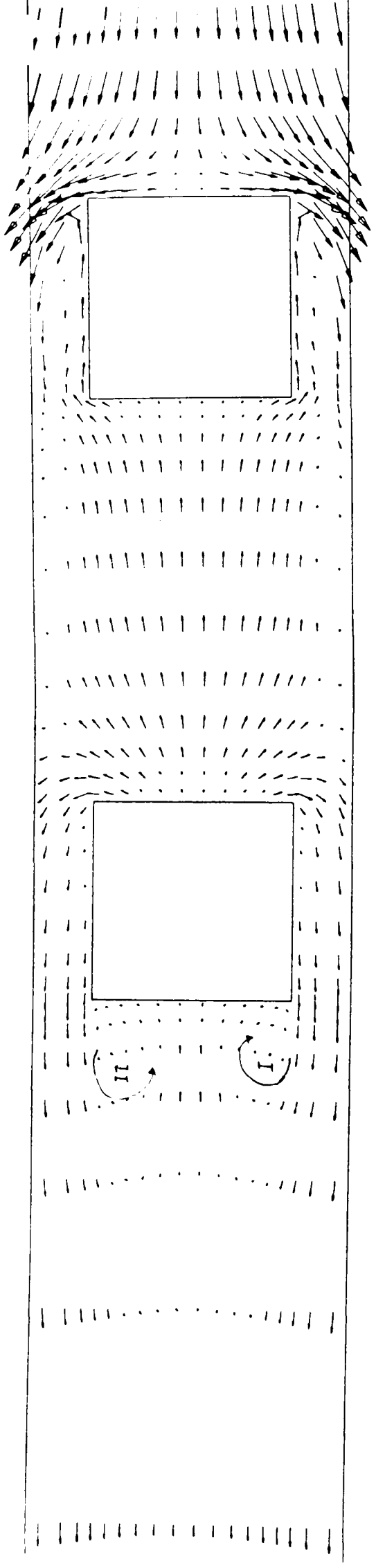
Figure(4.49): Top view of flow field over two cubes near the floor ($\alpha = 0°$)

a) d = h

b) d = 2h
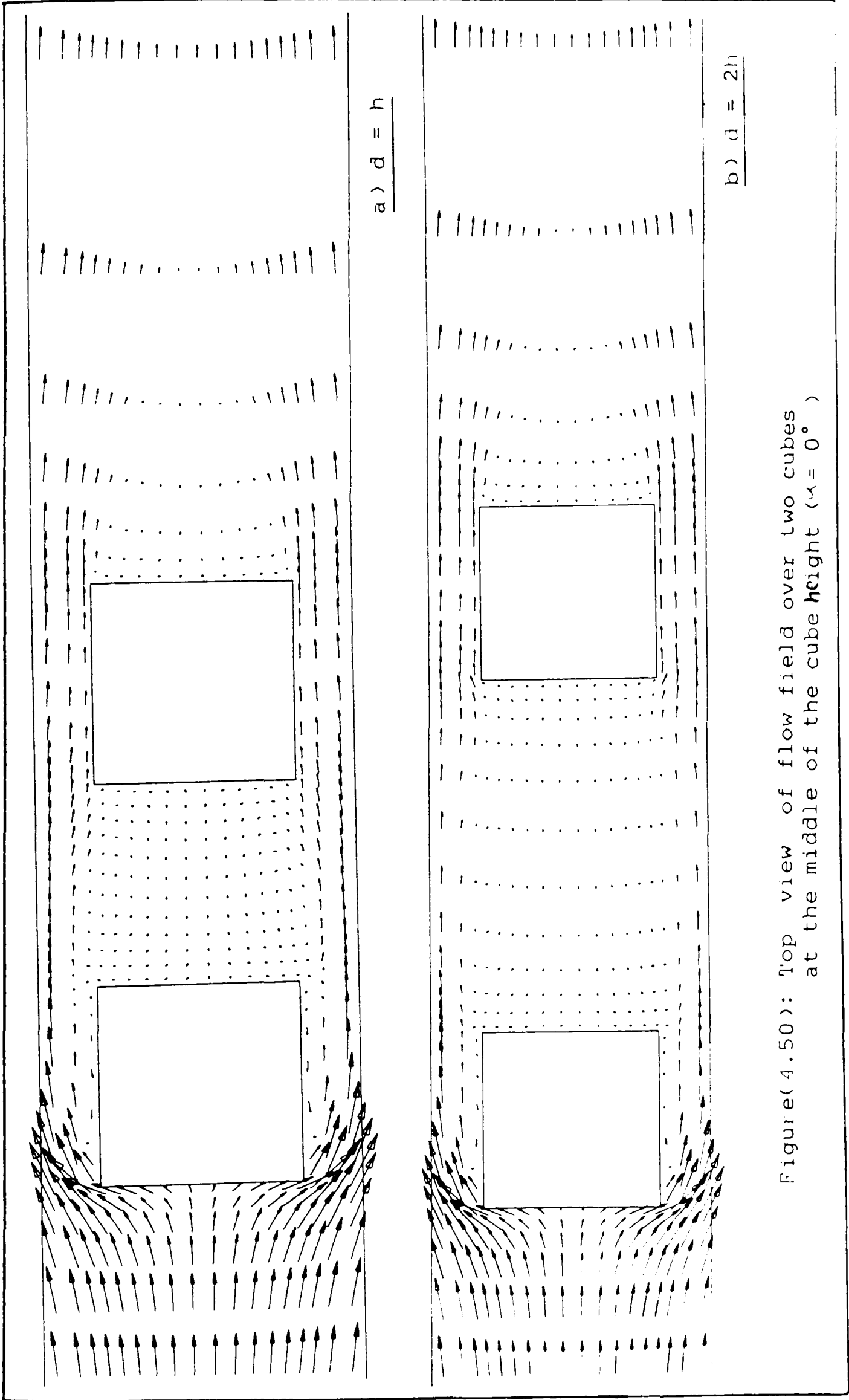
Figure(4.50): Top view of flow field over two cubes at the middle of the cube height ($\alpha = 0°$)

a) d = h

b) d = 2h

a) d = h

b) d = 2h

Figure(4.51): Top view of flow field over two cubes
near the top (α = 0°)
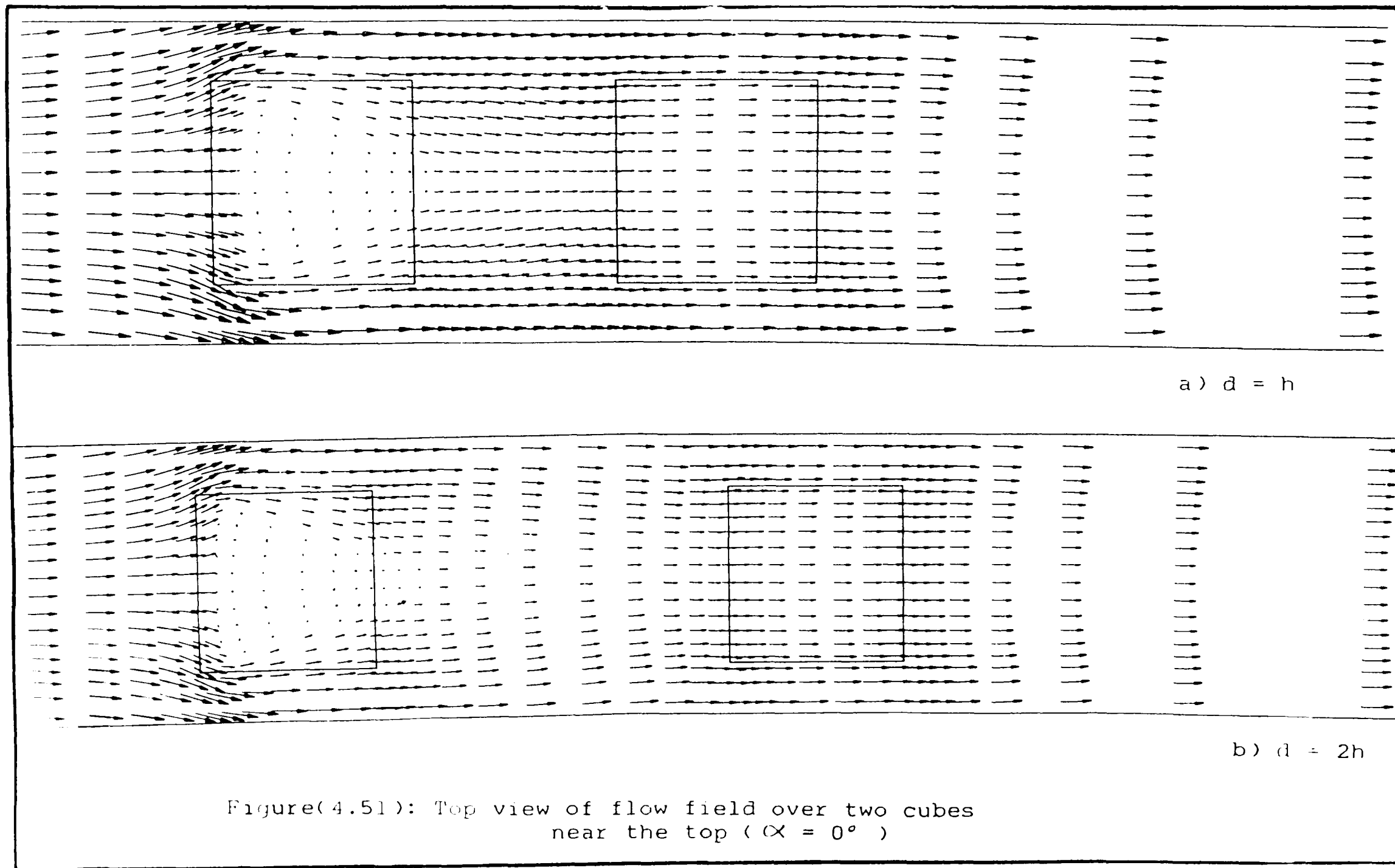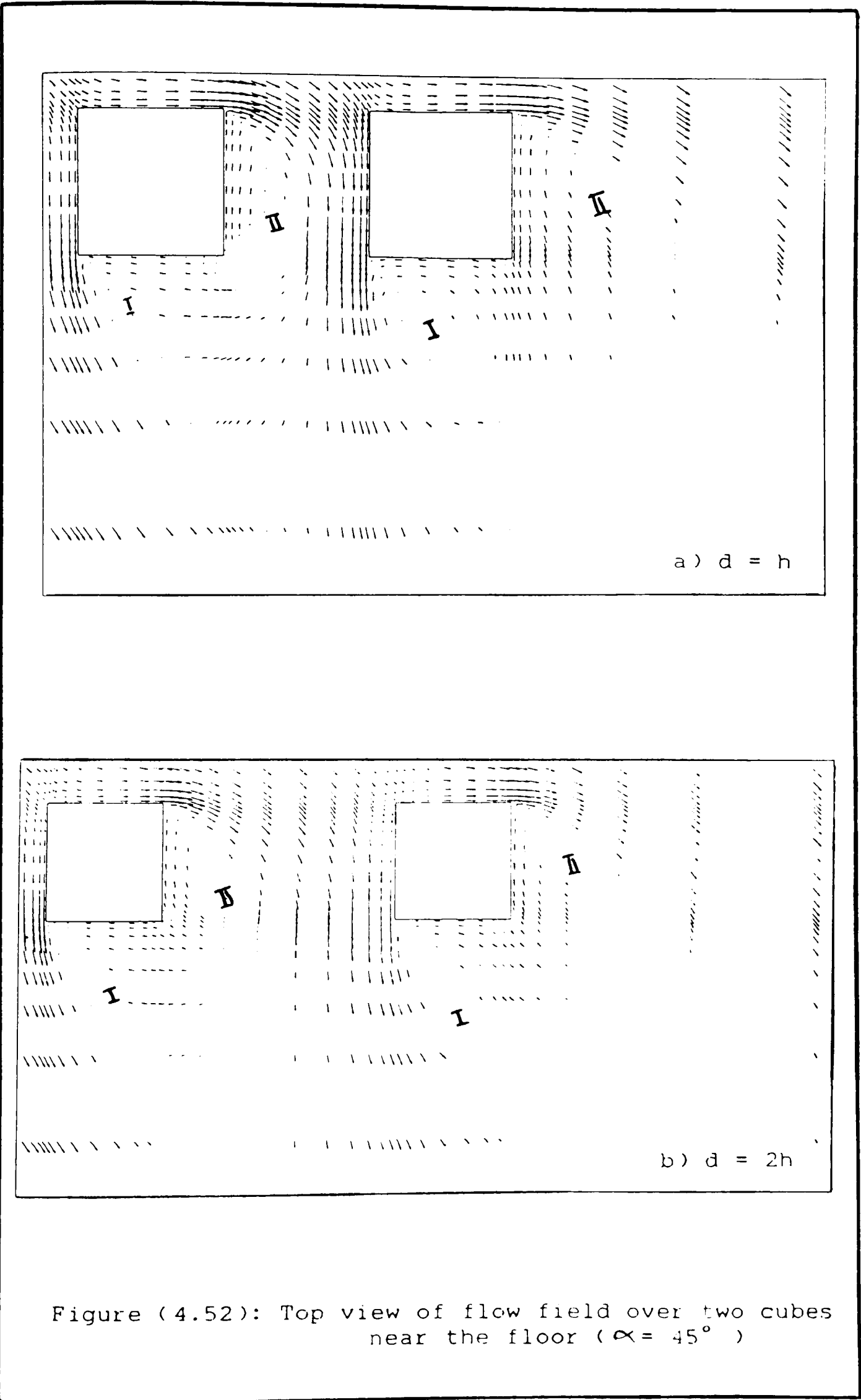
Figure (4.52): Top view of flow field over two cubes near the floor ($\alpha = 45°$)
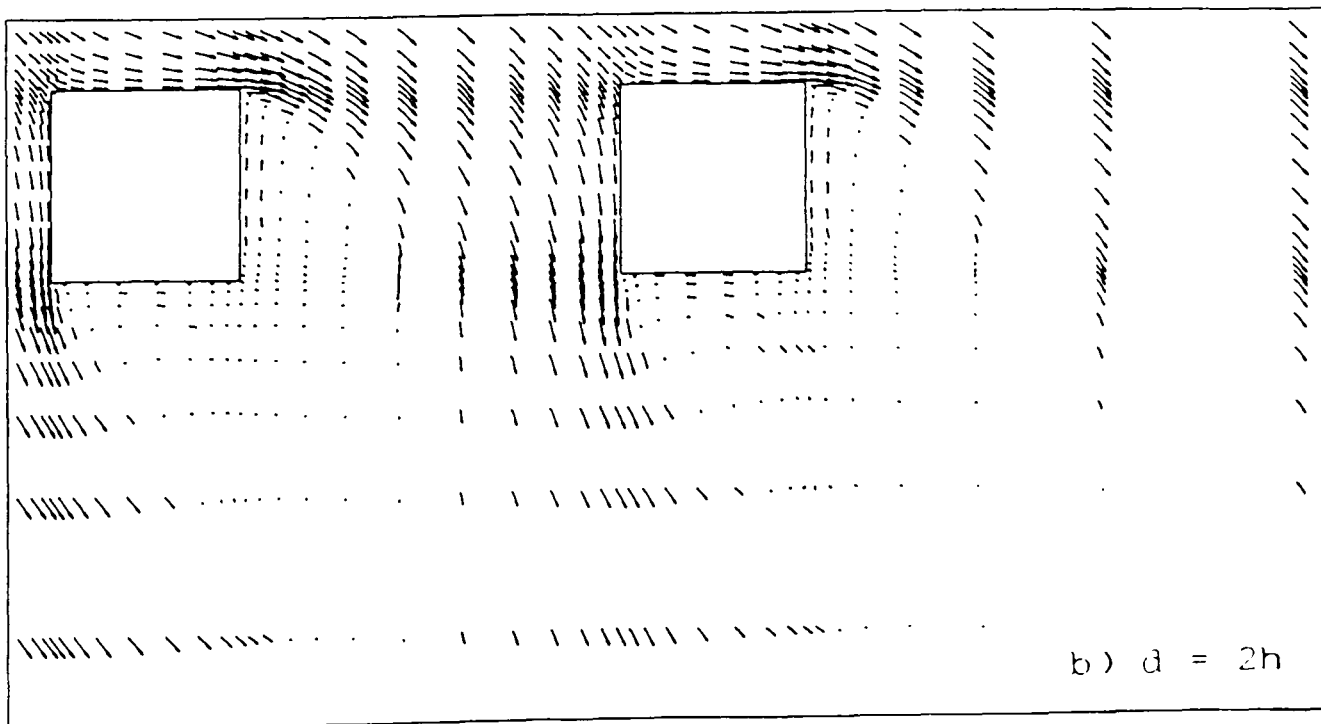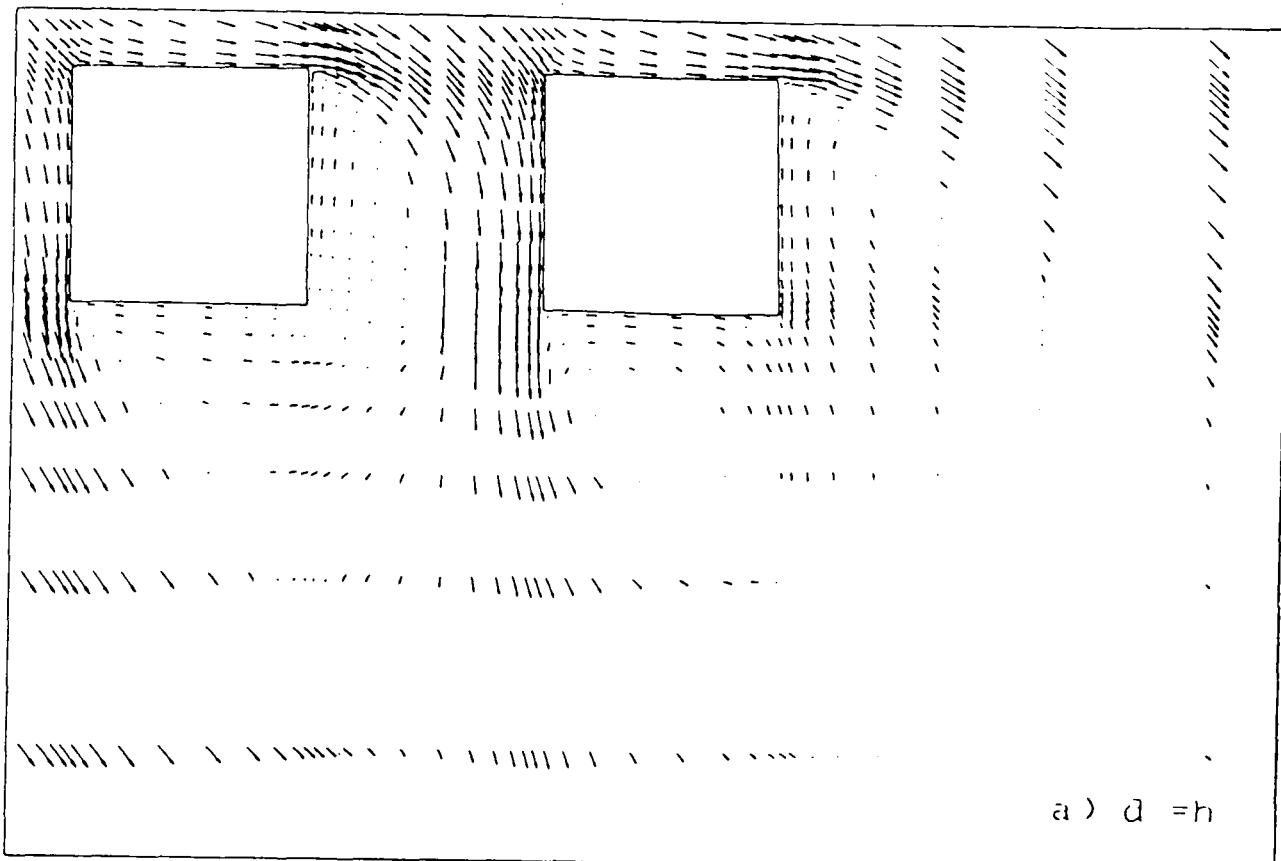
Figure (4.53): Top view of flow field over two cubes at y/h=0.250 (α = 45°)

183

a) d = h
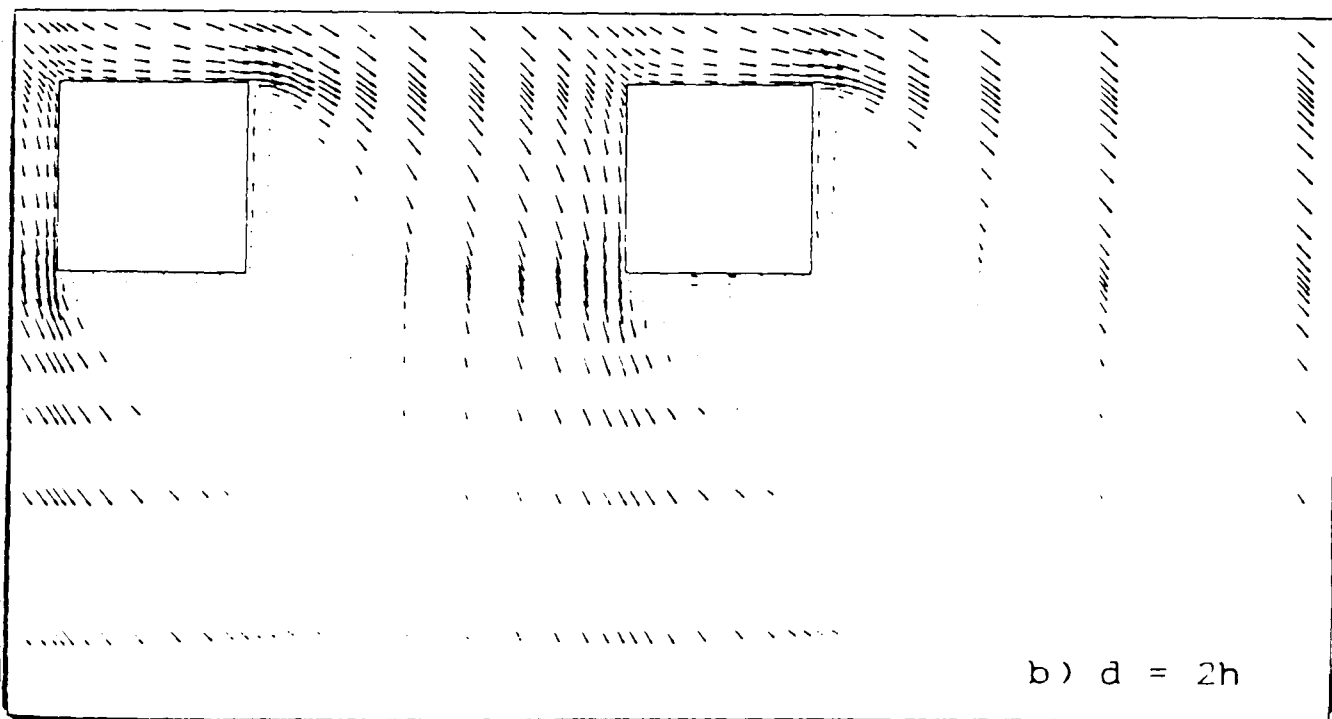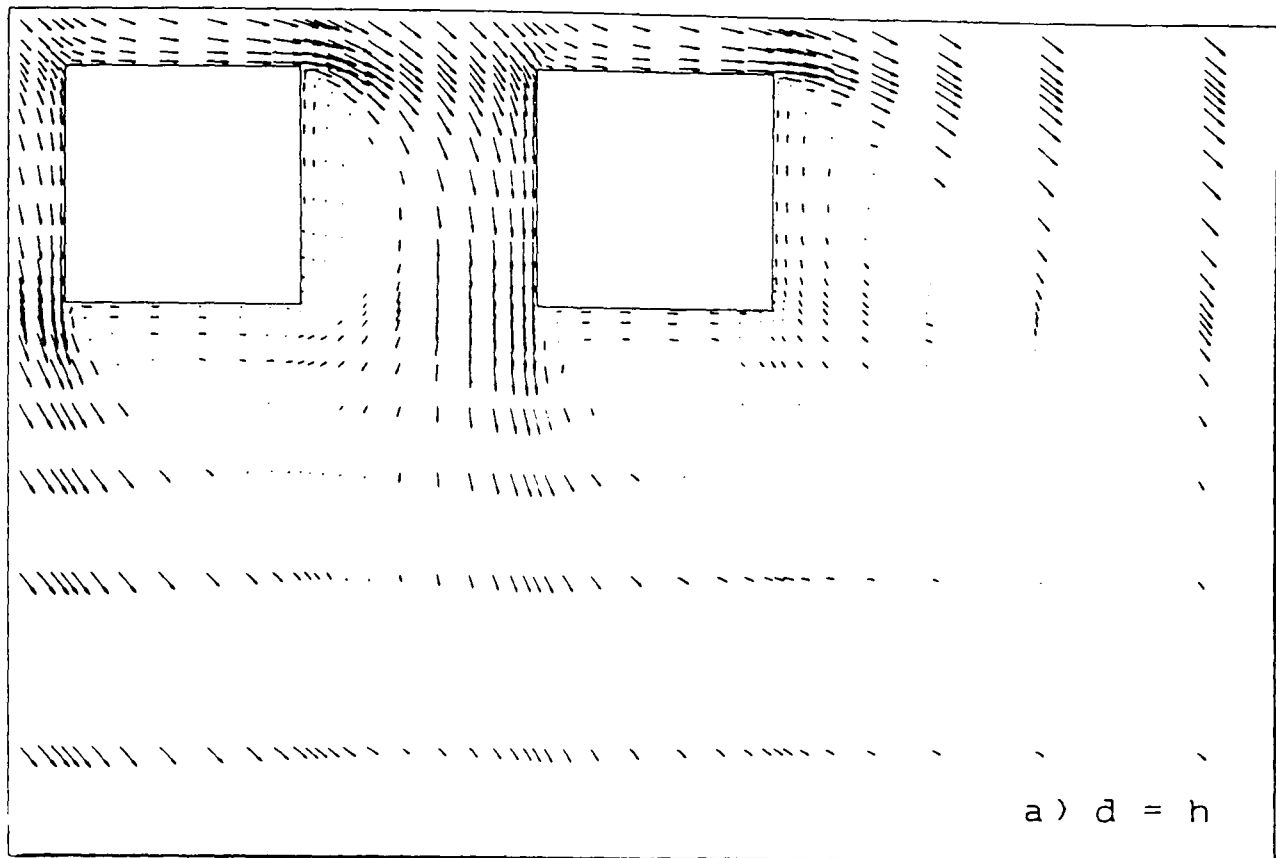
b) d = 2h

Figure (4.54): Top view of flow field over two cubes
at y/h=0.50 (α = 45°)

a) d = h
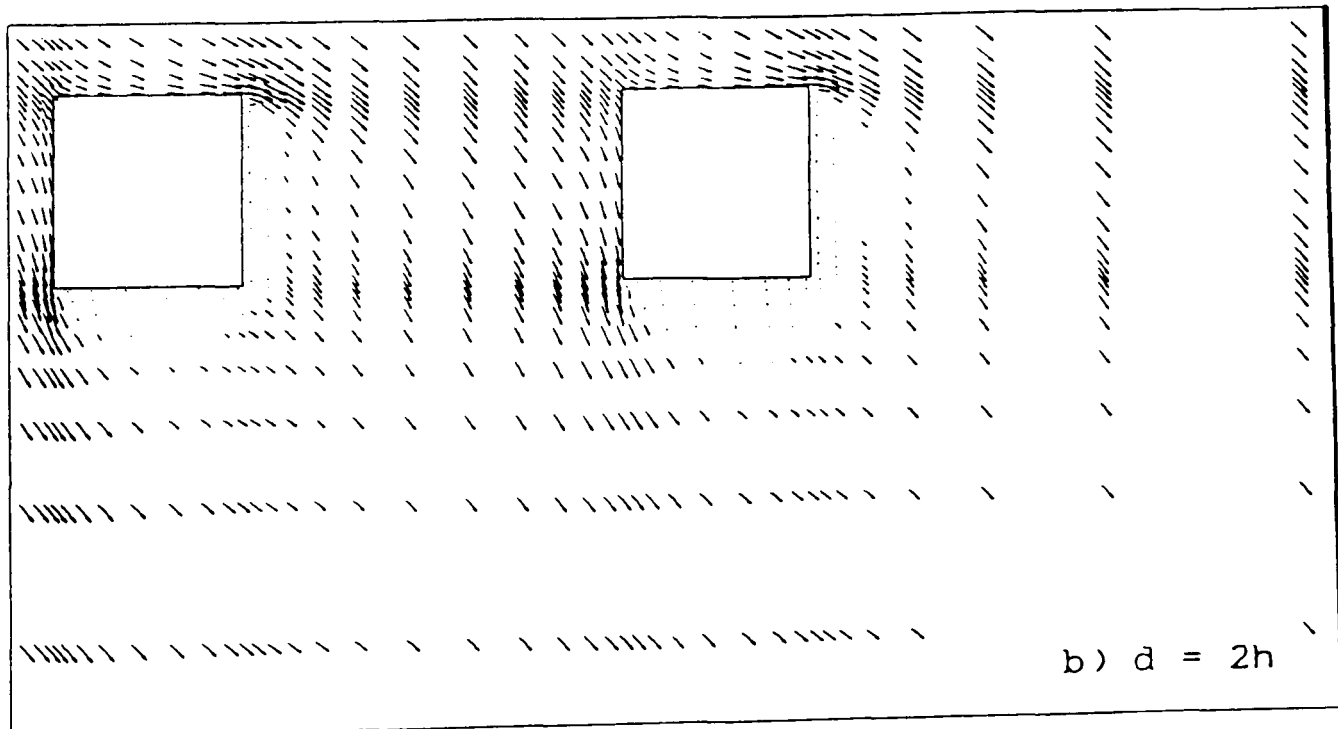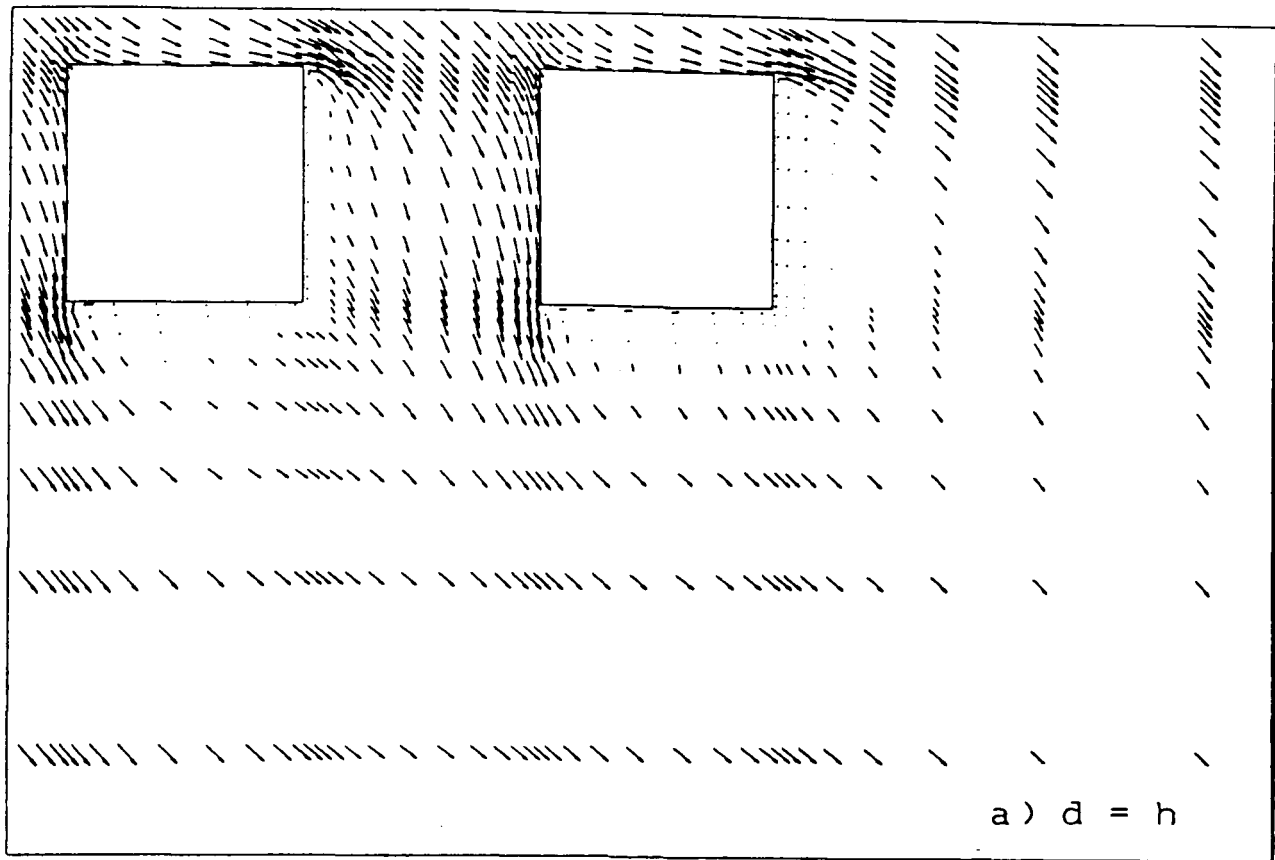
b) d = 2h

Figure (4.55): Top view of flow field over two cubes at y/h = 0.96 (α = 45°)
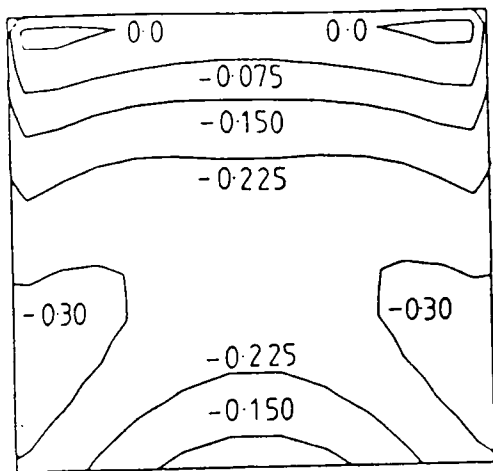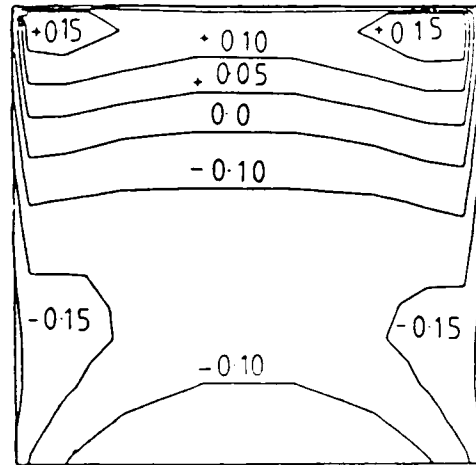
a) d = h   b) d = 2h

Figure(4.56-a):

Surface pressure contours over the front
face of the shielded cube (α = 0°)
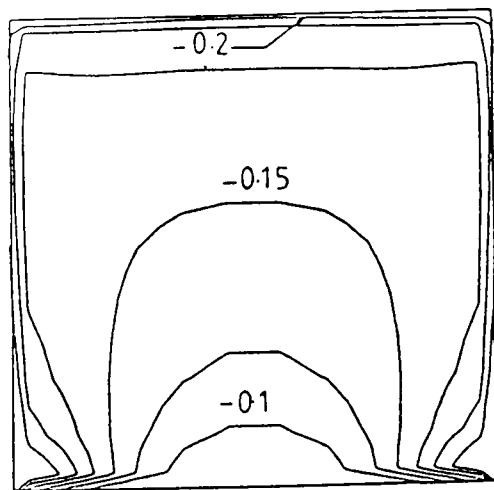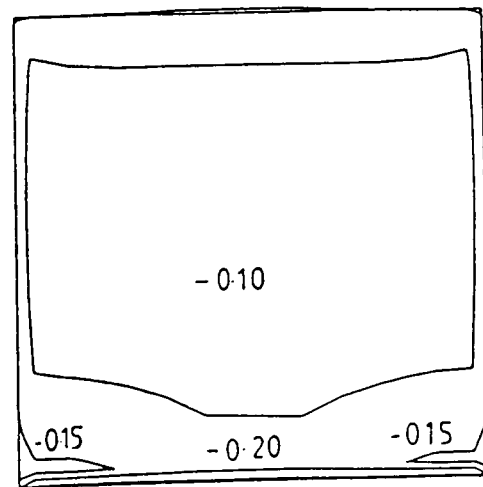
a)d = h   b) d = 2h

WIND

Figure(4.56-b):

Surface pressure contours over the top
face of the shielded cube (α = 0°)

186
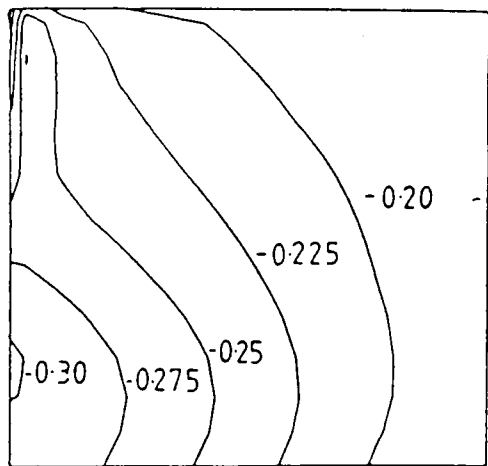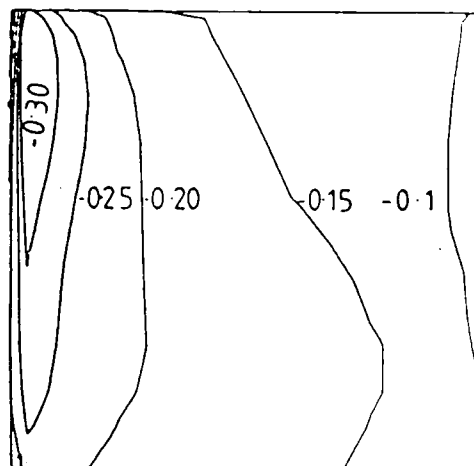
a) d = h   b) d = 2h

Figure(4.57-a):

    Surface   pressure contours over the   side
    face of the shielded cube (α = 0°)
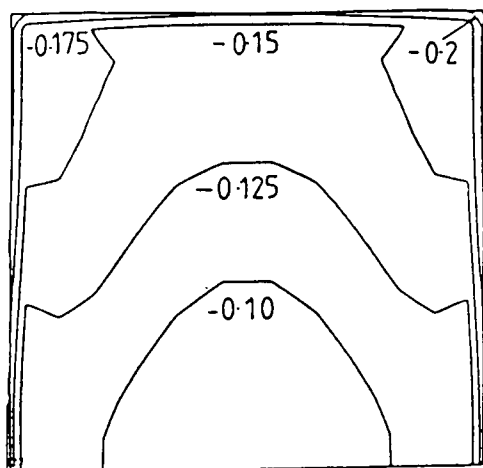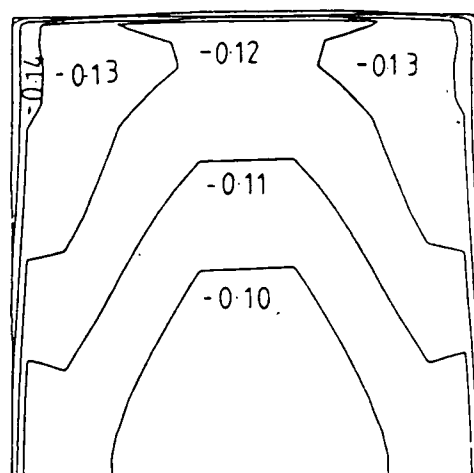
a) d = h   b) d = 2h

Figure(4.57-b):

    Surface   pressure contours over the   rear
    face of the shielded cube (α = 0°)
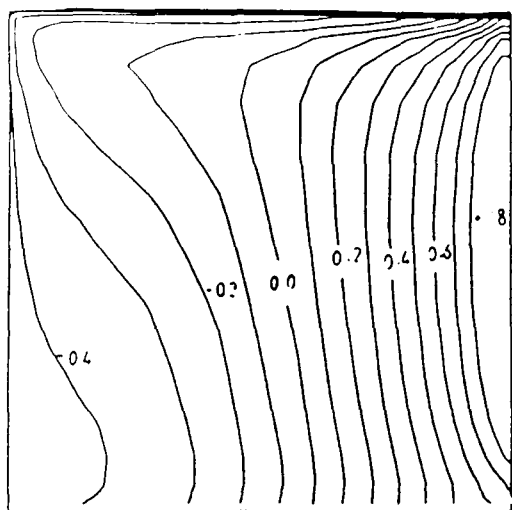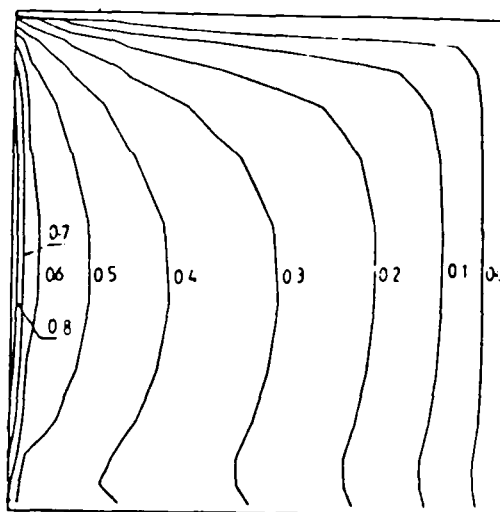
"Shielded front"   "Un-shielded front"

Figure(4.58-a):Surface pressure contours over the front
faces of the downwind cube (α =45°, d=h)
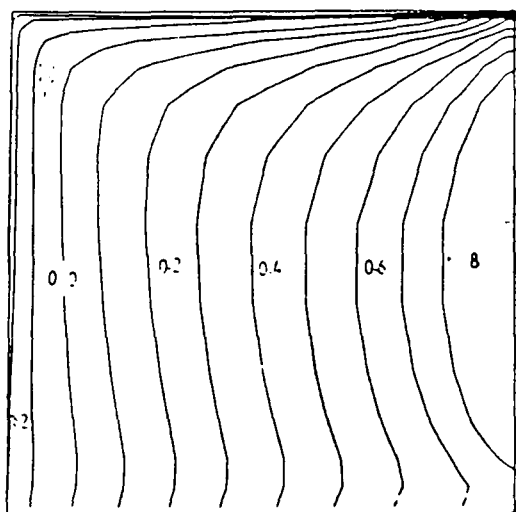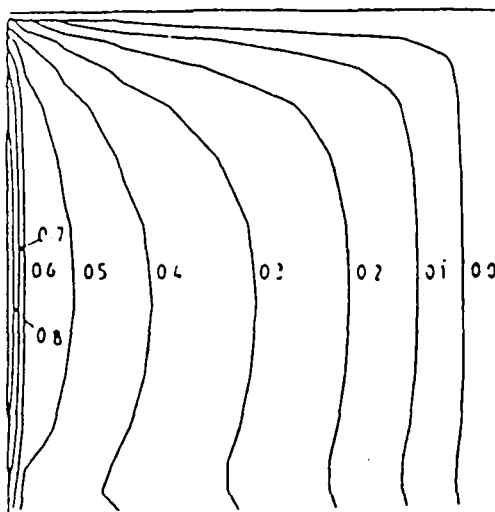
" Shielded front"   " Un-shielded front"

Figure(4.58-b):Surface pressure contours over the front
faces of the downwind cube (α =45° ,d=2h)

face "B"   face "A"
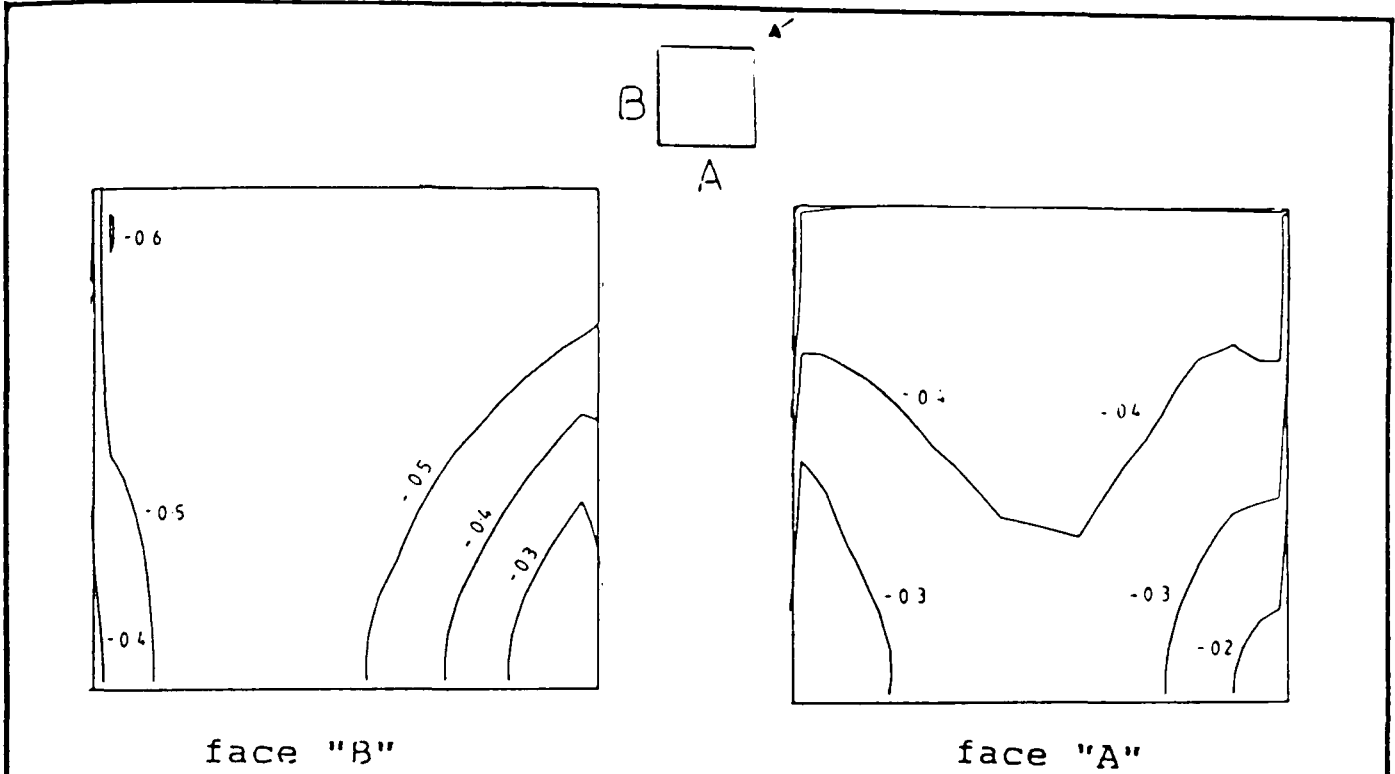
Figure(4.59-a):Surface pressure contours over the rear
faces of the downwind cube ($\propto$ =45°, d=h)

face "A"

face "B"
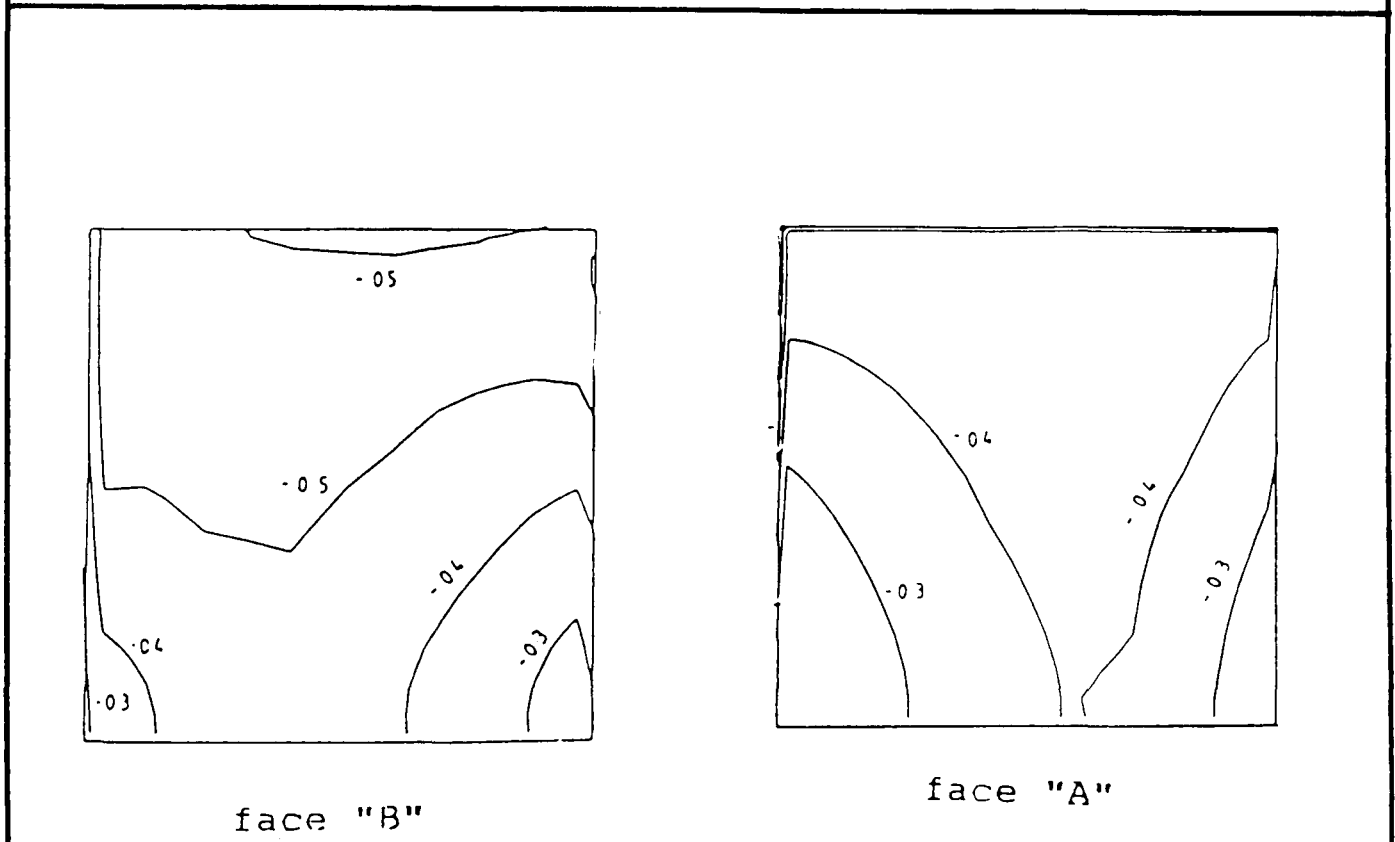
Figure(4.59-b):Surface pressure contours over the rear
faces of the downwind cube ($\propto$ = 45°,d=2h)

a) d = h

"Shielded side"

-0.4
-0.5
-0.6 -0.7
-0.8
-0.9 -1

"Un-shielded side"

WIND

b) d = 2h

"Shielded side "

-0.4
-0.5
-0.6
-0.7
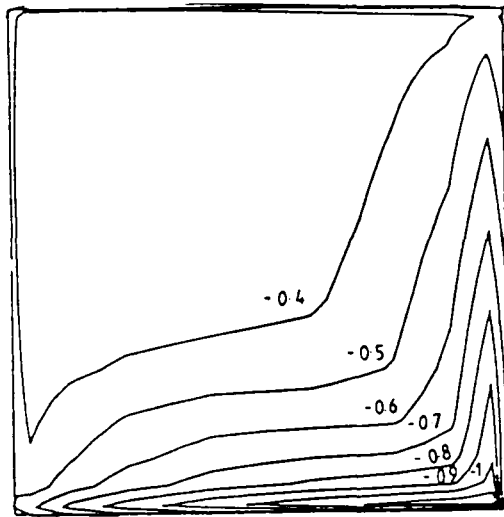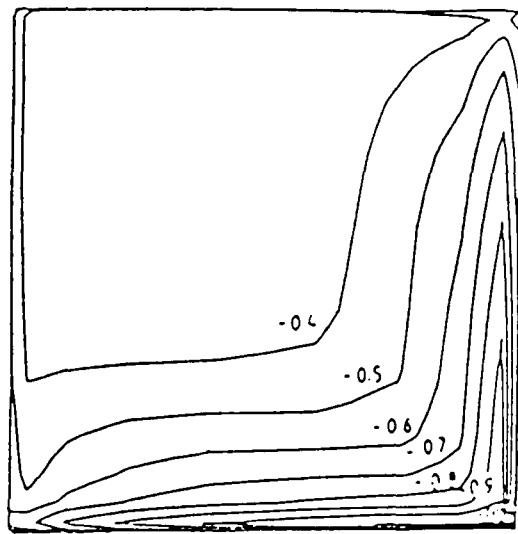
"Un-shielded side"

WIND

Figure(4.60): Surface pressure contours over the top
faces of the downwind cube (α =45°)
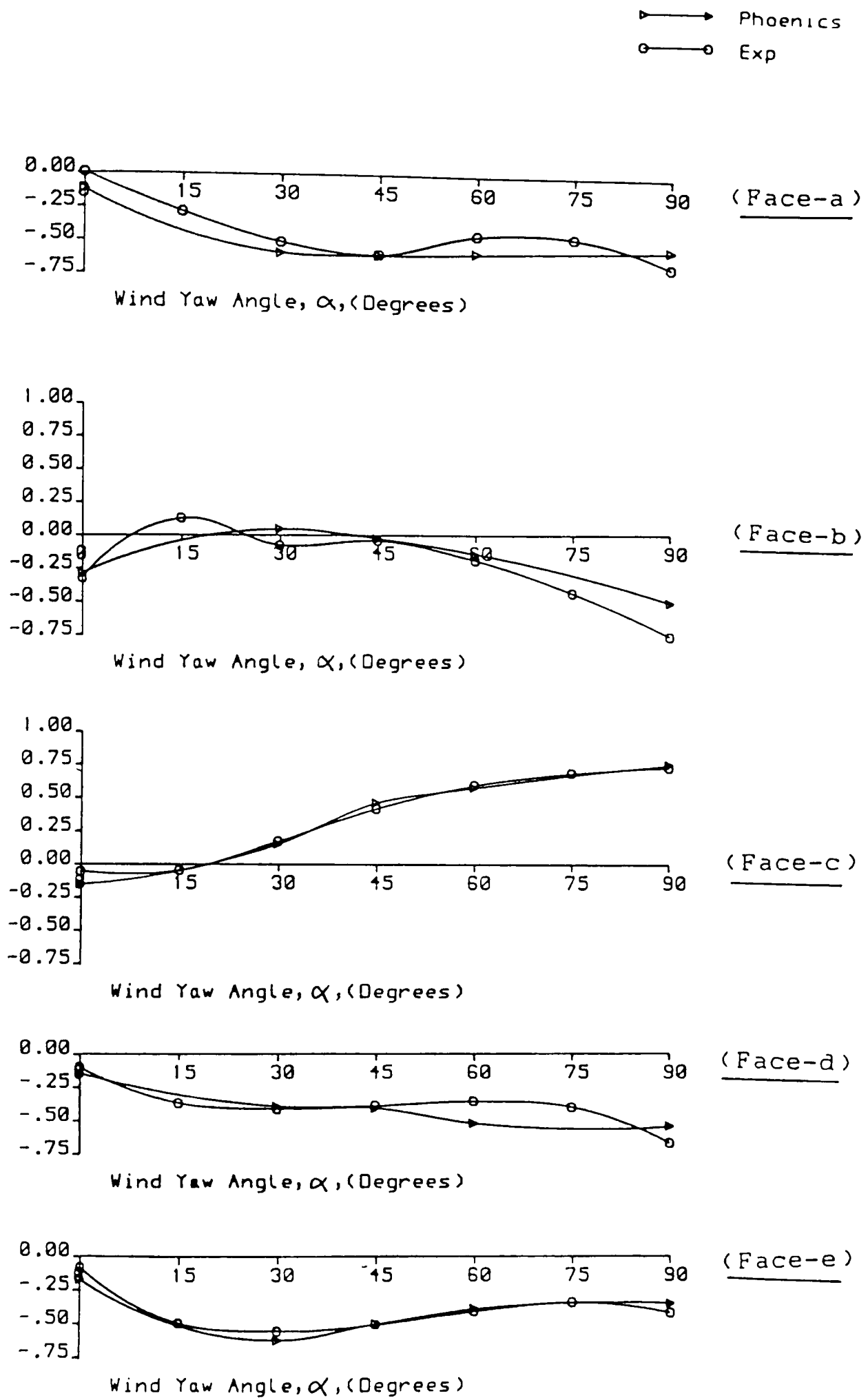
Figure(4.61):

Variation of the average pressure coefficient on a complete face of the shielded cube with wind yaw angle (d=h)

191
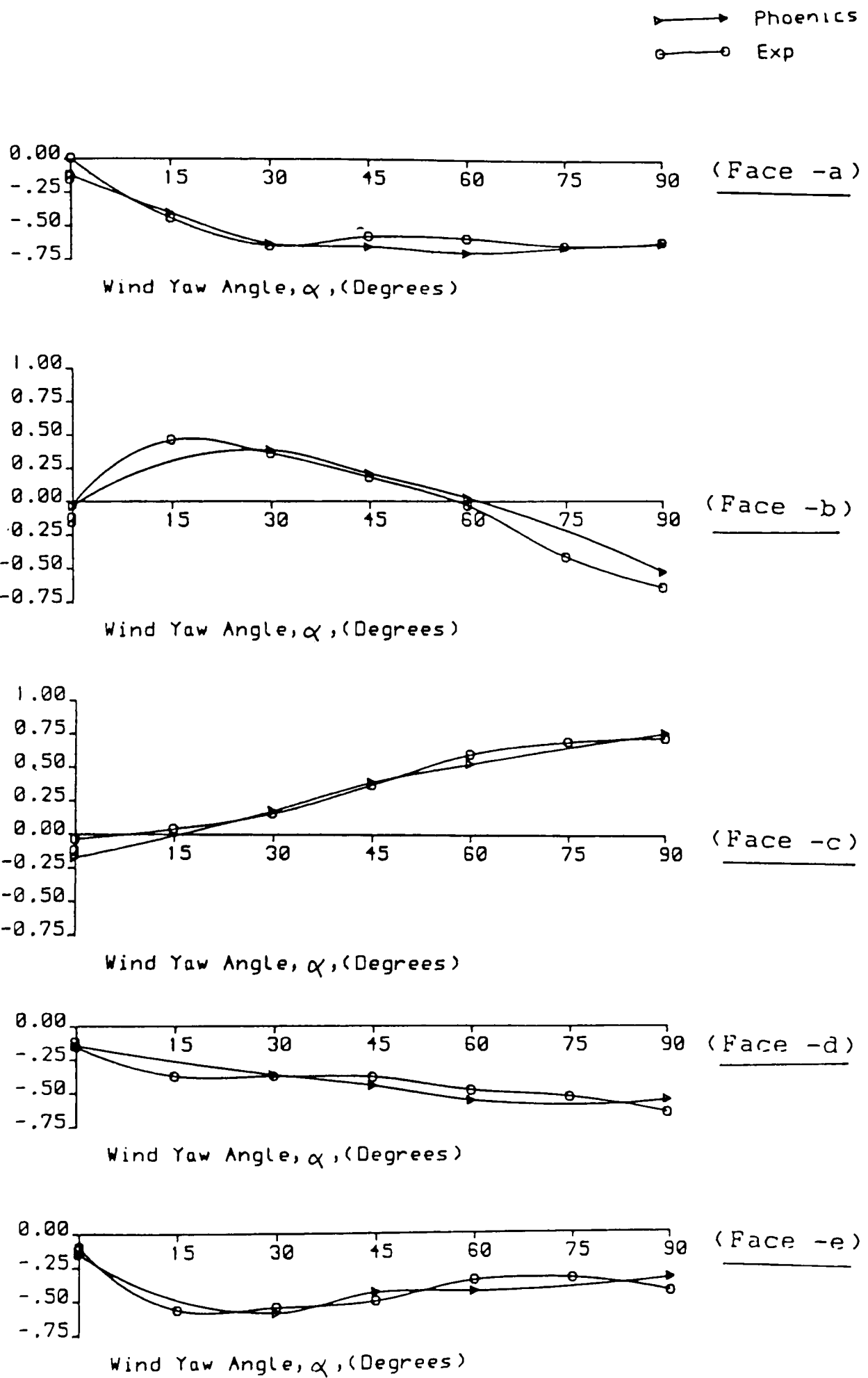
Figure(4.62):

Variation of the average pressure coefficient on a complete face of the shielded cube with wind yaw angle (d = 2h)

(Based on PHOENICS   prediction of Cp)

C_p

-1.0

-0.5

0.0

Rear Surface

R_e =   .206E 6

α =   0 degrees

Cavity space (d = h)

C_p

-1.0

-0.5

0.0

Top Surface

Left Side

C_p

-1.0

-0.5

0.0

Front Surface

Right Side

FORCE COEFFICIENTS
Body Axis System
C_x =-0.138
C_y = 0.000
C_z = 0.117
Wind Axis System
C_d =-0.138
C_c = 0.000
C_l = 0.117

193
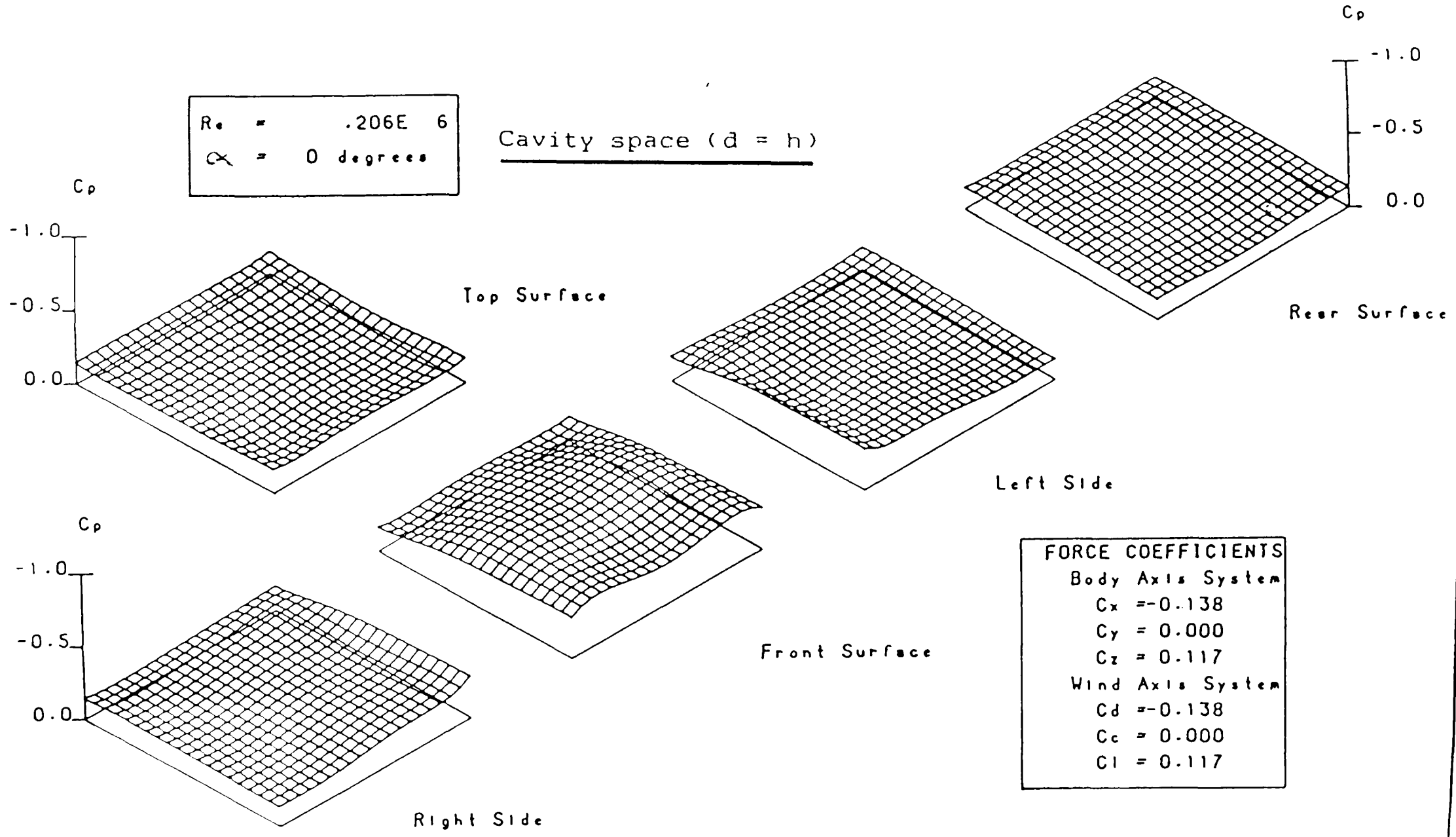
Figure 4.64) ISOMETRIC VIEW OF PREDICTED PRESSURE COEFFICIENT DISTRIBUTION OVER SHIELDED RECTANGULAR BOX

(Based on Wind Tunnel measurements of Cp)

Cavity space (d = h)

Re = .201E 6
α = 0 degrees

FORCE COEFFICIENTS
Body Axis System
Cx =-0.219
Cy = 0
Cz =-0.007

Wind Axis System
Cd =-0.219
Cs = 0.050
Cℓ =-0.002

Rear Surface

Left Side

Front Surface

Top Surface

Right Side

Cp

Figure 6.(b) ISOMETRIC VIEW OF PREDICTED PRESSURE COEFFICIENT DISTRIBUTION OVER SHIELDED RECTANGULAR BOX.

(Based on PHOENICS prediction of Cp)

Cavity space (d = 2h)

Re = .206E 6
α = 0 degrees

Cp
-1.0
-0.5
0.0

Rear Surface

Left Side

Top Surface

Front Surface

Right Side

FORCE COEFFICIENTS
Body Axis System
Cx = 0.131
Cy = -0.001
Cz = 0.122
Wind Axis System
Cd = 0.131
Cc = -0.001
CL = 0.122

195

ISOMETRIC VIEW OF PREDICTED PRESSURE COEFFICIENT DISTRIBUTION OVER SHIELDED RECTANGULAR BOX

(Based on Wind Tunnel measurements of Cp)

Cp

-1.0
-0.5
0.0

Rear Surface

Cavity space (d = 2h)

Left Side

FORCE COEFFICIENTS

Body Axis System
Cx = 0.130
Cy = 0.042
Cz = 0.008

Wind Axis System
Cd = 0.130
Cc = 0.042
Cl = 0.008

Front Surface

Top Surface

Re   =   .201E 6
α   =   0 degrees

Cp

-1.0
-0.5
0.0

Right Side

Cp

-1.0
-0.5
0.0

196
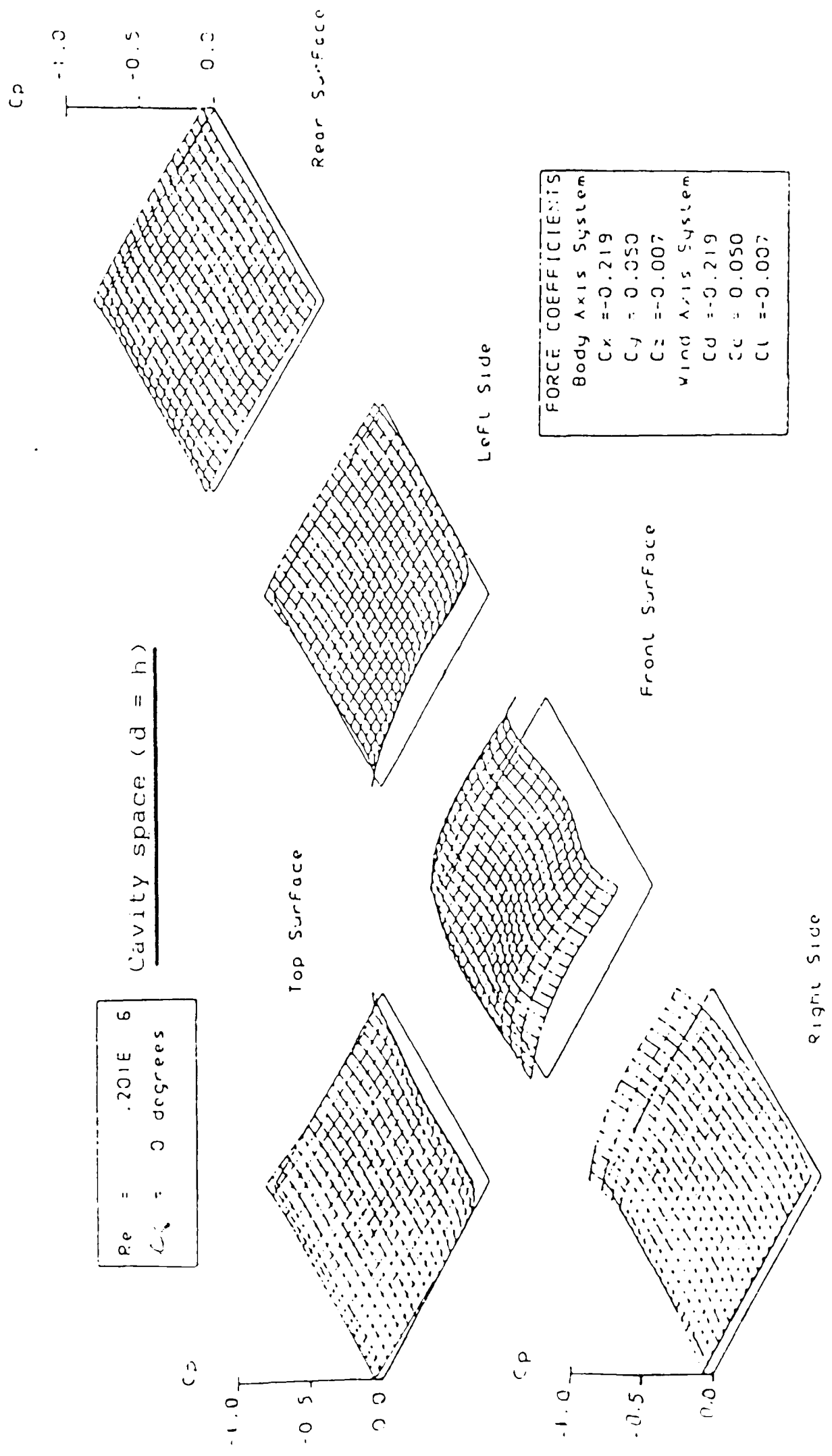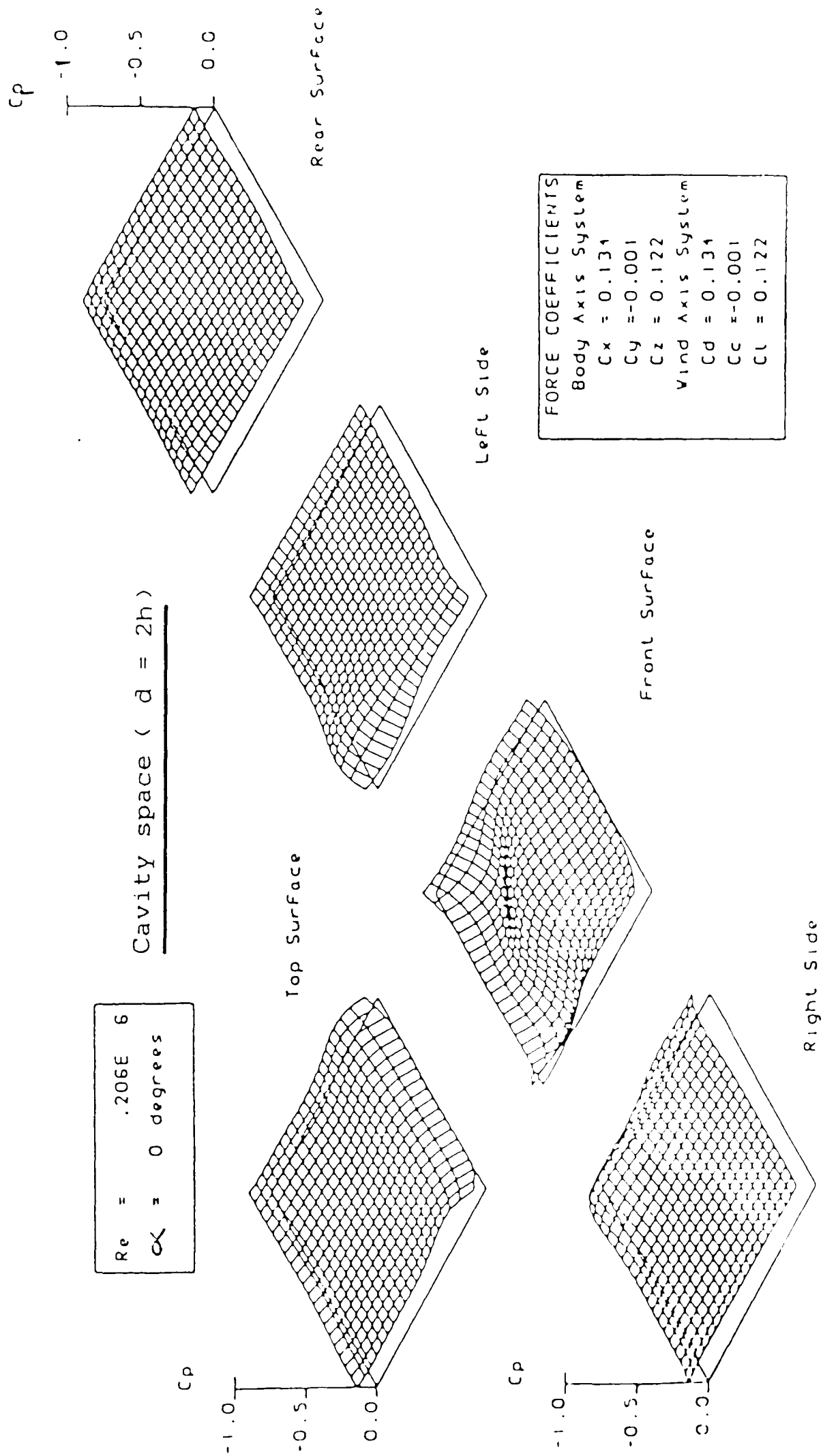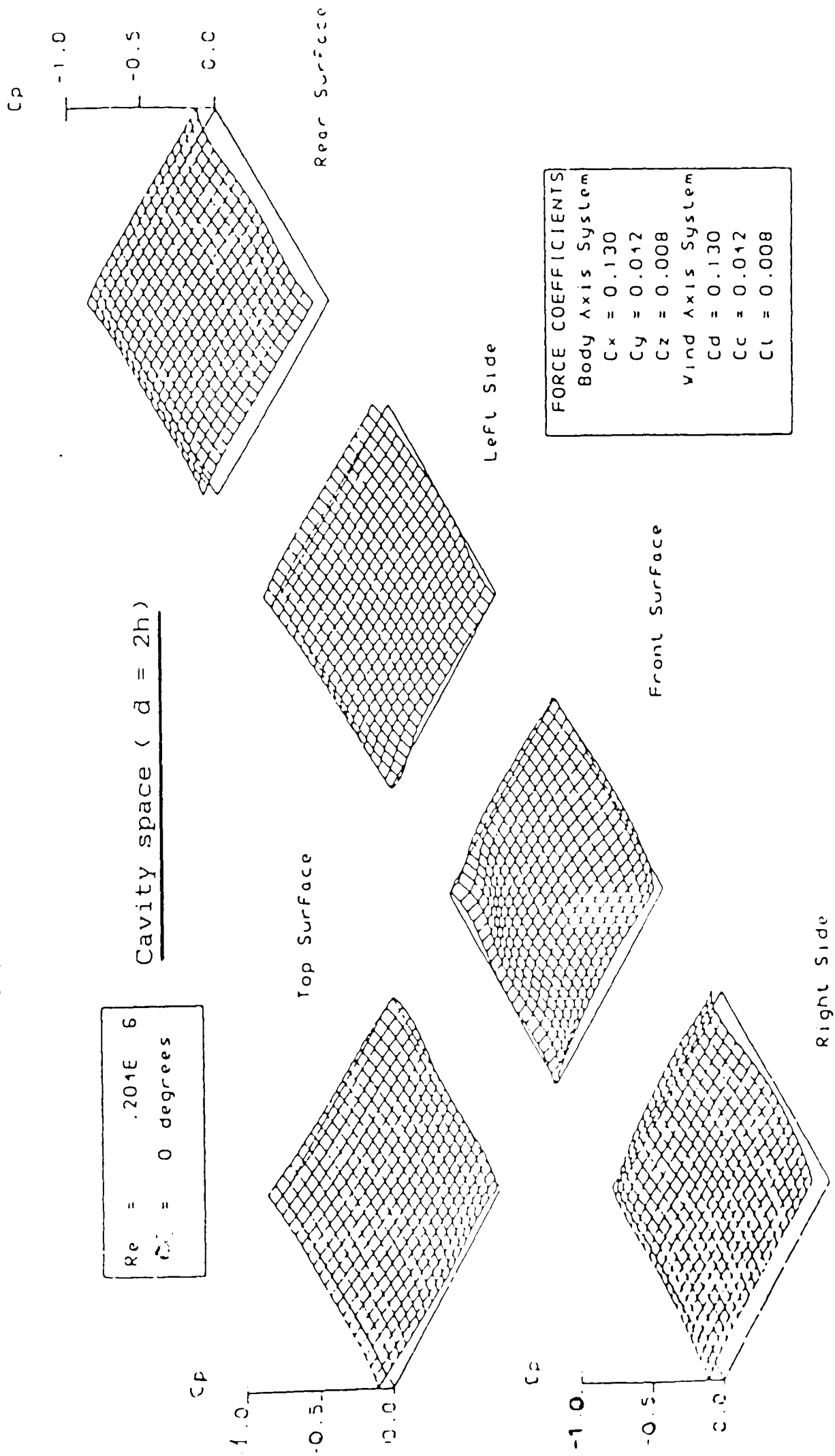
(Figure 4.67) ISOMETRIC VIEW OF PREDICTED PRESSURE COEFFICIENT DISTRIBUTION OVER   SHIELDED RECTANGULAR BOX.

(Based on PHOENICS prediction of Cp)

Cp

Re   =   .206E 6

α = 45 degrees

Cavity space (d = h)

Cp

−1.0

−0.5

0.0

Top Surface

Rear Surface

Cp

−1.0

−0.5

0.0

Left Side

Front Surface

Right Side

FORCE COEFFICIENTS
Body Axis System
Cx = 0.386
Cy = 0.893
Cz = 0.600
Wind Axis System
Cd = 0.905
Cc = 0.359
Cl = 0.600

197
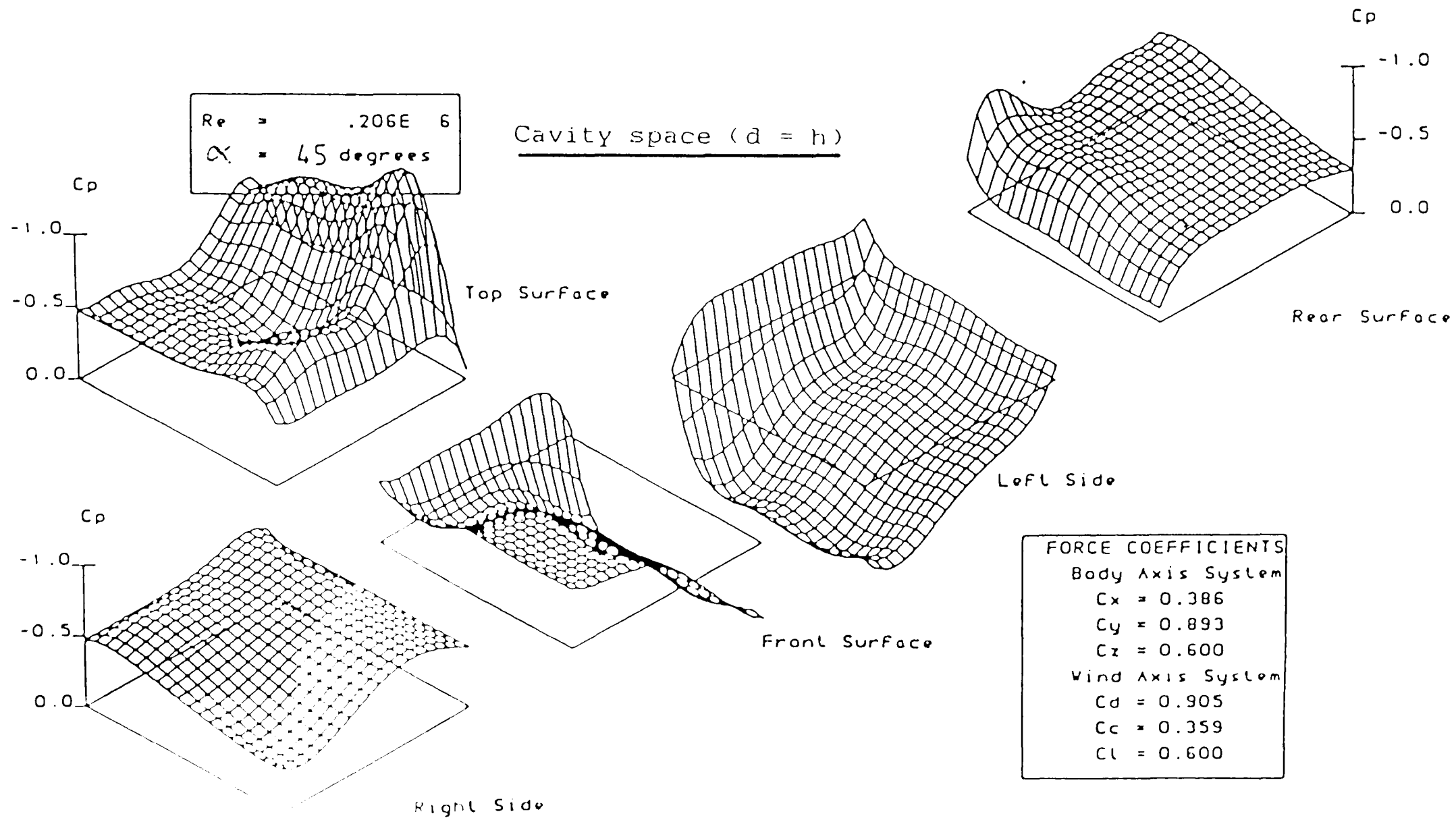
Figure(4.68) ISOMETRIC VIEW OF PREDICTED PRESSURE COEFFICIENT DISTRIBUTION OVER   SHIELDED RECTANGULAR BOX.

(Based on Wind Tunnel measurements of Cp)

R_c = .205E 6

α = 45 degrees

Cavity space (d = h)

Top Surface

Rear Surface

Left Side

Front Surface

Right Side

FORCE COEFFICIENTS
Body Axis System
C_x = 0.349
C_y = 0.879
C_z = 0.596
Wind Axis System
C_d = 0.868
C_c = 0.374
C_i = 0.596

198

(Based on PHOENICS prediction of Cp)

Re = .206E 6
α = 45 degrees

Cavity space (d = 2h)

Cp

-1.0

-0.5

0.0

Rear Surface

Cp

-1.0

-0.5

0.0

Top Surface

Left Side

Cp

-1.0

-0.5

0.0

Front Surface

Right Side

FORCE COEFFICIENTS
Body Axis System
Cx = 0.657
Cy = 0.936
Cz = 0.598
Wind Axis System
Cd = 1.126
Cc = 0.197
Cl = 0.598

199

ISOMETRIC VIEW OF PREDICTED PRESSURE COEFFICIENT DISTRIBUTION OVER   SHIELDED RECTANGULAR BOX.

(Based on Wind Tunnel measurements of Cp)

R_e = .201E 6

α = 45 degrees

Cavity space (d = 2h)

C_p

-1.0

-0.5

0.0

Rear Surface

C_p

-1.0

-0.5

0.0

Top Surface

Left Side

C_p

-1.0

-0.5

0.0

Front Surface

Right Side
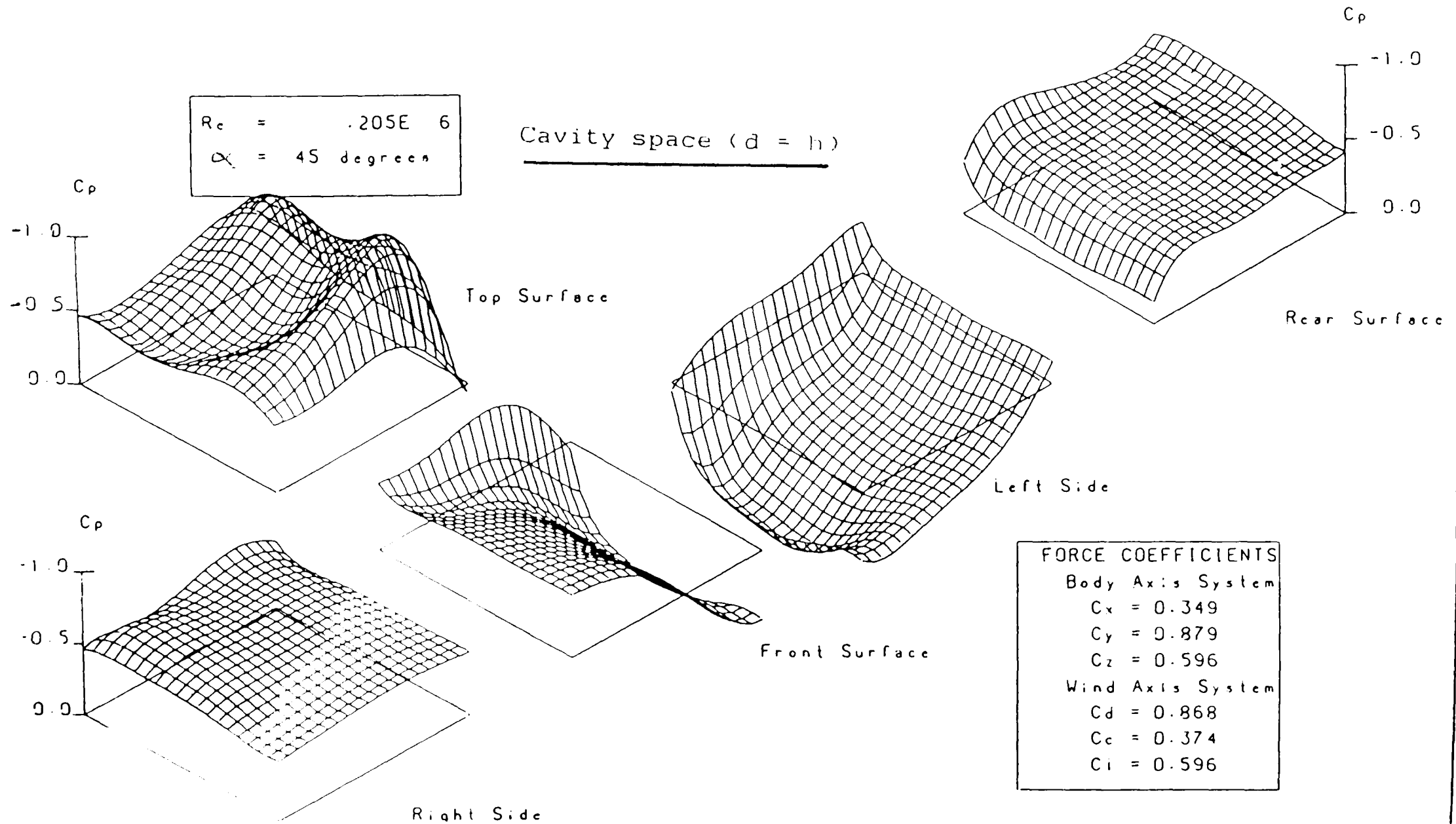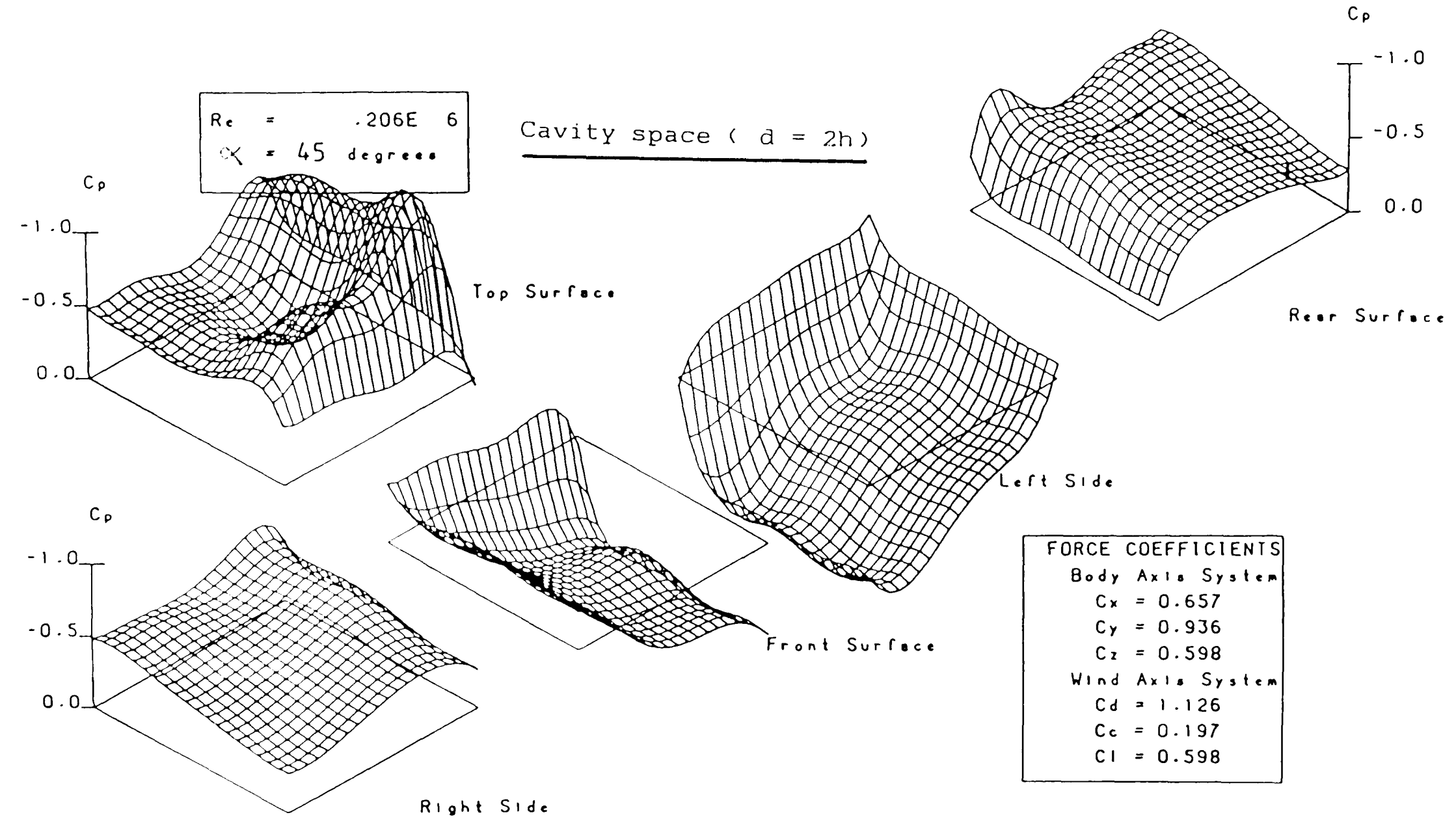
FORCE COEFFICIENTS
Body Axis System
C_x = 0.565
C_y = 0.920
C_z = 0.571
Wind Axis System
C_d = 1.050
C_c = 0.251
C_i = 0.571
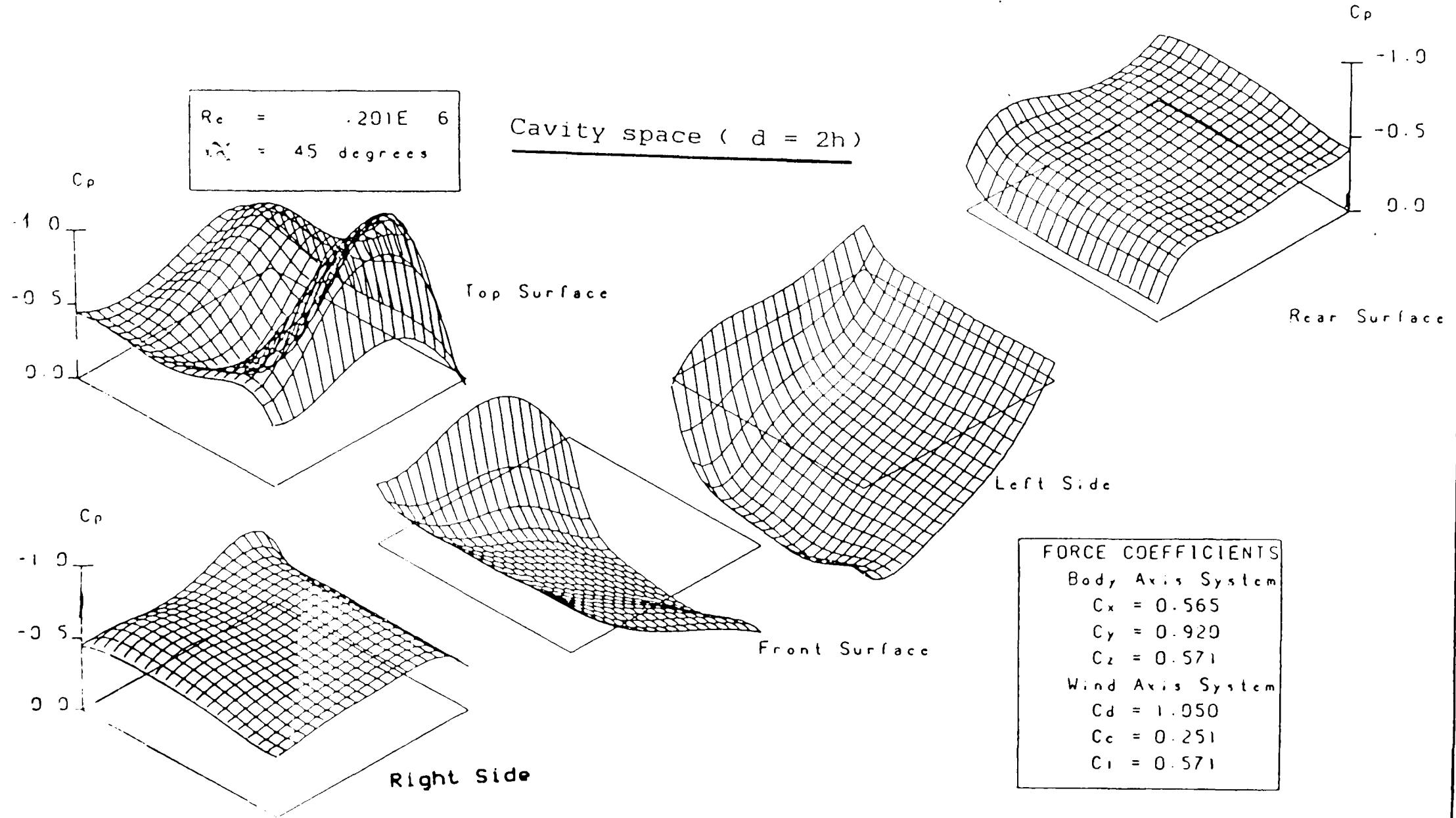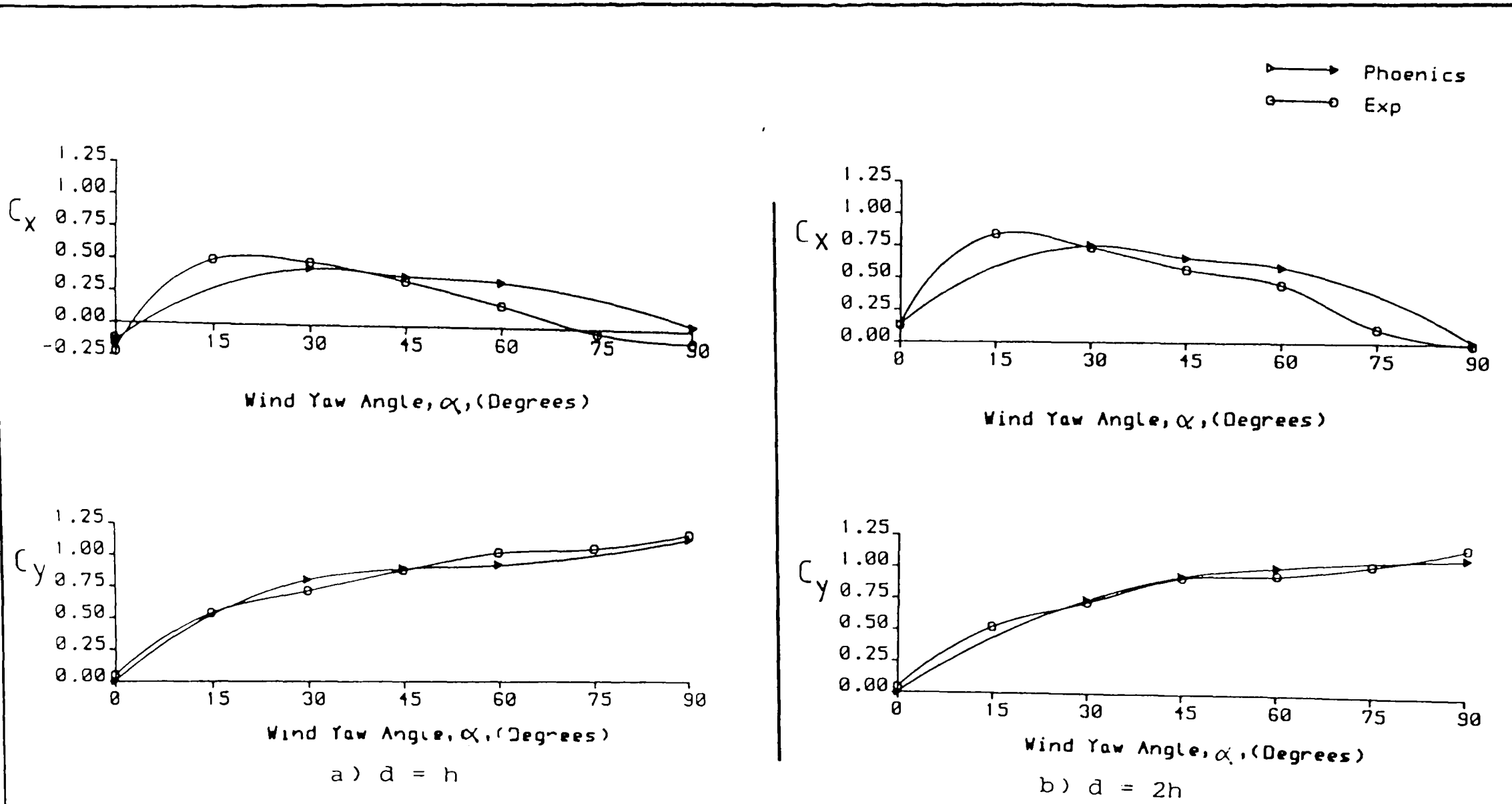
FIGURE(4.71):VARIATION OF THE BODY AXIS FORCE COEFFICIENTS
WITH WIND YAW ANGLE FOR THE SHIELDED CUBE
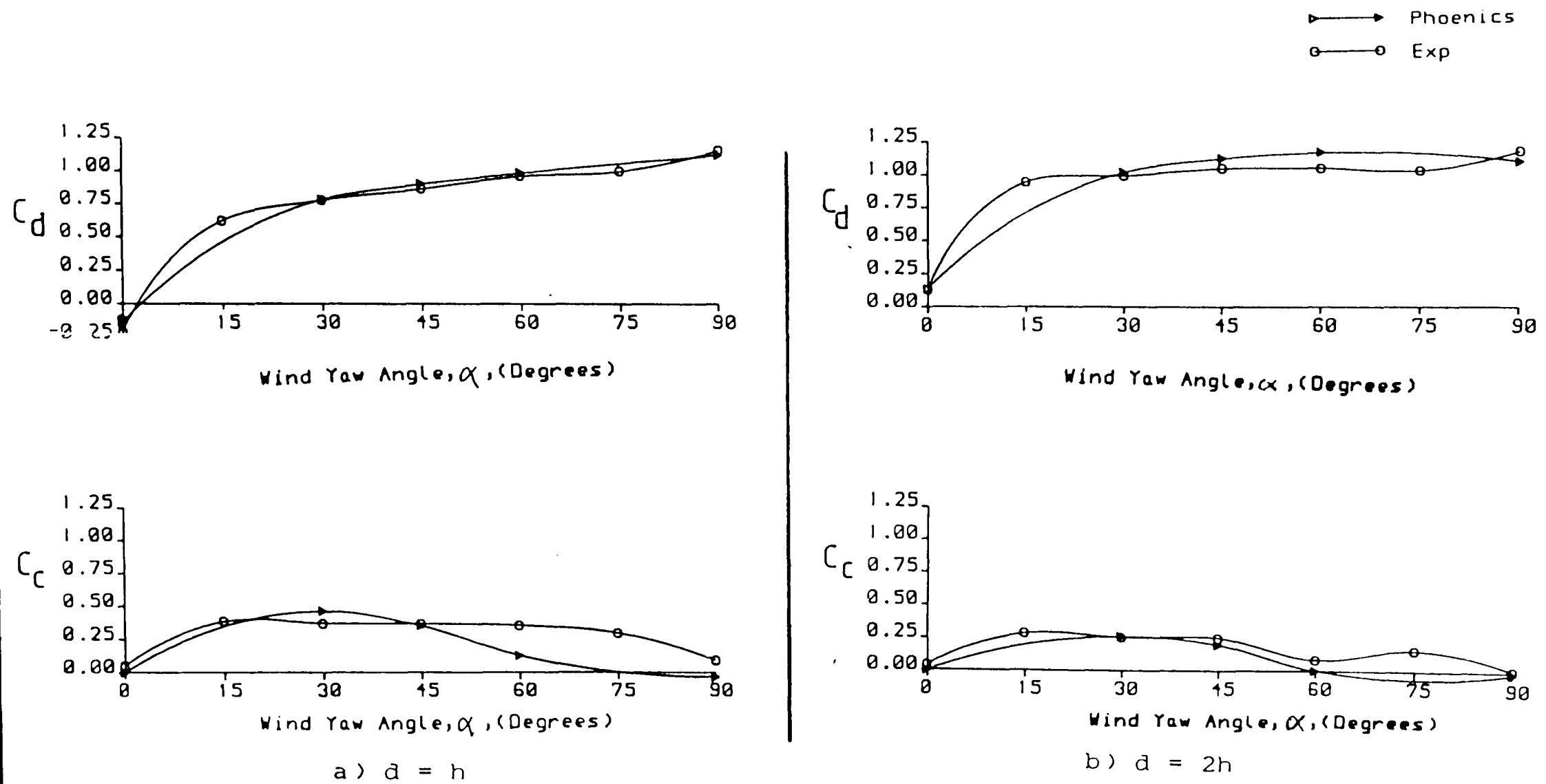
FIGURE(4.72):VARIATION OF THE WIND AXIS FOCE COEFFICIENTS
WITH WIND YAW ANGLE FOR THE SHIELDED CUBE
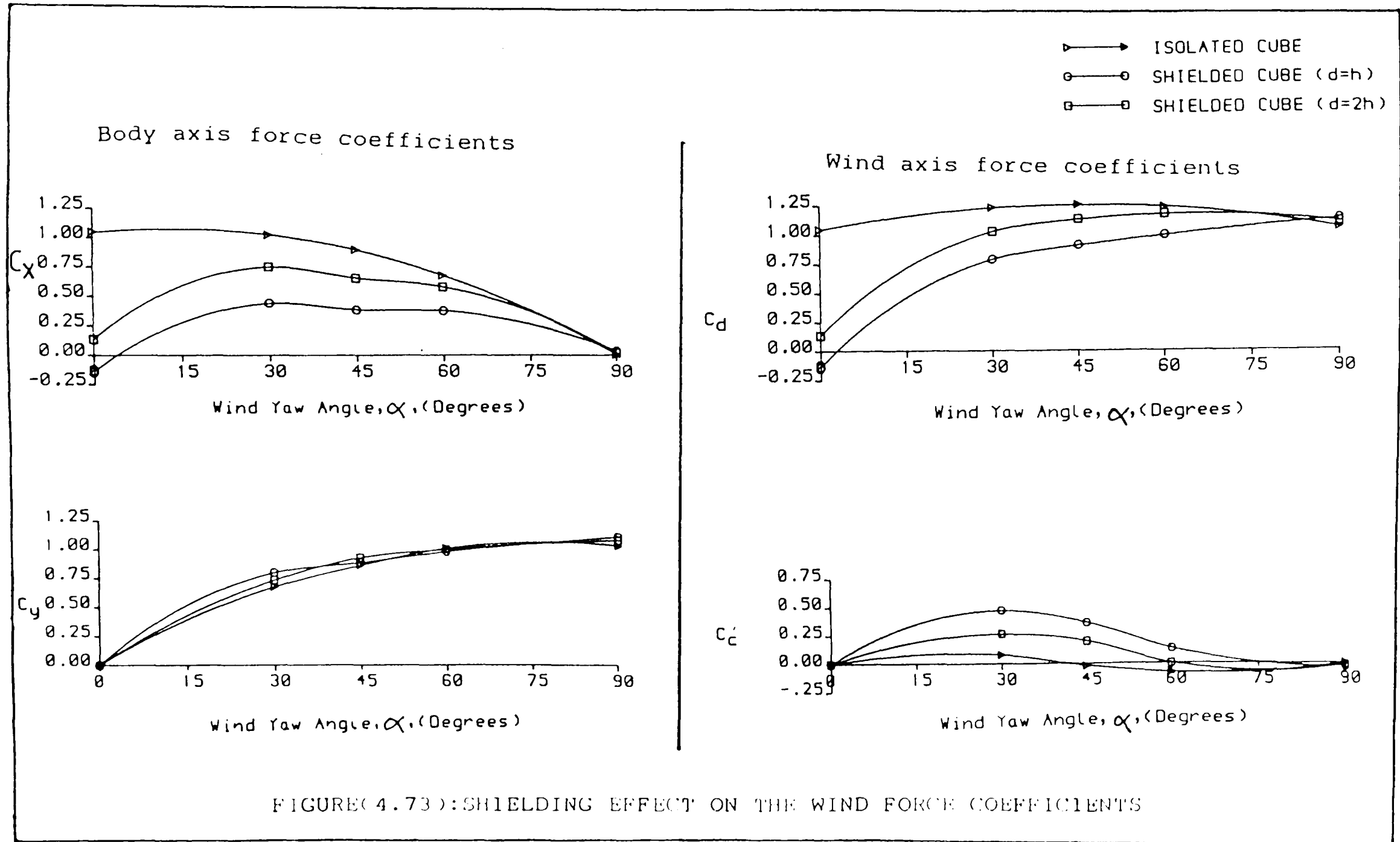
FIGURE(4.73):SHIELDING EFFECT ON THE WIND FORCE COEFFICIENTS
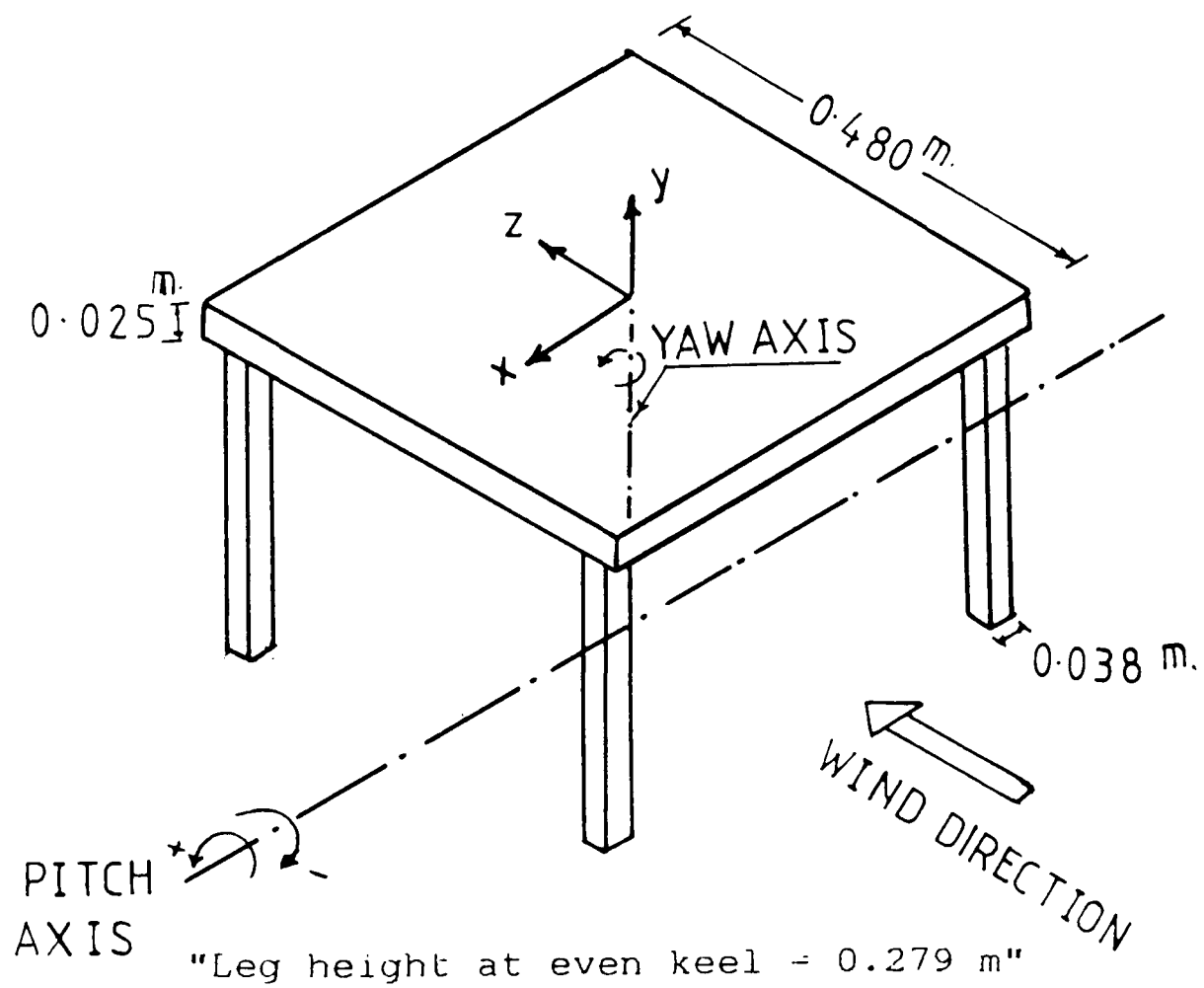
FIGURE(5.1): A SIMPLE FOUR-LEGGED PLATFORM MODEL
AND AXIS SYSTEM

204

VOLUME CONTAINS CLEAR OVERLAYS

OVERLAYS SCANNED SEPERATELY AND OVER THE RELEVANT PAGE.
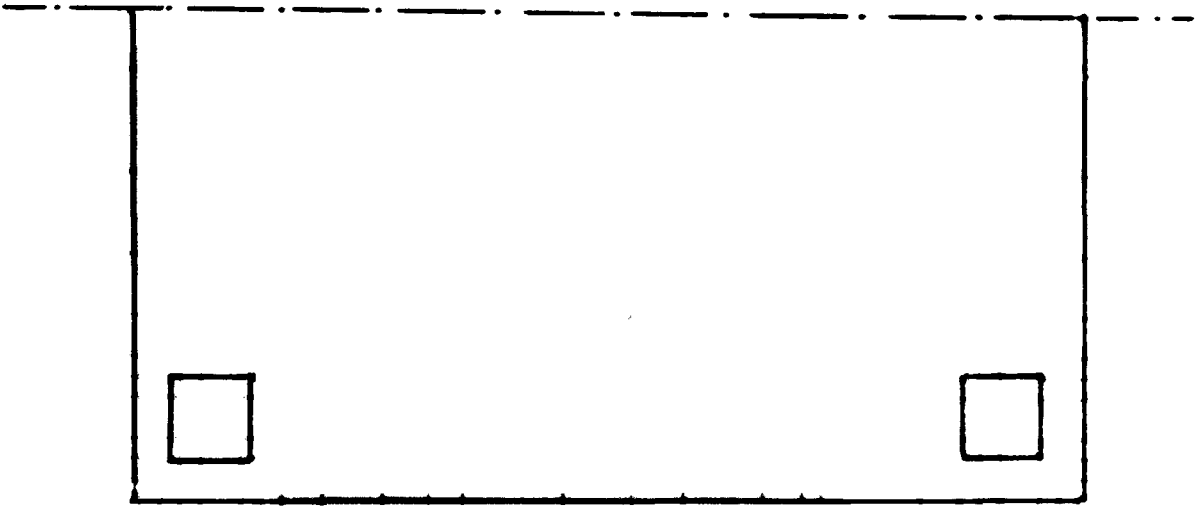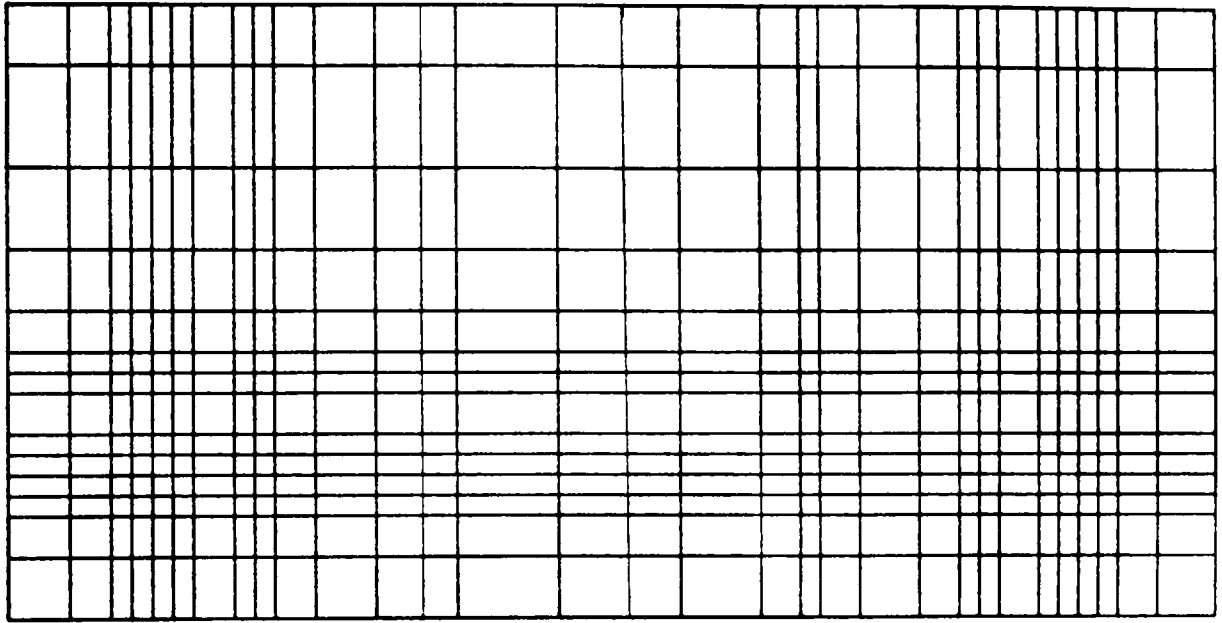
TOP VIEW

FIGURE(5.2): GRID GEOMETRY FOR PLATFORM MODEL
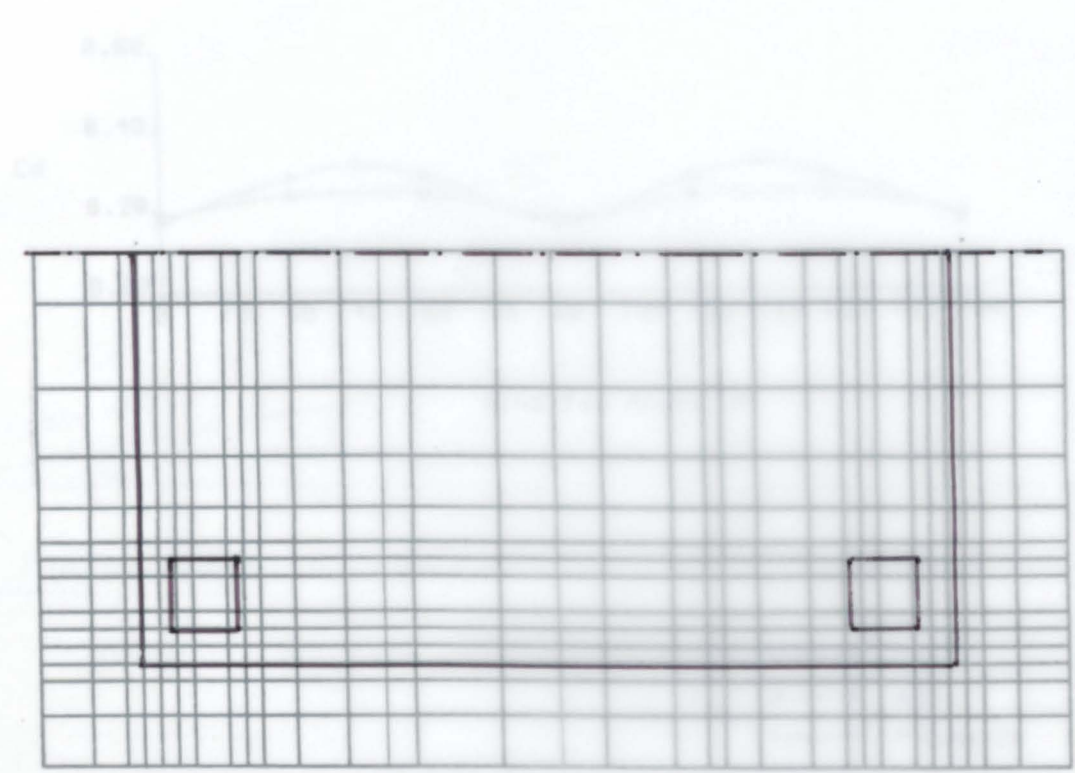
TOP VIEW

FIGURE(5.2): GRID GEOMETRY FOR PLATFORM MODEL

Figure(5.3):

Comparison, Variation of drag coefficient for
the platform model at even keel

206
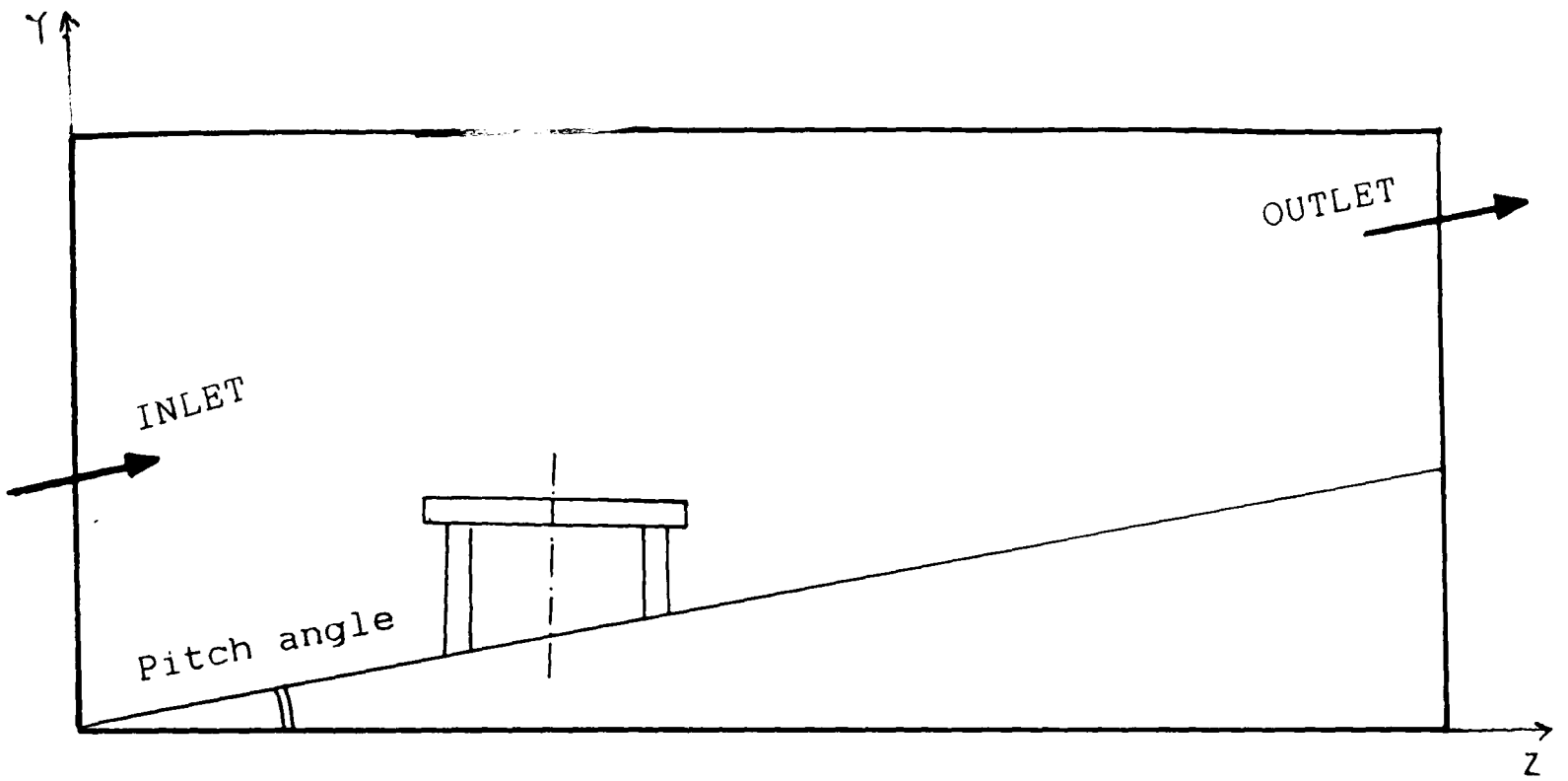
A) POSITIVE PITCH
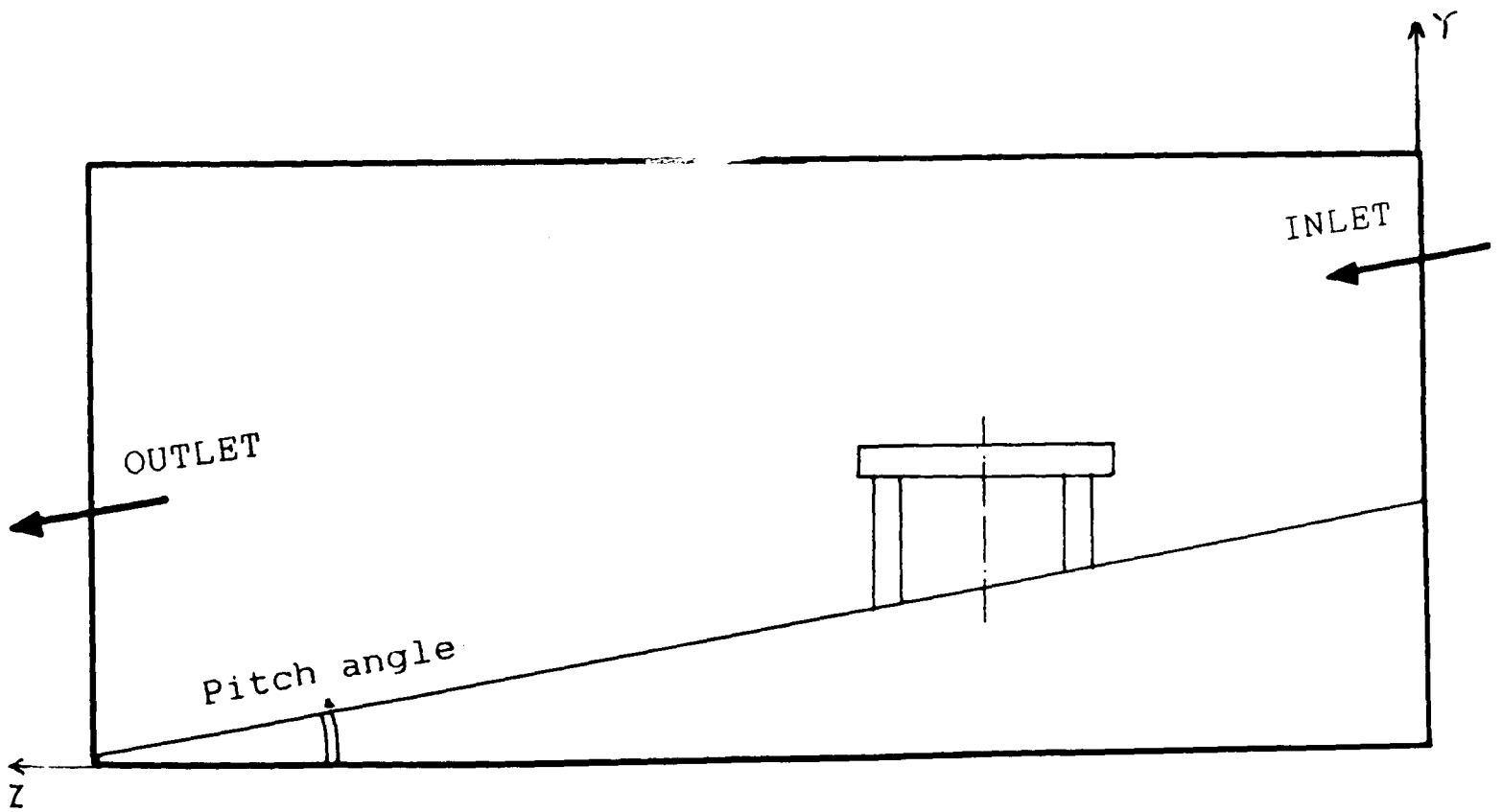
B) NEGATIVE PITCH

Figure(5.4): Terminology of inclined platform
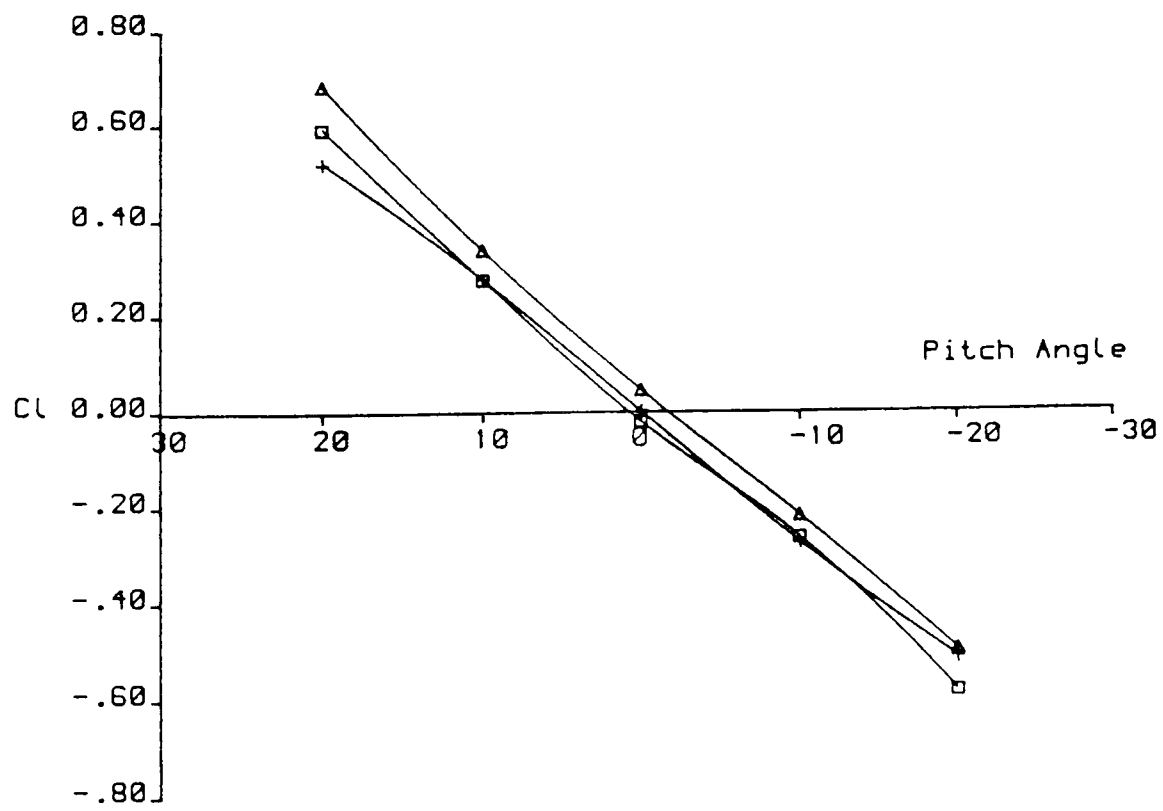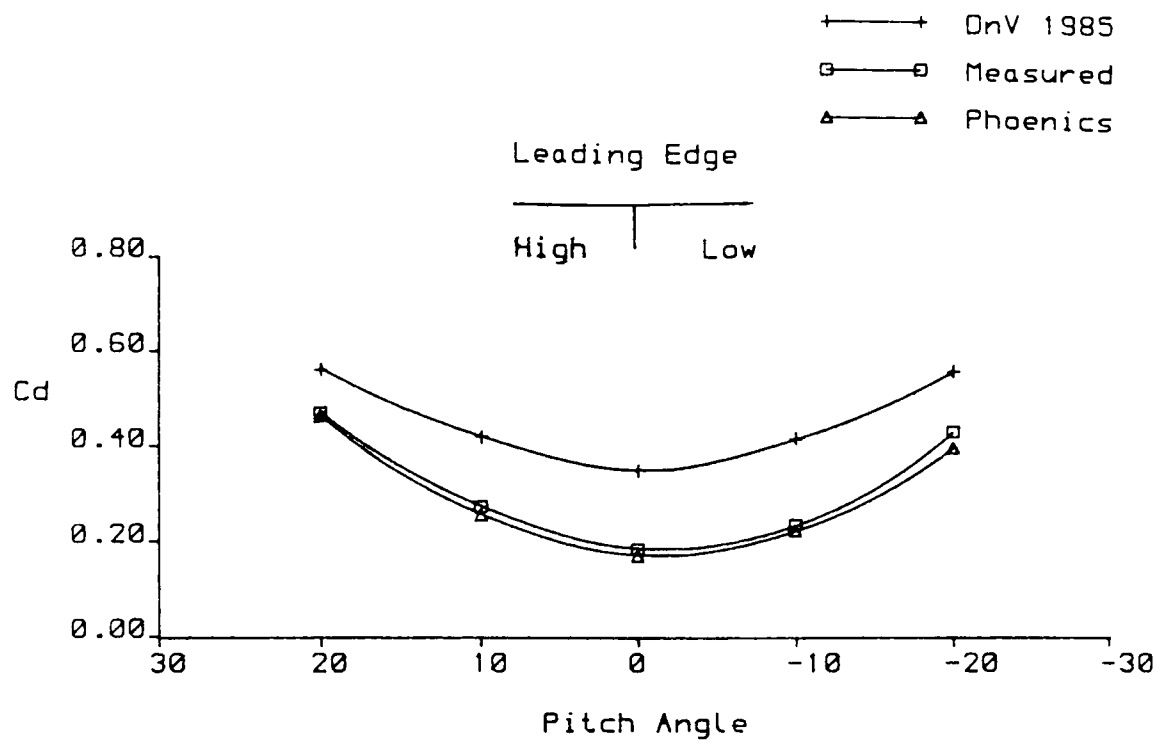
Figure(5.5):

Comparison, wind force coefficients for the
platform model with pitch angle
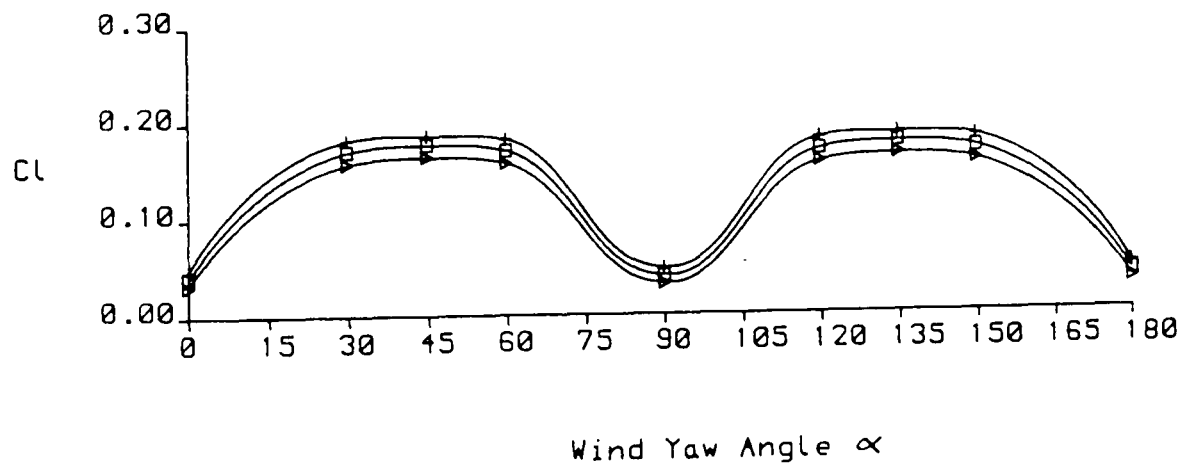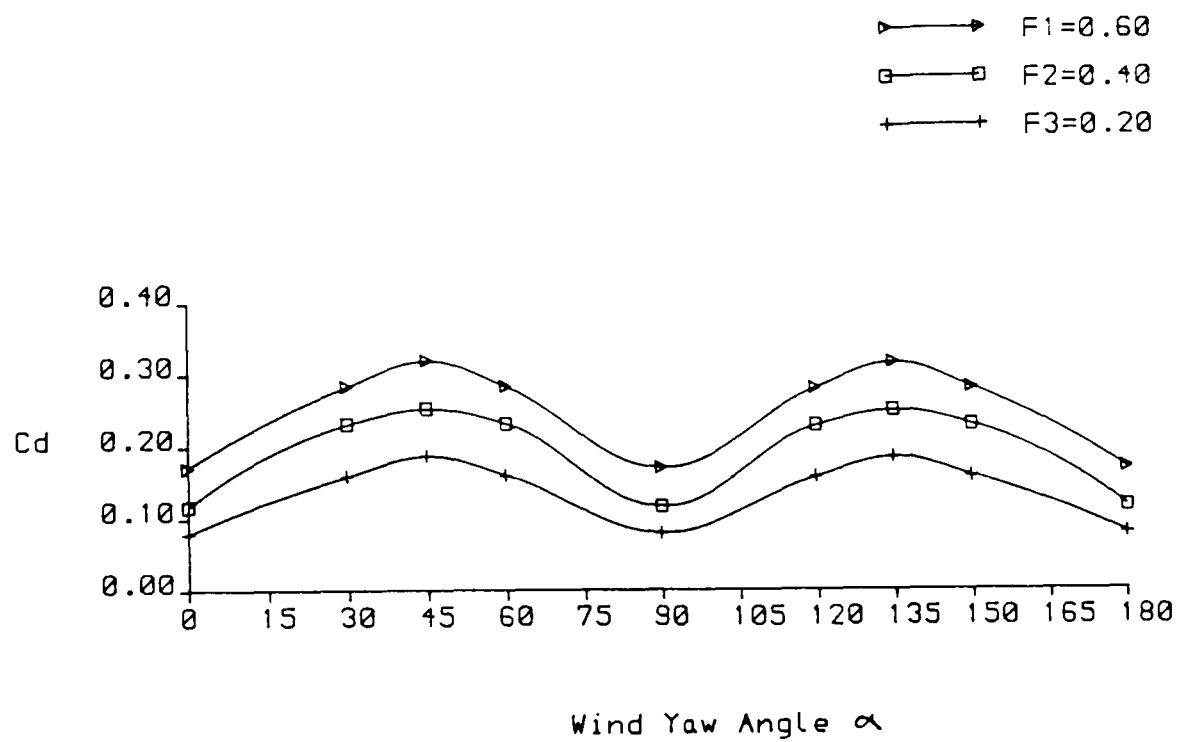
Figure(5.6):

Freeboard effect on wind force coefficients
at even keel
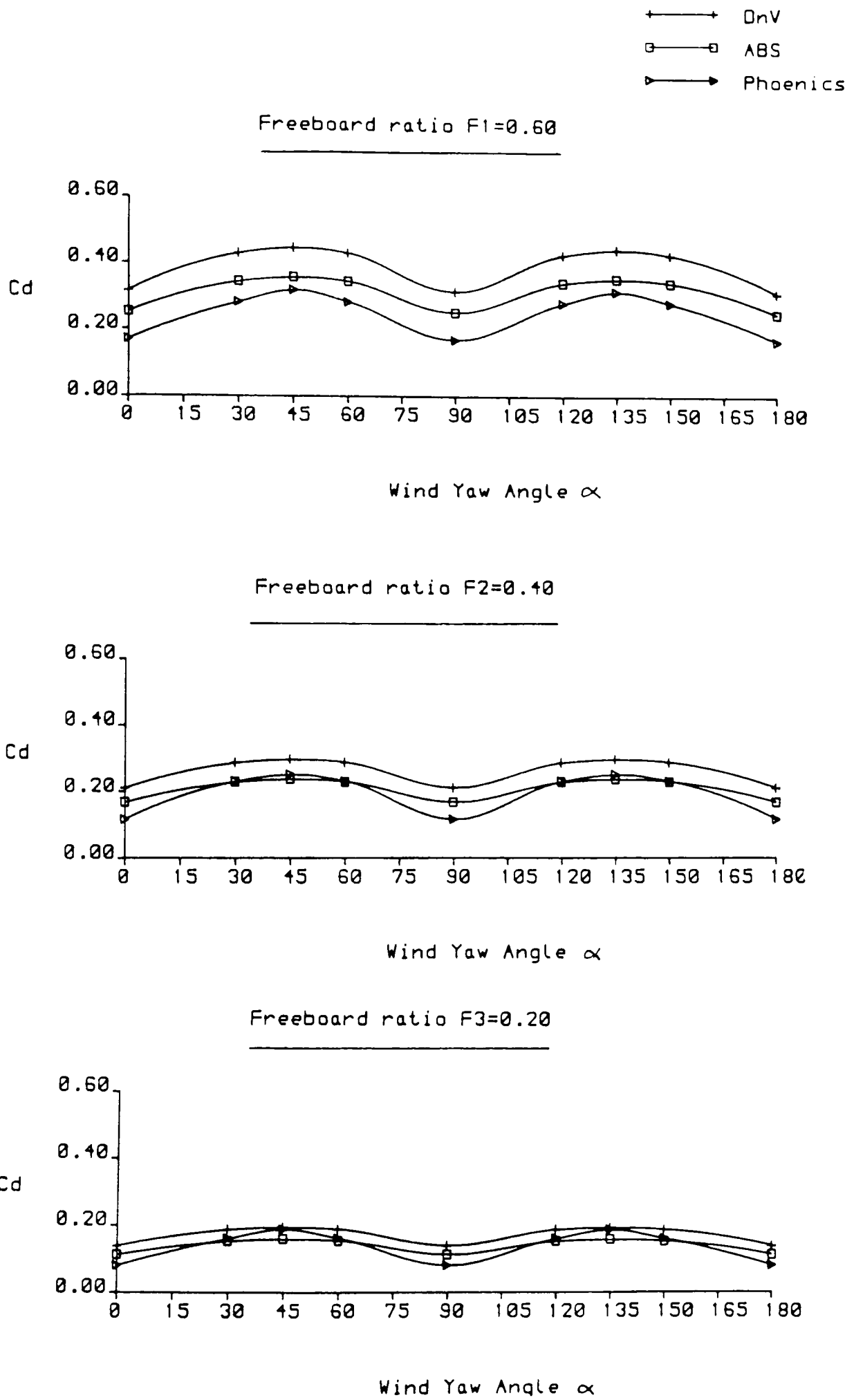
Figure(5.7):

Comparison, freeboard effect on drag coefficient
at even keel
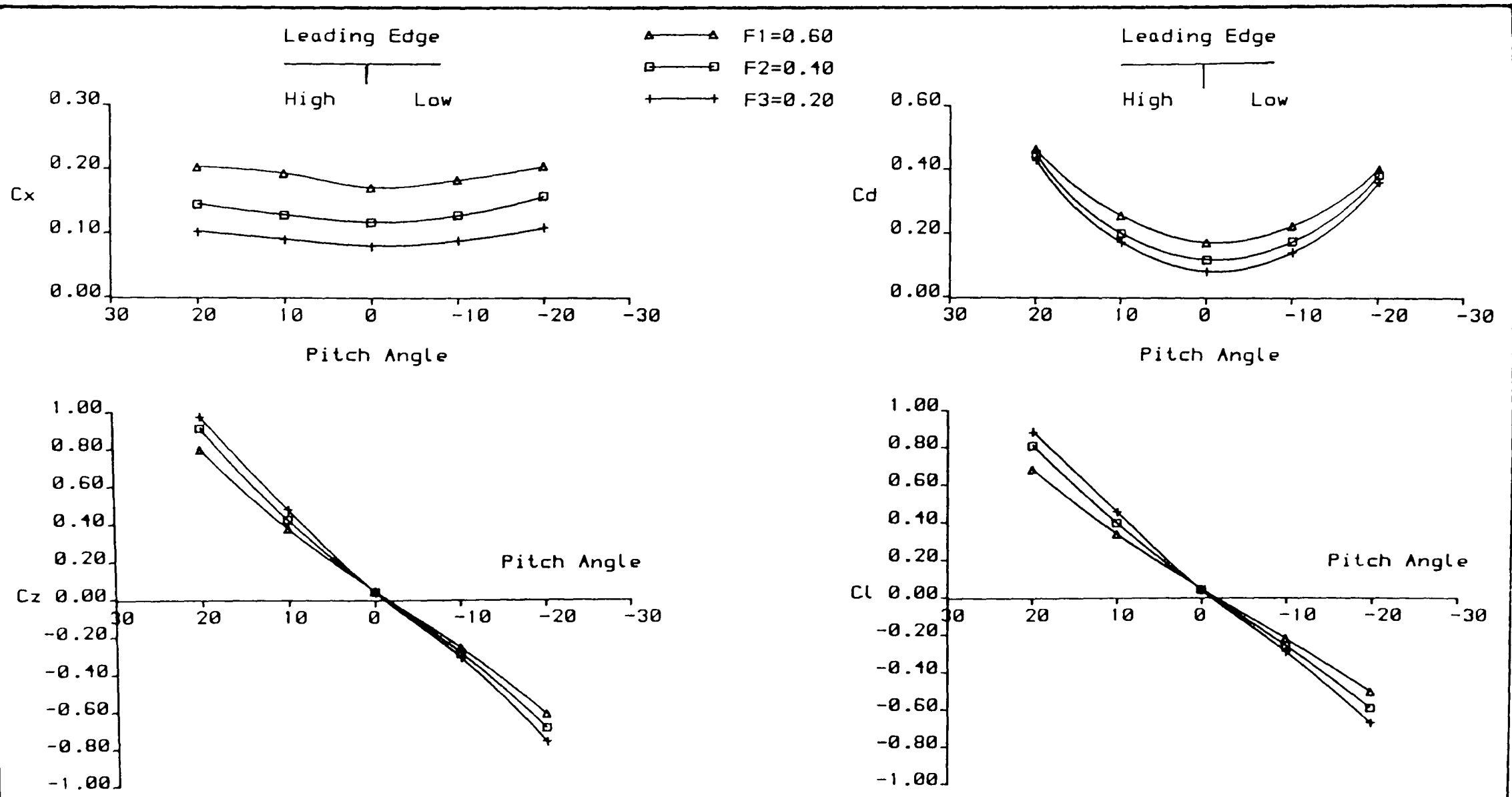
Figure(5.8): Freeboard effect on force coefficients
for pitching platform model
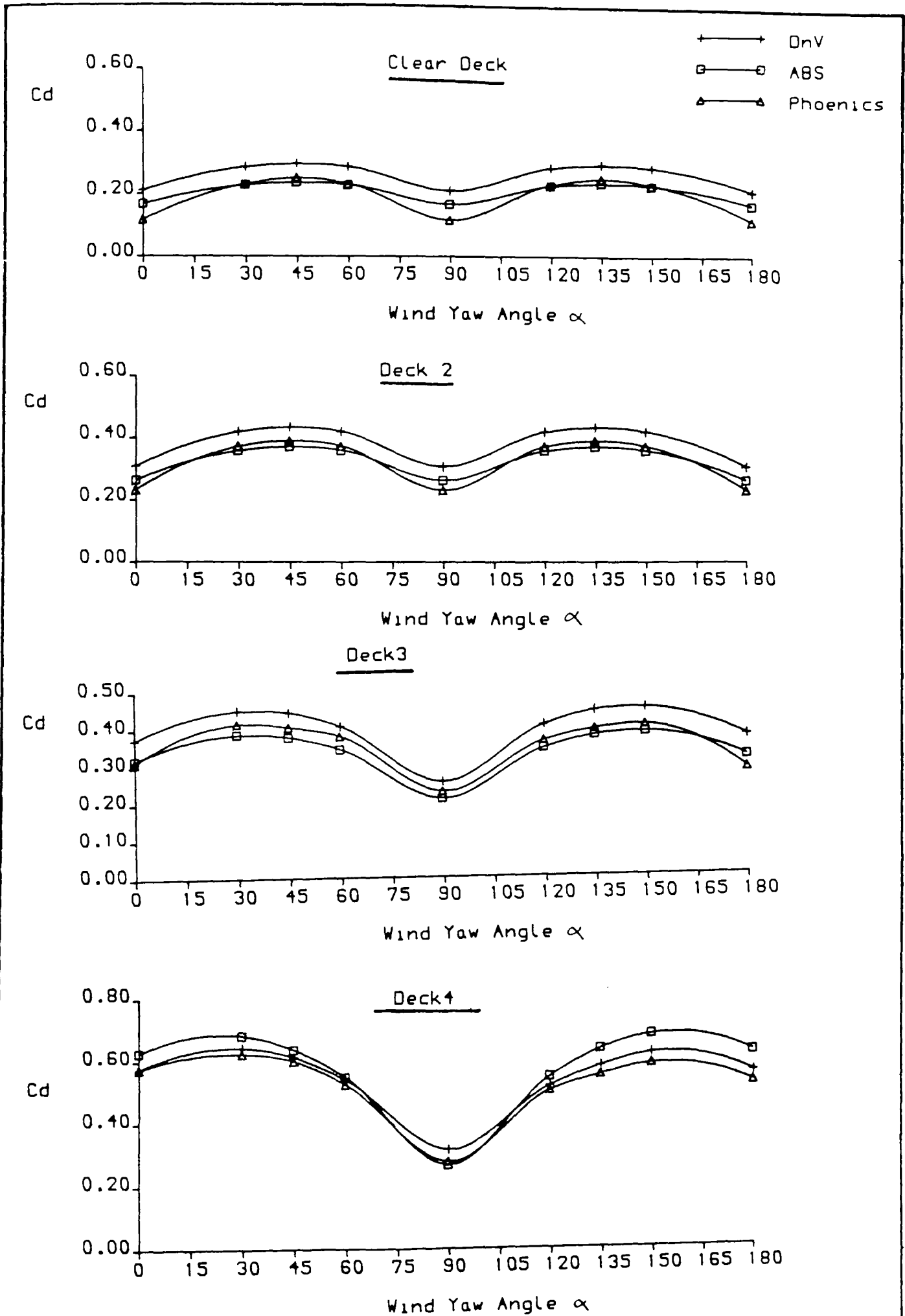
Figure(5.9):

Comparison, effect of deck layout on drag coefficient at even keel

212
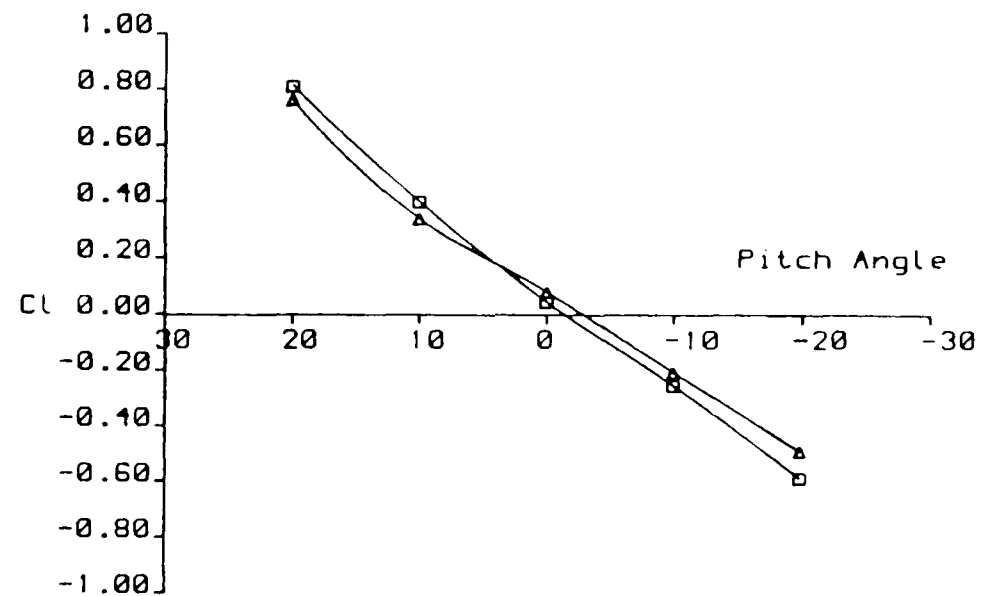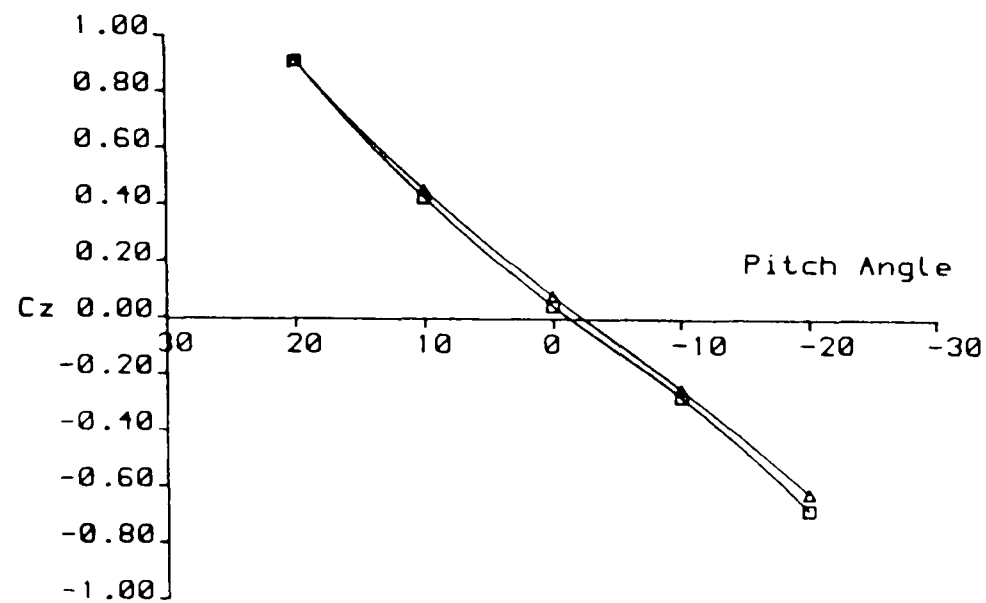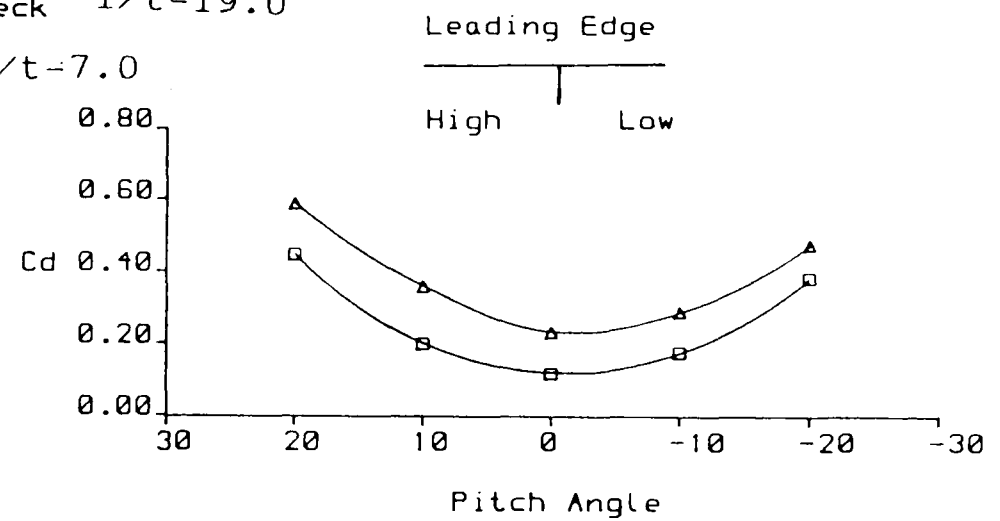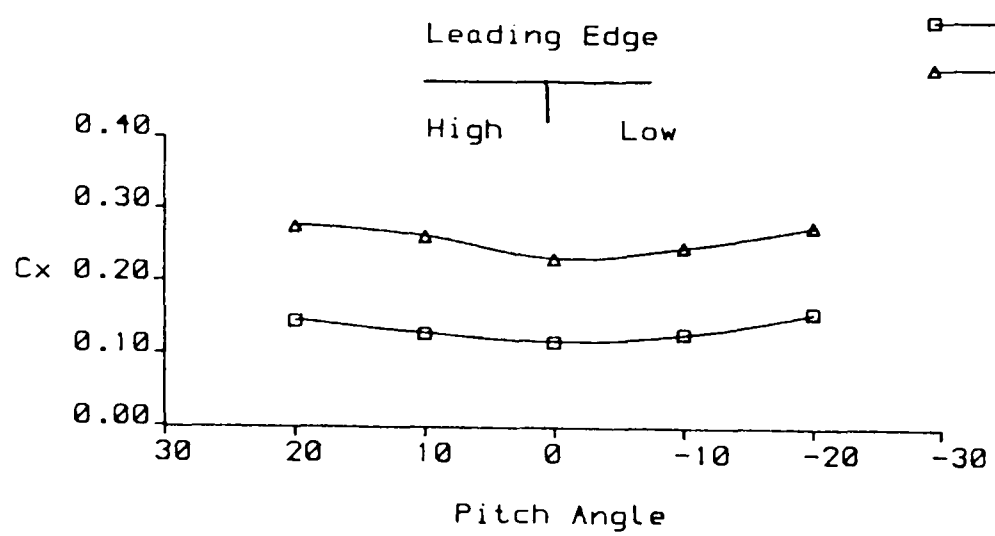
Figure(5.10):

Effect of (length/thickness) ratio of the main deck
on force coefficients for pitching platform model
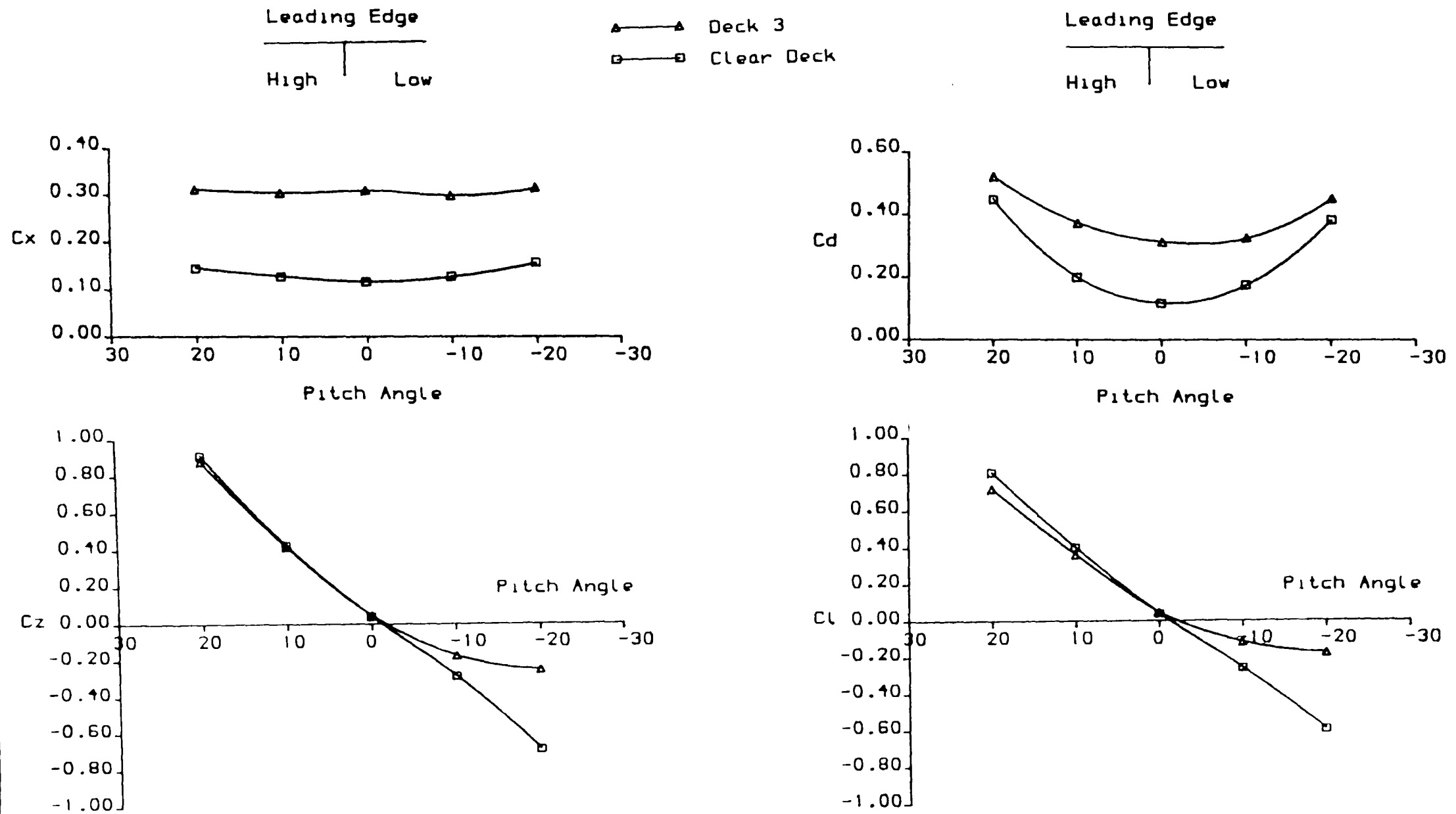
Figure(5.11): Comparison, Force coefficients of "DECK3" and "CLEAR DECK"

214
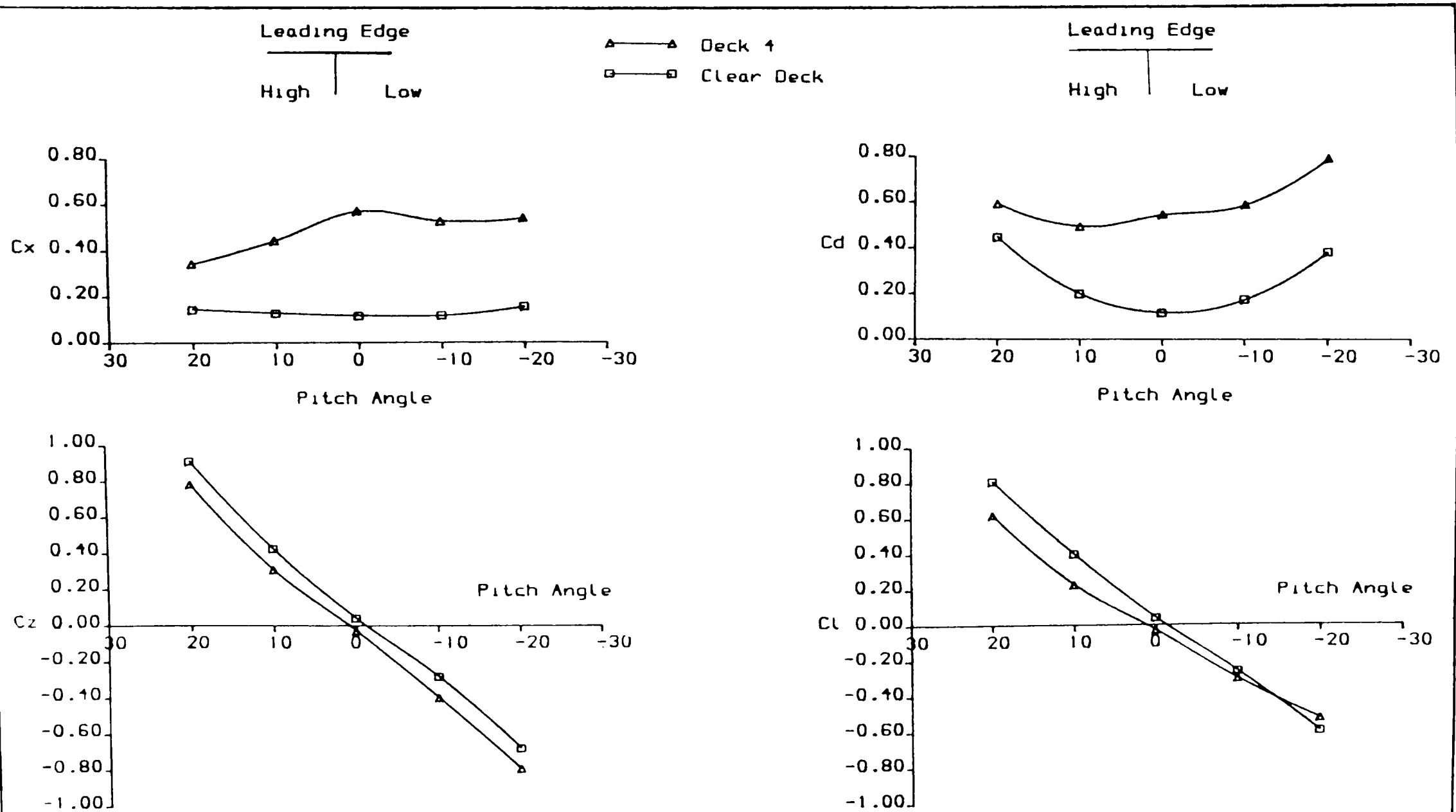
Figure(5.12): Comparison, Force coefficients of "DECK4" and "CLEAR DECK"

215
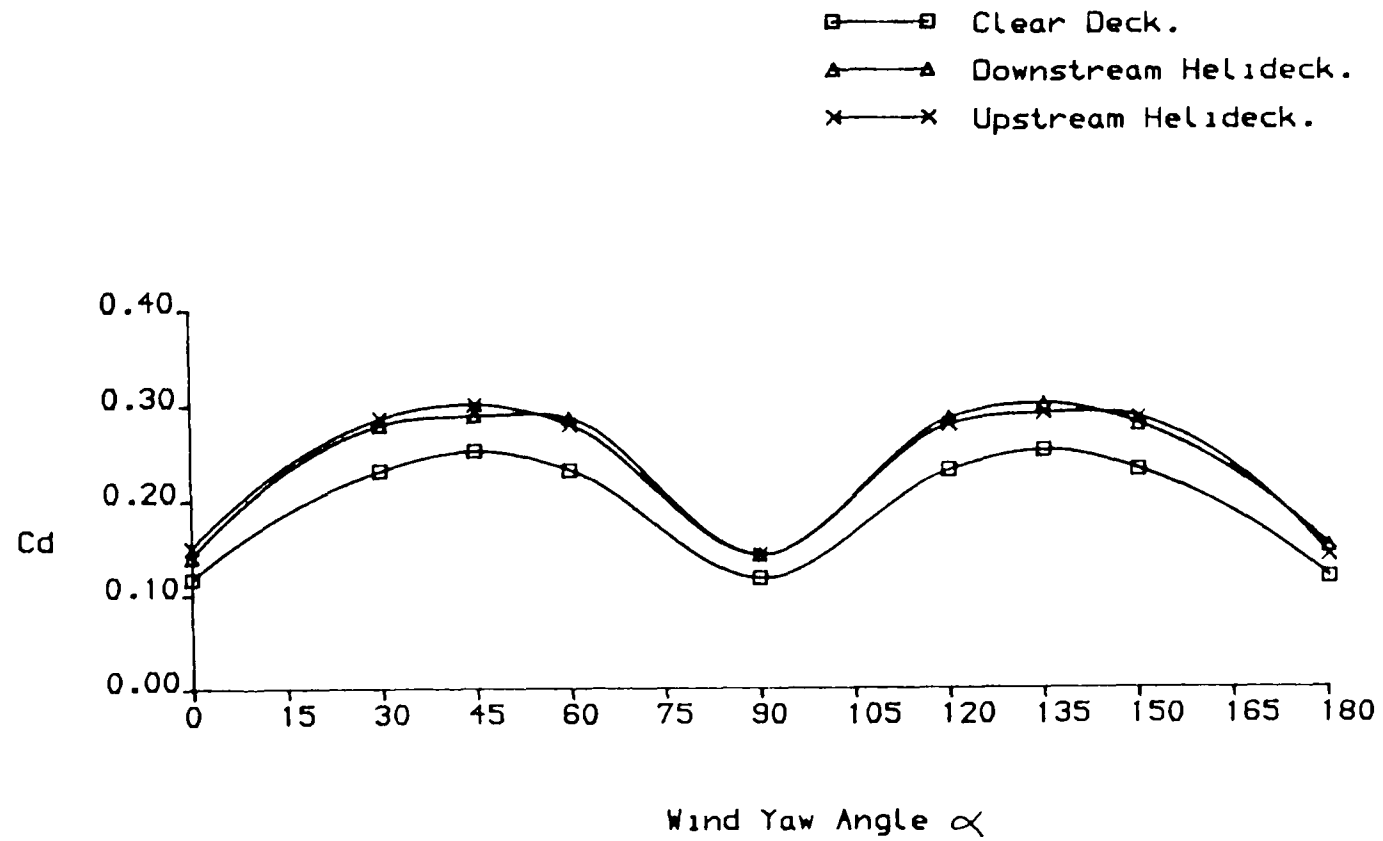
Figure(5.13):Effect of "HELIDECK" on force coefficients
at even keel
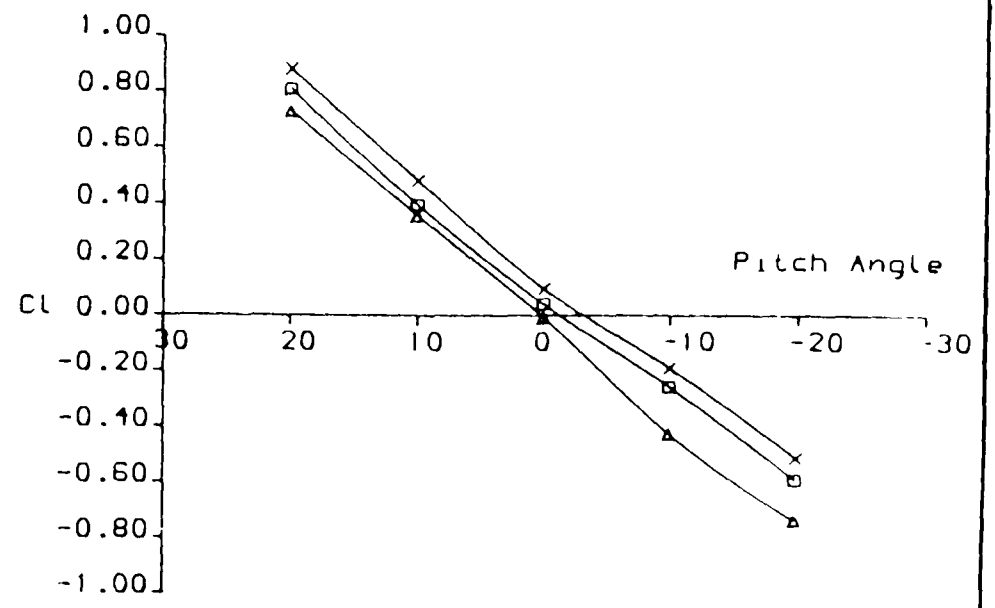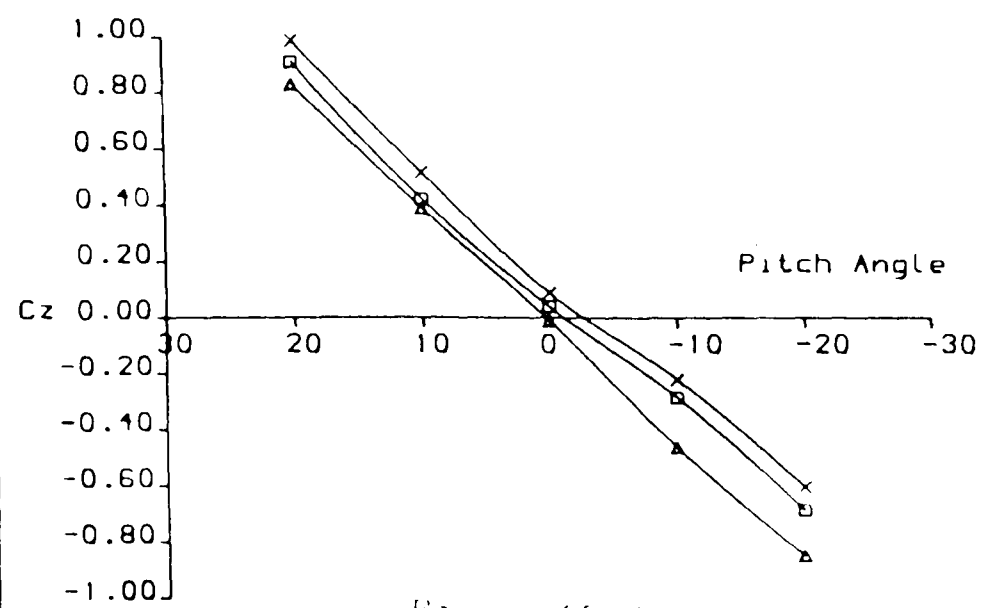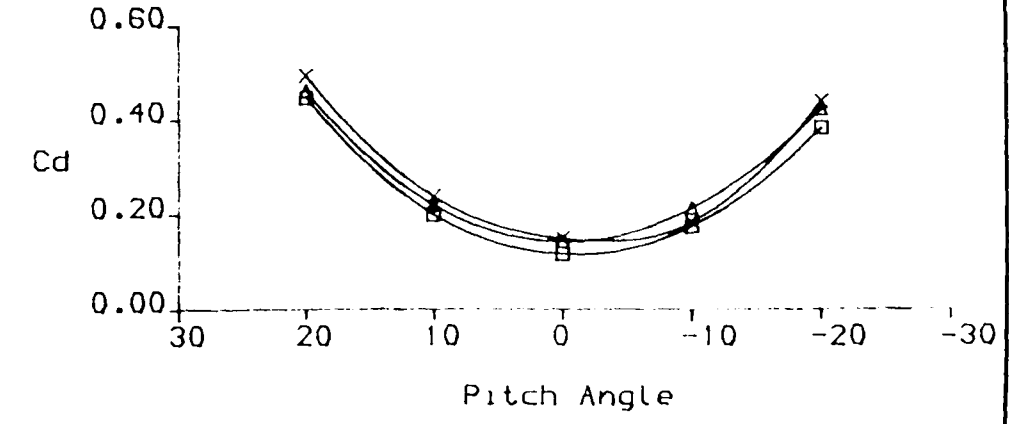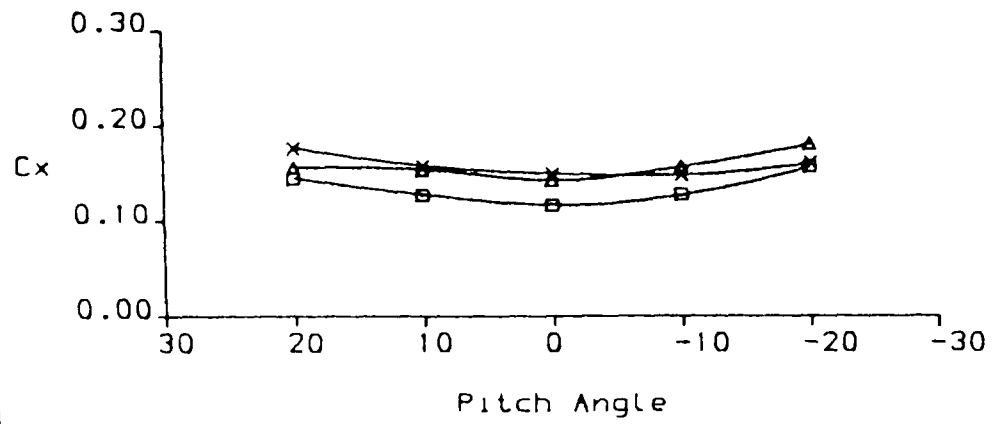
Figure(5.14):Effect of "HELIDECK" on force coefficients
for pitching platform model
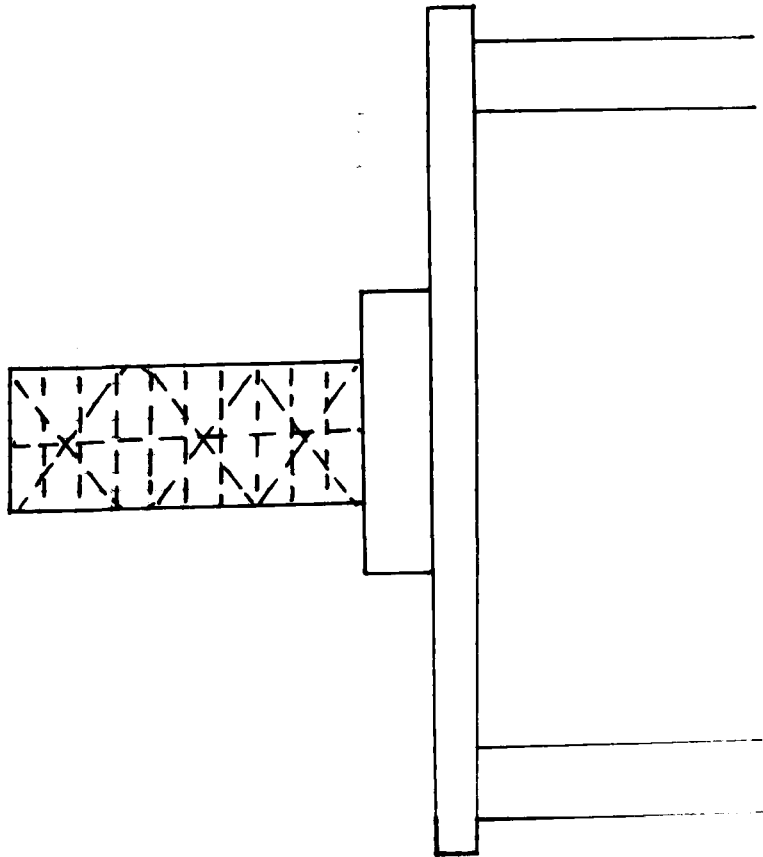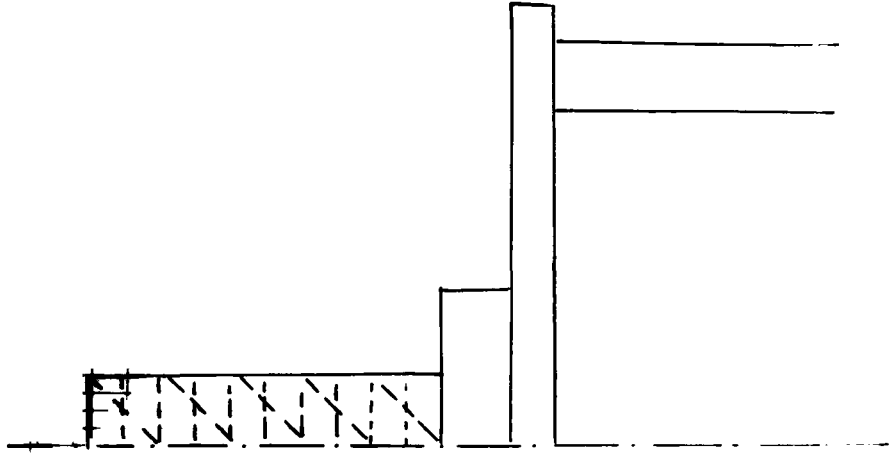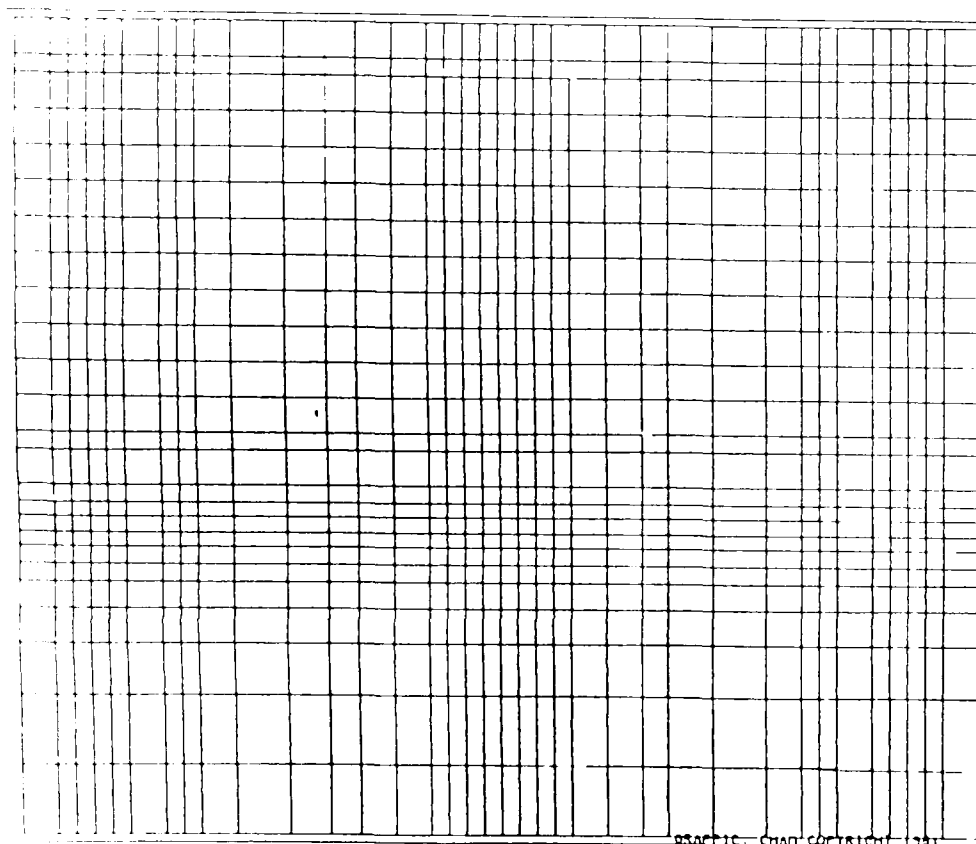
SIDE ELEVATION   END ELEVATION
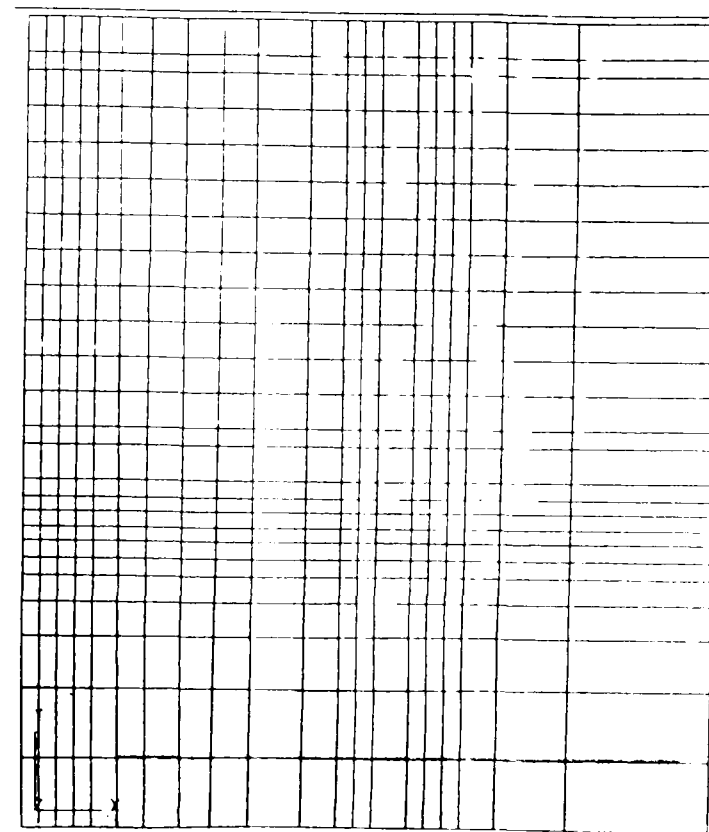
FIGURE (5.15): GRID GEOMETRY FOR PLATFORM MODEL
WITH DERRICK STRUCTURE
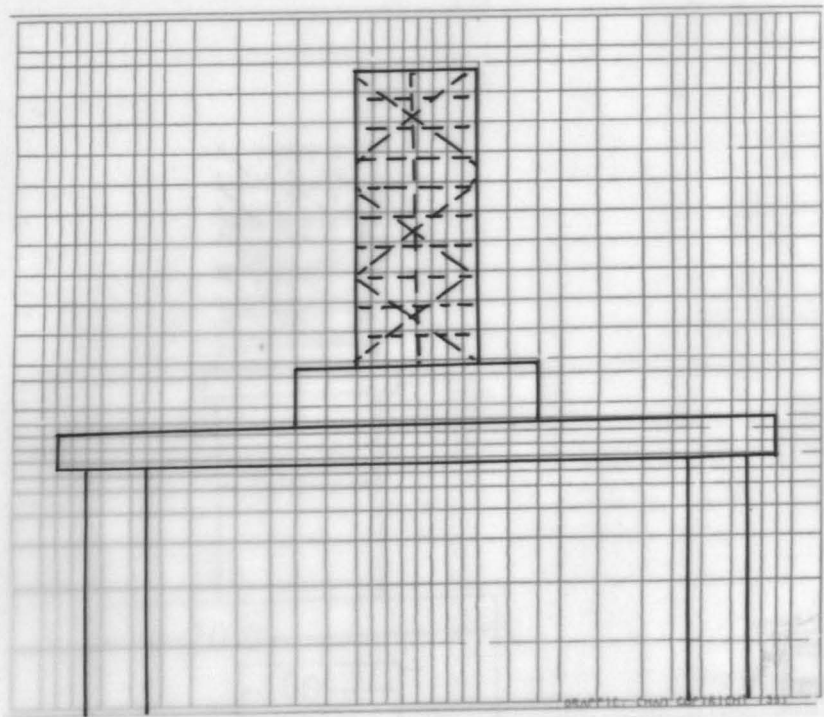
SIDE ELEVATION
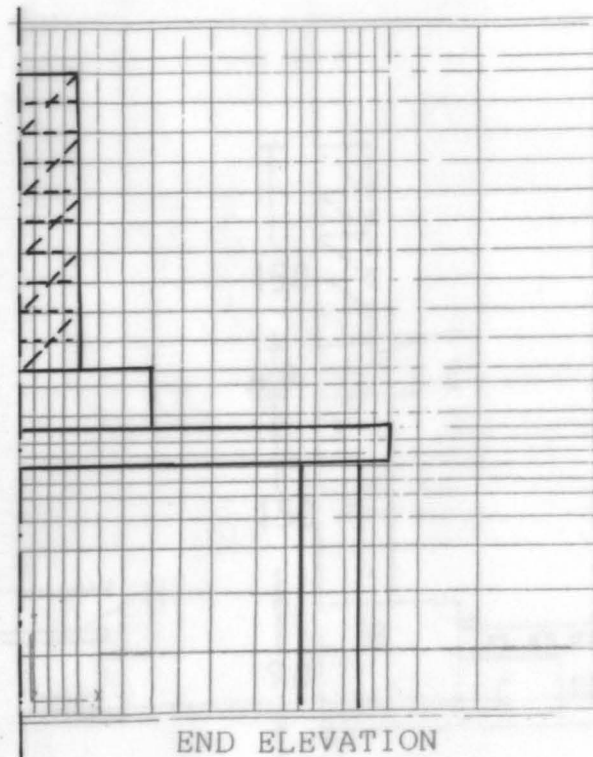
END ELEVATION

FIGURE (5.15): GRID GEOMETRY FOR PLATFORM MODEL
WITH DERRICK STRUCTURE
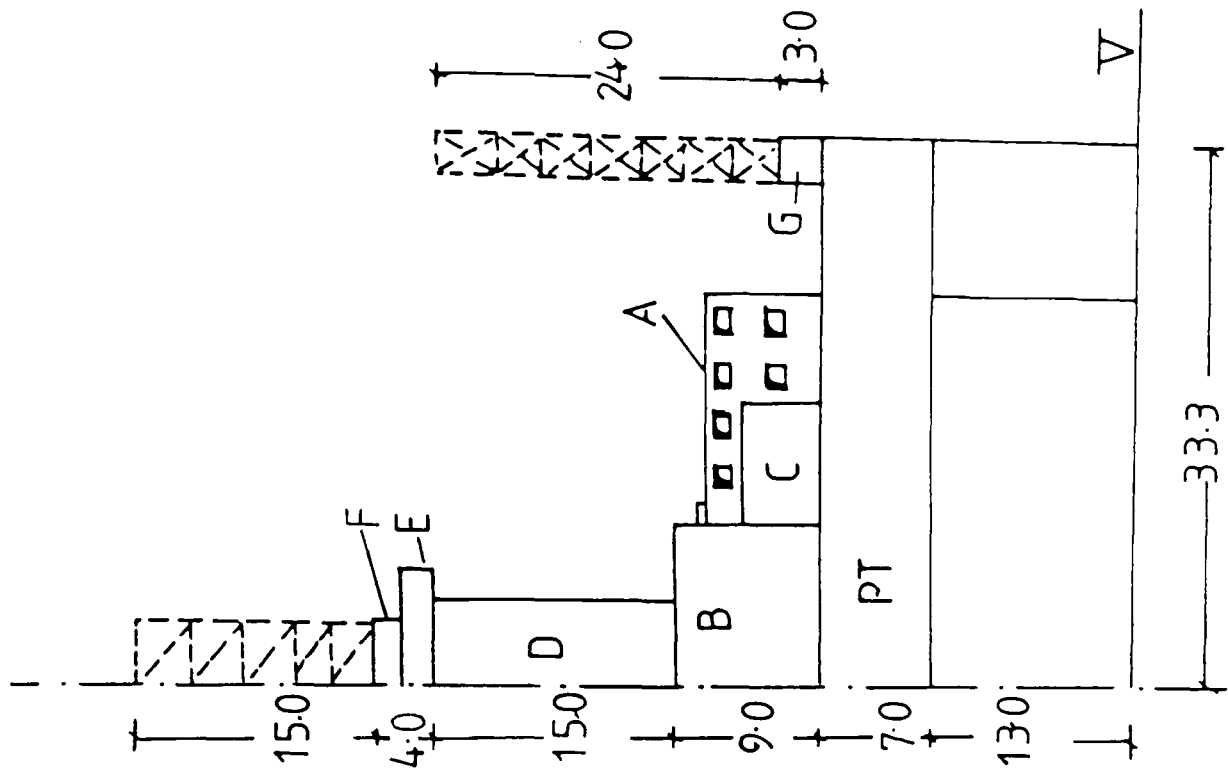
HALF-FORWARD ELEVATION
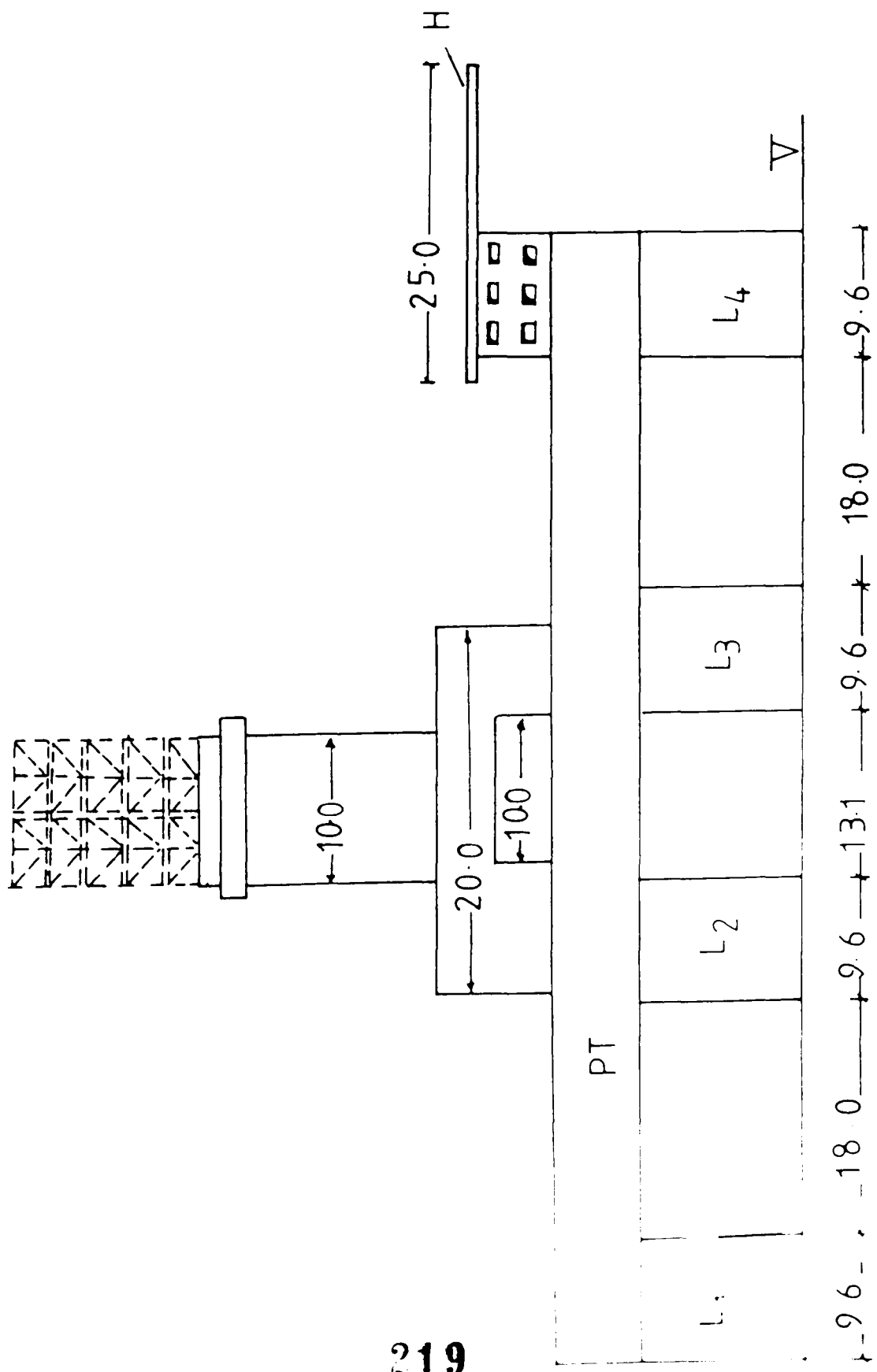
PORT ELEVATION

FIGURE 6.10:A GENERAL LAYOUT OF "AKER H-4.2" SEMI-SUBMERSIBLE

219
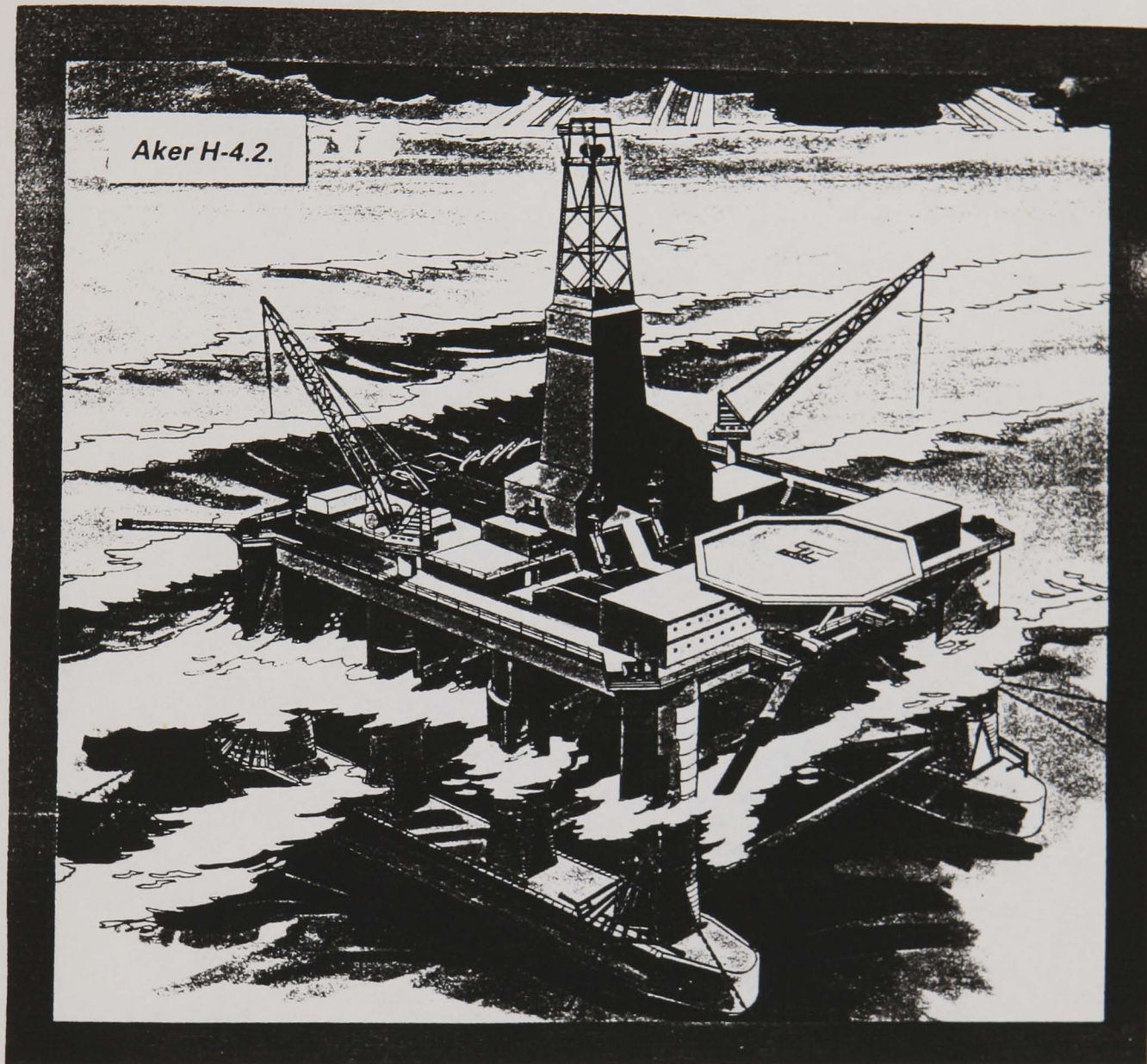
FIGURE(6.2): "AKER H-4.2 SEMI-SUBMERSIBLE"
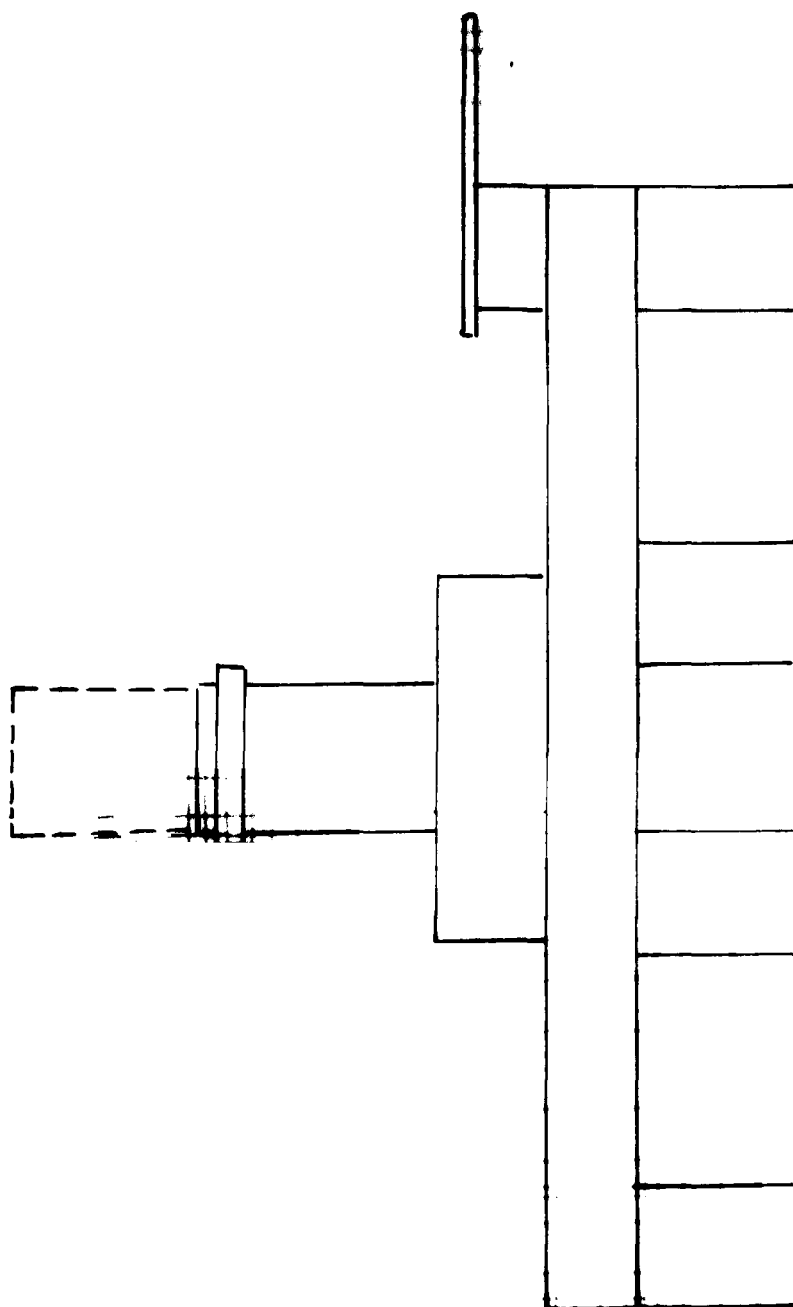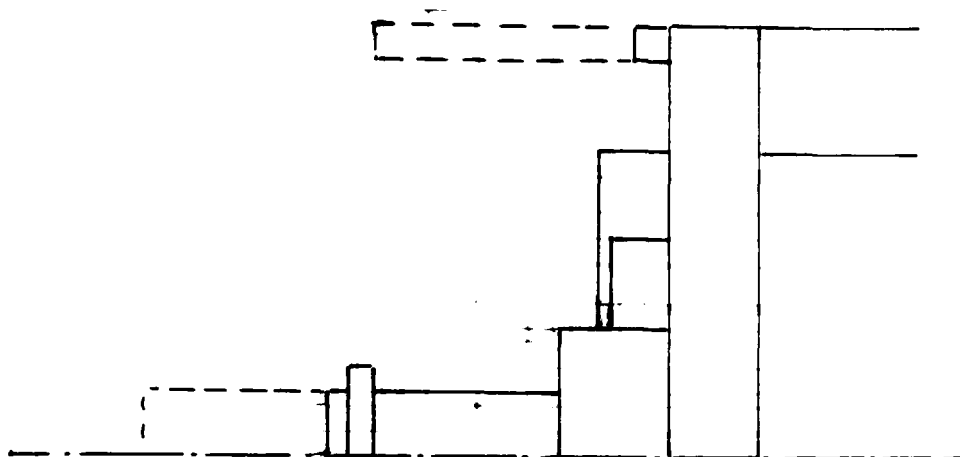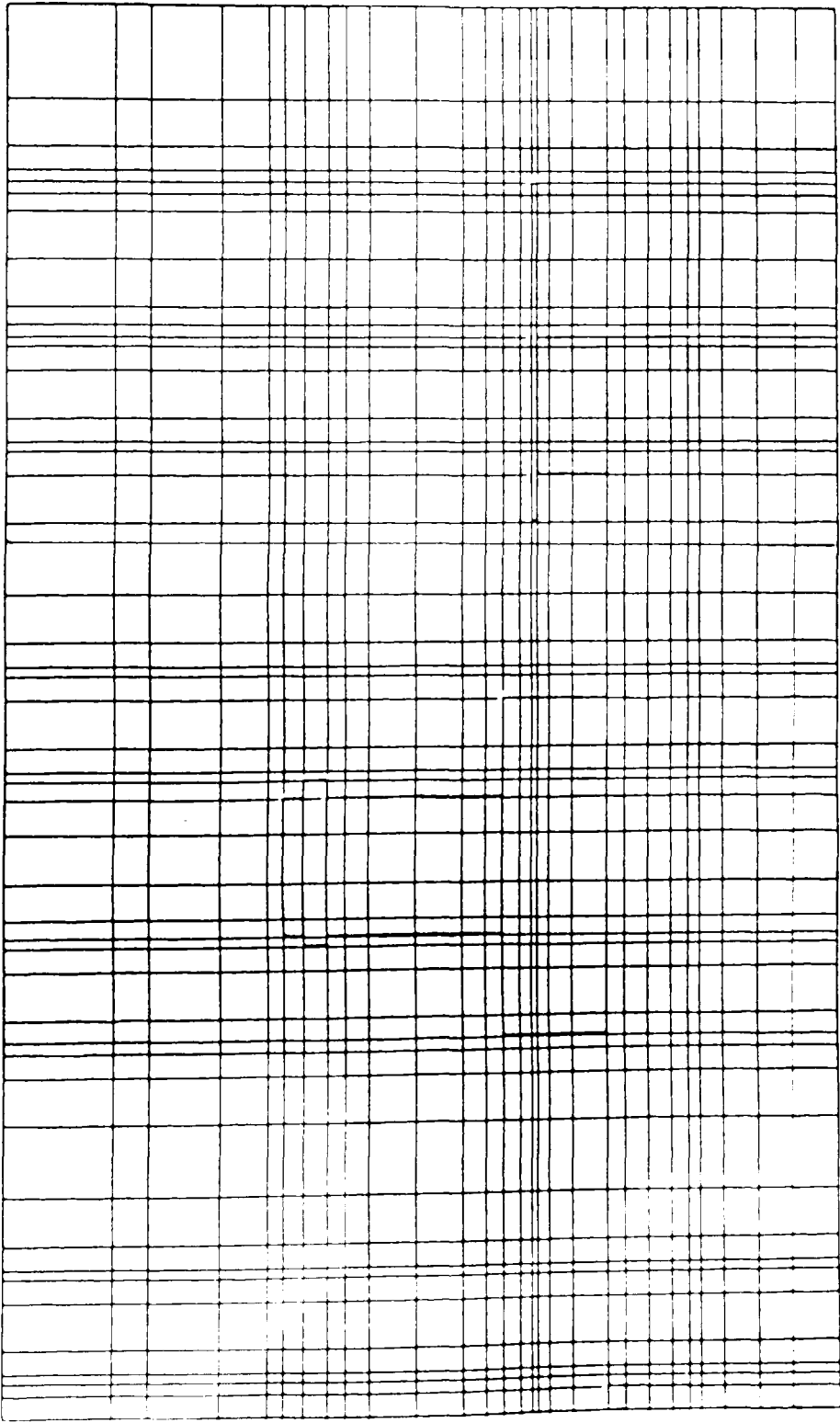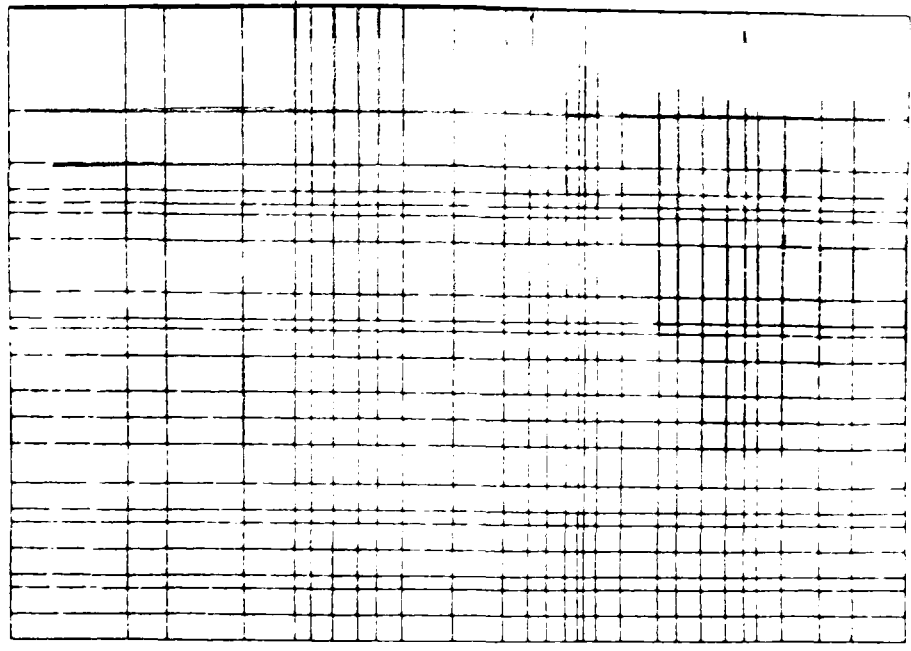
END ELEVATION

SIDE ELEVATION

FIGURE 6.3: GRID CONSTRUCTION FOR "AKER II-4.2"

221
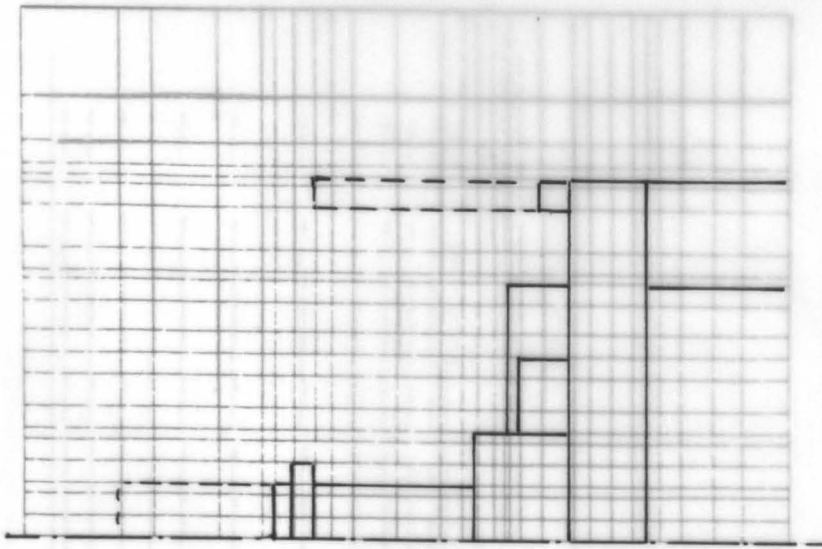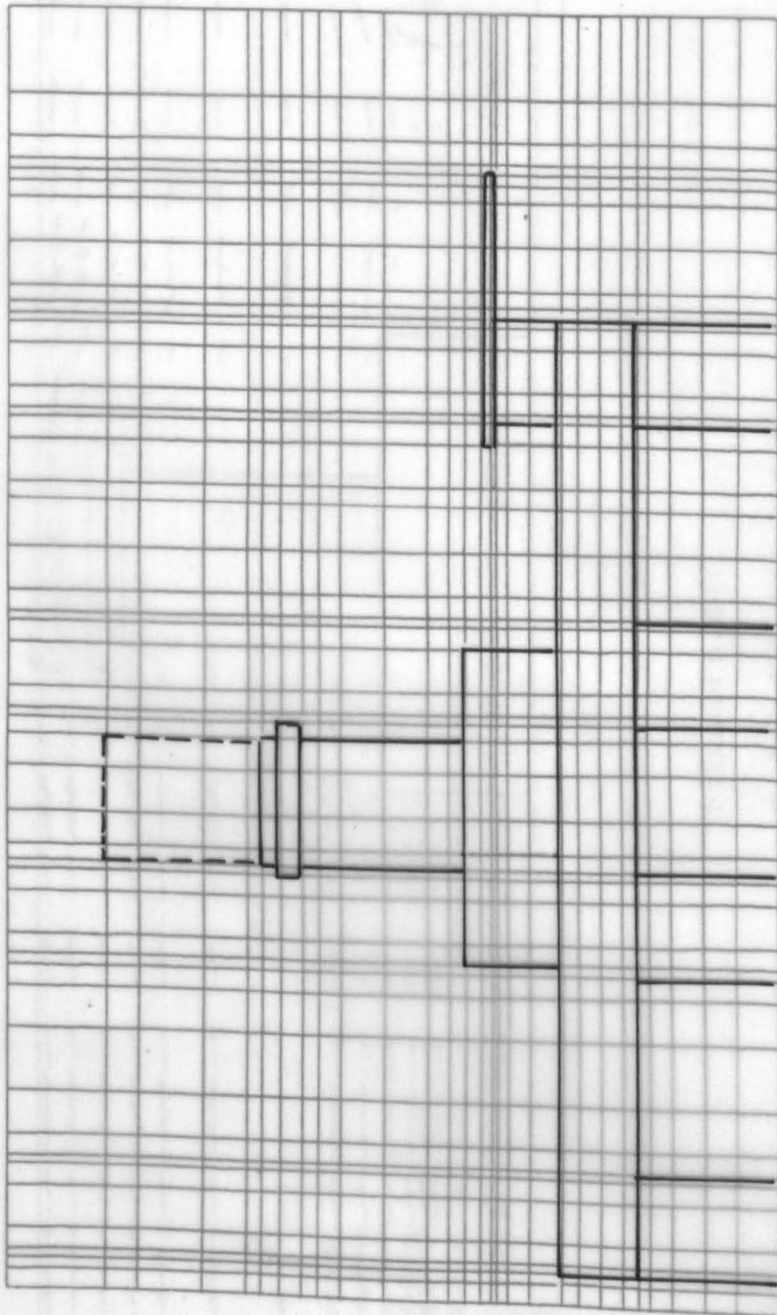
END ELEVATION

SIDE ELEVATION

FIGURE(6.3): GRID CONSTRUCTION FOR "AKER H-4.2"
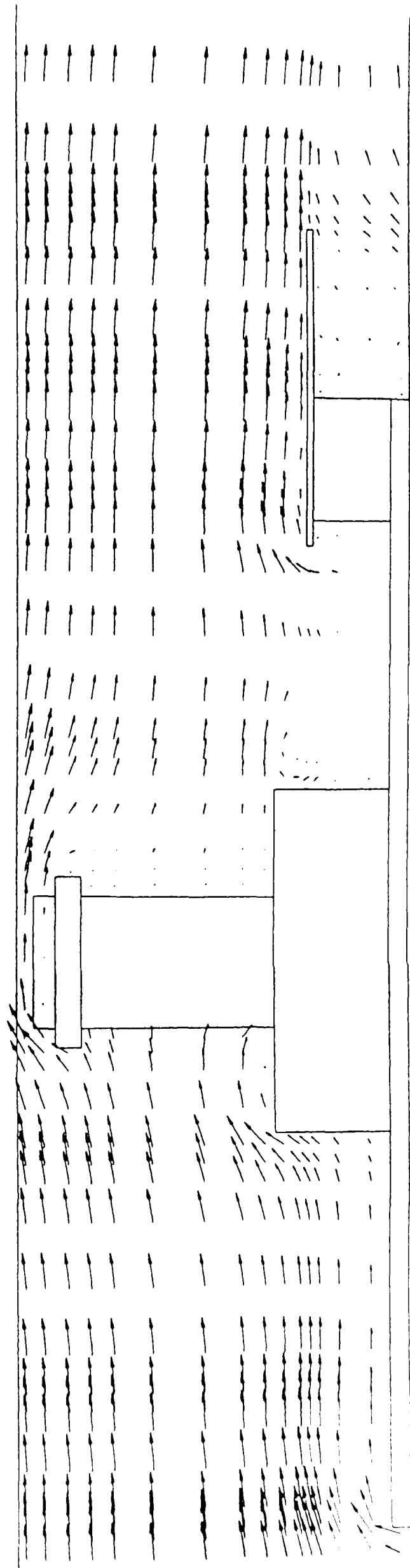
Figure(6.4):

Side elevation of flow field over the main deck
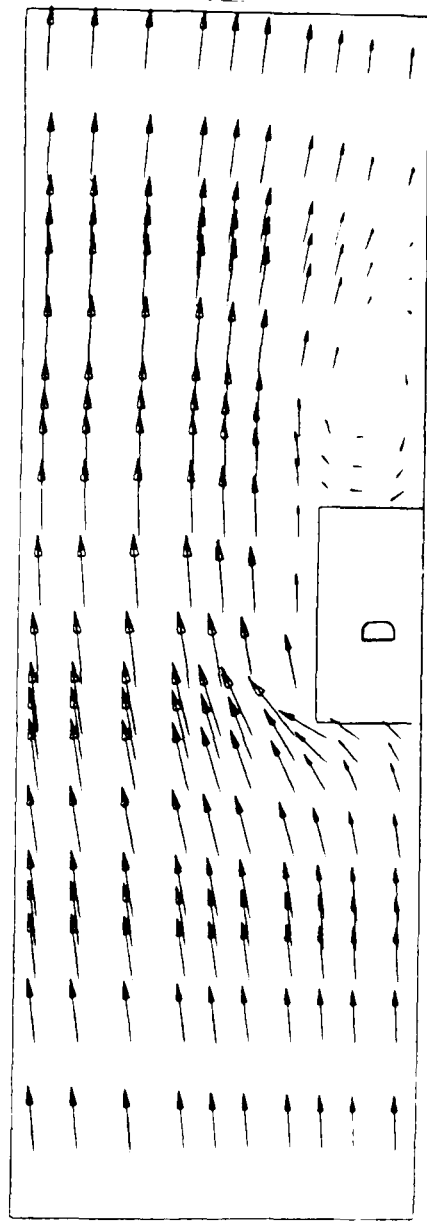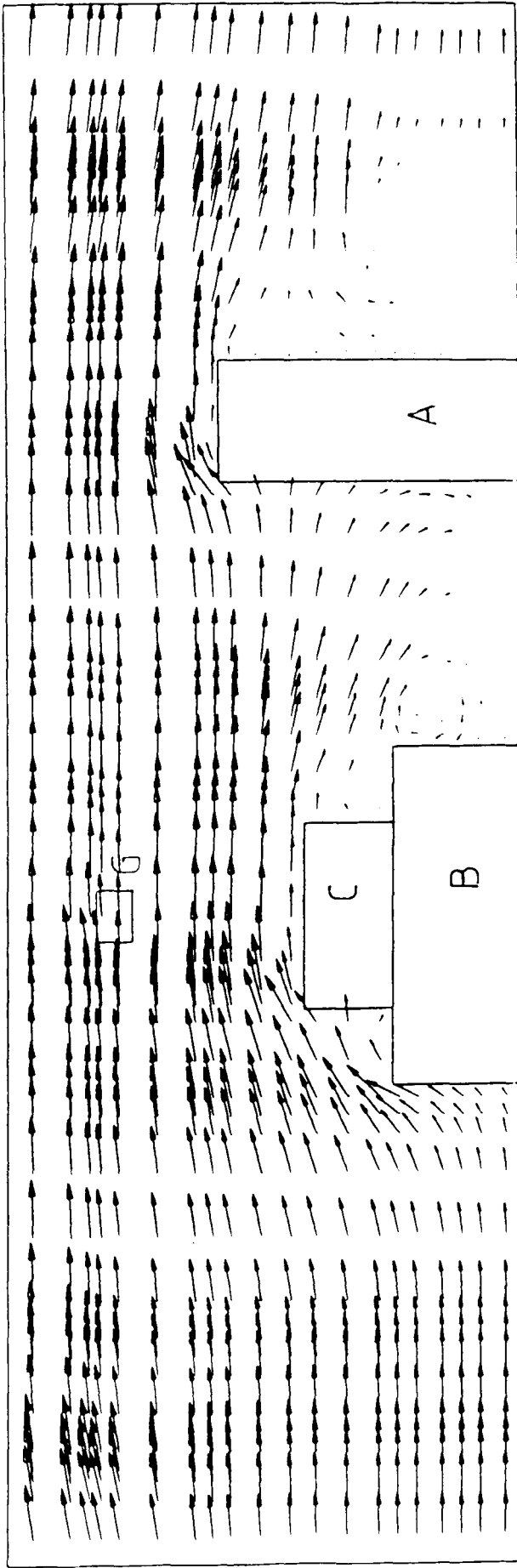
Figure(6.5):

Top view of the flow field on a plane through deck structures
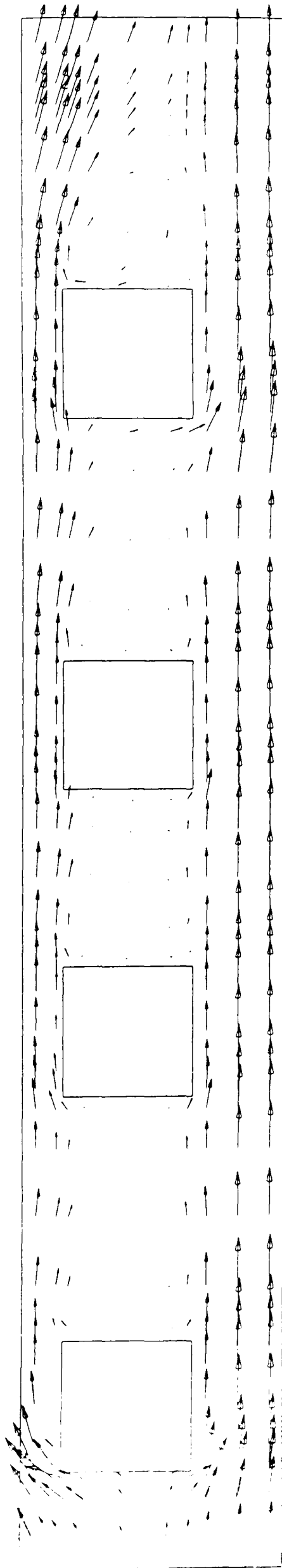
Figure(6.6):

Top view of flow field on a plane through the rig columns